

Université du Québec
Institut National de la Recherche Scientifique
Centre Énergie Matériaux Télécommunications

**ELECTROCHEMICAL BIOSENSORS FOR FOODBORNE
CONTAMINANTS BASED ON APTAMERS AND GRAPHENE
MATERIALS**

Par

Shimaa Hassan Hassan Eissa

Mémoire ou thèse présentée pour l'obtention du grade de
Philosophiaedoctor (Ph.D.)
en sciences de l'énergie et des matériaux

Jury d'évaluation

Président du jury et
examineur interne

Dongling Ma
INRS - Énergie, matériaux et
télécommunications

Examineur externe

Janine Mauzeroll
McGill University

Examineur externe

Clara Santato
École Polytechnique de Montréal

Directeur de recherche

Ana C. Tavares
INRS - Énergie, matériaux et
télécommunications

Codirecteur de recherche

Mohamed Siaj
Université du Québec à Montréal

ACKNOWLEDGMENTS

I would like to acknowledge everybody who supported me during this Ph.D. journey. I would like to sincerely thank my supervisors, Prof. Ana Tavares and Prof. Mohamed Siaj, for their encouragement, help and support during the last two years until the successful completion of this work.

I would like to thank my former supervisor, Prof. Mohammed Zourob for suggesting the research point, his encouragement and kind support during the first two years of this work.

I would like to express my appreciation to Dr. Raja Chinnappan and Dr. Andy Ng for sharing with me their knowledge for the SELEX experiments in the very early stage of this work. I also acknowledge Dr. Chaker Tlili for the useful discussion about the CVD graphene experiments for allergens. My appreciation also goes to Dr. Lamia L'Hocine from Agriculture and Agri-Food Canada for suggesting the allergens (β -LG and OVA) which were studied in this work. I also thank Christophe Chabanier for his help in performing the first XPS measurements at INRS. Thanks to all the characterization facilities (AFM at NanoQam, XPS service and DNA sequencing service at Laval University and (CM)², LCM laboratories at École Polytechnique de Montréal for SEM and Raman Spectroscopy facilities).

I sincerely thank all colleagues and friends from the former BBBL group at INRS and Prof. Siaj group at UQAM for being collaborative and supportive, especially, Reda Elshafey, Esen Sokullu, Teresa Simao, Dr. Mona Tolba, Dr. Irina Stateikina from INRS and Dr. Abdeladim Guermoune, Patrick Brisebois, Jeanne N'diaye, Gaston Contreras Jimenez, Farzaneh Mahvash, Somia Mehennaoui and Filip Popescu from UQAM.

Financial support from INRS, NSERC, FRQNT and NanoQuébec is gratefully acknowledged.

ABSTRACT

Food safety is a global health goal and food quality control is essential for authorities and professional players in the food supply chain. The presence of unsafe levels of foodborne contaminants such as allergens and toxins in food represents a growing public health problem that necessitates the development of efficient tools for their detection. Despite the relatively high sensitivity of some of the currently used detection methods, they are highly laborious, time consuming, require highly trained personnel and are expensive. These limitations encourage the research for alternative tools to be applied in a regulatory monitoring regime in order to guarantee a high level of consumer protection. Therefore, biosensors have appeared recently as interesting alternatives that exhibited potential applications for food quality analysis. Particularly, electrochemical biosensors have become an attractive choice due to their very low cost, high sensitivity, ease of use and capability of miniaturization. However, two main challenges are facing the wide applicability of the available electrochemical biosensors for the detection of food contaminants today. First, the sophisticated detection strategies which are used to obtain the required sensitivity, usually include a time consuming, costly labelling process and multiple reagents and washing steps. Second, the poor specificity of the available recognition receptors, their high cost as well as their limited stability are major disadvantages. To address these challenges, this work describes the development of novel, simple, sensitive, specific and low cost biosensing platforms for the detection of some foodborne contaminants, particularly allergens and toxins.

Advances in nanobiotechnology and its integration in biosensors result in the development of novel sensing platforms with highly improved performance. New biorecognition elements and nanomaterial-based transduction systems are among those nanobiotechnological concepts that are revolutionising the development of electrochemical biosensors. Here, we explore the use of DNA aptamers as recognition receptors as well as graphene platforms as transducers in electrochemical biosensors for food analysis.

First, a functionalization method of graphene electrodes was demonstrated by electrochemical reduction of in situ generated aryl diazonium salts in aqueous acidic solution. Two diazonium salts were utilised in order to show the versatility of this approach: nitrophenyl and carboxyphenyl diazonium salts. The electrochemical modification protocol was optimized in

order to generate monolayer of aryl groups on the graphene surface without complete passivation of the electrode. Unlike the reported methods for graphene functionalization, we demonstrated here the ability of the electrografting of aryl diazonium salt to attach an organic film to the graphene surface in a controlled manner by choosing the suitable grafting protocol. Next, the functionalized graphene electrodes were then used to develop label-free electrochemical immunosensors for the milk allergen β -lactoglobulin (β -LG) as well as the egg allergen ovalbumin (OVA) showing high sensitivity. Moreover, the electrografting approach was then applied on chemical vapour deposition (CVD) grown monolayer graphene in order to enable detailed investigation and characterization of the modified electrodes and subsequently applied for impedimetric biosensing of ovalbumin. This first attempt to use functionalized CVD graphene in biosensing represents a proof of concept that can be extended to other biosensing applications. The carboxyphenyl modified graphene electrodes (CP-GSPE) were also exploited to develop a direct competitive voltammetric immunosensor for the detection of the shellfish toxin okadaic acid (OA). A competitive assay between OA and fixed concentration of okadaic acid-ovalbumin conjugate (OA-OVA) for immobilized antibodies on the CP-GSPE was employed for the detection of OA. The developed immunosensor allowed the sensitive detection of OA in PBS buffer. The matrix effect studied with spiked shellfish tissue extracts showed a good percentage of recovery and the method was also validated with certified reference mussel samples.

Second, I successfully selected, identified and characterized DNA aptamers that bind with high affinity and specificity to OA and brevetoxin-2 (BTX-2), marine biotoxins that accumulate in shellfish. The aptamers were selected using systematic evolution of ligands by exponential enrichment (SELEX) and exhibited dissociation constants in the nanomolar range. The binding of target toxins to aptamer pools/sequences was monitored using fluorescence and electrochemical impedance spectroscopy (EIS) techniques. The aptamers with the highest affinities were then used for the fabrication of label-free electrochemical biosensors for the detection of OA and BTX-2. The selected aptamers offer promising alternatives to the currently employed antibodies and can be exploited in different detection assays for such small molecule toxins.

Third, by integrating the high affinity and specificity of DNA aptamers with the carbon nanomaterial graphene, highly sensitive and selective aptasensor for Microcystin- Leucine,

Arginine (MC-LR) was successfully developed. A specific DNA aptamer against MC-LR that did not show cross reactivity with Microcystin- Leucine, Alanine (MC-LA) and Microcystin-Tyrosine, Arginine (YR) has been utilized as a model. A facile strategy was used for the aptasensor fabrication based on the noncovalent assembly of DNA aptamer on GSPE. This new approach has led to a rapid, low-cost, sensitive and specific detection method for MC-LR in buffer and spiked fish extract samples, offering several advantages over previously reported methods. First, the aptasensor was fabricated without labelling, minimizing cost and complexity, as well as preserving the affinity of the aptamer to MC-LR. Second, the use of graphene electrodes has achieved good sensitivity, particularly when compared with other MC-LR sensors with sophisticated fabrication protocols and detection schemes. Lastly, this graphene-based aptasensor is highly specific to MC-LR, with selectivity against other microcystin congeners hardly achievable by previous attempts. Moreover, we demonstrated in this work that the mechanism of the detection was based on the conformation change in part of the aptamer sequence without complete release from the graphene surface. We believe that this finding is important for exploiting aptamers in the detection of other small molecules using graphene platforms in the future.

Finally, for a better understanding of the behaviour of different graphene samples that can be used for biosensing, a systematic study have been performed in order to investigate to which extent the size of graphene oxide (GO) sheets influence their structural properties as well as their biosensing performance. Graphene oxide sheets with different size ranges were separated. The sheets were then characterized via atomic force microscopy (AFM), scanning electron microscopy (SEM), Raman spectroscopy and X-ray photoelectron spectroscopy (XPS). The biosensing performance of these samples was compared using DNA aptamer against MC-LR toxin as well as an antibody against β -LG in label-free detection format. We observed different trends between the size of GO sheets and the sensitivity of MC-LR aptasensors and β -LG immunosensors fabricated either using covalent attachment or physical adsorption. Our results demonstrate that controlling the size of GO sheets may have profound impact on their use in specific biosensing applications.

Thus, my work lays solid foundations for the development of new electrochemical biosensors for foodborne contaminants based on graphene materials as transducers and aptamers as recognition receptors.

TABLE OF CONTENTS

CHAPTER 1. INTRODUCTION.....	1
1.1 FOODBORNE CONTAMINANTS	1
1.1.1 Allergens	1
1.1.2 Marine toxins	2
1.2 VARIOUS METHODS FOR THE DETECTION OF FOOD ALLERGENS AND TOXINS	5
1.3 BIOSENSORS IN FOODBORNE CONTAMINANTS DETECTION	6
1.3.1 Definition of biosensors	7
1.3.2 Biosensors for food allergens and toxins using different transducers	7
1.3.3 Electrochemical biosensor	8
1.3.3.1 Enzyme inhibition-based electrochemical sensors	9
1.3.3.2 Affinity sensors	10
1.3.4 Label-free electrochemical detection strategy	13
1.3.5 Electrochemical detection techniques	13
1.3.5.1 Voltammetry/amperometry	13
1.3.5.2 Electrochemical impedance spectroscopy	13
1.4 GRAPHENE IN BIOSENSORS	14
1.4.1 Preparation methods of graphene materials and their application in electrochemical biosensors.....	15
1.4.2 Functionalization of graphene.....	16
1.4.3 Size of graphene oxide sheet.....	18
1.5 APTAMERS IN BIOSENSORS	19
1.5.1 Challenges for small molecule aptamers such as toxins	20
1.6 INTEGRATION OF GRAPHENE AND ssDNA INCLUDING APTAMERS IN BIOSENSORS.....	21
1.7 OBJECTIVES, MOTIVATION AND ORIGINALITY OF THE THESIS	22
1.8 THESIS ORGANISATION AND CONTRIBUTION OF AUTHORS	25
CHAPTER 2. EXPERIMENTAL.....	28
2.1 MATERIALS AND REAGENTS	28
2.1.1 Chemical reagents.....	28

2.1.2	Analytes (Proteins and toxins).....	29
2.1.3	Buffer solutions.....	29
2.1.4	Toxin solutions.....	29
2.1.5	DNA aptamer sequences.....	30
2.1.6	Antibodies, ELISA and cloning kits.....	30
2.1.7	Materials for CVD graphene growth and connection.....	30
2.1.8	Filters for graphene oxide sheets separation.....	31
2.1.9	Filters for the SELEX experiments.....	31
2.1.10	Electrochemical cells.....	31
2.2	INSTRUMENTS.....	32
2.3	METHODS.....	33
2.3.1	Graphene oxide and CVD monolayer graphene preparation.....	33
2.3.2	Separation of graphene oxide flakes (Chapter 7).....	33
2.3.3	Preparation of graphene oxide modified electrodes (Chapter 7).....	34
2.3.4	CVD graphene transfer onto glass substrate (Chapter 3).....	34
2.3.5	Connection of CVD graphene sheet as working electrode (Chapter 3).....	34
2.3.6	Graphene functionalization by electrografting of aryl diazonium salts and immunosensors preparation (Chapter 3).....	35
2.3.6.1	β -Lactoglobulin immunosensor.....	35
2.3.6.2	Ovalbumin immunosensors.....	36
2.3.7	Competitive immunosensor for okadaic acid (Chapter 4).....	37
2.3.7.1	Synthesis of OA-OVA conjugates.....	37
2.3.7.2	Functionalization of graphene electrodes and immunosensor fabrication.....	37
2.3.8	In Vitro Selection of the DNA Aptamer against marine toxins (Chapter 5).....	38
2.3.8.1	Coupling of okadaic acid to diaminodipropylamine beads.....	38
2.3.8.2	Coupling of brevetoxin-2 to divinyl sulphone beads.....	38
2.3.8.3	SELEX protocol.....	39
2.3.8.4	Cloning and sequencing of the selected DNA.....	41
2.3.8.5	Binding analysis of the DNA pools and aptamer sequences to target toxins.....	42
2.3.8.5.1	Fluorescence method.....	42
2.3.8.5.2	Electrochemical methods.....	42

2.3.8.6	Dissociation constants determination by fluorescence Assay	42
2.3.8.7	Analysis of the conformation change of the aptamers using circular dichroism..	43
2.3.8.7.1	Okadaic acid aptamer.....	43
2.3.8.7.2	Brevetoxin aptamer.....	43
2.3.8.7.3	Microcystin aptamer (Chapter 6).....	43
2.3.9	Aptasensors for marine toxins (Chapter 5).....	44
2.3.9.1	Okadaic acid aptasensor.....	44
2.3.9.1.1	Preparation of the okadaic acid aptamer-modified electrodes.....	44
2.3.9.1.2	Okadaic acid detection assay	44
2.3.9.2	Brevetoxin aptasensor.....	45
2.3.9.2.1	Immobilization of brevetoxin-2 on the gold electrode	45
2.3.9.2.2	Brevetoxin-2 detection assay	45
2.3.9.3	Microcystin aptasensor (Chapter 6).....	46
2.3.9.3.1	Microcystin aptamer immobilization on graphene-modified screen printed electrodes	46
2.3.9.3.2	Microcystin-LR detection assay and control experiments.....	46
2.3.10	Real food samples analysis	46
2.3.10.1	Extraction of β -lactoglobulin from cake, snacks, and biscuit samples (Chapter 3)	46
2.3.10.2	Preparation of egg-free extract for OVA immunosensor (Chapter 3)	47
2.3.10.3	Extraction of toxins from fish, shellfish tissue and certified reference mussel samples (Chapters 4,5,6).....	47
2.3.10.4	Enzyme-linked immunosorbent assay (ELISA) analysis for β -Lactoglobulin (Chapter 3).....	48
2.3.11	Methods for graphene oxide-based biosensors using different sheet sizes (Chapter 7)	48
2.3.11.1	Physical immobilization of MC-LR Aptamer and β -LG antibody.....	48
2.3.11.2	Covalent Immobilization of NH_2 - modified MC-LR aptamer and β -LG antibody	48
2.3.11.3	Detection and selectivity experiments for B-lactoglobulin and microcystin-LR	49

2.3.12	Graphene-modified screen printed carbon electrodes characterisation	49
2.3.12.1	X-ray photoelectron spectroscopy measurements	49
2.3.12.2	Scanning electron microscopy	50
2.3.13	Characterization of graphene oxide samples	51
2.3.14	Fitting of impedance spectra.....	51
2.4	TECHNIQUES USED THROUGHOUT THE WORK	53

CHAPTER 3. LABEL-FREE ELECTROCHEMICAL IMMUNOSENSORS FOR MILK AND EGG ALLERGENS B-LACTOGLOBULIN AND OVALBUMIN BASED ON ELECTROGRAFTING OF ARYL DIAZONIUM SALTS ON GRAPHENE ELECTRODES 54

3.1	B-LACTOGLOBULIN IMMUNOSENSOR.....	54
3.1.1	Electrochemical functionalization	55
3.1.2	X-ray photoelectron spectroscopy surface characterization	59
3.1.3	Differential pulse voltammetric characterisation of the immunosensor stages	60
3.1.4	Cyclic voltammetric characterization of the mechanism of the electrochemical process on the modified graphene electrodes:	61
3.1.5	Dose response of the β -lactoglobulin immunosensor	62
3.1.6	Selectivity of the immunosensor.....	64
3.1.7	Stability and reproducibility of the immunosensor.....	64
3.1.8	Real Sample Analysis.	65
3.2	OVALBUMIN IMMUNOSENSOR USING GSPE.....	66
3.2.1	Electrochemical functionalization of graphene electrode surface	66
3.2.2	Differential pulse voltammetric characterisation of the immunosensor construction	68
3.2.3	Differential pulse voltammetry detection of ovalbumin on the immunosensor	68
3.3	OVALBUMIN IMMUNOSENSOR USING CVD GRAPHENE	70
3.3.1	Graphene functionalization and characterization.....	71
3.3.2	Electrochemical impedance immunosensor response.....	76
3.4	CONCLUSIONS	78

CHAPTER 4. A GRAPHENE-BASED ELECTROCHEMICAL COMPETITIVE IMMUNOSENSOR FOR THE SENSITIVE DETECTION OF OKADAIC ACID IN SHELLFISH 80

4.1	COMPETITIVE IMMUNOASSAY OF OKADAIC ACID ONTO MODIFIED GRAPHENE ELECTRODES.....	81
4.2	SELECTIVITY OF THE OKADAIC ACID IMMUNOSENSOR.....	83
4.3	STABILITY AND REPRODUCIBILITY OF OA IMMUNOSENSOR.....	83
4.4	MATRIX EFFECT AND OKADAIC ACID DETECTION IN CERTIFIED REFERENCE MUSSEL SAMPLES.....	84
4.5	CONCLUSIONS	84

CHAPTER 5. SELECTION, CHARACTERIZATION AND LABEL-FREE ELECTROCHEMICAL APTASENSORS FOR MARINE TOXINS..... 86

5.1	OKADAIC ACID APTASENSOR.....	86
5.1.1	Okadaic acid aptamer selection	86
5.1.2	Impedimetric aptasensor for OA detection.....	90
5.2	BREVETOXIN APTASENSOR.....	96
5.2.1	Immobilization of brevetoxin-2 on the divinyl sulfone activated beads.....	97
5.2.2	Immobilization of Brevetoxin-2 on the gold electrodes	97
5.2.3	In Vitro Selection of the DNA aptamers.....	100
5.2.4	Binding affinity analysis of the aptamers	102
5.2.5	Optimization of the aptamer-toxin binding conditions.....	104
5.2.6	Electrochemical Competitive Aptasensor.....	105
5.2.7	Analysis of brevetoxin-2 in Spiked Shellfish Samples.....	107
5.3	CONCLUSIONS	108

CHAPTER 6. LABEL-FREE VOLTAMMETRIC APTASENSOR FOR THE SENSITIVE DETECTION OF MICROCYSTIN-LR USING GRAPHENE-MODIFIED ELECTRODES 109

6.1	CHARACTERIZATION AND MECHANISM OF THE APTASENSOR.....	109
6.2	OPTIMIZATION OF APTAMER IMMOBILIZATION	112
6.3	OPTIMISATION OF MC-LR APTASENSOR	114

6.4	DOSE RESPONSE OF THE APTASENSOR.....	115
6.5	SELECTIVITY OF THE APTASENSOR	117
6.6	APPLICATION OF THE APTASENSOR FOR SPIKED FISH EXTRACTS AND TAP WATER SAMPLES.....	117
6.7	CONCLUSIONS	118
CHAPTER 7. INFLUENCE OF GRAPHENE OXIDE SHEETS SIZE ON ELECTROCHEMICAL BIOSENSORS PERFORMANCE		119
7.1	SEPARATION AND CHARACTERIZATION OF GRAPHENE OXIDE SHEETS ACCORDING TO THEIR SIZE	119
7.2	ELECTROCHEMICAL BIOSENSING PERFORMANCE OF THE VARIOUS SHEET SIZES	124
7.3	SELECTIVITY OF THE BIOSENSORS	130
7.4	CONCLUSIONS	132
CHAPTER 8. CONCLUSIONS AND FUTURE PROSPECTIVE.....		133
8.1	CONCLUSIONS	133
8.2	FINAL REMARKS AND FUTURE PERSPECTIVES	136
CHAPTER 9. REFERENCES.....		139
RÉSUMÉ.....		161

LIST OF TABLES

Table 2.1 Surface characterization techniques.....	53
Table 2.2 Electrochemical techniques	53
Table 3.1 Active surface coverage concentration (Γ) of nitrophenyl groups on the GSPE formed using different protocols.	58
Table 3.2 Comparison of performance of the different detection methods for β -lactoglobulin. ..	64
Table 3.3 F-test and t-test calculations for the three food samples analysis.....	65
Table 3.4 Values of I_D/I_G from the Raman spectra and the calculated values of the defect density, σ , for the graphene before and after electrografting.	74
Table 4.1 Recovery percentages with spiked OA and certified reference mussel samples of OA84	
Table 5.1 Sequences and dissociation constants (K_d) between OA and selected aptamers.	89
Table 5.2 Sequences and dissociation constants (K_d) between BTX-2 and selected aptamers. .	103
Table 5.3 Application of the BTX aptasensor in spiked shellfish extracts.....	108
Table 6.1 Results of the detection of MC-LR in fish extracts and water samples (n = 2).....	118

LIST OF FIGURES

Figure 1.1 Chemical structures of okadaic acid, dinophysis toxin-1 (DTX-1) and dinophysis toxin-2 (DTX-2).....	3
Figure 1.2 Chemical structures of brevetoxin-2 and brevetoxin-3.	4
Figure 1.3 Microcystin-LR and some congeners (YR, LA) chemical structures.	4
Figure 1.4 Schematic diagram of the enzyme inhibition-based electrochemical sensors.....	9
Figure 1.5 General scheme for indirect competitive electrochemical immunosensor.....	11
Figure 1.6 General scheme for direct competitive electrochemical immunosensor.....	12
Figure 1.7 Mechanism of diazonium salt electrografting	17
Figure 1.8 Affinity and cross reactivity of the microcystin-targeting aptamers.	21
Figure 1.9 Schematic representation summarizes the objectives of the study and relating the chapters of the thesis.....	22
Figure 2.1 Electrochemical cells used throughout the work. (A) conventional electrochemical cell using gold as working electrode which was used for the OA and BTX aptasensors testing, (B) GSPEs that were used for β -LG, OVA, OA immunosensors and MC-LR aptasensor, (C) DEP electrodes that was modified with GO by drop casting for the testing of the sheet size effect and (D) CVD monolayer graphene connected as a working electrode that was used in a conventional three electrode cell with Ag/AgCl and Pt electrodes.	32
Figure 2.2 Schematic diagram of the SELEX protocol.	41
Figure 2.3 XPS survey spectra for bare GSPE, B) XPS C1s core level spectra for bare GSPE...	50
Figure 2.4 SEM image of bare GSPE.	50
Figure 2.5(A) Nyquist plot of bare graphene electrode in 10 mM $[\text{Fe}(\text{CN})_6]^{4-/3-}$ solution at 0.2 V over a frequency range between 0.1 Hz and 100 Hz. The symbols represent the experimental data and the red curve represent the fitted data using the equivalent circuit (B) The equivalent circuit model used to fit the experimental data. C, is the double layer capacitance; R_{ct} , is the charge transfer resistance; R_s , is the solution resistance.	51
Figure 2.6(A) Example of Nyquist plot of aptamer modified Au electrode. The symbols represent the experimental data and the red curve represent the fitted data using the equivalent circuit. The goodness-of-fit (χ^2) was calculated to be < 0.001 for all the impedance spectra which	

indicates good fit between the theoretical and the experimental data. (B) Modified Randles equivalent circuit which used to fit the impedance results.	52
Figure 3.1 Functionalization of the graphene electrode surface and the covalent immobilization of antibodies.....	55
Figure 3.2(A) Cyclic voltammogram for the <i>in situ</i> generated 4-nitrophenyl diazonium salt in the diazotization mixture (2 mM NaNO ₂ + 2 mM 4-nitroaniline in 0.5 HCl) at graphene modified screen printed electrode, (B) Successive cyclic voltammograms of the reduction of NP/GSPE in 0.1M KCl at scan rate of 100 mVs ⁻¹ . The solid lines represent the first CV and the dotted lines represent the subsequent cycles.....	56
Figure 3.3 XPS survey spectra for bare GSPE (A) and NP-GSPE (B).....	59
Figure 3.4 XPS core level N1s spectra of NP-GSPE and AP-GSPE.....	60
Figure 3.5 DPVs of 5 mM [Fe(CN) ₆] ^{4-/3-} probe in PBS, pH 7.4 for bare GSPE (a); 4-nitrophenyl/ GSPE modified electrode (b), 4-aminophenyl/ GSPE modified electrode (C), GA/4-AP/ GSPE (d), Ab/4-AP/ GSPE modified electrode (e), after blocking with 0.25% BSA for 45 min (f) and After incubation with 100 ng ml ⁻¹ of β-lactoglobulin solution for 45 min (g). .	60
Figure 3.6 CVs of the modified electrode at different scan rates (from inner to outer): 10, 20, 30, 40, 50, 60, and 70 mV/s in 5 mM [Fe(CN) ₆] ^{3-/4-} solution. The inset shows the dependence of the oxidation and reduction peak currents on the square root of scan rates.	62
Figure 3.7(A) DPVs of the immunosensor incubated with different concentrations of β-lactoglobulin (1–7): the concentrations of β- LG are 0.000, 0.001, 0.01, 0.1, 1.0, 10 and 100 ng mL ⁻¹ . The inset is the calibration curve based on the change of the DPV peak currents versus the logarithm of the concentrations, (B) Comparison of response of GSPE voltammetric immunosensor to 1000 ng ml ⁻¹ ovalbumin or 100 ng ml ⁻¹ β-lactoglobulin....	63
Figure 3.8 Schematic of the electrografting process of carboxyphenyl groups on the graphene electrode and the subsequent antibody immobilization.	66
Figure 3.9(A) Successive CVs for the <i>in situ</i> generated 4-carboxyphenyl diazonium salt at scan rate of 100 mVs ⁻¹ on GSPE, the black line represent the first CV and the red lines represent the subsequent cycles, (B) DPVs of bare GSPE and 4-CP-GSPE functionalized by diazonium salt reduction using different CV cycles in 5 mM [Fe(CN) ₆] ^{4-/3-} at 100 mV/s. Inset is the plot of the reduction peak current for 5 mM [Fe(CN) ₆] ^{4-/3-} measured at 4-CP-GSPE vs. the number of CV scanning cycles for diazonium reduction on GSPE.....	67

Figure 3.10 DPVs of 5 mM $[\text{Fe}(\text{CN})_6]^{4-/3-}$ probe in PBS, pH 7.4 for bare GSPE (a), 4-CP/ GSPE (b), Ab/4-CP/ GSPE (c), and after blocking with 0.1% BSA for 30 min (d).	68
Figure 3.11(A) DPVs of the immunosensor incubated with different concentrations of ovalbumin. The inset is the calibration curve, (B) Comparison of response of the immunosensor to 100 ng ml ⁻¹ ovalbumin, BSA, Casein, Lysozyme, and β -lactoglobulin...	69
Figure 3.12 Optical microscopic image of monolayer graphene film on Cu foil. (B) SEM image of graphene (C) Monolayer graphene film transferred onto a glass sheet, (D) Schematic of the procedure for connecting monolayer graphene sheets into working electrodes for electrochemical measurements.	70
Figure 3.13 Optical microscopy images of CVD monolayer graphene film before (A) and after (B) the transfer process; (C) Raman spectra of CVD monolayer graphene film before (bottom) and after (top) the transfer process; (D) XPS C1s core level spectra for CVD monolayer graphene film before (bottom) and after (top) the transfer process.	71
Figure 3.14 Successive CVs for the 4-carboxyphenyl diazonium salt at scan rate of 100 mVs ⁻¹ on CVD graphene.	72
Figure 3.15(A) Raman spectra of the graphene electrode before (Black curve) and after subjected to the electrografting process using one (red curve) and three (blue curve) CV cycles and (b) XPS C1s core level spectra of graphene electrode before (bottom) and after (top) the carboxyphenyl functionalization.....	73
Figure 3.16(A) AFM images of bare graphene and (B) carboxyphenyl modified graphene. (C) The height profiles with two selected line scans. Green line indicates the bare graphene, and blue line indicates the modified graphene. The average height of the carboxyphenyl groups is around 0.69 nm and (D) theoretical estimation of the length of the carboxyphenyl moiety using ChemDraw Ultra 13.0 software.	75
Figure 3.17(A) Nyquist plot of bare GE and 4-CP-GE functionalized by diazonium salt reduction using different CV cycles in 10 mM $[\text{Fe}(\text{CN})_6]^{4-/3-}$ at 100 mV/s. Inset: The equivalent circuit used for fitting the experimental results; (B) Plot of R_{ct} of 4-CP-GE in 10 mM $[\text{Fe}(\text{CN})_6]^{4-/3-}$ vs. the number of CV scanning cycles for diazonium reduction on GE.	76
Figure 3.18 Nyquist plot of bare GE; 4-CP/ GE, Ab/4-CP/ GE and after blocking with 0.1% BSA for 30 min. in the presence of 10 mM $[\text{Fe}(\text{CN})_6]^{4-/3-}$ probe in PBS, pH 7.4.	77

Figure 3.19(A) Nyquist plot of OVA immunosensor before (black) and after (red) incubation with 0.1 ng/ml OVA. (B) Dependence of the immunosensor response on OVA concentration (plot of $(R-R_0)/R_0$ % vs. C_{OVA}). Inset: calibration curve for OVA, plot of $(R-R_0)/R_0$ % vs. $\log C_{OA}$ and (C) Comparison of response of the immunosensor to 100 ng ml⁻¹ ovalbumin, 1 μg/ml Lysozyme, and β-lactoglobulin..... 78

Figure 4.1 Schematic diagram of the working principal of the immunosensor with direct competitive immunoassay..... 80

Figure 4.2 SWVs of the immunosensor before the competition step (1) and after incubated with different concentrations of OA mixed with 1 μg/ml of OA-OVA (2–6): the concentrations of OA are 0.000, 1.00, 10.0, 100 and 1000 ng L⁻¹. 81

Figure 4.3(A) Dependence of the immunosensor response on OA concentration (plot of the difference in the peak current vs. C_{OA}). Inset: calibration curve for OA, plot of peak current vs. $\log C_{OA}$, (B) Comparison of the response of GSPE voltammetric immunosensor to 10 μg L⁻¹ OA and MC-LA. 82

Figure 5.1 Enrichment of okadaic acid-specific aptamers during SELEX. The bar graph shows the amounts of ssDNA eluted from OA-coated beads in each selection round. In round five, a counter selection step (CS) was introduced to remove ssDNA nonspecifically bound to the bead matrix..... 87

Figure 5.2 Analysis of the selected sequences by multiple sequence alignment using PRALINE software. The sequences were grouped into eight families (A-H) and a representative sequence was chosen from each group (OA 24, 21, 34, 18, 11, 32, 6, 26)..... 88

Figure 5.3(A) Fluorescence binding assay of OA and aptamer OA34. The K_d was determined to be 77 nM. Each point is the mean of three experiments and error bars represent the standard deviations of the measurements, (B) Circular dichroism spectra of 0.67 μM aptamer OA34 in binding buffer before (black) and after (red) binding with 0.66 μg/ml of OA at room temperature. 90

Figure 5.4 Scheme of the fabrication of the impedimetric aptasensor based on label-free target-induced folding of the aptamer. 91

Figure 5.5 Cyclic voltammetry (A) and Nyquist plots (B) of 5 mM $[Fe(CN)_6]^{4-/3-}$ redox couple in PBS, pH 7.4, for bare Au electrode (black), Au/ aptamer (red), Au/aptamer/MCH (green), and after binding with 60 ng/ml OA (blue). The cyclic voltammetry was performed at scan

rate of 100 mV/s and the EIS was performed using a frequency range of 10 ⁴ to 0.1 Hz, a DC potential of +0.23 V and AC amplitude of 5 mV. The inset is the equivalent circuit applied for fitting.	92
Figure 5.6(A) The effect of adding extra concentration of MCH, (B) the effect of the OA incubation time on aptasensor response towards 30 ng/ml OA in 10 mM PBS (pH 7.4) containing 5 mM [Fe(CN) ₆] ^{4-/3-} redox couple.....	93
Figure 5.7(A) Nyquist plots of the aptasensor after incubation with different concentrations of OA 0.00, 0.1, 1.0, 10, 20, 30, 40, 50 and 60 ng/ml. (B). The calibration curve for OA, plot of ΔR _{ct} /R _o % vs. C _{OA} . The error bars show the standard deviation of three repetitive measurements.....	94
Figure 5.8(A) Linearized adsorption isotherm of OA binding to its aptamer immobilized on gold electrode based on the Langmuir model. The line is the best linear fit to the experimental data from which the dissociation constant K _d was determined. (B) Comparison of response of the aptasensor after incubation with 10 ng ml ⁻¹ OA, binding buffer, MC-LR, DTX-1, and DTX-2.	96
Figure 5.9 Attachment of BTX-2 to the divinyl sulfone beads.....	97
Figure 5.10(A) Modification of the gold electrode surface and covalent immobilization of BTX-2, (B) the working principal of the aptasensor with competitive assay.	98
Figure 5.11 Cyclic voltammetry (A) and Nyquist plots (B) of 5 mM [Fe(CN) ₆] ^{4-/3-} redox couple in PBS, pH 7.4, for bare Au electrode (black), Cys/Au (red) and BTX/PDIC/Cys/Au (blue). The CV was performed at scan rate of 100 mV/s and the EIS was performed using a frequency range of 10 ⁴ to 0.1 Hz, a DC potential of +0.20 V and AC amplitude of 10 mV. The inset in Figure 5.11(B) is the equivalent circuit applied to fit the impedance spectra. .	99
Figure 5.12 Binding of ssDNA pools to BTX-2 after each selection round monitored by calculating the recovery percentage from the fluorescence of eluted DNA (red) and % R _{CT} change ; (R _{CT} -R _I)/R _I %; of the BTX electrodes after binding (black).	101
Figure 5.13 Multiple sequence alignment of the selected aptamers	101
Figure 5.14(A) Binding assays with the individual aptamer clones BTX 1, 10, 5, 3, 31, 22 and 9, to test their ability to bind to BTX-beads (red) and BTX electrodes (black). The unenriched initial library was used as the negative control. (B) Fluorescence binding curve of BTX-2 to aptamer BT10 (black) and a scrambled DNA sequence (red).	102

Figure 5.15 Secondary structure prediction for the BT10 aptamer.	103
Figure 5.16 The effect of incubation time (A), Mg^{2+} ions concentration (B) and pH of the binding buffer (C) on BTX-aptamer binding, monitored by measuring the % R_{CT} change in 10 mM PBS (pH 7.4) containing 5 mM $[Fe(CN)_6]^{4-/3-}$ redox couple after incubating the BTX electrodes with 500 nM aptamer. The error bars represent the standard deviation of the measurements. (D) The CD spectra of the BTX aptamer in binding buffer with different pHs.	104
Figure 5.17(A) Nyquist plots of the BTX electrode before and after incubation with different concentrations of BTX-2 mixed with 500 nM aptamer, (B) the calibration curve for BTX-2, plot of analytical response (% Signal, $[(R_{CT} - R_I)/(R_{max} - R_I) \times 100]$) vs. BTX-2 concentration. The error bars show the standard deviation of two repetitive measurements.	106
Figure 5.18 Comparison of response of the aptasensor to 1 ng/ml BTX-2, BTX-3, MC-LR, and OA.	107
Figure 6.1 Schematic of MC-LR detection based on SWV on aptamer-functionalized GSPE.	110
Figure 6.2(A) SWVs of 1 mM $[Fe(CN)_6]^{4-/3-}$ probe in PBS, pH 7.4 for bare GSPE (black), MC-LR aptamer-functionalized GSPE (red), and after MC-LR toxin incubation (blue) (concentration of the aptamer, 10 μ M; concentration of MC-LR, 1 nM); (B) CD spectra of 0.67 μ M MC-LR aptamer in binding buffer before (black) and after (red) binding with 0.67 μ M of MC-LR at room temperature; (C) CD spectra of 0.4 μ M Fc/Ap in binding buffer before (black) and after (red) binding with 0.4 μ M of MC-LR at room temperature; (D) SWV in blank 10 mM PBS buffer solution pH 7.4 for Fc/Ap/GSPE (black), after incubation of Fc/Ap/GSPE with 1 nM MC-LR (red), and after incubation of Fc/Ap/GSPE with cDNA (green).	111
Figure 6.3(A) SWVs of 1 mM $[Fe(CN)_6]^{4-/3-}$ probe in PBS, pH 7.4 for GSPE after 2, 5 and 10 min incubation with 10 μ M MC-LR aptamer. The inset is the percentage of the $[Fe(CN)_6]^{4-/3-}$ peak current change vs. the immobilization time of MC-LR aptamer on GSPE. (B) SWVs of 1 mM $[Fe(CN)_6]^{4-/3-}$ probe in PBS, pH 7.4 for GSPE incubated with different concentrations of MC-LR aptamer for 10 min. The inset is the percentage of the $[Fe(CN)_6]^{4-/3-}$ peak current change vs. the MC-LR aptamer concentration.	113
Figure 6.4(A) The effect of incubation time on aptasensor response towards 1 nM MC-LR. (B) The aptasensor response towards 1 nM MC-LR in binding buffer contains different	

concentration of MgCl₂. (C) The aptasensor response towards 1 nM MC-LR in binding buffer with different pHs. All the measurements were done in 10 mM PBS (pH 7.4) containing 1 mM [Fe(CN)₆]^{4-/3-} redox couple. (D) The CD spectrum of the MC-LR aptamer in binding buffer with pH 7.5 (black), 8.8 (red), and 3.4 (green curve). 115

Figure 6.5(A) SWVs of the aptasensor after 45 min incubation with 0.00, 0.1, 1.0, 10, 100 and 1000 pM MC-LR. The inset is the dependence of the aptasensor response on MC-LR concentration (plot of the percentage of the peak current change vs. C_{MC-LR}), the small Inset: calibration curve for MC-LR detection in binding buffer; is a plot of the percentage change in the peak current versus the logarithm of the MC-LR concentrations. (B) Response of the aptasensor to 1.0 nM of MC-LR, OA, MC-LA, and MC-YR. The inset is the comparison between the response of modified GSPE with MC-LR aptamer and non specific DNA sequence to 1 nM MC-LR. Error bars correspond to duplicate measurements. 116

Figure 7.1(A) Digital camera images of the ultracentrifuge tubes after centrifugation, (B) SEM image of graphene oxide sheets separated only by centrifugation. 120

Figure 7.2 AFM and SEM images of the graphene oxide sheets..... 121

Figure 7.3 Scanning electron micrographs of the GO-modified electrodes (sheet sizes: 0.2, 2.0, 300 μm)..... 121

Figure 7.4 Raman spectra of the different GO samples..... 122

Figure 7.5(A) XPS C 1s spectra of different sized graphene oxide sheets, (B) a plot of P_{GO}/P_G versus the size of GO sheet and (C) ¹³C NMR spectra for the smallest (0.22 μm) and largest (>100 μm) GO sheets..... 123

Figure 7.6 Schematic diagrams of the four different biosensing platforms..... 125

Figure 7.7 SWVs of the aptasensor fabricated using physical adsorption (A) and covalent immobilization (B) for bare GO-DEP electrodes (black), MC-LR aptamer-functionalized electrodes (red), and after MC-LR toxin incubation (blue) (concentration of the aptamer, 10 μM; concentration of MC-LR, 1 nM); SWVs of the immunosensors fabricated using physical adsorption (C) and covalent immobilization (D) for bare GO-DEP electrodes (black), β-LG antibody-functionalized electrodes (red), and after β-LG incubation (blue) (concentration of the antibody, 10 μg/ml; concentration of β-LG, 1 μg/ml). All measurements were done in 1 mM [Fe(CN)₆]^{4-/3-} probe in PBS, pH 7.4. 126

Figure 7.8 Comparison of the change in the SWV peak current towards the various amounts of A) MCAP , B) NH₂-MCAP, C) β-LG antibody and D) covalently immobilized β-LG antibody deposited onto graphene oxide modified DEP electrode surface. Signal is represented as $(i_o-i)/i_o\%$. Red columns represent the smallest GO sized sheets and green columns represent the largest GO sized sheets. Error bars correspond to duplicate measurements. All measurements were performed with 10 mM [Fe(CN)₆]^{4-/3-} in PBS buffer, pH 7.4 at room temperature. 127

Figure 7.9 Comparison of change in SWV peak current of the different GO sized-sheets electrodes after the incubation with MC-LR (1 nM) or β-LG (1μg/ml) for the four different cases. Binding signal response represented as $(i_p-i)/i\%$ for the aptasensors fabricated by physical adsorption (A), and covalent immobilization (B) and as $(i-i_p)/i\%$ for the immunosensors fabricated by physical adsorption (C), and covalent immobilization (D). 129

Figure 7.10 Selectivity experiments of the biosensors prepared using smallest GO sized sheets (red columns) and largest GO sized sheets (green columns); response of the aptasensors fabricated using physical adsorption (A) and covalent immobilization (B) to 1.0 nM of MC-LR, OA, and MC-LA; response of the immunosensors fabricated using physical adsorption (C) and covalent immobilization (D) to 1.0 μg/ml of β-LG, OVA, and BSA.. 131

Figure 8.1 Schematic representation of the secondary structures of the aptamers which exhibited good binding to okadaic acid as predicted by the mfold program. (A) OA 11, (B) OA 32, (C) OA 21, (D) OA 22, (E) OA 24, and (F) OA 34..... 137

LIST OF ABBREVIATIONS

PDIC	1,4-phenylene diisocyanate
EDC	1-ethyl-3-(3-dimethylaminopropyl) carbodiimide hydrochloride
MES	2-N-morpholino ethanesulfonic acid
AP	4-aminophenyl
CP	4-carboxyphenyl
4-CPDS	4-carboxyphenyl diazonium salt
MCH	6-mercapto-1-hexanol
AP-GSPE	Aminophenyl graphene-modified screen printed electrodes
ASP	Amnesic shellfish poisoning
anti-OA-MAb	Anti-okadaic acid monoclonal antibody
anti-OVA-MAb	Anti-ovalbumin monoclonal antibody
AFM	Atomic force microscopy
AZP	Azaspiracid shellfish poisoning
BSA	Bovine serum albumin
BTX-2	Brevetoxin-2
CP-GSPE	Carboxyphenyl modified graphene electrodes
CRM-DSP Mus-b	Certified reference mussel samples
R_{CT}	Charge transfer resistance
CVD	Chemical vapour deposition
CA	Chronoamperometric
CEP	Ciguatera fish poisoning
CPE	Constant phase element
CS	Counter selection step
CV	Cyclic voltammetry
Cys	Cysteamine hydrochloride
Cys/Au	Cysteamine-modified gold electrodes
TDI	Daily intake value
DADPA	Daminodipropylamine agarose

DSP	Diarrheic shellfish poisoning
DPV	Differential pulse voltammetry
DTX-1,2	Dinophysistoxin 1,2
DEP	Disposable electrical printed
DVS	Divinyl sulfone
EIS	Electrochemical impedance spectroscopy
ELISA	Enzyme-linked immunosorbent assays
Fc/Ap	Ferrocene-labelled aptamer
GA	Glutaraldehyde
AuNPs	Gold nanoparticles
GO	Graphene oxide
GSPE	Graphene-modified screen printed carbon electrodes
HRP	Horseradish peroxidase
HPLC	High-performance liquid chromatography
MC-LR	Microcystin- Leucine, Arginine
MC-LA	Microcystin- Leucine, Alanine
MC-YR	Microcystin- Tyrosine, Arginine
MCs	Microcystins
NSP	Neurologic shellfish poisoning
NHS	N-hydroxysuccinimide
4-NPDS	Nitrophenyl diazonium salt
OA	Okadaic acid
OA-OVA	Okadaic acid-ovalbumin conjugate
PSP	Paralytic shellfish poisoning
PMMA	Poly methyl methacrylate
PP	Protein phosphatases
SEM	Scanning electron microscopy
SAM	Self-assembled monolayer
ssDNA	Single-stranded DNA
SDS	Sodium dodecyl sulfate
SWV	Square wave voltammetry

Rs	Solution resistance
SPR	Surface plasmon resonance
SELEX	Systematic evolution of ligands by exponential enrichment
CDC	US Centers for Disease Control and Prevention
Z _w	Warburg impedance
WHO	World Health Organization
XPS	X-ray photoelectron spectroscopy
β-LG	β-lactoglobulin

LIST OF VARIABLES AND CONSTANTS

Symbol	Name	Unit
i	Current	A
E	Potential	V
R	Resistance	Ω
C	Concentration	M or g/l
ν	Frequency	Hz
v	Scan rate	V/s
Z	Impedance	Ω
Q	Charge	C
Γ	Surface coverage	mol./cm ²
A	Surface area	cm ²
Θ	Elipticity	mdeg
σ	Defect density	mol/cm ⁻²
L_D	Mean defect spacing	cm
r_s	Radius of damage region around each sp ³ bond	nm
r_A	Radius of activated area around it	nm
F	Faraday constant	C mol ⁻¹
n	number of electrons transferred	e
K_d	Dissociation constant	M

CHAPTER 1. INTRODUCTION

1.1 Foodborne contaminants

The contamination of food is a serious issue due to its harmful impact on the public health. Foodborne illness has very negative effect on the world's economy in terms of medical costs, lost productivity, and product recalls. It costs the European economy hundreds of millions of Euros each year ¹⁻². The US Centers for Disease Control and Prevention (CDC) estimates that more than 36 million cases of illness occur annually in USA because of foodborne contaminants ³. Similar trend is also recorded in Canada, where the Public Health Agency of Canada estimates that each year roughly one in eight Canadians (or four million people) get sick due to foodborne diseases ⁴. Therefore, food quality and safety is a priority area of research worldwide. Food contamination can be due to the presence of either biological (pathogenic bacteria, parasites, viruses), chemical contaminants (natural toxins, pesticides) or allergens which results in consumer illness. In the following two subsections, we will provide a brief introduction about allergens and marine toxins with a special focus on the analytes under study (β -lactoglobulin, ovalbumin, okadaic acid, brevetoxins and microcystins).

1.1.1 Allergens

Food allergy has become one of the major health concerns nowadays ⁵⁻⁶. Eating certain types of food can trigger an immune reaction in allergic individuals leading to serious health problems. So far, there is no effective treatment for food allergens suffers and the only way to manage the health hazards resulting from allergens is to avoid the specific allergen containing food. Food allergy affects millions of people worldwide. Global estimates suggest that up to 6–8% of infants ⁷ and 4% of the adult population are affected ⁸. Extrapolating these figures to the current population of Canada suggests a total of about a million food allergy sufferers. Recent studies in USA indicate approximately 125,000 emergency department visits ⁹ and 53,700 episodes of anaphylaxis ¹⁰ from foods each year. Food-induced anaphylaxis has resulted in a 350% increase in hospitalizations during the last decade and the CDC report in 2008 indicated an

18% increase in childhood food allergy from 1997 to 2007 ¹¹. Data for Canada is expected to be proportionally similar.

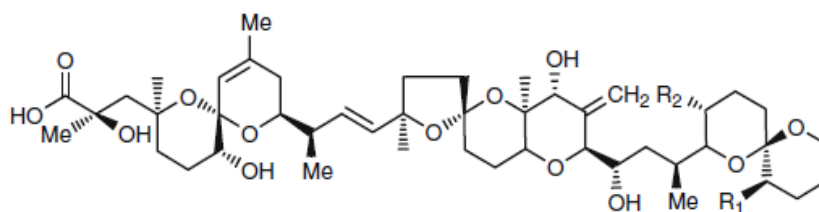
Egg is one of the most common causes of food allergies in children, particularly infants under 3 years old ¹²⁻¹⁵. It is considered the first cause of allergens in some countries exceeding even the cows' milk allergy. The most common allergens in egg are the four chicken egg white proteins; ovalbumin, ovomucoid, ovotransferrin, and lysozyme ¹⁶⁻¹⁷. Ovalbumin is the most abundant protein in egg white comprising 58% of the whole egg white proteins, therefore it can be used as a marker for the presence of egg contamination in food products.

Milk is another common cause of food allergy ¹⁸⁻¹⁹, affecting between 2% and 3% of infants ²⁰. β -lactoglobulin which represents 10 % of the cow's milk proteins is considered the most important milk allergen especially for children. Although egg and milk are among the food components which should be listed on the label of the food products, most of the allergenic reactions in sensitive consumers occur due to unexpected exposure of those proteins in a product where egg or milk are not included in the ingredient list. This can be due to inadequate cleaning of the food processing equipment or during transfer or storage processes. This hidden or accidentally introduced allergens may cause serious allergic reactions for the sensitive individuals and leads to urticaria, angioedema, or anaphylaxis ¹⁵. Therefore, reliable detection methods for traces of food allergens on food production equipment and in food products are needed for regulatory agencies, food processors and manufacturers to ensure that the risks to allergic individuals are minimized.

1.1.2 Marine toxins

Marine toxins are naturally occurring chemicals which usually are produced by several species of dinoflagellates and diatoms and accumulate in certain seafood. The seafood contaminated with these chemicals usually looks, smells, and tastes normal. Eating such seafood can lead to intoxication in human. Different types of poisoning from marine toxins have been identified with each one being responsible for different symptoms such as 1) diarrhetic shellfish poisoning (DSP); 2) paralytic shellfish poisoning (PSP); 3) amnesic shellfish poisoning (ASP); 4) neurologic shellfish poisoning (NSP); 5) azaspiracid shellfish poisoning (AZP); 6) ciguatera fish poisoning (CFP); 7) puffer fish poisoning.

Okadaic acid is a lipophilic marine biotoxin produced by *Dinophysis* and *Prorocentrum* dinoflagellates and accumulates in various species of shellfish, mainly in mussels, scallops, oysters and clams ²¹. OA has several analogues such as the dinophysis toxins (DTX1, DTX2) (Figure 1.1) which have very similar structures but not all of them have the same toxicity levels.



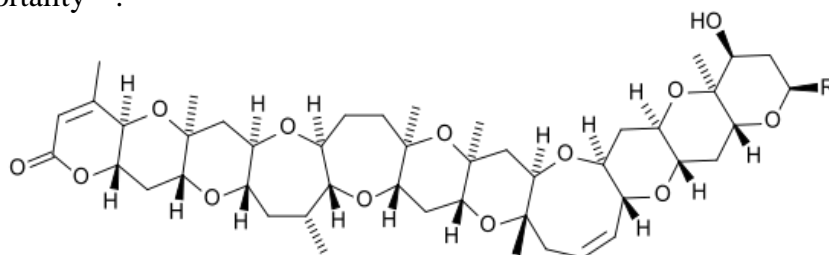
Substance	R1	R2
OA	H	H
DTX-1	Me	Me
DTX-2	Me	H

Figure 1.1 Chemical structures of okadaic acid, dinophysis toxin-1 (DTX-1) and dinophysis toxin-2 (DTX-2).

Okadaic acid is tasteless, odourless and has no harmful effect on the shellfish. However, the consumption of OA contaminated shellfish by human results in severe toxic effect known as diarrhetic shellfish poisoning ²². It leads to gastroabdominal disturbances including nausea, vomiting, and diarrhea. Studies have shown that the OA toxicity is due to the inhibition of protein phosphatases (PP), PP1 and PP2A ²³⁻²⁴ and some studies have also proven that OA has carcinogenic and immunotoxic effects ²⁵. Okadaic acid contaminated shellfish has become a serious food safety problem affecting the shellfish industry worldwide. The maximum allowed level of OA is 160 $\mu\text{g kg}^{-1}$ of mussels ¹³.

Brevetoxins are potent cyclic polyether neurotoxins naturally produced by the marine “red tide” dinoflagellates *Karenia brevis* and accumulate also in shellfish. They exhibit toxicity towards marine mammals, birds, fish and humans ²⁶. Brevetoxins have increased in geographical distribution in the past decade causing the illness clinically described as neurological shellfish poisoning. BTXs are tasteless, odourless, heat and acid stable. The exposure of human to BTXs can occur through consumption of contaminated shellfish as well as aerosol exposure in coastal areas. BTX-2 and -3 (Figure 1.2) are the most predominant forms among ten BTXs that have

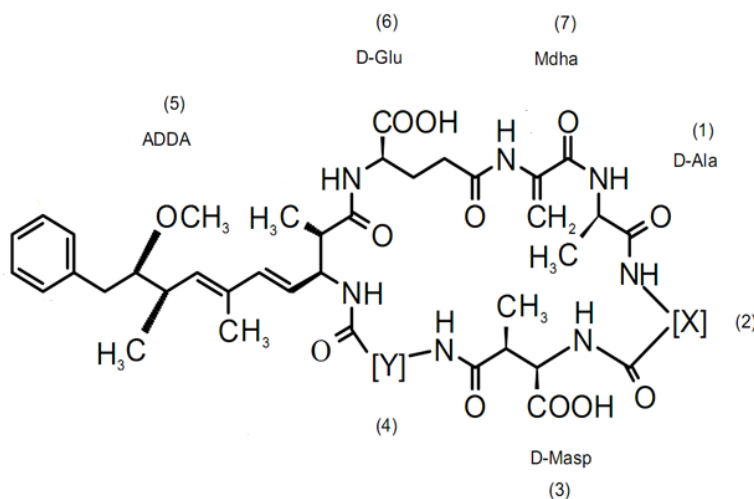
been isolated and characterized from aerosols, field blooms and *Karenia brevis* cultures²⁷⁻²⁸. BTXs bind to the voltage-gated sodium channels in nerve cells leading to neurologic poisoning and even mortality²⁸.



- Brevetoxin-2 (PbTx-2) R = $-\text{CH}_2\text{C}(\text{=CH}_2)\text{CHO}$
- Brevetoxin-3 (PbTx-3) R = $-\text{CH}_2\text{C}(\text{=CH}_2)\text{CH}_2\text{OH}$

Figure 1.2 Chemical structures of brevetoxin-2 and brevetoxin-3.

Microcystins are well known group of toxins produced from cyanobacteria or blue-green algae which have harmful effect on animals and human health. Microcystins (MCs) are cyclic polypeptides consisting of five constant amino acids and two varying L-amino acids, forming a family of congeners which have different toxicities²⁹ (Figure 1.3).



Substance	X	Y
MC-LR	Leucine	Arginine
MC-YR	Tyrosine	Arginine
MC-LA	Leucine	Alanine

Figure 1.3 Microcystin-LR and some congeners (YR, LA) chemical structures.

Acute or chronic exposure to microcystins via skin contact, consumption of poisoned drinking water or agriculture products irrigated by contaminated water can cause liver damage and may even lead to death ³⁰. It was also established recently that fish consumption might be dominant source of microcystin exposure for humans ³¹. Microcystins have also shown tumor promotion effect ³²⁻³³ as well as potent inhibition of protein phosphatases 1A (PP1A) and 2A (PP2A) ³⁴⁻³⁵, two key enzymes in cellular processes. Microcystin-LR (MC-LR), which contains leucine and arginine at the two variable positions, is the first chemically identified and widely studied microcystin among more than 80 microcystin congeners isolated so far ³⁶. Moreover, MC-LR is considered the most hepatotoxic congener among all microcystins with a LD50 of 43 µg/kg ³⁷. In 1998, the World Health Organization (WHO) has set a maximum permitted level of 1 µg/L for MC-LR in drinking water and daily intake value (TDI) of 0.04 µg/kg MC-LR/body weight ³⁸.

1.2 Various methods for the detection of food allergens and toxins

Several analytical methods have been developed for the detection of allergens such as enzyme-linked immunosorbent assays (ELISA) ³⁹, HPLC (High-performance liquid chromatography) ⁴⁰ and capillary electrophoresis ⁴¹⁻⁴² methods with laser-induced fluorescence detection ⁴³, enzyme linked immunoaffinity chromatography ⁴⁴, and size-exclusion chromatography ⁴⁴. Protein-based methods such as western blot ⁴⁵ and immunoperoxidase staining ⁴¹ were also used. A rolling circle amplification-procedure has been also developed to enhance signals of ovalbumin immunoassay combined with fluorescent dye and a circular DNA probe allowing the sensitive and real-time detection of OVA ⁴⁶.

For small molecule toxins (such as okadaic acid, brevetoxins and microcystins), the current detection methods are mainly based on animal assays, chromatographic techniques, enzymatic assays and immunological methods. Each of these techniques has different strengths and weaknesses: **1. Chromatography:** The most commonly used chromatography technique is HPLC that is usually equipped with different detection methods such as absorbance, UV and diode array detector. However, separation of different toxins variants is difficult because they are structurally very similar. **2. Chromatography coupled with mass spectrometry (HPLC-MS):** Coupling of HPLC to mass spectrometry resulted in an improvement in the detection limit and

specificity. However, these machines are very expensive (\$1M each) and are unsuitable for field application. They also cannot be used for routine screenings and require highly skilled personnel to operate. **3. Animal assays:** Mouse bioassay detects sample toxicity by injection into male swiss Albino mice followed by observation that lasts several days. During the observation period clinical symptoms and mortality are recorded. The mouse bioassay is a measure of total toxicity but it is neither specific nor sensitive enough. Furthermore, a license is required to perform this assay and in some countries the use of this test is not permitted. Mouse bioassays have been widely considered as a reference method for the detection of most of marine biotoxins including MCs, OA and BTXs based on the European regulations ⁴⁷⁻⁴⁸ until it was prohibited in January 2011 due to ethical concerns. **4. Protein phosphatase inhibition assays:** Phosphatase assay initially involves the release of ³²P-phosphate from radio-labelled substrate by the phosphatase activity of PP1 and PP2A. This assay is sensitive to nanogram level and is relatively quick. The major disadvantage is the use of radioactivity. A colorimetric phosphatase inhibition assay has thus been developed. The level of MCs or OA is determined from the reduced phosphatase activity in these assays. However, these enzymatic assays suffer from the low stability of the enzyme, its sensitivity to the food matrix and are not specific because of the inhibition of the PP2A enzyme by different groups of toxins. **5. Immunological methods** Commercial ELISA kits are available in single test or microtitre assay formats for OA, BTXs and MCs. However, they suffer from cross-reactivity to the toxin variants. For example, other MCs congeners cross react with MC-LR, against which antibodies have been raised. In summary, ELISA is the simpler, commercially available and relatively sensitive method which can be routinely used for the detection of allergenic proteins including ovalbumin and β -lactoglobulin ⁴⁹⁻⁵⁴ as well as most of toxins ⁵⁵⁻⁵⁶. However, it is still time-consuming and costly, particularly when multiple targets need to be screened and sometimes suffers from cross-reactivity between the different variants of the toxins which makes it difficult to be used for field applications.

1.3 Biosensors in foodborne contaminants detection

In order to enhance the food safety, the end product testing is not sufficient. However, the analysis of contaminants has to be performed throughout the food chain from primary production to final consumption. For this, the detection techniques must be able to be done rapidly on-site at

extreme sensitivity and specificity, without the needs for laboratory equipments for samples processing. They must also operate with user-friendly, low-cost, robust, reliable and rapid detection devices that are suitable for field applications. After giving an overview on the currently used conventional methods for allergens and toxins detection, it is clear that these methods are slow, costly and laborious and sometimes requires sophisticated instruments operating in centralized laboratories. Hence, the development of simple, rapid and sensitive biosensor technology that overcome these limitations is crucial. Biosensors represent an attractive alternative to the conventional detection methods and provide one of the most promising ways for simple, fast, reproducible, and cheap multi-analyte detection. The following subsections will provide an overview over the recent advances of the biosensors application in food analysis. Particular emphasis is given to the application of electrochemical biosensors in food allergens and toxins.

1.3.1 Definition of biosensors

A biosensor is an integrated device consists of a biological recognition element (biorecognition receptor) in direct spatial contact with transduction element, which converts the biological-recognition event into a measurable chemical- physical signal, that is proportional to the target concentration. The biorecognition receptor can be a protein such as enzyme or antibody raised against certain food analyte, a single-stranded DNA molecule capable of hybridizing with an allergen-specific DNA fragment, or a synthetic ssDNA or RNA aptamer selected to bind the food target analyte. The transduction systems can be classified into four types: electrochemical (voltammetric, potentiometric, impedimetric), optical (luminescent, fluorescent, reflective, ellipsometric, surface plasmon resonance (SPR), and waveguide), microgravimetric (piezoelectric or acoustic wave) and thermometric (calorimetric). The biosensor's performance is evaluated according to its sensitivity, limit of detection, dynamic ranges, reproducibility, selectivity and stability.

1.3.2 Biosensors for food allergens and toxins using different transducers

Several optical biosensors have been reported for the detection of β -LG based on the optical near-field phenomenon called resonance enhanced absorption⁵⁷ and surface plasmon resonance⁵⁸. For the egg white allergen ovalbumin, Anraku *et al.*⁵⁹ have reported a polymer

brush modified cap-shaped gold nanoparticles as a sensing element for ovalbumin using localized-surface plasmon resonance. Recently, an optical immunochip biosensor has been reported for OVA utilizing resonance-enhanced absorption⁴. In this approach, gold nanoparticles (AuNPs) have been used as signal transducers in interferometric setup yielding colorimetric response. An optical planar waveguide array sensing platform has been also developed for the detection of multiple analytes including ovalbumin using fluorescence sandwich immunoassays⁶⁰. The samples were run over the sensor surface functionalized with capture antibodies, and then secondary labeled fluorescent antibodies were introduced.

Various immunosensors have been reported for the detection of OA using different transducers such as chemiluminescent⁶¹, surface plasma resonance⁶², piezoelectric detection⁶³ and quartz crystal microbalance⁶⁴. A quartz crystal microbalance immunosensor based on displacement assay using graphene functionalized sensing interface has been also reported for brevetoxin detection⁶⁵. Attempts have been made to develop immunosensors for microcystins based on fluorescent⁶⁶, chemiluminescent⁶⁷⁻⁶⁸, colorimetric⁶⁹, surface plasmon resonance⁷⁰, piezoelectric cantilever⁷¹ or electrochemical⁷²⁻⁷⁴ detection. Immunodetection has also been integrated with nanomaterials such as single-walled carbon nanotube⁷⁵, gold nanoparticles⁷⁶, silver nanoparticles⁷⁷, and quantum dots⁷⁸, in order to improve the sensitivity. These biosensing platforms are relatively sensitive, however, they are not suitable for routine analysis due to the bulky and costly instrumentation. Furthermore, most of the assays required secondary recognition receptors and labeling with fluorescent tags which is laborious as well as costly.

1.3.3 Electrochemical biosensor

Electrochemical Biosensors are subclass of biosensors in which the selective binding of the biorecognition element with the target analyte produces a change in an electrical signal that can be potential, current, conductance, or impedance. This change is proportional to the concentration of the analyte. This type of biosensors exhibit great advantages as it combines the high selectivity of the biorecognition processes with the high sensitivity, possibility of multiplexing, capability of miniaturization and low cost of electrochemical transducers. Moreover, unlike optical biosensors, electrochemical biosensors are not affected by sample turbidity, or interference from fluorescing compounds commonly found in biological samples. To the best of our knowledge, no electrochemical biosensors has been reported before this study

for the detection of β -lactoglobulin and ovalbumin allergens. For the toxins under study, various electrochemical biosensors have been previously reported that can be divided into two main classes according to the nature of the biorecognition process: enzyme inhibition based sensors and affinity sensors. These two classes will be briefly discussed in the next two subsections

1.3.3.1 Enzyme inhibition-based electrochemical sensors

Enzymes are globular proteins that catalyze biochemical reaction. It is the oldest and most common biorecognition elements used in biosensors so far. The arrangement of amino acids at the active site of the enzyme bind to specific substrate that gives each enzyme its selectivity to certain type of substrate molecules. Direct enzyme-based biosensors are usually fabricated by immobilization of an enzyme on electrodes surface by different immobilization techniques. This immobilized enzyme recognises substrate or analyte and yields electroactive species or other detectable product. Alternatively, enzyme inhibition-based biosensors indirectly monitors inhibitors such as toxins that specifically interact with immobilized enzyme and inhibits its biocatalytic reaction as shown in the schematic diagram (Figure 1.4).

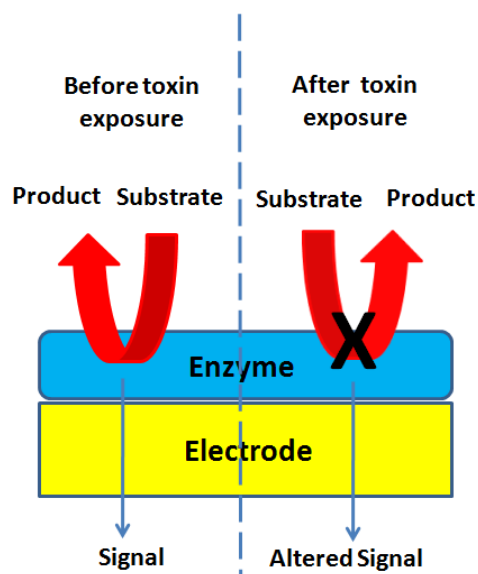


Figure 1.4 Schematic diagram of the enzyme inhibition-based electrochemical sensors

The enzymes are usually very sensitive to a very low concentration of inhibitors, thus increase the sensitivity of biosensor. Campas et al. ⁷⁹ have reported an enzyme sensor for the electrochemical detection of OA. The detection strategy was based on the inhibition of immobilised PP2A enzyme by OA. The enzyme activity was monitored by measuring the electrochemical signal of the enzyme substrates (catechyl monophosphate and p-aminophenyl phosphate) after dephosphorylation by the enzyme. A bienzyme electrochemical biosensor have been also developed for the detection of OA ⁸⁰. Two enzymes were coimmobilized and the detection of the toxin was achieved by electrochemically measuring the H₂O₂ produced as a final product of two sequential enzymatic reactions. The enzyme PP2A has significant activity toward glycogen phosphorylase which catalyzes the conversion of glycogen to glucose-1-phosphate. Glucose-1-phosphate reacts with alkaline phosphatase to produce glucose, then glucose reacts with glucose oxidase to producing hydrogen peroxide. The inhibition of PP2A enzyme by OA leads to alteration of the detected H₂O₂. A protein phosphatase 2A-based inhibition electrochemical biosensor for the detection of microcystin has been also reported ⁸¹ in which the enzyme has been immobilised by entrapment using a poly(vinyl alcohol) azide-unit pendant water-soluble photopolymer. Three substrates were compared; catechyl monophosphate, -naphthyl phosphate and 4-methylumbelliferyl phosphate and amperometric detection was used to monitor the enzyme activity. However, these methods suffer from major limitations which are the low stability of the enzyme, its sensitivity to the food matrix and also the poor selectivity due to the possible inhibition of the enzyme by different groups of toxins as well as other inhibitors that may lead to unexpected results. Moreover, these types of biosensors requires substrate and other reagents which complicate the overall design of biosensor.

1.3.3.2 Affinity sensors

Affinity sensors are sensors in which selective and high affinity biomolecules such as antibodies, membrane receptors, or oligonucleotides bind with a target analyte to produce a measurable electrochemical signal. The molecular recognition in affinity biosensors is mainly based on the complementary size and shape of the binding site of the receptor to the analyte. Because of their high affinity and selectivity, antibodies have been considered the " gold

standard " in molecular recognition for several decades and have been widely exploited into immunosensors (Ab-based affinity biosensors) for food analysis ⁸².

An Ab is a large Y-shape glycoprotein of MW \approx 150KDa that can be raised against a particular analyte by the immune system of a host animal. Antibodies can be easily produced against large antigens (high molecular weight analytes). However, the production of antibody against small molecules such as toxins (MW $<$ 1000 g mol⁻¹) is more challenging as it usually requires the use of carrier proteins. The development of large number of antibodies against various targets including food analytes allowed the development of immunosensors that offered several advantages over other methods in terms of sensitivity and selectivity. The successful production of antibodies against OA, MC-LR and BTX has lead to the development of several electrochemical immunosensors for these toxins. For examples, indirect competitive immunosensors have been reported for OA. In these methods, OA was immobilized on the electrode surface using carriers such as ovalbumin ⁸³, magnetic beads ⁸⁴ or directly using diazonium coupling reaction ⁸⁵. This is usually followed by indirect competitive assay using fixed concentration of OA antibody in the solution, followed by enzyme-labelled secondary antibody and substrate for signal generation (Figure 1.5).

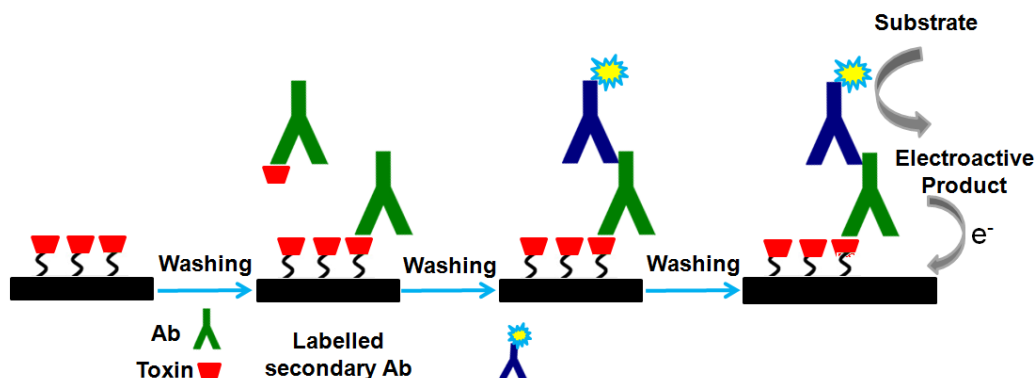


Figure 1.5 General scheme for indirect competitive electrochemical immunosensor.

Direct competitive immunosensors for MC-LR have been also developed (Figure 1.6). These sensors are usually fabricated by immobilization of MC antibody on the electrode surface and then the competition is established between a fixed concentration of an enzyme labelled MC-LR with the free MC in the sample for the immobilized antibody. A glucose oxidase labelled MC-LR have been used and an amperometric signal is measured for the enzymatically generated H_2O_2 after incubation with glucose solution as substrate ⁷². Based on similar detection strategy, horseradish peroxidase (HRP) labeled MC-LR has been also used and electrochemical measurements were performed for the hydrogen peroxide catalysis using either 5-methylphenazinium methyl sulfate ⁷⁴ or hydroquinone ⁷³ as mediators.

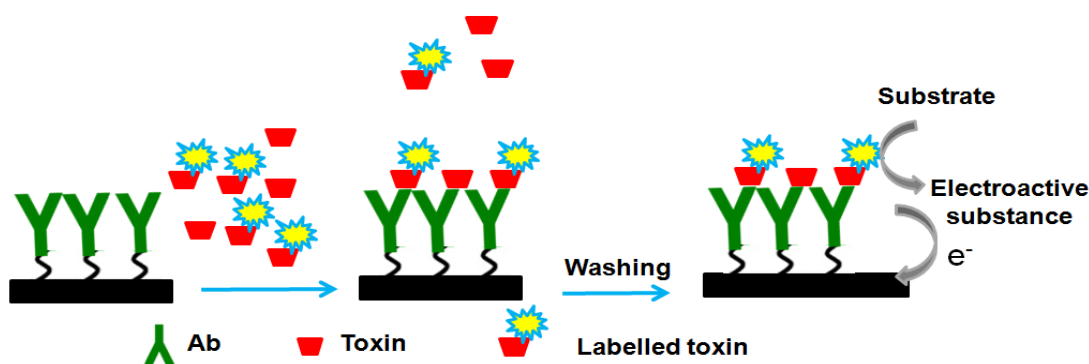


Figure 1.6 General scheme for direct competitive electrochemical immunosensor.

Competitive type electrochemical immunosensors for BTXs using gold nanoparticles-decorated dendrimer ⁸⁶ and guanine-functionalized graphene nanoribbons ⁸⁷ have been also developed.

Despite that the introduction of immunosensors represents a significant advancement in detection methods, the high cost of these test, along with the fragility, sophisticate production and cross-reactivity of antibodies still do not completely satisfy current needs. Moreover, these approaches need a number of incubations and washing steps and are limited by the instability of the enzymes and reporter reagents. Therefore, simpler, more stable and sensitive electrochemical biosensors are still in high demand.

1.3.4 Label-free electrochemical detection strategy

The electrochemical detection strategies in affinity biosensors can be classified into two major categories: labelled and label-free detection systems. In the labeled detection, the signal is generated from redox label or reporter reagent that changes upon receptor-target binding such as the detection schemes described in section 1.3.3.2. Despite the sensitivity of these methods, they require extra time, expense, and the labeling may alter the receptor affinity to the target. On the other hand, label-free detection methods monitor the changes in electrical properties of the surface when a target bioanalyte interacts with a probe-functionalized surface without any labelling. Therefore, label-free biosensors are simpler, easier, lower cost and can enable detection of target-probe binding in real time⁸⁸.

1.3.5 Electrochemical detection techniques

Electrochemical techniques can be generally classified based on the measured signal into three categories: current, potential and impedance. A brief definition of the techniques that measures current and impedance will be given since they are the most relevant to this thesis.

1.3.5.1 Voltammetry/amperometry

Voltammetric and amperometric methods are based on applying a potential to a working electrode and measuring the current that results from electrochemical reduction or oxidation at the working electrode. While amperometric techniques measures the current at constant voltage, voltammetric techniques measures current over a set potential range yielding a peak. Voltammetric techniques include cyclic voltammetry, linear sweep voltammetry, differential pulse voltammetry, and square-wave voltammetry. In amperometric biosensors, the measured current should be proportional to the concentration of the receptor-target complex. Because most of the biomolecules are not electroactive, it cannot be detected directly using these techniques. Thus, the use of electroactive labels such as enzymes or electroactive molecules are generally used. Voltammetric label-free biosensors can be also designed based on measuring the current signal change of a redox probe such as $[\text{Fe}(\text{CN})_6]^{3-/4-}$ upon receptor-target binding.

1.3.5.2 Electrochemical impedance spectroscopy

Electrochemical impedance spectroscopy is a powerful and non destructive technique that measures the resistive and capacitive properties of an electrode upon perturbation of a system

with a small amplitude sinusoidal ac excitation signal over a wide range of frequencies. This small amplitude perturbation is safe to the biomolecules. Impedance methods are capable of sampling mass transport at low frequency and electron transfer at high frequency. Impedimetric detection is widely used for affinity biosensors to monitor the receptor-target binding by altering the impedance features (capacitance and electron transfer resistance) of the interface. There are two type of impedance measurements: Faradaic impedance which is measured in the presence of a redox probe and non-Faradaic impedance which is measured in the absence of redox probe. Faradaic impedance spectroscopy is usually used for biosensing application because of its sensitivity to any modification of the electrodes surface offering a label- free mode of detection. A redox couple (often $[\text{Fe}(\text{CN})_6]^{3-/4-}$ ions) is added to the electrolyte solution which provides the Faradaic current upon applying the formal potential of this redox couple. The charge transfer resistance (R_{CT}) is usually the most sensitive electrical element that can be used to characterize the events occurring at the electrode interface ⁸⁹, therefore, it is usually used to monitor the bioaffinity complex formation.

1.4 Graphene in biosensors

Great interest has been devoted recently to the integration of nanomaterials and biomolecules for the development of biosensor devices. Among these nanomaterials, graphene is 2 D carbon nanomaterial, comprises a single layer of sp^2 -hybridized carbon atoms joined by covalent bonds to form a flat hexagonal lattice. Graphene and related materials have drawn great research interest because of their unique electronic, mechanical and thermal properties ⁹⁰⁻⁹¹. Graphene has shown variety of potential applications in nanoelectronics ⁹², protective coatings ⁹³, polymer composites ⁹⁴, catalysis ⁹⁵, energy storage devices ⁹⁶, drug delivery, optics ⁹⁷ as well as sensing and biosensing platforms ⁹⁸. Graphene has been explored in developing optical biosensors using fluorescence ⁹⁹⁻¹⁰¹, surface plasmon resonance ¹⁰²⁻¹⁰³ and colorimetric ¹⁰⁴⁻¹⁰⁶ methods. Several biosensors based on graphene field effect transistors ¹⁰⁷⁻¹⁰⁸ have been also demonstrated. The superior advantages offered by electrochemical transducers for sensing, such as their lower cost, easier operation, capability of automation and miniaturization, have also led to significant interest in developing graphene-based electrochemical biosensors [16]. Graphene has been utilized previously in developing electrochemical biosensors using two main

approaches: first, as an electrode material ¹⁰⁹⁻¹¹¹, second, as label-bearing nanocarrier ¹¹². Graphene has been employed as electrode material in various electrochemical biosensors using enzymes, antibodies, ssDNA or aptamers as recognition receptors ⁹⁸. Superior electrochemical biosensing performance of graphene to carbon nanotubes has been also reported in terms of sensitivity, signal-to-noise ratio, electron transfer kinetics and stability ¹¹³⁻¹¹⁴. Graphene has shown two major advantages over carbon nanotubes: lower production cost and higher purity as it does not contain the metallic impurities which could affect both the stability and the reproducibility of the carbon nanotube-based sensors ¹¹⁵. The large surface area of graphene offers higher extent of immobilization of biomolecules on the electrode surface and thus, a higher number of binding sites. Moreover, the high conductivity and the fast electron transfer rate of the electroactive species on the graphene electrodes play an important role in the sensitivity of the graphene-based electrochemical sensors ¹¹⁶.

1.4.1 Preparation methods of graphene materials and their application in electrochemical biosensors

The preparation of graphene is an extremely active and rapidly moving research field, and none of the reported preparation approaches to date is suitable for all applications. Several methods have been used for preparation of graphene such as chemical vapour deposition technique ¹¹⁷, epitaxial growth ¹¹⁸, unzipping of carbon nanotubes ¹¹⁹ and adhesive tape-exfoliation of graphite ⁹⁰. However, most of graphene preparation methods are typically used to produce small amounts of graphene. For applications where large quantities are required, industrial scale production of graphene is commonly achieved using solution-based approaches ¹²⁰ or CVD growth. CVD growth of graphene on metal substrates such as (ruthenium ¹²¹, Ni ¹²²⁻¹²³, and Cu ¹²⁴) as well as substrate free CVD ¹²⁵ have been reported. CVD graphene has offered some interesting advantages such as low cost, ease of preparation, producing large areas of graphene, its ability to be transferred to other desired substrates by dissolving the metallic support. However, CVD grown graphene may also suffer from metallic impurities that has been shown before in CNTs. Recently, the electrochemical behaviour of CVD monolayer graphene has been investigated in some reports. Li et al. ¹²⁶ have reported the electrochemical behaviour of CVD-grown graphene towards the redox reaction of ferrocenemethanol showing 10-fold electron transfer rate compared with the basal plane of bulk graphite. A superior electrocatalytic activity

of nitrogen doped CVD-grown graphene towards the electrochemical reduction of oxygen has been presented by Quet al. ¹²⁷. However, the application of CVD graphene in electrochemical biosensors has not been reported intensively. On the other hand, the majority of graphene based materials used in the reported electrochemical biosensing platforms are produced by solution-based approaches such as Hummers method. These approaches involve the chemical oxidation of graphite and consequent exfoliation to individual sheets of graphene oxide either via rapid heating or ultrasonication ¹²⁸⁻¹³⁰. These synthetic methods result in abundant structural defects and polar oxygen-containing functional groups, such as carboxyl, epoxide, and hydroxyl groups on the graphene surface which significantly affects its electrochemistry and consequently its sensing behaviour ¹³¹. This process is considered the most economical way to produce graphene. Although, the produced reduced graphene oxide using this method is not the same as graphene in conductivity and flatness and contains a significant amount of carbon–oxygen bonds ¹³²⁻¹³⁴, it has been widely exploited in electrochemical applications ¹³⁵⁻¹³⁸

1.4.2 Functionalization of graphene

An important factor in the application of a material as electrode in electrochemical biosensors is the functionalization method and the subsequent immobilization of biomolecules. Various strategies for the covalent modification of solid electrodes which enable the subsequent attachment of biomolecules are known such as self-assembly of thiols on gold ¹³⁹⁻¹⁴⁰, silane on glass or indium tin oxide ¹⁴¹⁻¹⁴² as well as electrografting of organic layer on various conducting substrates using different reagents such as alcohols, amines, carboxylates, Grignard reagents, diazoniums, other onium salts and halides ¹⁴³. Among these modification protocols, the electrochemical reduction of aryl diazonium salt has appeared as a promising alternative to conventional electrode modification schemes and used to modify different electrode materials such as carbon, metals, semiconductors, oxides and polymers ¹⁴³.

Pinson et al. ¹⁴⁴ have studied the mechanism of the diazonium electrografting, and attributed the covalent attachment to the reduction of the diazonium cations via a single electron transfer process. The diazonium salt reduction led to the elimination of a nitrogen molecule and the formation of an aryl radical which forms a covalent bond with the carbon surface (Figure 1.7). It was also shown that the surface coverage can be controlled by changing the diazonium salt concentration and electrolysis duration ¹⁴⁵. The versatility of this approach to modify the

surface with a wide range of function groups, along with the ease of preparation and the stability of the covalently attached organic layer on the surface, have made it the method of choice for the immobilization of biomolecules in several reported biosensors.

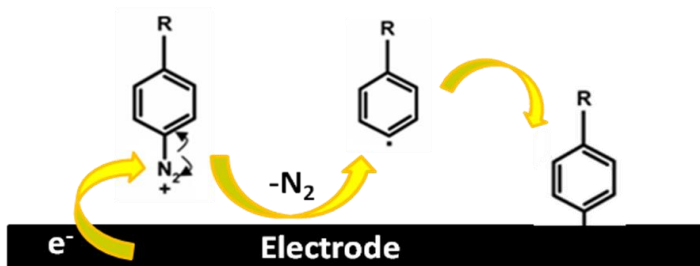


Figure 1.7 Mechanism of diazonium salt electrografting

Recently, significant effort has been devoted to graphene functionalization using various covalent and noncovalent approaches¹⁴⁶. However, covalent functionalization schemes of graphene appear to be more promising due to their more robust nature as well as their more ability to significantly change the electronic properties of the graphene sheet. Among the reported approaches for the covalent modification of graphene, the use of aryl diazonium salt has been well investigated¹⁴⁷. This functionalization method is easy to achieve and to control, and enables a wide variety of grafting groups that can be used to carry out further chemistries. The covalent functionalization of graphene using aryl diazonium salt has been reported with epitaxial graphene¹⁴⁸, graphene nanoribbons¹⁴⁹, chemically converted graphene¹⁵⁰, mechanically exfoliated graphene¹⁵¹ as well as CVD graphene. The reactivity of CVD-grown graphene towards the diazonium functionalization has been recently reported¹⁵². Jin et al.¹⁵³ have also shown the successful functionalization of CVD graphene with 4-propargyloxybenzenediazonium tetrafluoroborate and the subsequent attachment of a short chain polyethylene glycol with a terminal carboxylic group. In all these reports, the graphene diazonium functionalization occurred via spontaneous electron transfer mechanism, typically requiring several hours for completion^{148,154} and sometimes heat or surfactants^{150,154}. We have recently reported a robust, fast, and controlled modification of graphene modified screen printed carbon electrodes by electrochemical reduction of aryl diazonium salt¹⁵⁵⁻¹⁵⁷ that will be presented in this thesis. Similarly, an electrografting method of nitrophenyl groups using diazonium salt reduction on CVD monolayer graphene transferred to silicon substrate was also reported¹⁵⁸. The authors have

shown the successful grafting of uniform thin films using electrochemistry and demonstrated the modulation of the electronic properties of graphene by opening a band gap upon functionalization ¹⁵⁸. More recently, a mechanistic investigation of electrografted diazonium-based films on few layered graphene (vapour-deposited) on nickel has been reported ¹⁵⁹. However, diazonium functionalized monolayer CVD graphene sheets has yet to be applied to biosensing.

1.4.3 Size of graphene oxide sheet

Graphene prepared using different approaches as well as different experimental conditions often shows different properties in terms of oxygen functionalities and defect density. These properties greatly influence the material performance in different applications. For instance, Pumera et al. ¹⁶⁰ has reported that the chemically reduced graphene materials with different oxygen contents exhibited different electron transfer properties. Moreover, it was shown that the density of defects, conductivity and aggregation tendency of the materials are important factors that can influence application of graphene in electrochemistry .

It has been also reported that the solution-based approaches for graphene preparation does not usually allow precise control over sheet size and therefore, does not result in monodisperse GO samples ¹⁶¹⁻¹⁶³. Previous studies have revealed several factors that can influence the size of graphene oxide sheets ¹⁶⁴⁻¹⁶⁹. McAllister et al. ¹⁶⁵ have reported that the size of the GO sheets is not controlled by the size of parent graphite particles used for the synthesis. However, it was shown by Zhang et al. ¹⁶⁶ that the degree of oxidation is a crucial factor that significantly influence the size of the resulting GO particles prepared using Hummers method. Zhao et al. ¹⁶⁷ have also reported a decrease in the GO sheets size with increasing their oxygen content which was explained to be attributed to the higher density of carbon-oxygen bonds that facilitates cracks formation during sonication. Other study has shown that the larger crystal size in the parent graphite yields larger GO sheets with shorter sonication times, regardless of the C/O ratio of the graphite oxide ¹⁶⁸. Moreover, Su et al. ¹⁶⁹ have shown the decrease of graphene oxide sheets size with increasing sonication time. Therefore, because of the numerous variables that may affect the overall synthesis process, the size of GO sheets may vary from synthesis to synthesis and the resultant material is usually polydisperse that contains sizes from few nanometers to tens of micrometers ¹⁶². Since, the size-controlled synthesis of GO has not been

extensively studied so far ^{162,166}, it was essential to understand whether this material has size-dependent properties. Some work has been previously done to explore the size dependent properties of GO flakes. For instance, Kim et al. ¹⁷⁰ have revealed that smaller GO sheets are more hydrophilic due to presence of more ionized -COOH groups on their edges, and thus the colloidal stability of GO is also size-dependent. It has been also reported that the size of graphene sheets can have significant impact on the behaviour of graphene electrodes and composites ¹⁷¹. Hicks et al. ¹⁷¹ have demonstrated that larger graphene sheets have higher conductivity due to the lower contribution of contact resistance ¹⁷² which results from the reduced number of graphene-graphene contacts for a given number of conducting paths. Furthermore, larger graphene sheets were shown to be more effective when graphene is used as reinforcement or plate like fillers in composites ¹⁷³⁻¹⁷⁴. Pumera et al. ¹⁷⁵ have also recently studied the effect of parent graphite particle size on the electrochemistry of thermally reduced graphene oxide. It was demonstrated in this report that the size of parent graphite particles has no clear effect on the defect density, number of oxygen containing groups and rate of heterogeneous electron transfer of Ferro/ferricyanide redox probe. Instead, it was shown that the electrochemical behaviour depended on the structural properties of the produced graphene materials irrespective of their sheet size ¹⁷⁵. However, despite the relatively large number of graphene-based electrochemical biosensors reported to date, no systematic study has yet examined the extent to which varying graphene oxide sheet size impact biosensor performance.

1.5 Aptamers in biosensors

Aptamers are single stranded DNA or RNA molecules selected *in vitro* from large libraries of synthetic random sequences. The first aptamers have been reported in 1990 ¹⁷⁶⁻¹⁷⁷ and much progress has been made to date. Many aptamers have been selected against wide range of targets, including proteins, small molecules, viruses and cells ¹⁷⁸. Aptamers as recognition receptors have several advantages over antibodies: **1-** Aptamers are prepared by *in vitro* selection procedure without using experimental animals, **2-** they can be developed even against toxins or low molecular weight compounds which is hardly achievable with antibodies, **3-** they can be selective to different parts of the target molecule, **4-**once the aptamer sequence is identified, it can be synthesized with high purity, reproducibility and very low cost, in contrast to antibodies

that needs experimental animals and suffers from batch to batch reproducibility, **5-** aptamers can be chemically modified easily by various chemical tags allowing the immobilization of aptamers onto various solid supports and **6-** they are also highly stable at different conditions. Due to these advantages, aptamers as recognition receptors are emerging as novel capturing agents to replace antibodies in biosensor applications. Aptamer-based sensors (aptasensors) have been designed using different strategies, particularly the conformation change of the aptamer upon binding with the target. Moreover, the binding of aptamers to their complementary nucleic acids can be exploited in sensing schemes.

1.5.1 Challenges for small molecule aptamers such as toxins

Over the past years, the majority of the aptamers has been selected against protein targets and less than a quarter of existing aptamers have been generated for small molecule targets ¹⁷⁹. Larger targets that contain more functional groups and structural motifs have higher probability to select high affinity sequences that binds via hydrogen bonds, electrostatic and hydrophobic interactions ⁸⁸. However, some small molecule-binding aptamers are among the most successful aptamers reported to date such as ATP, cocaine, theophylline aptamers. Aptamers has been shown extremely high selectivity allowing over 10,000-fold discrimination between L- and D-amino acid. A 10-fold improvement in selectivity of theophylline aptamer against caffeine and xanthine that differs by a single methyl group over antibodies has been also reported ⁸⁹. Due to the increasing awareness of the risk arises from food and water contamination with small molecule toxins, aptamers targeting toxins are being explored ¹⁷⁹. Until now, few aptamers targeting toxins such as ochratoxin A ¹⁸⁰, fumonisin B1 ⁹¹, saxitoxin ¹⁸¹, anatoxin-A ¹⁸² and cylindrospermopsin ¹⁸³ have been selected. For OA, Campas et al. ⁹⁴ have reported the selection of an aptamer targeting OA and its use in the development of competitive colorimetric assay. However, the aptamer sequence and the detection results have not been published so far. An ongoing work and submitted patent by another research group has been recently referred to ¹⁸⁴. However, no results have been published yet. For microcystin detection, an aptamer reported in 2001 ¹⁸⁵ has been employed in a direct label-free MC-LR detection based on surface plasmon resonance. However, a detection range of 50 µg/ml to 1mg/ml was obtained, indicating a poor detection limit due to the low affinity of the selected aptamer. Recently, we have reported the selection and characterization of high affinity DNA aptamer against the three MC congeners,

LR, YR, LA. Moreover, on the selected sequences showed very high degree of selectivity to MC-LR against MC-LA and MC-YR¹⁸⁶. The summary of the binding affinity and cross reactivity of the MC aptamers is shown in Figure 1.8.

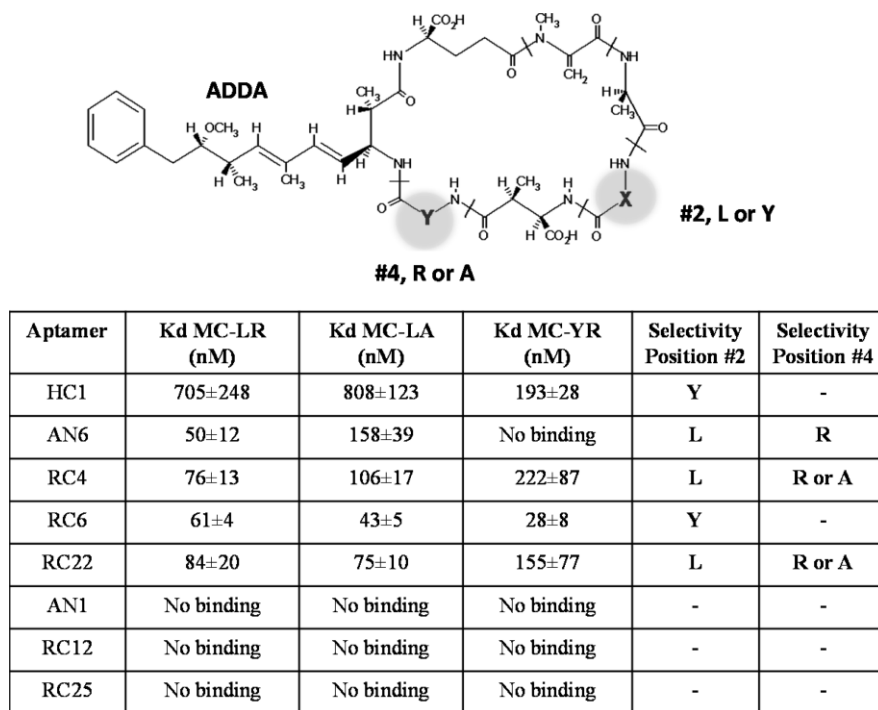


Figure 1.8 Affinity and cross reactivity of the microcystin-targeting aptamers.

1.6 Integration of graphene and ssDNA including aptamers in biosensors

The integration of graphene and biomolecules has recently been exploited in the development of various biosensing platforms^{98,115,131}. There are reports on the combination of graphene and single-stranded DNA (ssDNA) for the detection of HIV1⁹⁹, thrombin¹⁰⁰, ochratoxin A¹⁸⁷, multiple DNA targets¹⁸⁸ and helicase-induced duplex-DNA unwinding¹⁸⁹. Graphene-based DNA assays usually rely on the quenching of the fluorophore of a labelled ssDNA which, in its target-free form, is in close proximity to the graphene surface. Interaction with the target causes its release from the graphene and abolishment of fluorescence quenching, resulting in an increase in fluorescence. In this regard, label-free electrochemical biosensing is more favourable as it combines the decreased cost of unlabeled DNA, along with the sensitivity of electrochemical techniques and miniaturization potential. An aptamer-graphene assembly for the detection of thrombin has been reported using electrochemical impedance spectroscopy¹⁹⁰.

The detection mechanism was explained to be due to the release of the aptamer from graphene surface upon protein- aptamer binding. However, to our knowledge, no work has yet been reported on the detection of small molecules using graphene-based electrochemical aptasensor. It is worth noting that, the release of the aptamer from graphene surface upon protein- aptamer binding cannot lead to universal detection schemes to be applied for small molecules which are, in general, less likely to cause a change of the conformation in the entire aptamer sequence.

1.7 Objectives, motivation and originality of the thesis

The overall objective of this thesis is to explore the use of new aptamers and graphene platforms in biosensing applications of some foodborne contaminants, particularly allergens and toxins, using electrochemical biosensors. A visual guide relating the chapters of the thesis is shown in Figure 1.9.

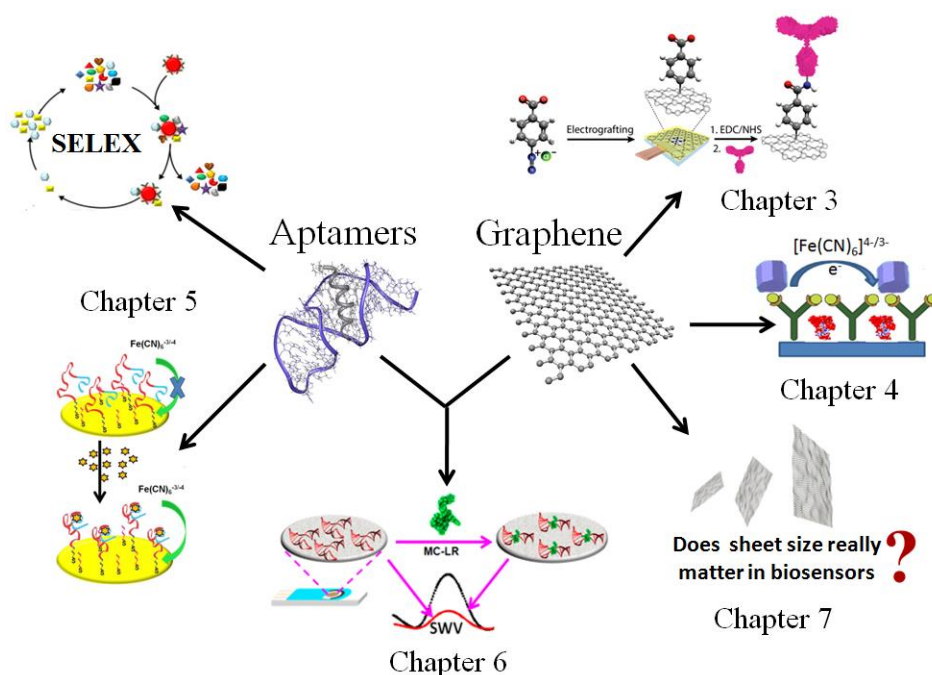


Figure 1.9 Schematic representation summarizes the objectives of the study and relating the chapters of the thesis.

By surveying the literature we highlighted some challenges and questions that still have to be addressed in the field of electrochemical biosensors for foodborne contaminants using graphene and aptamers. First, the majority of the developed biosensors of food allergens such as milk and egg are based on optical immunosensors that needs expensive machines and not

suitable for field applications. To the best of our knowledge no electrochemical biosensors has been reported before for the detection of β -lactoglobulin and ovalbumin. Therefore, developing label-free electrochemical immunosensor for such proteins is expected to have potential role in food safety and consumer protection. We aim to investigate the use of graphene as electrode material for developing these immunosensors. Commercial graphene-modified screen printed carbon electrodes as well as CVD grown graphene prepared at Université du Québec à Montréal were utilized. For this, graphene has been functionalized using electrografting of aryl diazonium salts unlike the reported approaches which are usually done using spontaneous electron transfer. we also report the first application of CVD monolayer graphene as a label-free electrochemical biosensing platform for the detection of protein. This will be shown in Chapter 3.

Second, by using the carboxyphenyl functionalized graphene demonstrated in Chapter 3, a novel sensitive, fast and single step electrochemical immunosensor of OA based on indirect competitive assay was developed without the need of enzyme labelling reducing both the time and cost of the detection assay. This will be demonstrated in Chapter 4.

Third, despite that the presence of several immunosensors for marine toxins represents a significant advancement in detection methods, the high cost of these sensors, the sophisticated production and cross-reactivity of antibodies still do not satisfy current needs. Success in biosensor design largely depends on the development of novel, low cost, stable, and high affinity recognition receptors. Aptamers is appearing as promising alternative that fulfill these characteristics. Prior to my study, no available aptamer targeting marine toxins has been reported in the literature, thus, motivates us to target such group of toxins. Therefore, the selection, identification, characterization, and biosensing application of high affinity aptamers against okadaic acid and brevetoxin will be shown in Chapter 5.

Next, significant effort has been focused on the integration of graphene and biomolecules in biosensing applications. However, no work have been previously investigated the detection of small molecule using graphene-based aptasensor prepared using non covalent assembly of aptamer on graphene. In the reported graphene-based protein aptasensors, the detection mechanism is usually shown to be due to the release of the aptamer from graphene surface upon protein- aptamer binding. This raises a fundamental question if small molecule toxins which are in general, less likely to cause a change of the conformation in the entire

aptamer sequence upon binding, will be able to cause such release from the graphene surface? The answer of this question will be addressed in Chapter 6 using MC-LR aptamer as a model.

Finally, most of the graphene materials which are used in the electrochemical biosensors in literature are prepared using solution-based approaches such as Hummers method which usually leads to polydispersed GO sample. However, despite the relatively large number of graphene-based electrochemical biosensors reported to date, no systematic study has yet examined the extent to which varying graphene oxide sheet size impact biosensor performance. Significant graphene-based label-free biosensors are being developed which motivates us to focus on such systems^{98,155,191}. Therefore, in Chapter 7, I investigate the effect of varying the lateral size of graphene oxide sheet produced from graphite route on the performance of two representative label-free electrochemical aptasensing and immunosensing systems employing either physical or covalent immobilization of bioreceptors.

By pointing out these challenges, the main objectives of this thesis can be summarized as follows:

- 1- Developing simple label-free electrochemical biosensors for OVA, β -LG and OA as important model allergens and toxins based on aryl diazonium functionalized graphene electrodes.
- 2- Selection of DNA aptamers for the shellfish toxins; okadaic acid and brevetoxin and their incorporation in electrochemical biosensors.
- 3- Studying the integration of MC-LR aptamer as model with graphene electrodes to fabricate an electrochemical aptasensor for MC and to develop a detection scheme that can be generalized for other small molecule toxins.
- 4- Studying the effect of varying the lateral size of graphene oxide sheet on the performance of two representative label-free electrochemical aptasensors and immunosensors for MC-LR and β -LG, respectively.

1.8 Thesis organisation and contribution of authors

This thesis is organised as follows:

Chapter 1 gives a general introduction including the objectives and motivation of the thesis.

Chapter 2 describes the experimental details including the materials and reagents, instrumentations, and methods employed in the work.

Chapter 3 demonstrates the development of label free electrochemical immunosensors for milk and egg allergens based on electrografting of aryl diazonium salt on graphene modified screen printed electrodes. The publications related to this chapter:

- 1- Shimaa Eissa, Chaker Tlili, Lamia L'Hocine, Mohammed Zourob, Electrochemical immunosensor for the milk allergen β -lactoglobulin based on electrografting of organic film on graphene modified screen-printed carbon electrodes, *Biosens. Bioelectron.*, 2012, 38, 308–313.
 - **All work described in this paper in terms of the experimental study, data analysis, explanations and writing of the manuscript were carried out by me.** The XPS measurements were done by Christophe Chabanier at INRS-EMT. I thank Dr. Chaker Tlili for the useful discussion about the detection experiments and Dr. Lamia L'Hocine for proposing the β -lactoglobulin analyte.
- 2- Shimaa Eissa, Lamia L'Hocine, Mohamed Siaj, Mohammed Zourob, Graphene-based label-free voltammetric immunosensor for sensitive detection of the egg allergen ovalbumin, *Analyst*, 2013, 138, 4378–4384.
 - **All work described in this paper in terms of the experimental study, data analysis, explanations and writing of the manuscript were carried out by me.** I thank Dr. Lamia L'Hocine for proposing the Ovalbumin analyte.
- 3- Shimaa Eissa, Gaston Contreras Jimenez, Farzaneh Mahvash, Abdeladim Guermoune, Chaker Tlili, Thomas Szkopek, Mohammed Zourob, and Mohamed Siaj, Functionalized CVD monolayer graphene for label-free impedimetric biosensing, *Nano research*, 8, 1698-1709.

- **All work described in this paper in terms of the experimental study, data analysis, explanations and writing of the manuscript were carried out by me.** The CVD graphene samples were grown by Abdeladim Guerroune and Farzaneh Mahvash at UQAM, therefore the CVD growth was not described in the thesis. Gaston Contreras has helped me to estimate the size of carboxyphenyl group by Chemdraw software.

Chapter 4 presents the development of graphene-based electrochemical competitive immunosensor for the sensitive detection of okadaic acid in shellfish. This chapter has been published in the following article:

- 4- Shimaa Eissa, Mohammed Zourob, A graphene-based electrochemical competitive immunosensor for the sensitive detection of okadaic acid in shellfish, *Nanoscale*, 2012, 4, 7593–7599.

- **All work described in this paper in terms of the experimental study, data analysis, explanations and writing of the manuscript were carried out by me.**

Chapter 5 discuss the Selection, identification characterization of aptamers targeting okadaic acid and brevetoxin and their application in label-free electrochemical aptasensors for these marine toxins. The publications related to this chapter:

- 5- Shimaa Eissa, Andy Ng, Mohamed Siaj, Ana C. Tavares, Mohammed Zourob, Selection and identification of DNA aptamers against okadaic acid for biosensing application, *Anal. Chem.*, 2013, 85, 11794–11801.

- **All work described in this paper in terms of the experimental study, data analysis, explanations and writing of the manuscript were carried out by me.** I thank Dr. Andy Ng for useful discussion about some problems in SELEX experiments.
- 6- Shimaa Eissa, Mohamed Siaj, Mohammed Zourob, Aptamer-Based Competitive Electrochemical Biosensor for Brevetoxin-2, *Biosens. Bioelectron.*, 2015, 69, 148–154.
- **All work described in this paper in terms of the experimental study, data analysis, explanations and writing of the manuscript were carried out by me.**

Chapter 6 shows the development of Label-Free Voltammetric Aptasensor for the Sensitive Detection of Microcystin-LR Using Graphene-Modified Electrodes. The publications related to this chapter:

- 7- Shima Eissa, Andy Ng, Mohamed Siaj, Mohammed Zourob, Label-free voltammetric aptasensor for the sensitive detection of microcystin-LR using graphene-modified electrodes, *Anal. Chem.*, 2014, 86, 7551–7557.
- **All work described in this paper in terms of the experimental study, data analysis, explanations and writing of the manuscript were carried out by me.** Dr. Andy Ng had selected the MC-LR aptamer sequence that was published in our previous article (Andy Ng, Raja Chinnappan, Shima Eissa, Hechun Liu, Chaker Tlili, Mohammed Zourob, Selection, Characterization and Biosensing Application of High Affinity Congener-Specific Microcystin-Targeting Aptamers, *J. Environ. Sci. Technol.*, 2012, 46, 10697–10703).

Chapter 7 shows the influence of graphene oxide sheet size on the performance of label electrochemical biosensors. The article related to this chapter:

- 8- Shima Eissa, Jeanne N'diaye, Patrick Brisebois, Ricardo Izquierdo, Ana C. Tavares and Mohamed Siaj, Probing the Influence of Graphene Oxide Sheets Size on the Performance of Label-Free Electrochemical Biosensors, in preparation.
- **All work described in this manuscript in terms of experiments, data analysis, explanations and writing of the manuscript were carried out by me** except the GO preparation which was done by Patrick Brisebois, therefore it was not described in the thesis. **The separation of the GO sheets was done by me and Patrick. The material characterization was a collaborative work between me, Jeanne and Patrick (the AFM and Raman spectra measurements were done by Jeanne N'diaye and me and the NMR measurement was done by Patrick).** The XPS measurements were done by the characterization service at Laval University and the **XPS peak fitting was done by me.**

Chapter 8 briefly summarizes important contributions of this work and highlights future perspectives.

CHAPTER 2. EXPERIMENTAL

In this chapter, the materials, reagents and instrumentations which were used throughout this thesis will be presented. Then, the detailed methods will be described including electrodes functionalization protocols and bioreceptors immobilizations, biosensors fabrications, aptamers selection protocols, binding affinity experiments, parameters for the electrochemical measurements as well as the applications of the developed immunosensors and aptasensors in real samples.

2.1 Materials and reagents

2.1.1 Chemical reagents

Graphite powder (500 mesh), sulfuric acid (99.99%), phosphoric acid (85 wt. % in H₂O), potassium permanganate, hydrogen peroxide solution 30 % (w/w) in H₂O, hydrochloric acid (37%), ethanol (>99.8 %), 4-nitroaniline, 4-aminobenzoic acid, potassium ferrocyanide (K₄Fe(CN)₆) (98.5-102.0%), potassium ferricyanide (K₃Fe(CN)₆) (≥99.0%), dipotassium hydrogen orthophosphate (≥99.0%), potassium dihydrogen orthophosphate (≥99.0%), sodium chloride (≥99.5%), magnesium chloride, sodium nitrite, glutaraldehyde (50%), ammonium persulfate, sodium dodecyl sulfate (SDS) (≥99.0%), 3-aminopropyltriethoxysilane, hydroxylamine hydrochloride, 2-(N-morpholino) ethanesulfonic acid (MES), cysteamine hydrochloride, 1,4-phenylene diisocyanate (PDIC) and toluene were purchased from Sigma (Ontario, Canada). 1-ethyl-3-(3-dimethylaminopropyl) carbodiimide hydrochloride (EDC) and N-hydroxysuccinimide (NHS) and diaminodipropylamine agarose (DADPA) beads were obtained from Fisher Scientific (Ontario, Canada). Divinyl sulfone (DVS) activated sepharose beads were obtained from Syd Labs, Inc (Malden, USA). Sodium carbonate anhydrous, sodium bicarbonate, sodium azide, Taq plus DNA polymerase, acrylamide/bis-acrylamide (40% solution), urea, Tris-base, boric acid, methanol and EDTA disodium dehydrate were purchased from Bioshop Inc. (Ontario, Canada).

2.1.2 Analytes (Proteins and toxins)

bovine serum albumin (BSA), β -lactoglobulin, ovalbumin from chicken egg white, chicken egg lysozyme and casein were purchased from Sigma (Ontario, Canada). Microcystin-LR, LR, YR and okadaic acid sodium salt were purchased from Enzo Life Sciences (Ontario, Canada). Brevetoxin-2 and Brevetoxin-3 were purchased from Marbionc development group, LLC (North Carolina, USA). Certified reference mussel sample (CRM-DSP-Mus-b) containing 10.1 $\mu\text{g/g}$ okadaic acid and dinophysistoxin 1,2 (DTX-1,2) were obtained from the Institute for Marine Bioscience of the National Research Council Canada (Halifax, Canada).

2.1.3 Buffer solutions

A phosphate buffered saline PBS solution (10 mM, pH 7.4) was used for the preparation of all antibodies (β -LG, OVA and OA) and proteins (β -LG, OVA) standard stock solutions and dilutions and in the ELISA experiments. PB buffer, (200 mM, pH 7.0, $\text{KH}_2\text{PO}_4+\text{K}_2\text{HPO}_4$) was used to dilute the gluteraldehyde solution for the activation of the amine groups. A 2-(N-morpholino)ethanesulfonic acid buffer solution (100 mM, pH 5.0) was used in the activation of the carboxylic groups. Binding buffer was used during the SELEX and aptasensors experiments which consists of 50 mM Tris, pH 7.5, 150 mM NaCl, 2 mM MgCl_2 except for the BTX aptasensor experiments in which the MgCl_2 solution was optimised to be 10 mM. MES buffer, 0.9% NaCl, pH 4.7 was used for coupling of okadaic acid with the DADPA beads. Elution buffer is 7 M urea in binding buffer. Tris-EDTA buffer (TE buffer) is 10 mM Tris, pH 7.4, 1 mM EDTA. 0.1 M carbonate buffer, pH 8.5 was used for the coupling of brevetoxin-2 to the DVS beads. All solutions were prepared using Milli-Q grade water.

2.1.4 Toxin solutions

Standard MC-LR solutions were prepared by dissolving the toxin in binding buffer. Okadaic acid was firstly dissolved in methanol (0.1 g L^{-1}) and subsequently diluted in the binding buffer for the aptasensors fabrication or diluted in PBS buffer for the immunosensor fabrication. Stock solution of BTX-2 was prepared in DMSO and then diluted with binding buffer for the aptasensor experiments.

2.1.5 DNA aptamer sequences

The DNA library (5'-ATACCAGCTTATTCAATT-N₆₀-AGATAGTAAGTGCAATCT-3'), primers for polymerase chain reaction (PCR), and the unmodified and modified aptamer sequences (NH₂-modified MC aptamer (NH₂-MCAP)): 5'- NH₂ (CH₂)₆ / GGC GCC AAA CAG GAC CAC CAT GAC AAT TAC CCA TAC CAC CTC ATT ATG CCC CAT CTC CGC/ -3', the complementary sequence of MC aptamer (cDNA): 5'-GCG GAG ATG GGG CAT AAT GAG GTG GTA TGG GTA ATT GTC ATG GTG GTC CTG TTT GGC GCC-3') were custom-synthesized by Integrated DNA Technologies Inc. (Coralville, USA). The 5'-C6 disulfide terminated OA aptamer (5'HO-(CH₂)₆-S-S-(CH₂)₆/GGTCACCAAC AACAGGGAGC GCTACGCGAA GGGTCAATGT GACGTCATGC GGATGTGTGG/-3'), Ferrocene labelling of the 3'-terminus of the MC-LR aptamer (Fc/Ap=Ferrocene-C(=O)-NH-CH₂-CH(OH)-CH₂-O-Oligo5') and disulfide labelling of the 5'-terminus were synthesized by GenScript (NJ, USA).

2.1.6 Antibodies, ELISA and cloning kits

Anti- β -lactoglobulin antibody, anti-ovalbumin monoclonal antibody (anti-OVA-MAb) and anti-okadaic acid monoclonal antibody (anti-OA-MAb, developed in mouse) were obtained from Abcam (Cambridge, USA). Brevetoxin ELISA kit was purchased from Abraxis Bioscience (Mississauga, ON, Canada). β -lactoglobulin ELISA Kit was purchased from ELISA Systems (Queensland, Australia). TOPO TA Cloning Kit with One Shot MAX Efficiency DH5 α -T1, 3,3',5,5'-tetramethylbenzidine (TMB) stabilized chromagen and HRP-labelled goat anti-mouse IgG antibodies were purchased from Invitrogen (NY, USA).

2.1.7 Materials for CVD graphene growth and connection

Twenty-five micrometer thick, Cu foils (Alfa Aesar, 25 μ m thick, N# 13382) were used as the substrate for CVD graphene growth. H₂ (99.9 %) and CH₄ (99.9 %) used in graphene growth were directly connected to the CVD system. Poly (methyl methacrylate) (PMMA, 950 kDa, 4% solution in

anisole) was obtained from MicroChem (Newton, USA). Kapton® Tape, (6.4mm), Copper Conductive Tape (6.3 mm) and Silver Paint were obtained from Ted Pella, Inc (CA, USA).

2.1.8 Filters for graphene oxide sheets separation

Polycarbonate membrane filters with pore size of 5, 10 μm which used for the graphene oxide separation were obtained from Sterlitech Corporation (WA, USA). Cellulose acetate (0.22, 0.45 μm pore size) and Nylon filters (30, 60, 100 μm pore size) were obtained from Millipore Corporation (MA, USA).

2.1.9 Filters for the SELEX experiments

Amicon Ultra-0.5 mL Centrifugal desalting Filters with a 3kDa molecular cut-off were obtained from EMD Millipore (Alberta, Canada). Centrifuge tube filters with a cellulose acetate membrane with pore size of 0.45 μm were purchased from Corning life sciences (Tewksbury MA, USA).

2.1.10 Electrochemical cells

Disposable graphene-modified screen printed carbon electrodes (GSPE) were obtained from Dropsens, Inc. (Spain, ref. 110GPH). The electrodes comprises a carbon working electrode modified with graphene, carbon counter and silver reference electrode. Disposable electrical printed (DEP) electrodes were obtained from BioDevice Technology (Nomi, Japan), using three-electrode configuration which comprises a carbon working electrode, carbon counter and silver/silver chloride reference electrode. A three-electrode system was used for the okadaic acid and brevetoxin aptasensors electrochemical measurements, consisting of a gold working electrode, an Ag/AgCl electrode as the reference and a Pt wire as the auxiliary electrode. For the CVD graphene experiments, three electrode system was also utilized using Ag/AgCl electrode as the reference and a Pt wire as the auxiliary electrode and a homemade CVD graphene (as will be described in sections 2.3.4 and 2.3.5) as working electrode. Figure shows the four different electrochemical cells used throughout this thesis.

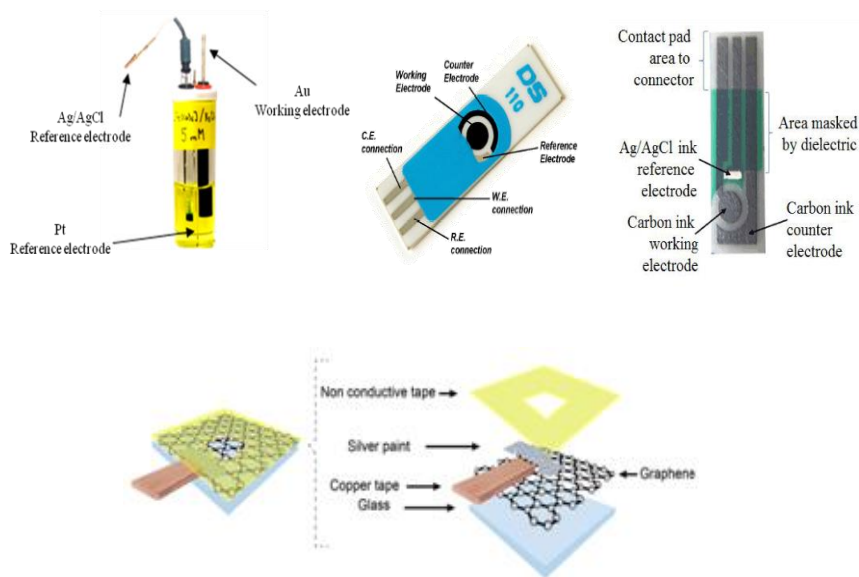


Figure 2.1 Electrochemical cells used throughout the work. (A) conventional electrochemical cell using gold as working electrode which was used for the OA and BTX aptasensors testing, (B) GSPES that were used for β -LG, OVA, OA immunosensors and MC-LR aptasensor, (C) DEP electrodes that was modified with GO by drop casting for the testing of the sheet size effect and (D) CVD monolayer graphene connected as a working electrode that was used in a conventional three electrode cell with Ag/AgCl and Pt electrodes.

2.2 Instruments

The electrochemical experiments were carried out using Autolab PGSTAT302N (Eco Chemie, The Netherlands) potentiostat/galvanostat that is controlled by NOVA software version 1.9. However, the okadaic acid aptasensor experiments were performed using a model 660D potentiostat/galvanostat (CH Instrument Inc. USA), controlled by a personal computer via a CH Instruments software. Sensors connectors used to connect the GSPE and the DEP electrodes to the Autolab potentiostat were obtained from (Dropsens, Inc., Spain) and (BioDevice Technology, Nomi, Japan), respectively. The UV and fluorescence measurements were performed using NanoDrop 2000C Spectrophotometer and

NanoDrop 3300 Fluorospectrometer, respectively (Fisher Scientific, Canada). Circular dichroism (CD) measurements were done using Jasco-810 spectropolarimeter. A centrifuge (Beckman Avanti J-25, Canada) was used for GO sheets preparation/separation protocols. Ultrasonication of GO dispersions was performed in a 50W ultrasonicator (Shenzhen Co., China), at a frequency of 42 kHz. Ultrasonication temperature was controlled and always maintained at 55 °C. X-ray photoelectron spectroscopy (XPS) measurements for the GSPE and CVD graphene were performed with VG Escalab220iXL instrument using a Mg polychromatic source ($MgK\alpha=1253.6$ eV) at a base pressure between 5×10^{-10} and 1×10^{-9} mbar. The survey spectra were recorded using 300 watts of X-ray power, 100 eV pass energy and 1.0 eV step size. The high-resolution scans were run using power of 300 watts, 20eV pass energy and step size of 0.1 eV. XPS measurements for the GO electrodes were performed with XPS PHI 5600-ci instrument (Physical Electronic, Inc., USA) using a Mg polychromatic source ($MgK\alpha=1253.6$ eV) at 150 W. Raman spectroscopy measurements were performed using a micro-Raman spectrometer (RenishawInVia Reflex, Model: RM3000) with excitation from an argon ion laser beam (514 nm) in a backscattering geometry. Atomic force microscopy images were obtained using Veeco/Bruker AFM instrument in ScanAsyst mode. Scanning electron microscopy (SEM) images were acquired on a JEOL JSM7600F system operating at an accelerating voltage of 5 kV.

2.3 Methods

2.3.1 Graphene oxide and CVD monolayer graphene preparation

Graphene oxide was prepared using improved Hummers method ¹⁹². Monolayer graphene sheets were prepared by a CVD process using Cu foil as catalytic substrate as reported in detail in our published work ¹⁹¹.

2.3.2 Separation of graphene oxide flakes (Chapter 7)

Separation of GO sheets according to their lateral size was realised by a size fractionation process involving a repeated ultracentrifugation step for 10 min at 4000 rpm followed by separation of

fractions and successive filtration using membranes with different pore sizes to obtain the required size range. Different centrifugation speeds and times were used to optimize the separation. The separated fractions were then dried and 1 mg/ml GO of each size was redispersed in water by shaking for 24 h to achieve maximum dispersion of material.

2.3.3 Preparation of graphene oxide modified electrodes (Chapter 7)

The GO modified DEP electrodes were prepared by drop casting. 5 μ L of GO solution (1 mg/ml in Milli-Q water) was deposited onto the electrode surface and allowed to dry at room temperature. Excess material that had not been absorbed was then removed from the electrode surface by gentle rinsing with milli-Q water.

2.3.4 CVD graphene transfer onto glass substrate (Chapter 3)

After growth, polymethyl methacrylate was spin coated onto the surface of the graphene coated Cu and baked at 120 °C for 1 min. The sample was then immersed in ammonium persulfate (0.1 M) solution to etch the Cu foil at room temperature. The floating PMMA-supported graphene film was then carefully transferred to a de-ionized water bath to remove the residual etchant. The transfer of the PMMA-graphene film to a clean DI water solution is repeated at least three times to ensure thorough washing. A glass sheet is then used to extract the PMMA-supported graphene from the water bath. The graphene sample was then dried at ambient temperature for 48 h in a clean environment to ensure complete adhesion to the glass. The PMMA was then dissolved in a warm acetone bath to produce a pristine graphene layer on glass sheet.

2.3.5 Connection of CVD graphene sheet as working electrode (Chapter 3)

The graphene sheet was connected using conductive tape and silver paste is used to improve the connection between the copper and the graphene sheet. A nonconductive adhesive polyimide tape was then used to insulate the metal contacts and to expose a well defined area of the graphene surface (3 \times 5 mm) to the solution during the electrochemical measurements (Figure 2.1 D). The electrode was then connected to the potentiostat through the copper contact.

2.3.6 Graphene functionalization by electrografting of aryl diazonium salts and immunosensors preparation (Chapter 3)

2.3.6.1 β -Lactoglobulin immunosensor

The diazonium cations were synthesized in situ by mixing 1.0 mM sodium nitrite and 1.0 mM 4-nitroaniline in 0.5 M HCl solution. The mixture was stirred and left to react for about 5 min at room temperature. The electrochemical modification was immediately performed in the in situ generated 4-nitrophenyl diazonium salt (4-NPDS) by chronoamperometric (CA) step at -0.4 V for 45 s. The electrode was then thoroughly washed with water, transferred to 0.1 M KCl solution and subjected to five cyclic voltammetry (CV) scans between 0.4 and -1.4 V at 100 mVs^{-1} for reduction of the nitro groups on the surface to amine groups. Then, the 4-aminophenyl (AP) film on the electrode surface was activated by incubation with 2.5% glutaraldehyde (GA) solution in phosphate buffer PB (200 mM, pH 7.0) for 60 min. After activation the electrodes were washed with PBS buffer pH 7.4 to remove the excess GA. Then 50 μL of β -lactoglobulin antibody solution (10 $\mu\text{g ml}^{-1}$ in 10 mM PBS buffer, pH 7.4) was used to cover the working area of the electrode and incubated for 60 min at room temperature in water-saturated atmosphere. After washing with PBS buffer (10 mM, pH 7.4) the electrode surface was then blocked by the addition of 50 μL blocking buffer (0.25 % of BSA in PBS buffer, pH 7.4) and incubated for 45 min to deactivate the remaining aldehyde groups and to block unreacted active sites. The modified electrode was then rinsed with PBS and used in the assay or kept at 4 $^{\circ}\text{C}$ in PBS buffer pH 7.4 until further use.

For the β -lactoglobulin detection measurements, 50 μL of β -lactoglobulin of the required concentration in PBS buffer pH 7.4 was pipetted onto the modified electrode and incubated for 45 min in water-saturated atmosphere. Then, the immunosensor was rinsed thoroughly with PBS buffer pH 7.4 prior to electrochemical measurements. All the electrochemical measurements were performed in 10 mM PBS (pH 7.0) containing 5.0 mM $[\text{Fe}(\text{CN})_6]^{3-/4-}$ redox pair using cyclic voltammetry, and differential pulse voltammetry (DPV) at room temperature. The decrease of the differential pulse voltammetric current which was relative to the concentration of β -lactoglobulin has been used to

construct the calibration curve. The parameters used for the DPV measurements: modulation amplitude 25 mV; modulation time 0.05 s; interval time 0.5 s, and step potential -5 mV.

2.3.6.2 Ovalbumin immunosensors

The 4- carboxyphenyl diazonium salt was prepared *in-situ* by mixing 2 mM sodium nitrite solution with 2 mM 4-aminobenzoic acid in 0.5 M HCl. The mixture was stirred for 5 min at room temperature. The functionalization of GSPE and CVD graphene electrodes were then performed by the electrochemical reduction of the *in-situ* generated diazonium cations using three cyclic voltammetry scan from +0.4 to - 0.6 V at a scan rate of 100 mV s⁻¹. The electrodes were then gently rinsed with Milli-Q water. The 4-carboxyphenyl (CP) film on the graphene surface was activated by incubating the electrodes in MES buffer (pH 5.0) containing; 100 mM EDC and 20 mM NHS for 60 min. After washing with MES buffer, the modified electrode surface was covered with a 50 μ L droplet of anti-OVA-MAb solution (10 μ g ml⁻¹ in 10 mM PBS buffer, pH 7.4) and incubated for 120 min at room temperature in water-saturated atmosphere. The removal of the unreacted antibodies was performed by gently washing the electrodes with PBS buffer (10 mM, pH 7.4). Then, the electrodes were blocked by the addition of 50 μ L blocking buffer (0.1 % of BSA in PBS buffer, pH 7.4) and incubated for 30 min to deactivate the remaining active groups and to block free surface. The prepared immunosensor was then rinsed with PBS and used in the assay or kept at 4°C in PBS buffer pH 7.4 until further use.

For the ovalbumin measurements and the negative control experiments, 50 μ L of either ovalbumin or the control proteins (lysozyme, casein, BSA, β -LG) of the required concentration in PBS buffer pH 7.4 were added onto the modified electrode surface and incubated for 45 min in water-saturated atmosphere. The immunosensors were then washed with PBS buffer and subjected to electrochemical measurements. For the immunosensor prepared using GSPE, DPV was performed in 5.0 mM [Fe(CN)₆]^{3-/4-} solution as previously described in the previous section 2.3.6.1. However, for the immunosensor prepared using CVD graphene, impedance measurements were recorded in a 0.1 M PBS buffer solution containing 10 mM [Fe(CN)₆]^{3-/4-} redox pair (1:1 molar ratio) over a frequency

range from 100 kHz to 0.1 Hz. using a DC potential of 0.2 V (vs a Ag/AgCl reference electrode). A sinusoidal voltage perturbation of 10 mV amplitude was superimposed on the applied DC potential.

2.3.7 Competitive immunosensor for okadaic acid (Chapter 4)

2.3.7.1 Synthesis of OA-OVA conjugates

Okadaic acid was conjugated to ovalbumin using carbodiimide chemistry as described previously¹⁹³. Briefly, 1.6 µg of OA (in 10 µl methanol) was added to 1 ml of ovalbumin solution (45 µg/ml in MES buffer pH 5.0). 1 mg of EDC was then added and the reaction mixture was stirred for 3 hours at room temperature. After the reaction, the OA–OVA conjugate was purified extensively using Amicon Ultra-0.5 mL Centrifugal desalting Filters with a 3kDa molecular cut-off (EMD Millipore, Canada) with PBS buffer solution pH 7.4 to remove the unreacted OA. The final product (OA-OVA) was stored at 4 °C until use. In order to confirm the conjugation of OA to OVA, we performed ELISA using the synthesized OA-OVA conjugate coated ELISA wells and free OVA coated well as a control. After incubation of the free and the conjugated proteins overnight on the ELISA wells, the wells were washed with PBS buffer, pH 7.4, and blocked with 2% BSA and then incubated with anti-OA-MAb (diluted 1:1000 in PBS buffer pH 7.4) for 1 hour. The wells were washed again and incubated with the secondary antibody-HRP conjugate for 1 hour. Finally, excess antibodies were washed out with PBS buffer and the stabilized chromogen (TMB) solution was added and left for 15 minutes. The color produced in the wells coated with the conjugate compared with the colorless well coated with the free protein was taken as a confirmation of the success of the conjugation reaction.

2.3.7.2 Functionalization of graphene electrodes and immunosensor fabrication

The GSPE were functionalized using in situ generated 4-carboxyphenyl diazonium salt (4-CPDS) and then the carboxylic groups were activated using EDC/NHS chemistry as previously described in section 3.2.6.2. After rinsing with MES buffer, followed by PBS buffer, the modified electrodes surfaces were covered with 50 µL droplets of anti-OA-MAb at dilution of 1/1000 in 10 mM PBS buffer, pH 7.4 and incubated for 120 min at room temperature in water-saturated atmosphere. After

washing with PBS buffer (10 mM, pH 7.4) the electrode surface was then blocked by the addition of 50 μ L blocking buffer (0.1 % of BSA in PBS buffer, pH 7.4) and incubated for 30 min.

2.3.8 In Vitro Selection of the DNA Aptamer against marine toxins (Chapter 5)

2.3.8.1 Coupling of okadaic acid to diaminodipropylamine beads

100 μ g of OA was firstly dissolved in 100 μ l of methanol and then diluted to 1 ml with coupling buffer. Two millilitres of DADPA beads were washed several times with coupling buffer. 30 mg of (EDC) was dissolved in 0.5 ml coupling buffer and mixed with the OA solution. Then, the mixture was immediately added to washed agarose beads and the final volume was made up to 4 ml with coupling buffer. The mixture was rotated for 3 hours at room temperature. After the reaction, the beads were washed with 1 M NaCl solution in order to remove the excess unreacted toxin. Then, the beads were equilibrated with 0.2 M carbonate buffer, pH 8.5, and 20 mg of sulfo-NHS acetate was added in order to quench the unreacted amine groups on the beads. The mixture was rotated for another hour, after which the beads were washed extensively with binding buffer. The success of the immobilization of OA on the beads was confirmed by direct ELISA using the OA-conjugated beads and free beads as a control. ELISA was performed by incubating the beads with anti-OA-MAb (diluted 1:1000 in PBS buffer pH 7.4) for 1 hour after washing with PBS buffer and blocking with 1% BSA solution. Then the beads were washed again and a secondary antibody-HRP conjugate was added and incubated for another 1 hour. The blue color produced in the OA beads after washing and incubating the beads for 15 minutes with stabilized chromogen (TMB) solution confirms the success of the coupling reaction. Simultaneously, negative beads were prepared for the counter selection round by adding 40 mg of sulfo-NHS acetate to 500 μ L of DADPA beads equilibrated in carbonate buffer, pH 8.5. Finally, the positive OA beads and the negative beads were stored in binding buffer containing 0.02 % sodium azide at 4°C until use.

2.3.8.2 Coupling of brevetoxin-2 to divinyl sulphone beads

A stock solution of 1mg/ml BTX-2 in DMSO was prepared. 200 μ l of the BTX-2 stock solution was diluted to 2 ml with coupling buffer (carbonate buffer, pH 8.5). Two millilitres of DVS beads were

washed three times with ultrapure water. The washed beads were then added to the diluted BTX-2 solution in a polypropylene tube and gently mixed end-over-end overnight at room temperature. After the reaction, the beads were washed three times, two minutes each time with coupling buffer solution to remove the excess unreacted toxin. Then, 4 ml of 0.1 M ethanolamine, pH 9.0 was added to the washed beads and stirred for 2 hours in order to block the unreacted divinyl sulfone groups on the beads. After that the beads were washed extensively with 0.7 M NaCl containing 0.05 % sodium azide to remove the unbound ethanolamine followed by washing with binding buffer. Simultaneously, negative DVS beads were also blocked using ethanolamine in order to use it for the counter selection rounds. Finally, the positive BTX-2 beads and the negative beads were stored in binding buffer containing 0.02 % sodium azide at 4°C until further use. The success of the immobilization of BTX-2 on the beads was confirmed by performing direct competitive ELISA for the BTX-2-coupled beads and the negative beads as control using commercial ELISA kit. ELISA was performed by incubating 10 µl of the washed beads, diluted to 50 µl with PBS buffer (pH 7.4), with sheep anti-BTX antibody that is immobilized on the wells of the microtiter plate. Then, 50 µL of BTX-HRP conjugate solution was added to each well and incubated for 60 minutes. The wells were then washed with the washing buffer provided with the ELISA kit and incubated for 15 minutes with 100 µl of stabilized chromogen (TMB) solution. The detection was based on the competition between the BTX-beads and BTX- HRP conjugate for the binding sites of the antibodies immobilised on the microtiter plate. A blue color was produced in the wells which were incubated with the negative beads whereas, no colour was observed in the wells incubated with the BTX- beads, thereby confirming the success of the coupling reaction. The stability of the BTX-beads were monitored during the SELEX rounds by repeating ELISA experiment several times and all the experiments confirmed the presence of BTX-2 and the stability of the beads over the whole SELEX process.

2.3.8.3 SELEX protocol

The library and the primer sets were designed according to the protocol reported previously¹⁸⁶. A random ssDNA library (3 nmol or 1.8×10^{15} sequences) was used which consisted of a central random region of 60 nucleotides flanked by two fixed regions of 18 nucleotides-sequences at the 3' and 5'

ends. These regions represent the primer binding sites for the amplification (5'-ATACCAGCTTATTCAATT - N₆₀-AGATAGTAAGTGCAATCT-3'). 100 µl of OA or BTX-2 beads were washed several times with binding buffer. (3 nmol at the first selection round, and 150 pmol in the subsequent rounds) of ssDNA pool were heated to 90°C for 5 minutes, cooled at 4°C for 10 minutes, kept at 25°C for 5 minutes and then added to the washed OA beads in 300 µL binding buffer in a centrifuge filter tube. The mixture was incubated at room temperature with end-over-end rotation for 2 hours. The beads were then washed several times with binding buffer. The DNA bound to toxin beads was eluted with 400 µL aliquots of elution buffer for 6 times with heating at 90°C for 10 minutes until no DNA is detected by fluorescence measurements. The eluted DNA was desalted and concentrated by ultrafiltration device. In a counter selection round, the DNA pool was first incubated with the negative beads, washed DNA were collected, subjected to the same heating and cooling treatment and subsequently incubated with toxin beads. The selected DNA pools were amplified by PCR in 15 parallel 75µL reactions each containing 2 units of Taq Plus and polymerase buffer, 2mM MgCl₂, 200µM dNTP, 0.2µM of forward and reverse primers. The primers were designed and modified with fluorescein and a PEG linker followed by a poly-A tail as reported previously^{186,194}. Forward primer: 5'-fluorescein-ATACCAGCTTATTCAATT-3'; reverse primer: 5'- poly-dA₂₀-PEG₆-AGATTGCACTTACTATCT-3'. PCR conditions: 94°C for 10 minutes, followed by 25 cycles of 94°C for 1 minute, 47°C for 1 minute, 72°C for 1 minute, and a final extension step of 10 minutes at 72°C. PCR products were dried by SpeedVac and resuspended in 50:50 water and formamide and heated to 55°C for 5 minutes. The relevant DNA strand (labelled with fluorescein) was separated from the double stranded PCR product in 12% denaturing PAGE and eluted from the gel band by freeze-thaw cycle. Eluted ssDNA in TE buffer was concentrated, desalted by ultra filtration, quantified by UV and used for the next selection round. A schematic diagram of the SELEX process is shown in Figure 2.2.

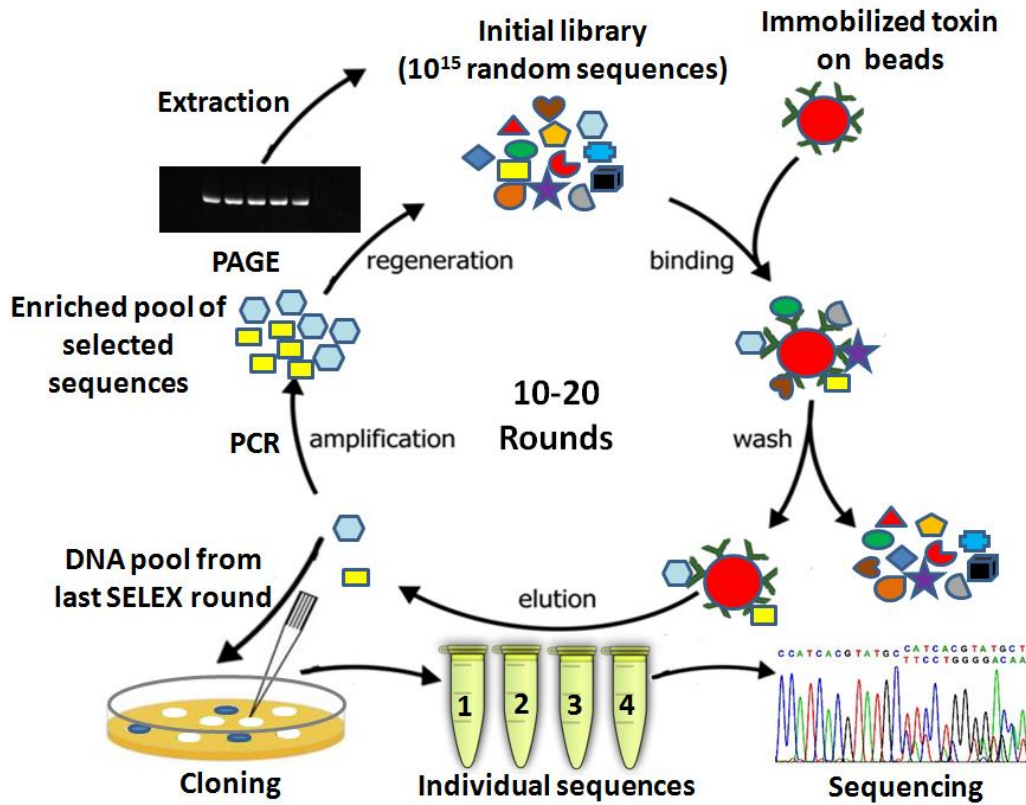


Figure 2.2 Schematic diagram of the SELEX protocol.

2.3.8.4 Cloning and sequencing of the selected DNA

After a number of selection rounds when DNA recoveries began to plateau (round 18 for OA aptamer and round 10 for BTX-2 aptamer), the selected ssDNA pool were amplified with the non-modified primer set and cloned into pCR2.1-TOPO vector using the TOPO TA Cloning Kit. Colonies were grown on LB-agar medium supplemented with ampicillin and X-Gal and IPTG. Positive colonies were picked and grown in liquid media. ssDNA inserts were PCR amplified using the M13 forward and reverse primer sites within the vector and sequenced. Sequences of the selected ssDNAs were analyzed and aligned using PRALINE¹⁹⁵.

2.3.8.5 Binding analysis of the DNA pools and aptamer sequences to target toxins

2.3.8.5.1 Fluorescence method

In order to monitor the enrichment of the library for target binding, the fluorescence of the eluted ssDNA from the toxin-beads after each round was measured. For the binding analysis of the aptamer sequences, the selected aptamers sequences were amplified by PCR with the labelled primers used during the SELEX, and the fluorescein-labeled sequences were separated by gel electrophoresis. A solution of 75 nM from each PCR amplified aptamer sequence was incubated with 10 μ l of BTX-beads in binding buffer after subjected to the heating and cooling treatment as described in the selection step (section 2.3.8.3).

2.3.8.5.2 Electrochemical methods

To monitor the enrichment: After PCR amplification and purification of the corresponding ssDNA aptamers, aliquots of 500 nM ssDNA from each pools were incubated with the BTX-modified electrodes for 30 mins. The electrodes were then washed with binding buffer and the impedance measurements were recorded. Similarly, the binding of the aptamer sequences to BTX-2 was assessed by incubating 500 nM of each amplified clone with the BTX-modified electrode for 30 min and EIS was recorded. The binding was then evaluated by measuring the charge transfer resistance (R_{CT}). The EIS were recorded over a frequency range from 10 kHz to 1.0 Hz using an alternative voltage with amplitude of 10 mV, superimposed on a DC potential of 0.20 V (vs a Ag/AgCl reference electrode). The impedance data were plotted in the form of complex plane diagram (Nyquist plot). The EIS and measurements were recorded in a 0.1 M PBS buffer solution containing 5 mM $[\text{Fe}(\text{CN})_6]^{3-/4-}$ redox pair (1:1 molar ratio).

2.3.8.6 Dissociation constants determination by fluorescence Assay

The affinity of the selected aptamers for OA and BTX-2 was investigated by performing binding assays as described above in section 2.3.8.5.1 but using a constant amount of BTX-beads (10 μ l) or OA-beads (20 μ l) and various concentrations of the aptamers (0 to 300 nM). The fluorescence of the eluted DNA from each sample was measured and saturation curve was obtained for each aptamer. The

dissociation constant (K_d) for each sequence with the corresponding target toxin was calculated by non-linear regression analysis.

2.3.8.7 Analysis of the conformation change of the aptamers using circular dichroism

Circular dichroism (CD) is a spectroscopic method that is originating from interactions of chiral molecules with circularly polarized light. Circularly polarized light is chiral, that is, occurs in two nonsuperimposable forms. The absorption of the right- and left-handed circularly polarized light by chiral molecules differs and the difference is called CD that can be expressed as degree of ellipticity. Nucleic acids contain chiral atoms that can absorb light in the UV range from 180-300 nm. Because the CD can sense the difference between enantiomers, it is sensitive to any change in the DNA conformation (i.e. different conformations of the same DNA molecule shows different CD spectra). Therefore, CD can provide information about the secondary structure of aptamers and about the conformation change upon aptamer/analyte binding.

2.3.8.7.1 Okadaic acid aptamer

Circular dichroism spectroscopy was used to examine the conformational change in the aptamer (OA32) after binding with OA. The assay was performed using solutions of DNA aptamer; 0.67 μ M with 0.67 μ M OA in a 1 cm path length, quartz cuvette in an optical chamber. The chamber was deoxygenated with dry purified nitrogen (99.99%) before use and kept in the nitrogen atmosphere during experiments. Each CD spectrum was collected from 230 nm to 340 nm at 0.1 nm intervals, accumulation of three scans at 20 nm/min with a 1 nm band width and a time constant of 1 s.

2.3.8.7.2 Brevetoxin aptamer

Circular dichroism spectroscopy was used to examine the change in the aptamer BT-10 conformational at different pH values. The assay was performed using solutions of 1.0 μ M BT-10 aptamer in binding buffer with pHs; 2.5, 5.1, 7.5, 9.0 and 10.3. The CD spectrum was collected at 50 nm/min scan rate.

2.3.8.7.3 Microcystin aptamer (Chapter 6)

Circular dichroism spectroscopy was also used to examine the conformational change of the MC-LR aptamer (AN6) in different pHs (7.5, 3.4, 8.8) and upon binding with MC-LR. For studying the pH

effect on the conformation, 1 μ M aptamer concentration was used in binding buffer with different pHs adjusted by addition of small amount of 0.1 M NaOH or 0.1 M HCl to the binding buffer. The binding assays were performed using solutions of unmodified aptamer: 0.67 μ M with 0.67 μ M MC-LR or ferrocene-labelled aptamer (Fc/Ap): 0.4 μ M with 0.4 μ M MC-LR in binding buffer, pH 7.5. The CD measurements were acquired at scans rate of 50 nm/min.

2.3.9 Aptasensors for marine toxins (Chapter 5)

2.3.9.1 Okadaic acid aptasensor

2.3.9.1.1 Preparation of the okadaic acid aptamer-modified electrodes

Prior to modification, the gold electrodes (2 mm in diameter) were polished with alumina slurry (Al_2O_3) of various particle sizes (1.0, 0.3, and 0.05 μm), followed by washing with Milli-Q water, ultrasonication for 2 min and drying in a nitrogen stream. The electrodes were then cleaned in piranha solution (3:1 mixture of concentrated H_2SO_4 and 30% H_2O_2 for 2 min) and washed with Milli-Q water. Next, the electrodes were electrochemically cleaned in 0.1 M H_2SO_4 by cyclic voltammetry scanning between 0.0 and 1.6 V for 5 min, followed by washing with ultrapure water and drying under nitrogen. Then, the aptamer sequence with the highest affinity to OA was immobilized on the gold electrodes by immersion in 1 μM solution of the 5'-disulfide terminated aptamer in binding buffer for 24 h. After modification, the electrodes were rinsed with binding buffer solution, followed by incubation in 1 mM 6-mercapto-1-hexanol (MCH) in 10 mM phosphate buffer, pH 7.0 for 30 min. The modified electrodes were then washed thoroughly with binding buffer and immediately used in the electrochemical experiments, or kept in binding buffer solution at 4 $^\circ\text{C}$ until further use.

2.3.9.1.2 Okadaic acid detection assay

For the OA detection, specificity and cross reactivity experiments, a 5 μL droplet of OA, MC-LR, DTX-1, DTX-2 or spiked shellfish extract (prepared as will be described in section 2.3.10.3) in binding buffer was added onto the aptamer-modified gold electrodes surface and incubated for 30 min. The electrodes were then washed with binding buffer to remove the nonspecifically bound toxins and subjected to electrochemical measurements. The CV experiments were conducted at a scan rate of

100 mV/s. The EIS were recorded over a frequency range from 10 kHz to 0.1 Hz using an alternative voltage with amplitude of 10 mV, superimposed on a DC potential of 0.23 V (vs a Ag/AgCl reference electrode). The impedance data were plotted in the form of complex plane diagram (Nyquist plot) with a sampling rate of 25 points per decade. The obtained spectra were fitted using the CH instrument fitting program. All the EIS and CV measurements were recorded in a 0.1 M PBS buffer solution containing 5 mM $[\text{Fe}(\text{CN})_6]^{3-/4-}$ redox pair (1:1 molar ratio).

2.3.9.2 Brevetoxin aptasensor

2.3.9.2.1 Immobilization of brevetoxin-2 on the gold electrode

First, the electrodes were cleaned as previously described in section 2.3.9.1.1. Then, the pretreated gold electrodes were immersed in 10 mM aqueous solution of cysteamine hydrochloride for 12 h at room temperature. After that, the electrodes were washed with absolute ethanol to remove excess cysteamine residues and dried. The terminal amine groups of the cysteamine-modified gold electrodes (Cys/Au) were then activated by immersing the electrodes in 6.5 mM solution of 1,4-phenylene diisocyanate (PDIC) for 2 h at room temperature. The 1,4-phenylene diisocyanate solution was prepared by dissolution in toluene using ultrasonication bath for 30 min. Then, the (Cys/ PDIC/Au) electrodes were rinsed with toluene and dried. Five microliters droplet of 100 $\mu\text{g}/\text{ml}$ BTX-2 solution in DMSO was immediately added onto the (Cys/ PDIC/Au) electrodes surface and incubated for 2 hours. The electrodes were extensively washed with methanol to remove the unreacted BTX-2. The remaining free isocyanate groups were then blocked by immersing the electrodes into methanol for 5 hours. The BTX-modified electrodes (BTX electrodes) were washed with water and stored at 4 °C in binding buffer until further use.

2.3.9.2.2 Brevetoxin-2 detection assay

For the BTX-2 electrochemical competitive assay, specificity, cross reactivity and real sample experiments, the BTX electrodes were incubated for 30 min with 5 μL of 500 nM BT10 aptamer mixed with specific concentrations of BTX-2, BTX-3, OA, MC-LR standard solutions or mussel extracts (prepared as will be described in section 2.3.10.3 and spiked with BTX-2). The electrodes were then washed with binding buffer and subjected to electrochemical measurements. The CV

experiments were conducted at a scan rate of 100 mV/s. The EIS were recorded over a frequency range from 10 kHz to 1.0 Hz using an alternative voltage with amplitude of 10 mV, superimposed on a DC potential of 0.20 V (vs a Ag/AgCl reference electrode). The impedance data were plotted in the form of complex plane diagram (Nyquist plot). The obtained spectra were fitted using the Nova 1.9 software. All the EIS and CV measurements were recorded in a 0.1 M PBS buffer solution containing 5 mM $[\text{Fe}(\text{CN})_6]^{3-/4-}$ redox pair (1:1 molar ratio).

2.3.9.3 Microcystin aptasensor (Chapter 6)

2.3.9.3.1 Microcystin aptamer immobilization on graphene-modified screen printed electrodes

Aptamer immobilization on the GSPE surface was performed by physical absorption. 50 μL of 10 μM MC-LR aptamer in binding buffer was incubated on the graphene electrode surface for 2 to 15 min at room temperature in the incubation time optimization experiments. In concentration optimization experiments, 0 to 20 μM MC-LR aptamer was incubated on the graphene electrodes for 10 min. For detection experiments, 50 μL of 10 μM unmodified aptamer or ferrocene-labelled aptamer were incubated for 10 min on the GSPEs. At the end of the incubation, the electrodes were extensively washed by binding buffer to remove excess non-adsorbed aptamer.

2.3.9.3.2 Microcystin-LR detection assay and control experiments

50 μL of MC-LR of the desired concentration in binding buffer was incubated on the aptamer-modified graphene electrodes at room temperature for 45 min. The electrodes were subsequently washed with binding buffer and subjected to electrochemical measurements. Negative control and cross reactivity experiments were performed by incubating the aptamer-modified electrodes prepared as mentioned above with 1nM of OA, MC-YR, MC-LA or 10 μM cDNA in binding buffer for the Fc-Ap experiment.

2.3.10 Real food samples analysis

2.3.10.1 Extraction of β -lactoglobulin from cake, snacks, and biscuit samples (Chapter 3)

Three commercial food samples labeled as "contain milk" were screened for β -lactoglobulin: (i) "cake" (from local store, Canada); (ii) "Doritos" cheese snacks (from Fritolay, Canada) and (iii)

“Desiree” sweet biscuit (from Hans Freitag, Germany). The food samples were blended to provide a homogeneous mixture. To 0.1 g of each food sample, 1 mL of preheated (60 °C) β -lactoglobulin ELISA Systems extraction buffer was added and the mixtures were vortexed. The extraction was done in a water bath at 60 °C with 15 min shaking. Then, the aqueous fractions were collected by centrifugation at 20,000 g for 15 min. Finally, the supernatants were recovered and divided into small aliquots (100 μ L) and stored at -20 °C until used for analysis using ELISA and the developed immunosensor. For the detection using ELISA, the extracts were diluted as follows: the cake and biscuit samples were diluted 1:10, and the snacks sample was diluted 1:100000 in 10 mM PBS buffer. However, for the immunosensor detection, the extracts were diluted as follows: 1:100 for the Biscuit, 1:150 for the Cake and 1:1000000 for the snacks in 10 mM PBS buffer.

2.3.10.2 Preparation of egg-free extract for OVA immunosensor (Chapter 3)

An egg-free cake sample (from Les Aliments Ange-Gardien, Quebec, Canada) was blended to form a homogeneous mixture. 0.1 g of the blended cake was mixed with 1 mL of PBS buffer and incubated at 60 °C for 1 hour with mixing. The clear supernatant was then collected after centrifugation at 3500 rpm for 10 min. The supernatant was diluted 1 : 100 in 10 mM PBS buffer and spiked with different concentrations of ovalbumin (0.01, 0.10, 10 ng mL⁻¹). Finally, the spiked extracts were incubated for 45 min with the immunosensor at room temperature and the DPV responses were recorded as previously described in section 2.3.6.2.

2.3.10.3 Extraction of toxins from fish, shellfish tissue and certified reference mussel samples (Chapters 4,5,6)

Toxin-free fish and mussel samples purchased from a local store (Quebec, Canada) were blended with hand held homogenizer and extracted with methanol:water (80:20; 0.6 g/mL) for 5 min at 1800 rpm. Crude extracts were centrifuged for 10 min at 4000 rpm. 1mL of extract was evaporated in a speed VAC concentrator and the residue was resuspended in 1mL of 10 mM PBS pH 7.4 for the OA immunosensor experiments or in binding buffer for the aptasensor experiments. The reconstituted solutions were passed through 0.45 μ m cut-off Whatman nylon membrane filters. After filtration, the samples were spiked with three different amounts of the stock solution of OA to make concentrations

of 0.1, 1, 5 $\mu\text{g L}^{-1}$ in order to study the matrix effect. The extraction of the certified reference mussel samples (CRM-DSP Mus-b) containing OA was performed using the same procedure described above. After extraction, a dilution step was performed to obtain concentrations of 0.16, 1.66, 8.33 $\mu\text{g/kg}$ of OA. For BTX aptasensor experiments, the extract solution was diluted 1:10 in binding buffer and then spiked with BTX-2 solution to prepare concentrations of 0.1, 10, 100 ng/ml.

2.3.10.4 Enzyme-linked immunosorbent assay (ELISA) analysis for β -Lactoglobulin (Chapter 3)

For the β -LG immunosensor testing, the samples was analyzed firstly using the β -lactoglobulin ELISA Systems kit. Briefly, 100 μL of the diluted extracted samples and the five standard solutions (negative, 0.1, 0.25, 0.5, 1.00 $\mu\text{g/ml}$) provided in the ELISA kit were incubated in the antibody coated test wells for 15 min. Then, the wells were washed thoroughly and incubated with the secondary antibody-enzyme conjugate, then washed again with the washing buffer and a 100 μL of the substrate solution were added to each well and incubated for 10 min. The reaction was finally stopped by addition of 1 M H_2SO_4 , and the absorbance was measured at 450 nm. The analysis of both standards and samples was carried out in duplicates.

2.3.11 Methods for graphene oxide-based biosensors using different sheet sizes (Chapter 7)

2.3.11.1 Physical immobilization of MC-LR Aptamer and β -LG antibody

5 μL of MC-LR aptamer in binding buffer and 5 μL of β -LG antibody in PBS buffer pH 7.4 at the optimum concentrations of 10 μM and 10 $\mu\text{g/ml}$, respectively were incubated on the GO electrodes surface for 1 hour until drying at room temperature. The electrodes were then washed with buffer to remove excess non-adsorbed molecules.

2.3.11.2 Covalent Immobilization of NH_2 - modified MC-LR aptamer and β -LG antibody

5 μL of 100 mM EDC and 20 mM NHS in MES buffer solution pH 5.2 was deposited on the GO-modified electrode surfaces for 1 hour in order to activate the carboxylic acid groups. Then, the

electrodes were rinsed with PBS buffer solution and incubated with NH₂-MCAP and β-LG antibody at the optimum concentrations of 10 μM and 10 μg/ml, respectively in PBS buffer for 3 hours under a wet environment. Subsequently, the aptasensor was washed with 0.05% SDS and the immunosensor was washed with PBS+0.1% Tween 20 to remove non specifically adsorbed NH₂-MCAP and β-LG antibody, respectively. Then the electrodes were incubated with 0.1M hydroxylamine hydrochloride for 30 min to deactivate any remaining carboxylic acid groups before another washing step with PBS buffer solution.

2.3.11.3 Detection and selectivity experiments for B-lactoglobulin and microcystin-LR

The desired concentrations of MC-LR in binding buffer and β-LG in PBS buffer were incubated for 1 hour on the surface of GO aptasensor and immunosensor, respectively. The electrodes were subsequently washed with binding buffer or PBS buffer with 0.1% Tween 20 and subjected to electrochemical measurements. Negative control and cross reactivity experiments were performed by incubating the aptasensors with MC-LA, OA in binding buffer and the immunosensors with OVA, lysozyme in PBS.

2.3.12 Graphene-modified screen printed carbon electrodes characterisation

For GSPE, no information about the graphene material that was coated on the screen printed carbon electrodes has been provided by the manufacturer, therefore, we have done some characterization experiments. X-ray photoelectron spectroscopy measurements have been done for the bare GSPE in order to know the chemical composition and SEM measurements have also been performed to characterise the morphology of the electrodes.

2.3.12.1 X-ray photoelectron spectroscopy measurements

The XPS measurements were performed at INRS-EMT (Varenes, Quebec, Canada) as described in section 2.2. Figure 2.3(A) shows the typical XPS survey spectra of the bare GSPE. A strong C1s peak and a weak O1s peak were observed. The oxygen peak could be attributed to some oxygen atoms at

the graphene edges. Figure 2.3(B) shows the high resolution of the C1s spectra of the bare GSPE. Four peaks were observed at binding energies of 284.6 eV which is assigned to the sp^2 hybridized carbon atoms of the graphene, 286.0 eV, 287.3 eV and 288.4 eV which corresponds to the C-O, C=O and O-C=O functional groups, respectively. These results confirm that the graphene used in this work is reduced form of graphene sheets as indicated by the manufacturer.

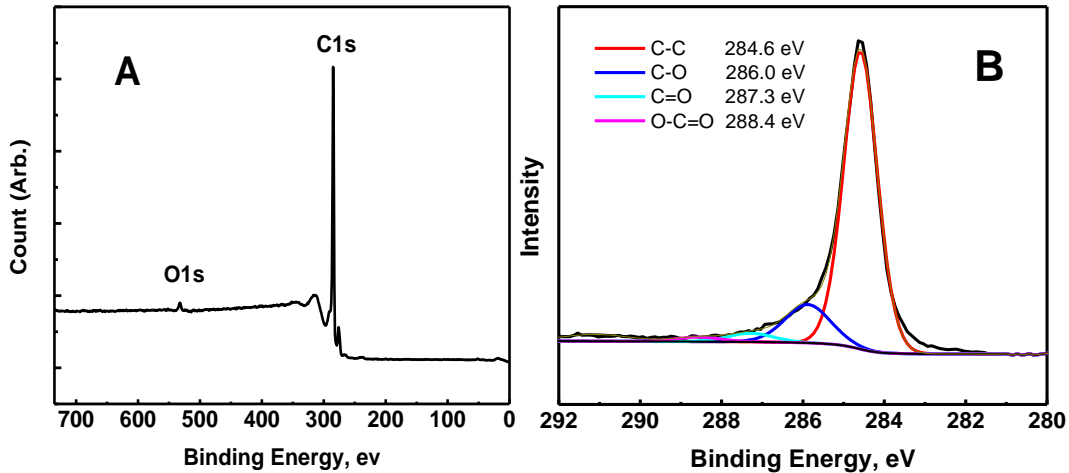


Figure 2.3 XPS survey spectra for bare GSPE, B) XPS C1s core level spectra for bare GSPE.

2.3.12.2 Scanning electron microscopy

Scanning electron microscopy image was also obtained at INRS-EMT using a JEOL, JSM 6300F apparatus. Figure 2.4 shows the SEM image of the GSPE which clearly indicates well-packed graphene layered structure. It is also possible to distinguish the edges of the individual sheets.

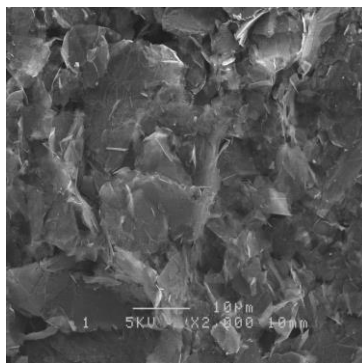


Figure 2.4 SEM image of bare GSPE.

2.3.13 Characterization of graphene oxide samples

For the AFM and SEM observation, freshly cleaved mica substrates were soaked in an aqueous solution of 3-aminopropyltriethoxysilane (APTES; 12 μL of APTES in 20 mL of H_2O) for 15 min. After being thoroughly rinsed with deionized H_2O and blow-dried with Nitrogen, the substrate was then soaked in a solution of GO. Then, the substrate was taken out from the solution and left to air dry at room temperature for 30 min. For Raman spectroscopy analysis, the graphene oxide solution (1mg/mL) was drop casted on a clean SiO_2/Si substrate and left to air dry at room temperature. The XPS analysis were done on the GO modified electrodes.

2.3.14 Fitting of impedance spectra

The impedance spectra represented as Nyquist plots in the complex planes of a bare CVD monolayer graphene electrode is shown in Figure 2.5(A). A semi-circle in the high frequency domain characterizes the Nyquist plot, which corresponds to an interfacial charge transfer mechanism. However, a Warburg line was not observed in the low frequency limit, indicating that charge transfer dominates over mass transport effects [46]. The impedance spectra were fitted with an equivalent circuit shown in Figure 2.5(B).

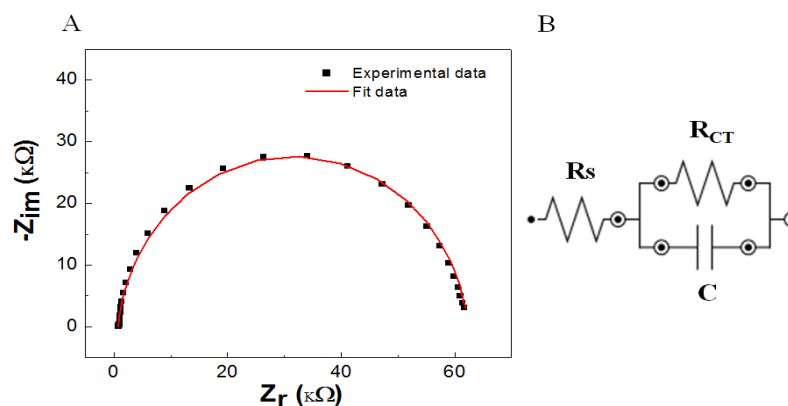


Figure 2.5(A) Nyquist plot of bare graphene electrode in 10 mM $[\text{Fe}(\text{CN})_6]^{4-/3-}$ solution at 0.2 V over a frequency range between 0.1 Hz and 100 Hz. The symbols represent the experimental data and the red curve represent the fitted data using the equivalent circuit (B) The equivalent circuit model used to fit the experimental data. C, is the double layer capacitance; R_{ct} , is the charge transfer resistance; R_s , is the solution resistance.

This circuit consists of the solution resistance, R_s , which represent the bulk properties of the electrolyte solution, the double-layer capacitance, C , and charge-transfer resistance, R_{CT} . The semicircle corresponds to the parallel combination of the charge-transfer resistance, R_{CT} , with the double layer capacitance, C . The goodness-of-fit (χ^2) was calculated to be in the range of 0.001-0.32 which indicates good fit between the theoretical and the experimental data Figure 2.5(A).

A representative example of the impedance spectra of the aptamers modified gold electrodes (OA or BTX aptasensors) is shown in Figure 2.6. The spectrum is composed of a semicircular part in a high frequency region and a linear part in a low frequency region, corresponding to the electron transfer process and the diffusion process of the redox couple from the bulk of the solution to the electrode interface, respectively. The impedance spectra were fitted by a modified Randles equivalent circuit (Figure 2.6), consisting of the solution resistance (R_s), charge-transfer resistance (R_{ct}), constant phase element (CPE) representing the electrical double layer capacitance and Warburg impedance (Z_w) resulting from the diffusion^{100,103}. The diameter of the semicircle corresponds to the charge-transfer resistance (R_{ct}).

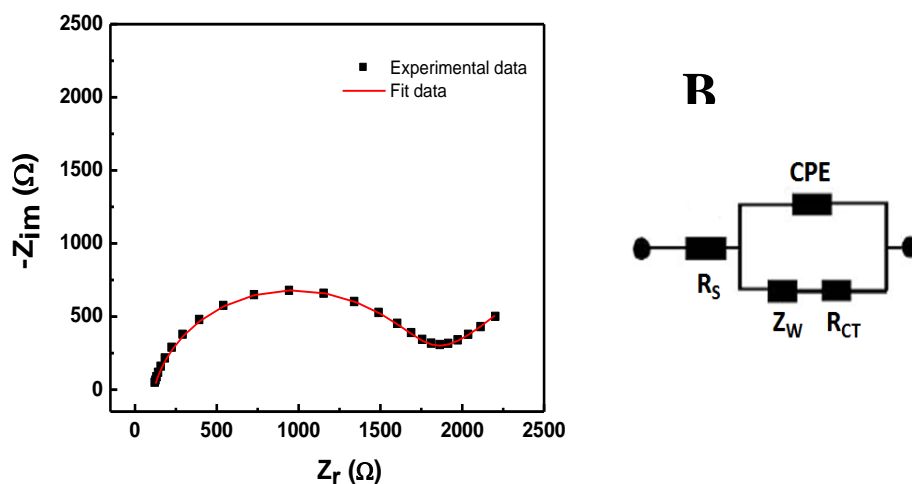


Figure 2.6(A) Example of Nyquist plot of aptamer modified Au electrode. The symbols represent the experimental data and the red curve represent the fitted data using the equivalent circuit. The goodness-of-fit (χ^2) was calculated to be < 0.001 for all the impedance spectra which indicates good fit between the theoretical and the experimental data. (B) Modified Randles equivalent circuit which used to fit the impedance results.

2.4 Techniques used throughout the work

The following tables summarises all the used surface characterization and electrochemical techniques.

Table 2.1 Surface characterization techniques

Technique	Purpose
XPS	Characterization of surface composition of GSPE, CVD graphene and GO electrodes before and after functionalization
SEM	Characterization of the surface morphology of GSPE, CVD graphene and GO electrodes
Raman spectroscopy	Characterization of the defect density of the CVD graphene before and after functionalization as well as the different sheet sizes of GO materials
AFM	Characterization of the size of GO sheets and their thickness
NMR	Characterization of the oxidation degree of small and large-sized GO sheets

Table 2.2 Electrochemical techniques

Technique	Purpose
CV	Characterization of electrodes functionalization, biosensor fabrication steps, electrografting steps and study the mechanism of the redox reaction.
SWV	Characterization of OA immunosensor and MC-LR aptasensor and detection.
DPV	Characterization of the β -LG and OVA immunosensors and detection.
EIS	Characterization of aptasensors fabrication steps and detection of toxins on the aptasensors as well as the detection of OVA on the CVD graphene immunosensor.

CHAPTER 3. LABEL-FREE ELECTROCHEMICAL IMMUNOSENSORS FOR MILK AND EGG ALLERGENS β -LACTOGLOBULIN AND OVALBUMIN BASED ON ELECTROGRAFTING OF ARYL DIAZONIUM SALTS ON GRAPHENE ELECTRODES

This chapter describes the development of label-free electrochemical immunosensors for milk and egg allergens using graphene as electrode material. In order to begin the investigation of graphene materials as transducer, it was necessary to study and optimise a general methodology for the functionalization of graphene surface. This chapter shows the modification of graphene electrodes using electrochemical reduction of aryl diazonium salts. In order to investigate the suitability of the proposed modification approach for different graphene materials, commercial GSPE as well as high quality monolayer graphene prepared via chemical vapour deposition were utilized in this study. The modified graphene was subsequently used for the detection of the two important model allergens β -LG and OVA.

3.1 β -Lactoglobulin immunosensor

The diazonium cations were first prepared by the diazotisation of 4-nitroaniline. Subsequently, the in situ generated diazonium cations were covalently grafted through an electrochemical reduction step on the GSPE surface, followed by the electrochemical reduction of the terminal nitro groups to generate an aminated surface. Then, the aminophenyl modified surface was activated with glutaraldehyde to give a stable intermediate derivative which was used for covalent immobilization of the β -lactoglobulin antibodies (Figure 3.1).

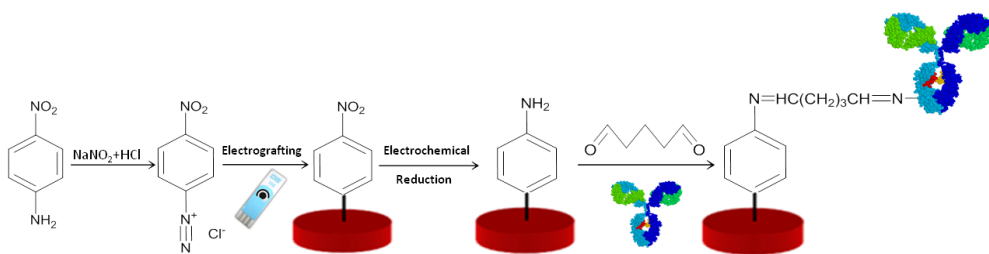


Figure 3.1 Functionalization of the graphene electrode surface and the covalent immobilization of antibodies

A simple differential pulse voltammetric immunoassay was used for the β -lactoglobulin detection based on the decrease of the $[\text{Fe}(\text{CN})_6]^{3-/4-}$ reduction peak current due to the specific binding of the β -lactoglobulin with the antibody modified electrodes. This approach enables a fast and simple electrochemical detection method of β -lactoglobulin detection.

3.1.1 Electrochemical functionalization

Previous studies¹⁹⁶ have shown that surface functionalization strategies is a determining factor in the performance of biosensor platforms as it greatly affects both the sensitivity and the selectivity of the biointerfaces. Therefore, different electrografting periods and protocols were studied to investigate their effect on the density of the deposited organic layer on graphene surface. Eight different electrochemical modification protocols has been used for the reduction of the diazonium salt; 1) spontaneous reaction for 180 s, 2) one CV from 0.4 to -0.6 V at 100 mV s^{-1} , 3) five CV scans from 0.4 to -0.6 V at 100 mV s^{-1} , 4) linear sweep voltammetry form 0.4 to -0.6 V at 100 mV s^{-1} , 5) 15 s duration CA, 6) 45 s duration CA, 7) 60 s duration CA, and 8) 180 s duration CA at -0.4 V. In each case the nitro groups attached the electrode surface after each electrografting process are reduced using five CV scans from +0.4 to -1.4 V in 0.1 KCl solution and the surface coverage of the NP groups has been calculated from the area under the reduction peaks.

The consecutive cyclic voltammograms for in situ-generated 4-nitrobenzene diazonium cation at a GSPE are shown in Figure 3.2. The CVs are characterized by a broad irreversible reduction wave in the first cycle at -0.35 V vs. Ag reference electrode. This behaviour corresponds to the

electroreduction peak of the diazonium salts via one electron transfer process resulting in elimination of a nitrogen molecule and production of an aryl radical which forms a covalent bond with the graphene surface¹⁴³⁻¹⁴⁴. During the second and subsequent cycles, the intensity of the reduction peak is decreased and not completely diminished. This behaviour could be attributed to the fact that the electrografting step using the CV scans was not enough to cover the entire electrode surface with the grafted organic layer, therefore, preventing the complete passivation of the electrode and allowing the reduction of other diazonium cations in solution.

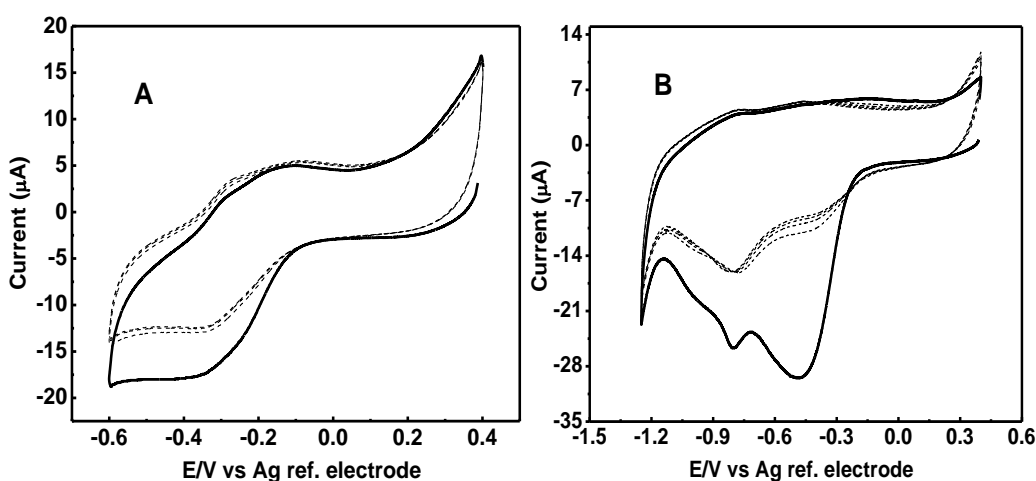


Figure 3.2(A) Cyclic voltammogram for the in situ generated 4-nitrophenyl diazonium salt in the diazotization mixture (2 mM NaNO₂ + 2 mM 4-nitroaniline in 0.5 HCl) at graphene modified screen printed electrode, (B) Successive cyclic voltammograms of the reduction of NP/GSPE in 0.1M KCl at scan rate of 100 mVs⁻¹. The solid lines represent the first CV and the dotted lines represent the subsequent cycles.

Figure 3.2(B) shows successive CVs for the reduction of 4-nitrophenyl modified GSPE in aqueous 0.1 M KCl solution from 0.4 to -1.4 V vs. Ag reference electrode. Two reduction peaks were observed in the voltammograms which correspond to the irreversible reduction of electrografted 4-NP groups on the graphene electrode surface. The two cathodic peaks are attributed to the reduction of the nitro groups to hydroxylamine derivatives in ($4e^-/4H^+$) process and further to the corresponding amines ($2e^-/2H^+$). Then, the reduction peaks significantly decreased in the subsequent scans indicates

almost a complete reduction of the nitro groups into amines. A similar behaviour was previously reported for the reduction of nitrophenyl groups on other surfaces ¹⁹⁷⁻¹⁹⁹.

The surface coverage in each case was then calculated by integration of the area under the reduction peak according to equation 1:

$$\Gamma = Q/nFA \quad \text{Eq. 1}$$

Where Γ is the coverage as number of moles. cm^{-2} , Q is the charge obtained by integrating the cathodic peak, n is the number of electrons transferred, F is Faraday's constant and A is the surface area. As shown in Table 3.1 all the values of the surface coverage of the nitrophenyl groups grafted using electrochemical methods (protocols 2-8) are significantly higher than that grafted using spontaneous electron transfer reaction by immersing the electrode in the diazonium salt solution for 180 s without applying potential (protocol 1). Furthermore, the surface coverage values of the electrografted NP groups on the graphene surface for 1 min. or less (protocol 2-7) were ranging from 4.00×10^{-10} to 13.0×10^{-10} mol. cm^{-2} , which is comparable with the value reported previously for the chemically grafted NP groups on epitaxial graphene ¹⁴⁸ as well as other carbon surfaces ^{145,200-201}. It was also noticed that the electrodeposition using cyclic voltammetry scans (protocols 2 and 3) produced the lowest NP coverage which confirm that the grafted film was not very compact as it was explained above. The linear sweep voltammetric method (protocol 4) gave higher coverage than the cyclic voltammetric procedure. However, the chronoamperometric method (protocols 5-8) gave the highest surface coverage indicating more compact layer even with 15 s duration and the density of the grafted nitrophenyl groups was increased by increasing the time from 15 to 180 s. The results demonstrated that both monolayers and multilayers can be obtained by the reduction of diazonium salts which is a known behaviour observed on other materials ²⁰²⁻²⁰³. The use of chronoamperometry step at -0.4 V for 45 s or 60 s (protocols 6 and 7) for the grafting has achieved the best agreement with the theoretical surface coverage of nitrophenyl groups (12.5×10^{-10} mol/ cm^2) which is based on ideal highly ordered closed packed monolayer ²⁰⁴. By increasing the time of the electrochemical grafting process the surface coverage increases, indicating the continuous growth of multilayer and higher film thickness. The formation of multilayer of 4-nitrophenyl (NP) is not desirable as it causes

disorder of the grafted film sterically hindering the access of the nitro groups on the layers closer to the electrode surface.

Table 3.1 Active surface coverage concentration (Γ) of nitrophenyl groups on the GSPE formed using different protocols.

Protocol number	Method	Surface coverage $\times 10^{-10}$ (mol. cm ⁻²)
1	Spontaneous reaction 180 s	0.80
2	One cyclic voltammetry	4.00
3	Five cyclic voltammetry	4.10
4	Linear weep voltammetry	4.80
5	Chronoamperometry 15 s	5.70
6	Chronoamperometry 45 s	7.35
7	Chronoamperometry 60 s	13.0
8	Chronoamperometry 180 s	19.9

The purpose of the present work was to modify in a reproducible way the graphene electrodes with a well ordered monolayer of aminophenyl groups enabling maximum antibody immobilization, but at the same time avoiding a complete surface passivation. Thus, the chronoamperometry reduction at -0.4 V for 45 s was selected as the optimum condition for the graphene modification. However, an easier electron transfer to the electrode surface would be an advantage for electrodes modified by cyclic and linear sweep voltammetry where non compact layer is formed. This could also find applications in some cases as enzyme-based amperometric biosensors in which the maximum electric communication between the enzyme and the electrode surface is required as previously reported elsewhere¹⁹⁸.

3.1.2 X-ray photoelectron spectroscopy surface characterization

The bare graphene, 4-nitrophenyl modified graphene electrode and the reduced form (4-aminophenyl film) were examined by XPS in order to confirm the functionalization and the subsequent reduction processes. Figure 3.3 shows the survey spectra of the nitrophenyl modified graphene electrodes with an additional N1s peak compared to the spectra of the bare GSPE.

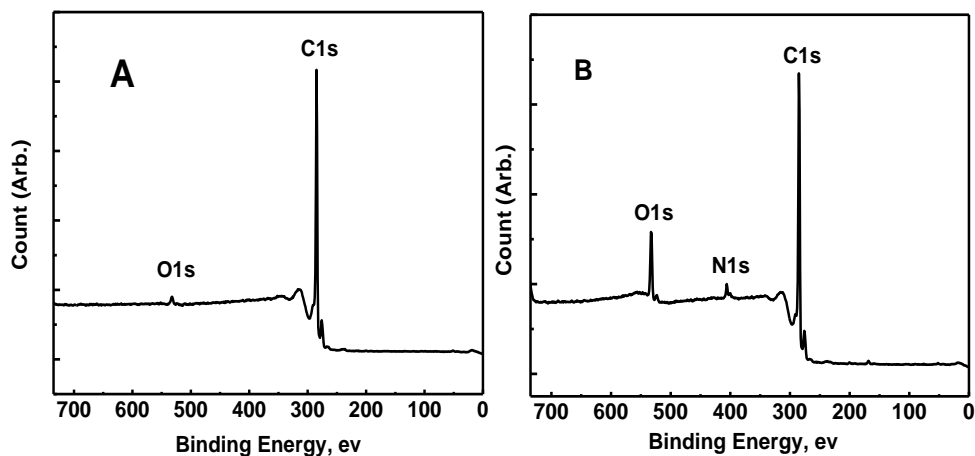


Figure 3.3 XPS survey spectra for bare GSPE (A) and NP-GSPE (B).

Moreover, the high resolution of the N1s spectrum of the NP sample (Figure 3.4) shows two peaks at 405.85 eV and 400.04 eV. The peak at higher binding energy is due to the nitro groups (NO_2) and confirms the presence of the nitrophenyl film on the graphene surface. The other peak at lower binding energy (400.04 eV) is assigned to the amino (NH_2) groups, which is most probably due to the reduction of some nitro groups in the XPS analysis chamber during the measurements as reported elsewhere^{148,199,205}. The electrochemical reduction of the nitrophenyl groups to aminophenyl groups was further confirmed by the XPS measurements of the aminophenyl graphene modified screen printed electrodes (AP-GSPE). Figure 3.4 shows the high resolution of the N1s spectrum of the AP-GSPE compared with NP-GSPE. A single peak at 400.04 eV was observed for the aminophenyl modified electrode assigned to the amino groups which confirm the conversion of the nitro groups to amines and also demonstrate the robust nature of the aryl modified graphene¹⁴⁸.

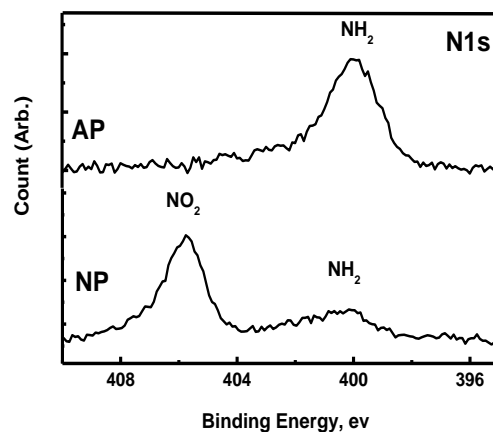


Figure 3.4 XPS core level N1s spectra of NP-GSPE and AP-GSPE.

3.1.3 Differential pulse voltammetric characterisation of the immunosensor stages

Differential pulse voltammetry has been used in order to characterise the stepwise modification of immunosensors. Fig. 3 shows the DPVs of 5 mM $[\text{Fe}(\text{CN})_6]^{4-/3-}$ probe in PBS, pH 7.4 for the bare GSPE (a), 4-NP/GSPE modified electrode (b), 4-AP/GSPE modified electrode (c), GA/4-AP/ GSPE (d), Ab/4-AP/ GSPE modified electrode (e), BSA/Ab/4-AP/ GSPE modified electrode (f) and after incubation with 100 ng mL^{-1} β -lactoglobulin solution for 45 min (g).

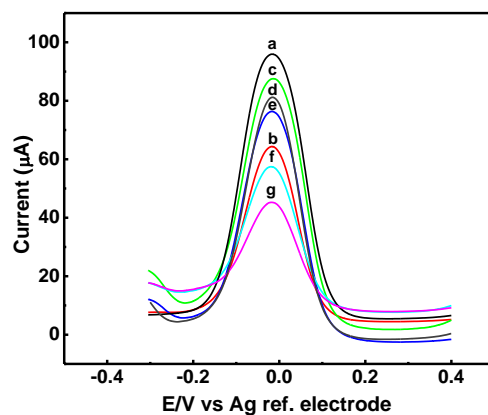


Figure 3.5 DPVs of 5 mM $[\text{Fe}(\text{CN})_6]^{4-/3-}$ probe in PBS, pH 7.4 for bare GSPE (a); 4-nitrophenyl/ GSPE modified electrode (b), 4-aminophenyl/ GSPE modified electrode (C), GA/4-AP/ GSPE (d), Ab/4-AP/ GSPE modified electrode (e), after blocking with 0.25% BSA for 45 min (f) and After incubation with 100 ng mL^{-1} of β -lactoglobulin solution for 45 min (g).

A well-defined reduction peak is clearly observed for the bare GSPE. The electrochemical grafting modification using chronoamperometry at -0.4 V for 45 s produced 4-NP film on the GSPE electrodes leading to further reduction of the intensity of the $[\text{Fe}(\text{CN})_6]^{4-/3-}$ reduction peak. This is due to the deposition of the organic layer which partially blocks the surface but in the same time the electron transfer still takes place. After the reduction of the nitro groups on the surface to amine groups the peak current increased again. This could be attributed to the ionisation of some amino groups on the surface, which lead to an electrostatic attraction with the $[\text{Fe}(\text{CN})_6]^{4-/3-}$ anions in solution as reported by Covaci et al. ²⁰⁶. The reduction peak currents of $[\text{Fe}(\text{CN})_6]^{4-/3-}$ was further decreased after the reaction of the amino groups with glutaraldehyde, then after the antibody immobilization and blocking the free active sites on the electrodes surface with BSA due to the blocking effect of these proteins. The formation of the immunochemical reaction of β -lactoglobulin molecules with the antibody modified electrodes was also accompanied by a decrease in the reduction peak current of the redox probe, showing that the electron-transfer kinetics of $[\text{Fe}(\text{CN})_6]^{4-/3-}$ is decreased. This current decrease after binding is not only due to the blocking effect from the β -lactoglobulin protein but could also be attributed to a number of factors. For example, the isoelectric point of the β -lactoglobulin equals 5.2 ²⁰⁷, which in turn offers a negative charge at pH 7.4, acting as an electrostatic barrier for the electron transfer. It could be also partly due to conformational changes of the antibody after binding with the protein ²⁰⁸.

3.1.4 Cyclic voltammetric characterization of the mechanism of the electrochemical process on the modified graphene electrodes:

The relationship between the peak current and the square root of the scan rate was studied in order to gain insight into the electrochemical mechanism taking place at the immunosensor. The CVs of the resulting immunosensor in 5 mM $[\text{Fe}(\text{CN})_6]^{3-/4-}$ at different scan rates were investigated in the range of 10-200 mVs⁻¹ (Figure 3.6). It is clear that both the anodic and cathodic peak currents increased linearly with the square root of scan rate, with correlation coefficients of 0.998 and 0.990 respectively, indicating diffusion-controlled process over the studied range of the scan rate.

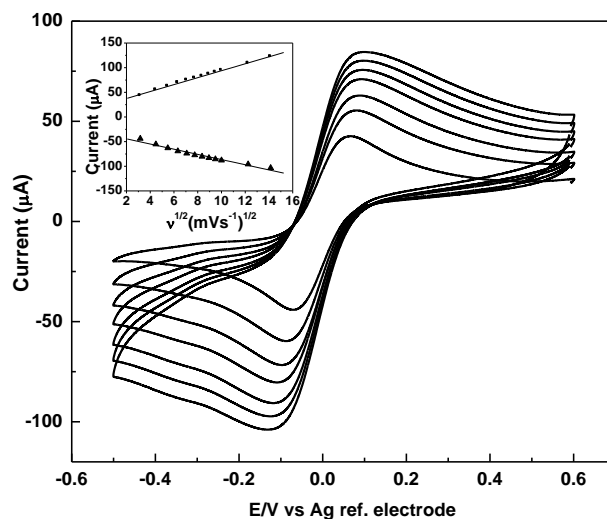


Figure 3.6 CVs of the modified electrode at different scan rates (from inner to outer): 10, 20, 30, 40, 50, 60, and 70 mV/s in 5 mM $[\text{Fe}(\text{CN})_6]^{3-/4-}$ solution. The inset shows the dependence of the oxidation and reduction peak currents on the square root of scan rates.

3.1.5 Dose response of the β -lactoglobulin immunosensor

The DPV technique was used to monitor the binding between the ovalbumin and the antibody bound electrode, by observing the change in the reduction peak current of the redox probe $[\text{Fe}(\text{CN})_6]^{3-/4-}$ on the electrode surface. The introduction of any blockage for the redox probe to access the graphene electrode surface, such as the introduction of bulky protein or negatively charged groups, will retard the charge transfer and consequently reduce the current. To evaluate the immunochemical reaction between the antibody and β -lactoglobulin, the immunosensor was exposed to various concentrations of β -lactoglobulin (0, 0.001, 0.01, 0.1, 1.0, 10 and 100 ng mL⁻¹). Figure 3.7(A) shows the decrease in the differential pulse voltammetric reduction peak of $[\text{Fe}(\text{CN})_6]^{4-/3-}$ with the increment of β -lactoglobulin.

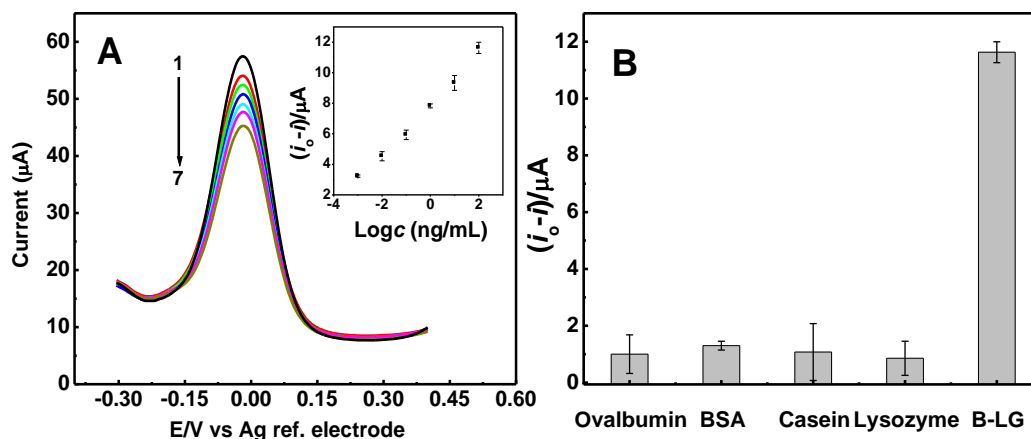


Figure 3.7(A) DPVs of the immunosensor incubated with different concentrations of β -lactoglobulin (1–7): the concentrations of β - LG are 0.000, 0.001, 0.01, 0.1, 1.0, 10 and 100 ng mL⁻¹. The inset is the calibration curve based on the change of the DPV peak currents versus the logarithm of the concentrations, (B) Comparison of response of GSPE voltammetric immunosensor to 1000 ng ml⁻¹ ovalbumin or 100 ng ml⁻¹ β -lactoglobulin.

The inset in Figure 3.7(A) shows a good linear relationship between the change of the cathodic peak currents obtained by DPV and the logarithm of β -lactoglobulin concentrations from 1.0 pg ml⁻¹ to 100 ng mL⁻¹. Each data point in the calibration plot represents three independent measurements and the error bars show the standard deviations of measurements. The relative standard deviations were from 1.6 % to 6.0 % indicates good reproducibility of the immunosensor. The linear regression equation was $i_o - i$ (μA) = 7.88 + 1.56 \times logC [ng ml⁻¹], R = 0.998, with a detection limit (LOD) of 0.85 pg mL⁻¹ (S/N = 3). The results indicated that the developed immunosensor in this study exhibited lower detection limit compared with other reported methods^{3,58,209} without any amplification steps. A comparison between our method and other reported detection methods is shown in Table 3.2.

Table 3.2 Comparison of performance of the different detection methods for β -lactoglobulin.

Method	Limit of detection	Analytical range	Reference
Voltammetric immunosensor	0.85 $\mu\text{g mL}^{-1}$	1 $\mu\text{g mL}^{-1}$ - 100 ng mL^{-1}	This work
Optical near field biosensor	n.a.	100 ng mL^{-1} -100 $\mu\text{g mL}^{-1}$	57
Colourimetric immunosensor	1 ng mL^{-1}	10 ng mL^{-1} -1 mg mL^{-1}	209
ELISA	9.7×10^{-13}	3.5×10^{-11} - 4.6×10^{-8} M	43

3.1.6 Selectivity of the immunosensor

It was very important to study the selectivity of the immunosensor to confirm that the immunosensor response is due to specific interaction between the β -lactoglobulin and the antibody immobilized on the electrode. A control experiment has been performed by incubating the immunosensor with four different non-specific proteins which may present in the food: ovalbumin, BSA, egg lysozyme and casein. Figure 3.7(B) shows non-significant change in reduction peak current for the antibody modified electrodes incubated with ($1.0 \mu\text{g mL}^{-1}$) of each protein for 45 min compared with another immunosensor prepared using identical protocol and incubated with 100 ng mL^{-1} of β -lactoglobulin. These results confirm that the immunosensor displayed good selectivity for the determination of β -lactoglobulin.

3.1.7 Stability and reproducibility of the immunosensor

The stability of the immunosensor was studied after storage at $4 \text{ }^\circ\text{C}$ for 15-day period. The immunosensor was used to detect 1 ng/mL β -lactoglobulin. The difference in the peak current was $7.88 \mu\text{A}$ before and $7.99 \mu\text{A}$ after (less than 2 % current change), demonstrating that the immunosensor had good stability. The reproducibility of the immunosensor was examined by performing three independent measurements for each concentration in the calibration plot. The relative standard deviations were from 1.6 % to 6.0 % indicates good reproducibility of the immunosensor.

3.1.8 Real Sample Analysis.

The developed immunosensor was then applied for the detection of β -lactoglobulin in commercial milk-containing food products. As can be seen in Table 3.3, a good correlation was obtained between the immunosensor and the ELISA results, which indicated that the developed immunosensor might be applied for the determination of β -lactoglobulin for routine use. Moreover, the low detection limit enabled the successful application of the immunosensor in the highly diluted real extracts which significantly minimized the matrix effect.

Table 3.3 F-test and t-test calculations for the three food samples analysis

Parameter	Sweet biscuit sample		Cake		Cheese snacks	
	Immunosensor	ELISA	Immunosenso r	ELISA	Immunosenso r	ELISA
N	3	3	3	3	3	3
S.D.	7.47	7.70	7.50	9.30	87330	92300
R.S.D. (%)	0.25	0.50	0.16	0.71	3000	6461
t-test	3.35	6.49	2.13	7.63	3.44	7.00
F-test	0.71	{t(P = 0.05)}	4.28	{t(P = 0.05)}	1.20	{t(P = 0.05)}
	4.00	= 2.78	19.69	= 2.78	4.64	= 2.78
		= 19.0		= 19.0		= 19.0

S.D. is the standard deviation, RSD is the relative standard deviation = (S.D./mean)X100

As shown in Table 3.3, the F-test and t-test calculations have been done for the three food samples. The results of the student's t-test and variance ratio F-test of the sweet biscuit and the cheese snacks show that there are no significant differences between the techniques with regard to accuracy and precision. However, the results of the cake sample showed more difference which could be attributed to the effect of the matrix of the cake extract on the ELISA detection which can cause overestimation of the β -lactoglobulin level, while the higher dilution of the same sample (1:150) for the detection by the immunosensor had significantly minimized the matrix effect. Moreover, the lower RSD of the

proposed immunosensor (2.13 %) compared with ELISA (7.63 %) indicates more precision of the developed immunosensor.

3.2 Ovalbumin immunosensor using GSPE

3.2.1 Electrochemical functionalization of graphene electrode surface

The electrochemical functionalization of graphene electrode surface was performed as described in section 2.3.6.2 by the cyclic voltammetry reduction of the *in situ* generated carboxyphenyl diazonium salts from 0.4 to -0.6 V at scan rate of 100 mV s^{-1} , leading to the formation of carboxyphenyl film on the graphene surface (Figure 3.8)

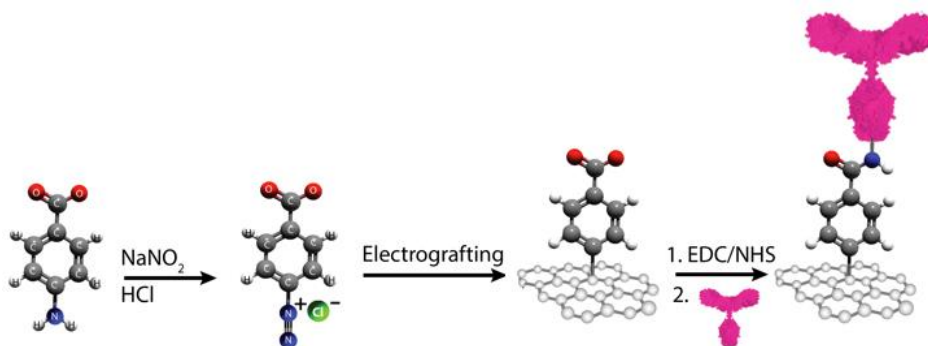


Figure 3.8 Schematic of the electrografting process of carboxyphenyl groups on the graphene electrode and the subsequent antibody immobilization.

A single irreversible cathodic peak at -0.12 V vs. Ag reference electrode was observed in the first cyclic voltammetry scan on GSPE as shown in Figure 3.9(A) which then gradually diminished in the second and the third CV scans as previously observed with the nitrophenyl diazonium salt. The electrochemical behaviour of the carboxyphenyl modified electrodes using different CV cycles was further studied using differential pulse voltammetry in the presence of $[\text{Fe}(\text{CN})_6]^{3-/4-}$ redox probe. As shown in Figure 3.9(B) the DPV reduction peak current of the $[\text{Fe}(\text{CN})_6]^{3-/4-}$ species was decreased with increasing the number of cyclic voltammetry reduction cycles used for the carboxyphenyl

grafting. This decrease in the reduction peak current of the $[\text{Fe}(\text{CN})_6]^{3-/4-}$ redox species indicates the blocking effect of the carboxyphenyl layer for the reduction of the $[\text{Fe}(\text{CN})_6]^{3-/4-}$ on the modified electrode surface. This effect is due to the thickness of the organic layer as well as the electrostatic repulsion between the negatively charged carboxylic groups and the $[\text{Fe}(\text{CN})_6]^{4-/3-}$ redox probe. The DPV peak currents of the $[\text{Fe}(\text{CN})_6]^{4-/3-}$ were plotted versus the number of CV scanning cycles used for the diazonium cations reduction.

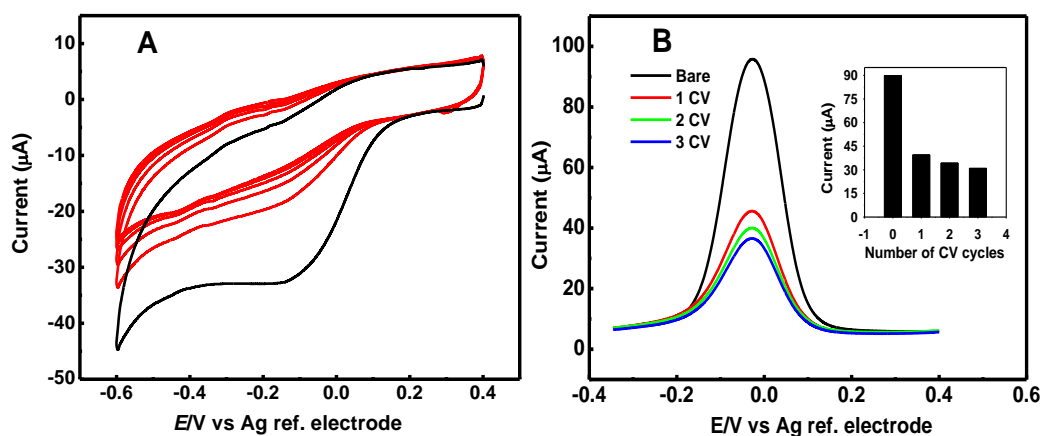


Figure 3.9(A) Successive CVs for the *in situ* generated 4-carboxyphenyl diazonium salt at scan rate of 100 mVs^{-1} on GSPE, the black line represent the first CV and the red lines represent the subsequent cycles, (B) DPVs of bare GSPE and 4-CP-GSPE functionalized by diazonium salt reduction using different CV cycles in $5 \text{ mM } [\text{Fe}(\text{CN})_6]^{4-/3-}$ at 100 mV/s . Inset is the plot of the reduction peak current for $5 \text{ mM } [\text{Fe}(\text{CN})_6]^{4-/3-}$ measured at 4-CP-GSPE vs. the number of CV scanning cycles for diazonium reduction on GSPE.

A decrease in the peak current was observed with increasing the number of CV scans as can be seen in the inset of Figure 3.9(B). However, the largest drop in the peak current was observed after the electrografting using one CV cycle, while a smaller difference in the peak current was observed after the subsequent cycles. These results confirm that the increase in number of CV cycles leads to an

increase in the density of the organic layer, formed in the electrode surface, which in turn results in more hindrance for the electron transfer process.

3.2.2 Differential pulse voltammetric characterisation of the immunosensor construction

The DPVs for all modification steps were shown in Figure 3.10. After the electrografting of carboxyphenyl groups on the GSPE the intensity of the $[\text{Fe}(\text{CN})_6]^{4-/3-}$ reduction peak was decreased (Figure 3.10b), due to the partial blocking of the surface as illustrated above. After the activation of the carboxylic group and the covalent antibody immobilization, the reduction peak current of $[\text{Fe}(\text{CN})_6]^{4-/3-}$ was increased again (Figure 3.10c). This increase in the current could be attributed to the neutralization of the negative charge of the terminal carboxylic groups on the surface with the positively charged antibodies. Similar behaviour was reported previously elsewhere^{157,198}.

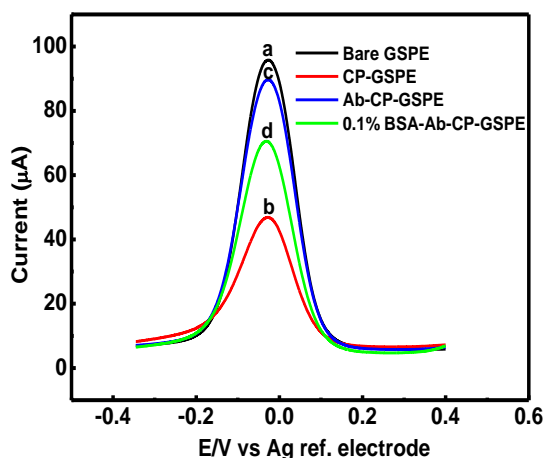


Figure 3.10 DPVs of 5 mM $[\text{Fe}(\text{CN})_6]^{4-/3-}$ probe in PBS, pH 7.4 for bare GSPE (a), 4-CP/ GSPE (b), Ab/4-CP/ GSPE (c), and after blocking with 0.1% BSA for 30 min (d).

3.2.3 Differential pulse voltammetry detection of ovalbumin on the immunosensor

As shown in Figure 3.11(A), a decrease in the differential pulse voltammetric reduction peak of $[\text{Fe}(\text{CN})_6]^{4-/3-}$ was observed with incubating the immunosensor with different concentrations of ovalbumin (0, 0.01, 0.1, 1.0, 10, 100 and 200 ng mL⁻¹). This decrease in the current upon binding is

attributed to the bulky size of the protein sterically hinders $[\text{Fe}(\text{CN})_6]^{4-/3-}$ anions to access the electrode surface. The ovalbumin also has isoelectric point equal 4.6²¹⁰, which has a negative charge at pH 7.4 resulting in repelling the $[\text{Fe}(\text{CN})_6]^{4-/3-}$ anions.

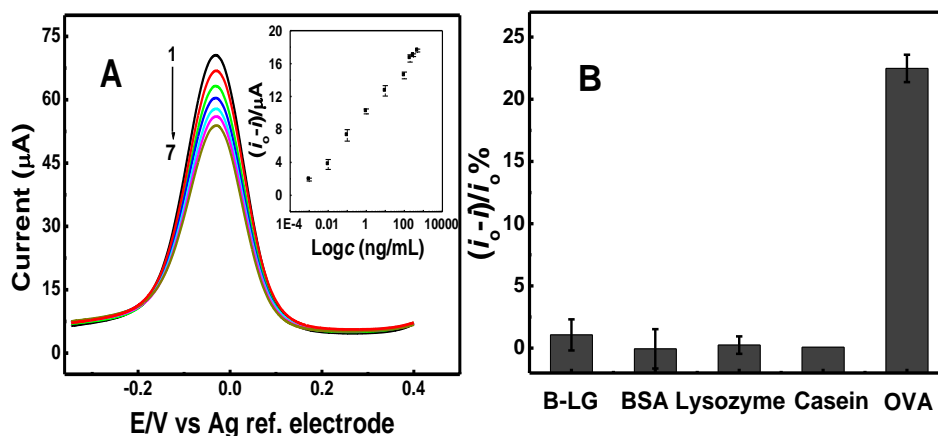


Figure 3.11(A) DPVs of the immunosensor incubated with different concentrations of ovalbumin. The inset is the calibration curve, (B) Comparison of response of the immunosensor to 100 ng ml⁻¹ ovalbumin, BSA, Casein, Lysozyme, and β -lactoglobulin.

As shown in the inset of Figure 3.11(A), a good linear relationship was obtained between the change of the cathodic peak current of $[\text{Fe}(\text{CN})_6]^{4-/3-}$ redox probe in the DPV, and the logarithm of the ovalbumin concentrations from 1.0 pg ml⁻¹ to 0.5 $\mu\text{g mL}^{-1}$. The data points in the calibration curve represent three independent measurements and the error bars show the standard deviations ranging from 2.6 % to 5.0 % indicating good reproducibility of the immunosensor. The linear regression equation was $i_o - i (\mu\text{A}) = 9.98 + 2.81 \times \log C [\text{ng mL}^{-1}]$, $R = 0.997$, with a detection limit (LOD) of 0.83 pg mL⁻¹ (S/N = 3). The results confirms that the proposed immunosensor exhibits lower detection limit compared with other previously reported methods^{4,60}. Moreover, as can be seen in Figure 3.12(B), the % decrease in the current for β -lactoglobulin, BSA, lysozyme and casein was much lower than that of the ovalbumin. These results indicates that the immunosensor exhibited good selectivity for the determination of ovalbumin with negligible effect of the non specific proteins.

3.3 Ovalbumin immunosensor using CVD graphene

High quality and uniform graphene sheets were grown by a CVD process using Cu foil as catalytic substrate (Figure 3.12(A)) as shown in the scanning electron microscopy image (Figure 3.12(B)). The graphene sheets were then transferred onto a clean glass substrate (Figure 3.12(C)).

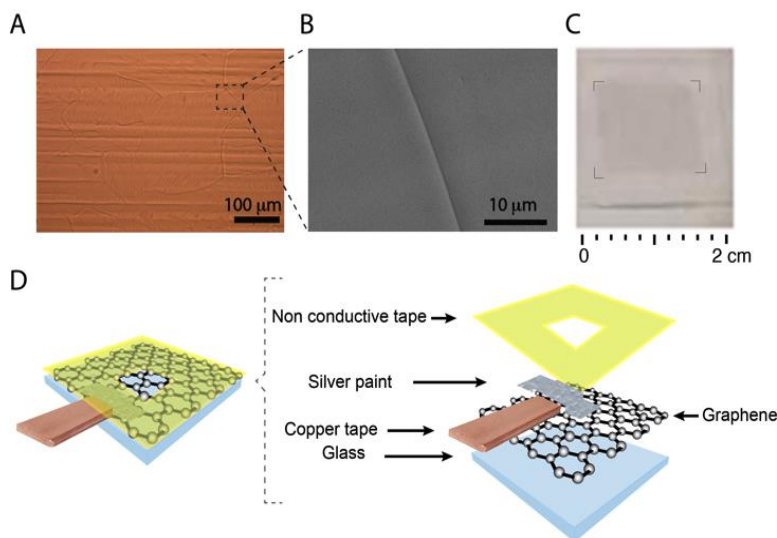


Figure 3.12 Optical microscopic image of monolayer graphene film on Cu foil. (B) SEM image of graphene (C) Monolayer graphene film transferred onto a glass sheet, (D) Schematic of the procedure for connecting monolayer graphene sheets into working electrodes for electrochemical measurements.

We used here glass as an insulating substrate to avoid the possible influence of the underlying metal substrate on the electrochemical behaviour of graphene. The characteristics of the graphene films were analysed before and after the transfer process by optical microscopy, Raman spectroscopy and X-ray photoelectron spectroscopy (Figure 3.13). No significant changes were observed, indicating that the chemical and structural composition of the graphene films was maintained through the transfer process. The graphene films were then connected as a working electrode using copper tape and silver paint and subsequently insulated to expose a well defined area of graphene as described in detail in the experimental section (Figure 3.12(D)). This simple design ensures that graphene is the only conductive surface exposed to the solution during electrochemical measurements.

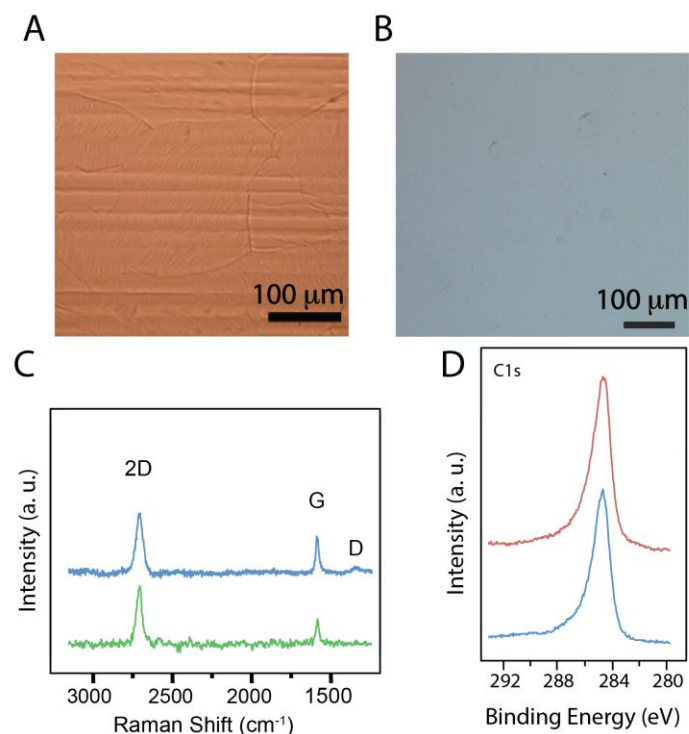


Figure 3.13 Optical microscopy images of CVD monolayer graphene film before (A) and after (B) the transfer process; (C) Raman spectra of CVD monolayer graphene film before (bottom) and after (top) the transfer process; (D) XPS C1s core level spectra for CVD monolayer graphene film before (bottom) and after (top) the transfer process.

3.3.1 Graphene functionalization and characterization

Functionalization of the CVD graphene surface was again performed by electrochemical reduction of carboxyphenyl diazonium salt using three consecutive CVs as previously shown in the scheme (Figure 3.8). Figure 3.14 shows that the CVs of the electrografting process were consistent with that obtained on the SPGE shown in the previous section (Figure 3.9).

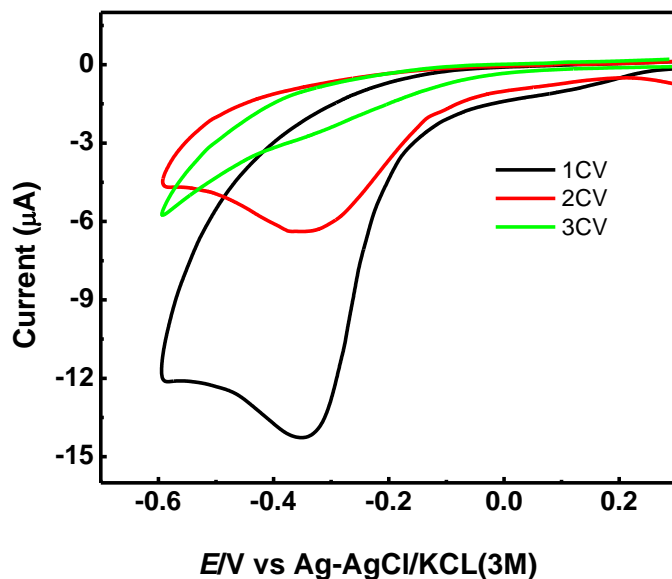


Figure 3.14 Successive CVs for the 4-carboxyphenyl diazonium salt at scan rate of 100 mVs^{-1} on CVD graphene.

We examined the graphene electrodes before and after the carboxyphenyl functionalization using Raman spectroscopy, X-ray photoelectron spectroscopy and atomic force microscopy. The Raman spectra of graphene electrodes before and after functionalization are shown in Figure 3.15(A). The bare graphene (black curve), exhibits two prominent Raman Stokes peaks, a single symmetric 2D peak at $\sim 2700 \text{ cm}^{-1}$ and a G peak at $\sim 1580 \text{ cm}^{-1}$. The intensity of the 2D peak is almost twice the intensity of the G peak over most of the sample area, characteristic of monolayer graphene and indicative that the graphene sheets transferred onto the glass substrate were continuous and uniform²¹¹⁻²¹². A small D peak at $\sim 1350 \text{ cm}^{-1}$ was also observed in the Raman spectra of the bare graphene, corresponding to a low defect density. After subsequent modification of graphene using one (Figure 3.15(A), red curve) to three CV (Figure 3.15(A), blue curve) scans in the diazonium solution, the intensity of the D peak was gradually enhanced and D' and D + D* peaks appeared at $\sim 1620 \text{ cm}^{-1}$ and $\sim 2950 \text{ cm}^{-1}$, respectively. These changes are attributable to the breaking of translational symmetry of the honeycomb lattice of C–C sp^2 bonds on the basal plane of the graphene due to the formation of localized C–C sp^3 bonds by carboxyphenyl grafting.

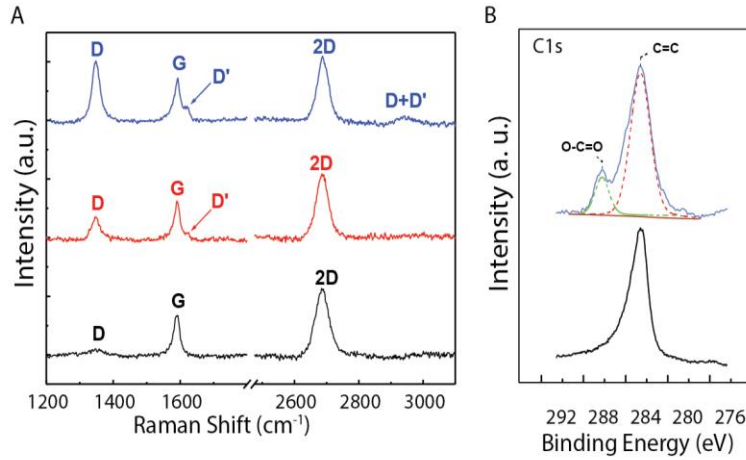


Figure 3.15(A) Raman spectra of the graphene electrode before (Black curve) and after subjected to the electrografting process using one (red curve) and three (blue curve) CV cycles and (b) XPS C1s core level spectra of graphene electrode before (bottom) and after (top) the carboxyphenyl functionalization.

Moreover, the defect density, σ , on the graphene lattice after covalent functionalization was quantified using the I_D/I_G ratio based on the empirical formula (equation 2) ²¹³:

$$\frac{I_D}{I_G} = C_A \frac{r_A^2 - r_S^2}{r_A^2 - 2r_S^2} \left[\exp\left(-\frac{\pi r_S^2}{L_D^2}\right) - \exp\left(-\frac{\pi(r_A^2 - r_S^2)}{L_D^2}\right) \right] + C_S \left[1 - \exp\left(-\frac{\pi r_S^2}{L_D^2}\right) \right] \quad \text{Eq. 2}$$

where L_D is the mean defect spacing ($L_D=1/\sigma^{1/2}$), r_S is the radius of the structurally damage region around each sp^3 bond / defect site, and r_A is the radius of the activated region around it. The C_A parameter is a measure of the maximum possible value of the I_D/I_G ratio in graphene. The C_S parameter is the value of the I_D/I_G ratio in the highly disordered limit. We used C_A (=4.56), C_S (=0.86), r_A (=1.0 nm), and r_S (=0.07 nm) as previously reported for aryl groups covalently attached to the graphene lattice ¹⁵². As shown in Table 3.4, The initial defect density, σ , is estimated for pristine CVD graphene to be very low ($7.1 \times 10^{11} \text{ cm}^{-2}$), whereas upon carboxyphenyl functionalization with one and three CV cycles, the defect density is increased to $4.1 \times 10^{12} \text{ cm}^{-2}$ and $1.1 \times 10^{13} \text{ cm}^{-2}$, respectively. These results confirm the gradual increase of the carboxyphenyl groups covalently attached to the graphene surface with the gradual increase of the number of CV cycles used in the

electrografting procedure. After the third cycle, no further change in the Raman spectra was observed which indicates that the coverage of the graphene surface with monolayer of aryl groups, a figure in good agreement with the observed saturation in CV Faradaic current data explained above.

Table 3.4 Values of I_D/I_G from the Raman spectra and the calculated values of the defect density, σ , for the graphene before and after electrografting.

Electrode	I_D/I_G	σ (cm ⁻²)	σ (mol cm ⁻²)
Bare graphene	0.10	7.1×10^{11}	1.2×10^{-12}
CP-GE, 1CV	0.55	4.1×10^{12}	6.8×10^{-12}
CP-GE, 3CV	1.42	1.1×10^{13}	1.9×10^{-11}

It is worth noting that the estimated defect density value obtained from our method at three CV cycles is consistent with that reported for the grafting of carboxyphenyl tetrafluoroborate on graphene supported on SiO₂ using spontaneous electron transfer chemistry¹⁵² as well as on Ni using an electrografting method in acetonitrile¹⁵⁹. For graphene/Ni electrografting, five CV scans were shown to be necessary to realize the maximum modification of the graphene surface. However, here we show that three CV scans were enough to cover the graphene surface with monolayer of aryl groups which indicates that the electrografting reaction in our case is faster. The slow reactivity of the graphene/ Ni towards the electrografting was explained to be due to the stabilizing lattice match between the monolayer graphene and the underlying Ni which makes the attachment of the aryl radicals on the basal plane more difficult¹⁵⁹. The modification of the graphene electrodes was also confirmed using X-ray photoelectron spectroscopy. Figure 3.15(B) shows the XPS C1s core level spectra of the graphene monolayers before and after the carboxyphenyl functionalization. For the bare graphene, a sharp peak at a binding energy of 284.2 eV was observed as expected for the sp² hybridized carbon atoms of graphene. However, after the carboxyphenyl modification, an additional peak centered at 288.8 eV appeared, typical of the carboxylic acid groups grafted on the graphene surface.

Examination of the modified CVD graphene electrodes by atomic force microscopy has also proved the formation of a carboxyphenyl layer. As shown in Figure 3.16(A), the AFM images obtained in ScanAsyst mode reveals significant difference between bare and modified graphene using three CV scans with an estimated average thickness value of 0.69 nm of the grafted layer.

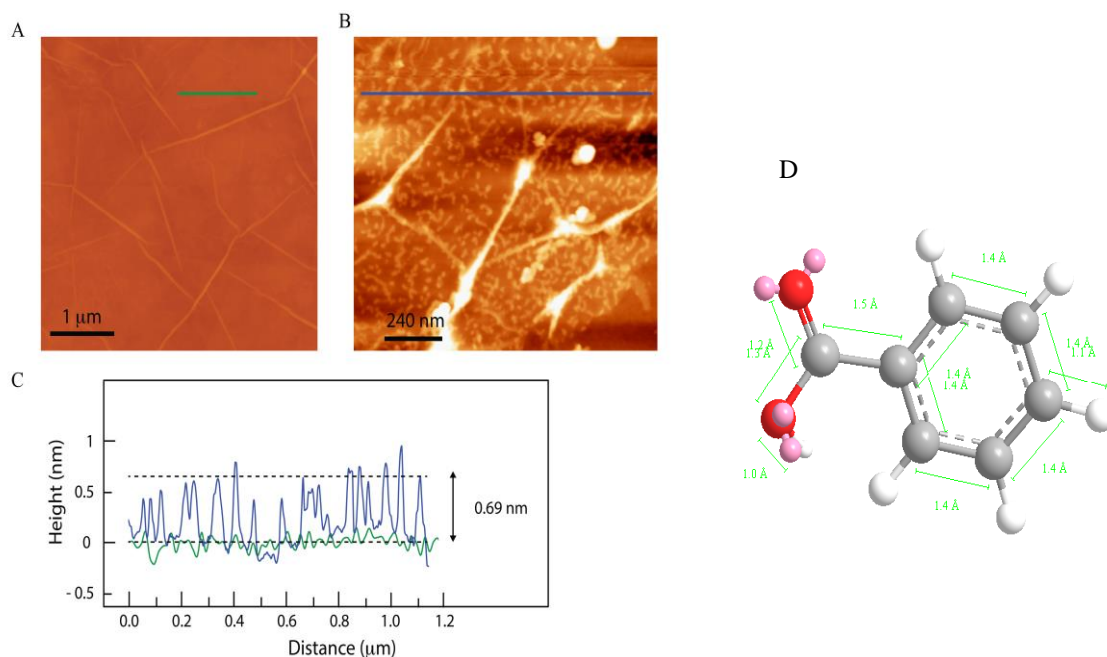


Figure 3.16(A) AFM images of bare graphene and (B) carboxyphenyl modified graphene. (C) The height profiles with two selected line scans. Green line indicates the bare graphene, and blue line indicates the modified graphene. The average height of the carboxyphenyl groups is around 0.69 nm and (D) theoretical estimation of the length of the carboxyphenyl moiety using ChemDraw Ultra 13.0 software.

This value is consistent with the theoretical length of 0.69 nm for the carboxyphenyl moiety estimated by the ChemDraw Ultra 13.0 software (Figure 3.16(D)) which indicates that the grafted thin film composed of monolayers. XPS, Raman spectroscopy and AFM thus confirms the covalent modification of graphene. EIS is also used to study the blocking effect of the modified electrodes. As shown in Figure 3.17, the diameter of the semicircle, corresponding to R_{CT} , is significantly larger in the case of the carboxyphenyl modified graphene electrodes as compared to bare graphene. This increase in the impedance is expected as a result of the hindrance for the electron transfer process of

the $[\text{Fe}(\text{CN})_6]^{4-/3-}$. In this work, three electrografting CV scans were chosen for impedimetric sensing on the basis of the saturation in Raman spectra following three CV scans.

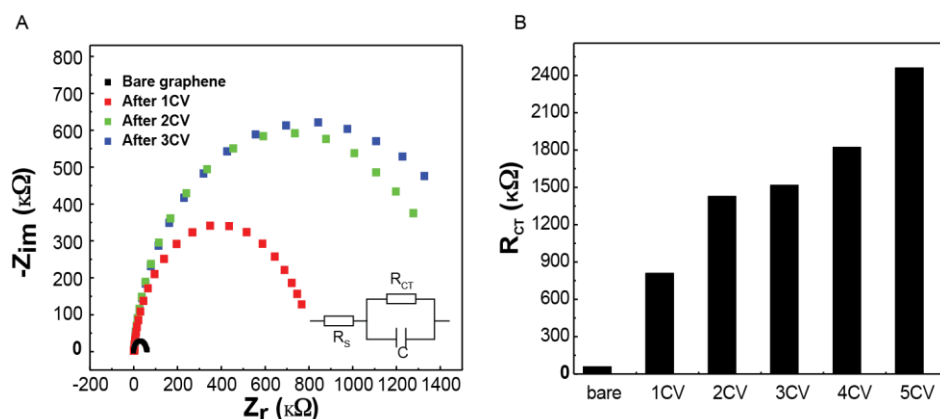


Figure 3.17(A) Nyquist plot of bare GE and 4-CP-GE functionalized by diazonium salt reduction using different CV cycles in 10 mM $[\text{Fe}(\text{CN})_6]^{4-/3-}$ at 100 mV/s. Inset: The equivalent circuit used for fitting the experimental results; **(B)** Plot of R_{CT} of 4-CP-GE in 10 mM $[\text{Fe}(\text{CN})_6]^{4-/3-}$ vs. the number of CV scanning cycles for diazonium reduction on GE.

3.3.2 Electrochemical impedance immunosensor response

EIS was also used to characterize the further fabrication steps for the immunosensor. The covalent immobilization of the ovalbumin antibodies caused a significant drop in the R_{CT} (Figure 3.18, green curve) from the CP/GE signal (Figure 3.18, blue curve). This decrease could be attributed to the neutralization of the negative charge of the carboxylic groups with the positively charged antibodies as previously seen in DPV (Figure 3.10). Finally, R_{CT} was subsequently increased after treatment with BSA solution (red curve) due to the blocking effect of this bulky protein.

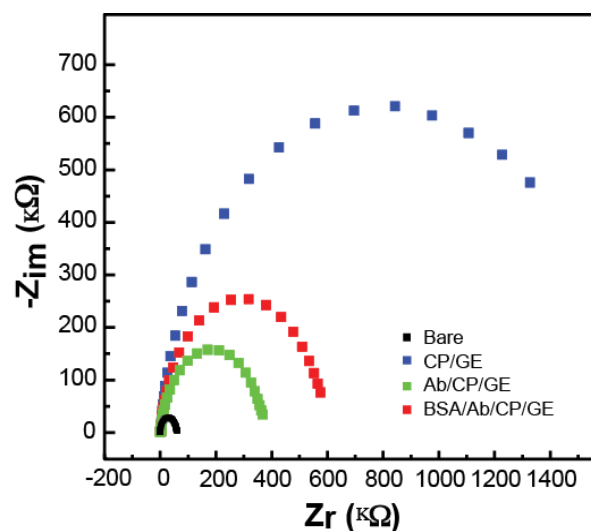


Figure 3.18 Nyquist plot of bare GE; 4-CP/ GE, Ab/4-CP/ GE and after blocking with 0.1% BSA for 30 min. in the presence of 10 mM $[\text{Fe}(\text{CN})_6]^{4-/3-}$ probe in PBS, pH 7.4.

Figure 3.19(A) shows the increase in R_{CT} upon ovalbumin binding that is the basis of ovalbumin detection. A calibration plot based on the percentage change in the R_{CT} following ovalbumin binding is shown in Figure 3.19(B). A good linear relationship was obtained between the percentage change in the R_{CT} of the immunosensor versus the logarithm of the ovalbumin concentrations in the range from 1 pg mL^{-1} to 100 ng mL^{-1} . The standard deviations of the measurements were ranging from 3.0 % to 7.0 % indicating good reproducibility of the immunosensor. The linear regression equation was $(R-R^0)/R^0 \% = 39.0 + 4.29 \times \log C [\text{ng mL}^{-1}]$, $R = 0.98$, with a calculated detection limit (LOD) of 0.9 pg mL^{-1} ($S/N = 3$). The result confirms that the CVD monolayer graphene platform offers good sensitivity and exhibits comparable detection limit to that reported with graphene modified screen printed carbon electrodes¹⁵⁵. Figure 3.19(C) shows the response of the impedimetric immunosensor to β -lactoglobulin and lysozyme binding which was much lower than that of the ovalbumin, illustrating good selectivity and negligible non-specific adsorption on the graphene platform.

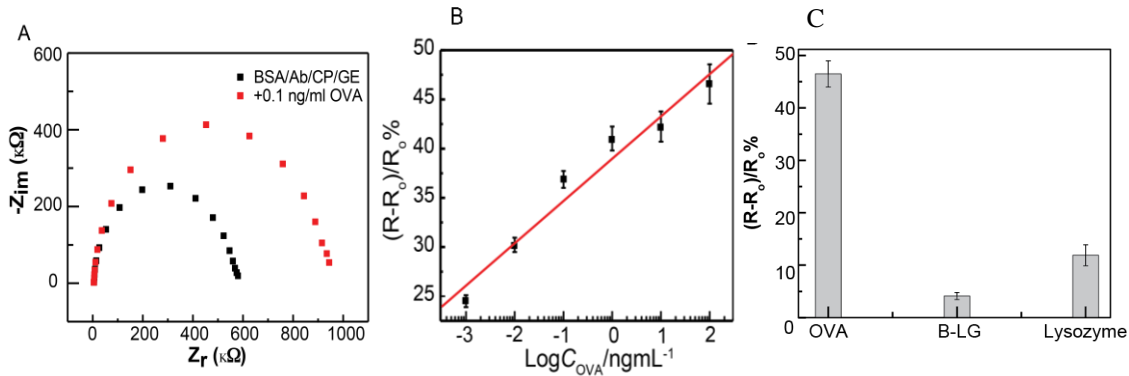


Figure 3.19(A) Nyquist plot of OVA immunosensor before (black) and after (red) incubation with 0.1 ng/ml OVA. (B) Dependence of the immunosensor response on OVA concentration (plot of $(R-R_0)/R_0$ % vs. $\log C_{OVA}$) and (C) Comparison of response of the immunosensor to 100 ng ml^{-1} ovalbumin, $1 \mu\text{g/ml}$ Lysozyme, and β -lactoglobulin.

3.4 Conclusions

Sensitive label-free voltammetric immunosensors for the detection of β -lactoglobulin and ovalbumin have been developed. A controlled electrografting method of organic film based on the reduction of diazonium salt on graphene-modified screen printed carbon electrodes was successfully achieved. This enabled a suitable, simple, and versatile platform for the immobilization of antibodies and immunosensors fabrication. Differential pulse voltammetric immunosensors has been developed based on signal-off detection strategy. The immunosensors developed using this approach offer a linear range of $0.001\text{--}100 \text{ ng mL}^{-1}$ for β -lactoglobulin and 1 pg/ml to $0.5 \mu\text{g/ml}$ for OVA without any amplification step. The immunosensors were successfully applied for the detection of β -LG and OVA in food samples, and the results were correlated to those of the commercial ELISA method. In fact, the signal-off sensors usually suffers from two main pitfalls: 1) the possibility of false positive results due to the non specific adsorption, however this effect was very small in our developed sensors due to the

effectiveness of the blocking step with BSA; 2) the high background noise and limited sensor gain as we cannot achieve more than 100% of the original signal unlike the Signal-on sensors.

The electrografting method has been also applied on CVD graphene. We have investigated for the first time the behaviour of the functionalized monolayer graphene for impedimetric immunosensing of protein. Our results show that carboxyphenyl functionalized CVD monolayer graphene can be used as a sensitive and selective platform for protein biosensing. Thus, this functionalized graphene can be exploited in extended biosensing applications such as small molecules detection which will be presented in the next chapter.

CHAPTER 4. A GRAPHENE-BASED ELECTROCHEMICAL COMPETITIVE IMMUNOSENSOR FOR THE SENSITIVE DETECTION OF OKADAIC ACID IN SHELLFISH

In Chapter 3, an easy, fast, versatile and controlled modification method of graphene surface has been demonstrated. The modified graphene was employed for the construction of label-free immunosensors for allergenic proteins. This Chapter aims to exploit the carboxyphenyl modified graphene platform developed in section 3.2 for the detection of the small molecule toxin OA. The functionalization of GSPE was followed by EDC/NHS activation of the terminal carboxylic groups and the covalent immobilization of OA antibody via amide bond formation. A simple square wave voltammetric (SWV) direct competitive immunoassay for the detection of OA based on the decrease of the $[\text{Fe}(\text{CN})_6]^{3-/4-}$ reduction peak current has been used. The competition was established between OA and fixed concentration of OA-OVA conjugate for the immobilized antibodies (Figure 4.1). This new approach enabled a sensitive, fast and single step electrochemical detection method of OA and was validated using certified reference mussel samples.

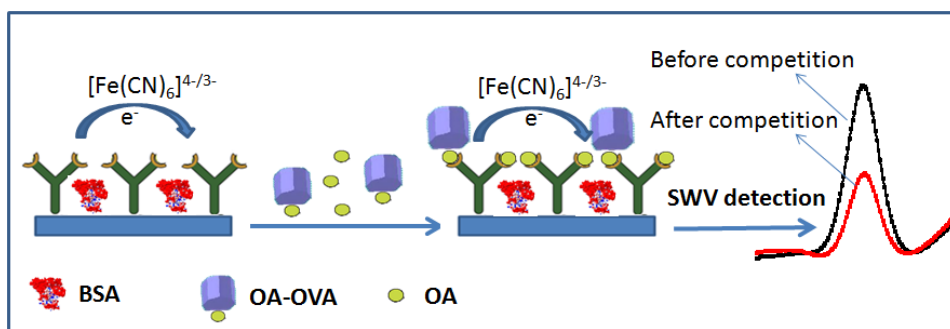


Figure 4.1 Schematic diagram of the working principle of the immunosensor with direct competitive immunoassay.

4.1 Competitive immunoassay of okadaic acid onto modified graphene electrodes

Direct competitive immunoassay was performed for OA analysis. A mixture containing a fixed concentration of OA–OVA ($1\mu\text{g mL}^{-1}$) and an increasing concentration of free OA was incubated with the immunosensors for 30 min. SWV reduction of $[\text{Fe}(\text{CN})_6]^{3-/4-}$ was performed at the immunosensor after washing with PBS buffer and the results obtained are shown in Figure 4.2.

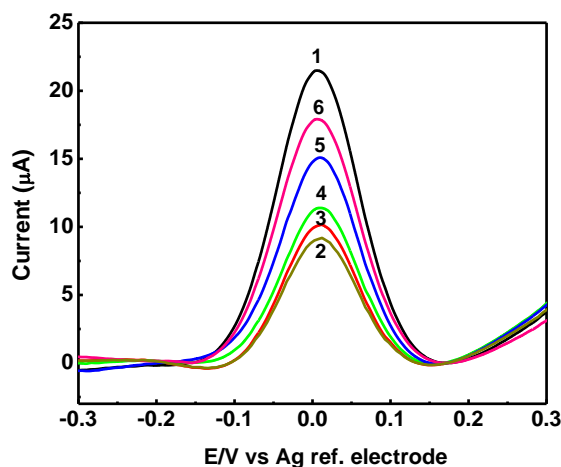


Figure 4.2 SWVs of the immunosensor before the competition step (1) and after incubated with different concentrations of OA mixed with $1\mu\text{g/ml}$ of OA-OVA (2–6): the concentrations of OA are 0.000 , 1.00 , 10.0 , 100 and 1000 ng L^{-1} .

A calibration plot based on the difference in peak current in SWV before and after the competition step is shown in Figure 4.3(A). The difference in the peak current decreased with increasing the concentrations of the free OA. The assay relied on the competition between the free and the conjugated OA for anti-OA-Mab immobilized on the electrode surface. The less the free OA in solution the more the OA-OVA conjugate will bind to the antibody on the electrode surface, which will subsequently decrease the electron transfer efficiency between the redox molecules and the

electrode causing a decrease in the current. This decrease is attributed to the bulky size of the ovalbumin as well as its negative charge at pH 7.4 as there is no significant signal can be obtained from OA molecule (low molecular weight). The linear relationship can be represented by the equation, i_o-i (μA) = 11.99 - 2.72 \times logC [ng L^{-1}], with a correlation coefficient of 0.992 (N=5). The immunosensor showed a linear response up to 5000 ngL^{-1} as shown in the inset of Figure 4.3(A). The detection limit (defined as the difference between the mean blank signal and three times the standard deviation of the blank) was 19.0 ngL^{-1} . The results demonstrated that the developed immunosensor exhibited lower detection limit compared with other reported sensors^{62,83-84,214} without any signal amplification steps. The ease of electron transfer to the graphene surface after the electrode modification has enabled the monitoring of the change in the voltammetric response upon OA-OVA binding and the homogeneous organic layer produced by the described method has enabled the access to all the function groups on the surface.

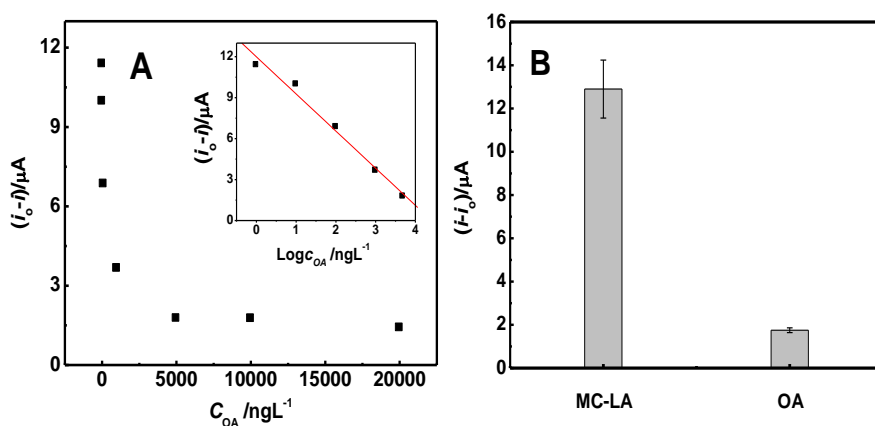


Figure 4.3(A) Dependence of the immunosensor response on OA concentration (plot of the difference in the peak current vs. C_{OA}). Inset: calibration curve for OA, plot of peak current vs. $\text{log } C_{\text{OA}}$, (B) Comparison of the response of GSPE voltammetric immunosensor to $10 \mu\text{gL}^{-1}$ OA and MC-LA.

4.2 Selectivity of the okadaic acid immunosensor

Control experiments were conducted in order to study the selectivity of the immunosensor. Microcystin-LA has been used as a control to confirm that the change in the peak current of the redox probe is due to the competition of the free OA and the OA-OVA conjugate and not due to nonspecific adsorption of the conjugate on the graphene surface. No significant difference in peak current was observed before and after incubation with the control toxin (Figure 4.3(B)). These results confirm that the SWV changes observed with OA are due to the competition caused by the specific OA and anti-OA-MAb binding.

4.3 Stability and reproducibility of OA immunosensor

The prepared immunosensors were kept at 4°C for 40 days. The sensors were then used to detect 0.1 $\mu\text{g L}^{-1}$ OA. The 40 days old immunosensor has shown 98% of the response (difference in the peak current (i_o-i)) of the freshly prepared immunosensor, which indicates a good stability of the immunosensor. This stability is attributed to the robust covalent attachment of the electrografted carboxyphenyl layer to the graphene surface and the subsequent OA antibody immobilisation via a strong amide bond. These covalent bonds prevent the leaching of the immobilized antibodies, thereby indicating the role of the current electrografting approach as potential modification scheme of graphene electrodes. The reproducibility of the OA immunosensor was also examined by performing three measurements for 1 $\mu\text{g L}^{-1}$ OA. The relative standard deviation was about 8% demonstrating good reproducibility of the immunosensor.

4.4 Matrix effect and okadaic acid detection in certified reference mussel samples

The effect of the interferences from the shellfish extracts was investigated by spiking uncontaminated shellfish extracts with three different concentrations of OA (0.1, 1.0, 5.0 $\mu\text{g L}^{-1}$). The Recovery % was then calculated using the calibration curve performed in PBS buffer. The results presented in Table 1 show good percentage of recovery indicating that no significant effect of the tissue matrix on the immunosensor detection.

Table 4.1 Recovery percentages with spiked OA and certified reference mussel samples of OA

OA concentration ($\mu\text{g L}^{-1}$)	Spiked OA		Certified OA	
	R%	RSD%	R%	RSD%
0.1	97.5	6.4	100.3	6.6
1	104	8.3	89.2	5.8
5	103	6.5	94.3	10.9

Experiments using certified reference mussel samples were also performed in order to validate the proposed immunosensor. The recovery % (Table 4.1) of the three tested concentrations indicates the possible applicability of the OA immunosensor in shellfish samples analysis. The relative standard deviation (RSD %) calculated for duplicate measurements of each concentration indicates good precision of the developed immunosensor.

4.5 Conclusions

Different from the reported approaches which uses indirect competitive assays, a simple voltammetric immunosensor was demonstrated in this chapter using graphene electrodes for the detection of OA.

Graphene surface modification was achieved using electrografting methods, which led to the formation of a stable carboxyphenyl film, facilitating the subsequent immobilisation of OA antibodies. The proposed sensor based on a direct competitive assay was proved to be very simple with good sensitivity and selectivity against other group of toxins. Finally, the immunosensor was successfully applied for the detection of OA in spiked mussel extracts showing good recovery % and has been also validated using certified reference mussel samples. Despite the advantages offered by this method, the high cost and low stability of antibodies are still major challenges. Therefore, in the next Chapter will show the selection of DNA aptamers against OA and BTX-2 which can offer new alternatives to the available antibodies.

CHAPTER 5. SELECTION, CHARACTERIZATION AND LABEL-FREE ELECTROCHEMICAL APTASENSORS FOR MARINE TOXINS

As shown in chapter 3 and 4, a covalent functionalization method of graphene electrodes was studied and consequently used to develop a sensitive immunosensor for OA based on direct competitive assay which enables simpler detection way compared with the reported approaches. Nevertheless, the high cost of the antibodies, the limited stability, and required special storage conditions are still challenges facing immunosensor technologies today. Therefore, in this chapter, the selection, identification and characterization of DNA aptamers against the two common marine toxins; OA and BTX-2 is described. The new selected aptamers can be used as alternative of the currently available antibodies. Moreover, the application of the selected aptamers on label-free impedimetric aptasensors for detection of these toxins is demonstrated ²¹⁵.

5.1 Okadaic acid aptasensor

Here, we present the selection, identification, characterization, and biosensing application of a high affinity aptamer for OA. The aptamer is selected using systematic evolution of ligand by exponential enrichment and successfully applied in designing a label-free aptasensor for OA detection.

5.1.1 Okadaic acid aptamer selection

We immobilized OA on DADPA agarose beads by coupling the terminal carboxylic groups on the toxin with the amine groups on the beads via EDC/NHS chemistry. This design keeps the rest of the functional groups on the OA molecule accessible for DNA binding during the selection. The remaining free amino groups on the beads were blocked with sulfo-NHS acetate in order to reduce the nonspecific binding of the beads with the DNA ¹⁸⁰. A DNA library consisting of 10^{14} random 60-nucleotide sequences was screened against OA beads in a SELEX procedure.

To follow the enrichment of the library for OA binding, the percent of the DNA recovered was monitored after each round using fluorescence measurements. Using about 150 pmol DNA input in each round, a stepwise increase of DNA recovery was observed, indicating enrichment of OA-binding DNA (Figure 5.1).

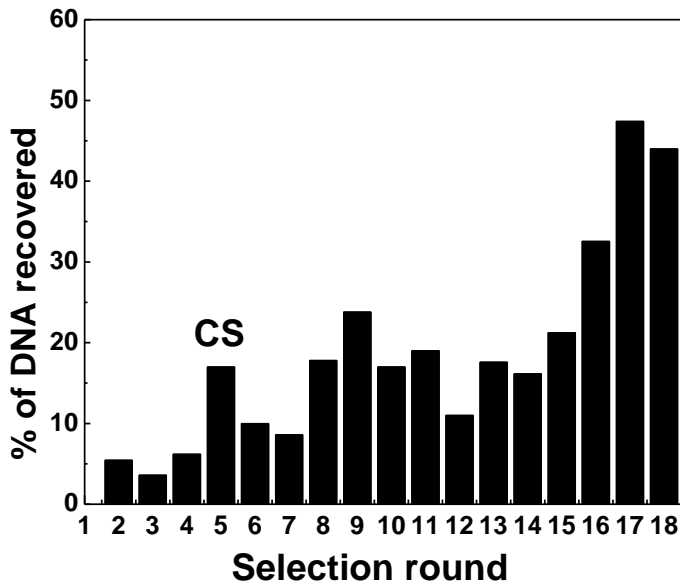


Figure 5.1 Enrichment of okadaic acid-specific aptamers during SELEX. The bar graph shows the amounts of ssDNA eluted from OA-coated beads in each selection round. In round five, a counter selection step (CS) was introduced to remove ssDNA nonspecifically bound to the bead matrix.

The stringency of the selection was increased by increasing the number of washing times after any observable increase in the DNA percent recovery. A counter-selection step was performed after the fourth round in order to remove the DNA which binds nonspecifically to the beads matrix. We have seen an increase in the DNA recovery in the eighth and ninth rounds; therefore we have cloned and sequenced the DNA recovered from the eighth and tenth rounds. However, no convergence was observed from both rounds which indicate that the DNA pool was not yet enriched. Some sequences were also tested, however, no binding to OA was obtained. Therefore, we continued the selection rounds. In the seventeenth and eighteenth round when a

significant increase in the DNA recovery was observed and a plateau was reached, the DNA from the last round was again cloned and sequenced. Significant consensus regions between the sequences from the last round were observed and some sequences were identical. Therefore, the selection cycles were stopped and the selected pool was subjected to the further analysis. We randomly selected 42 clones for sequencing and the identified sequences were analysed by multiple sequence alignment using the PRALINE software ¹⁹⁵ and then grouped into eight families based on their similarities. Significant consensus regions between the sequences in each group were observed and some sequences were identical (Figure 5.2).

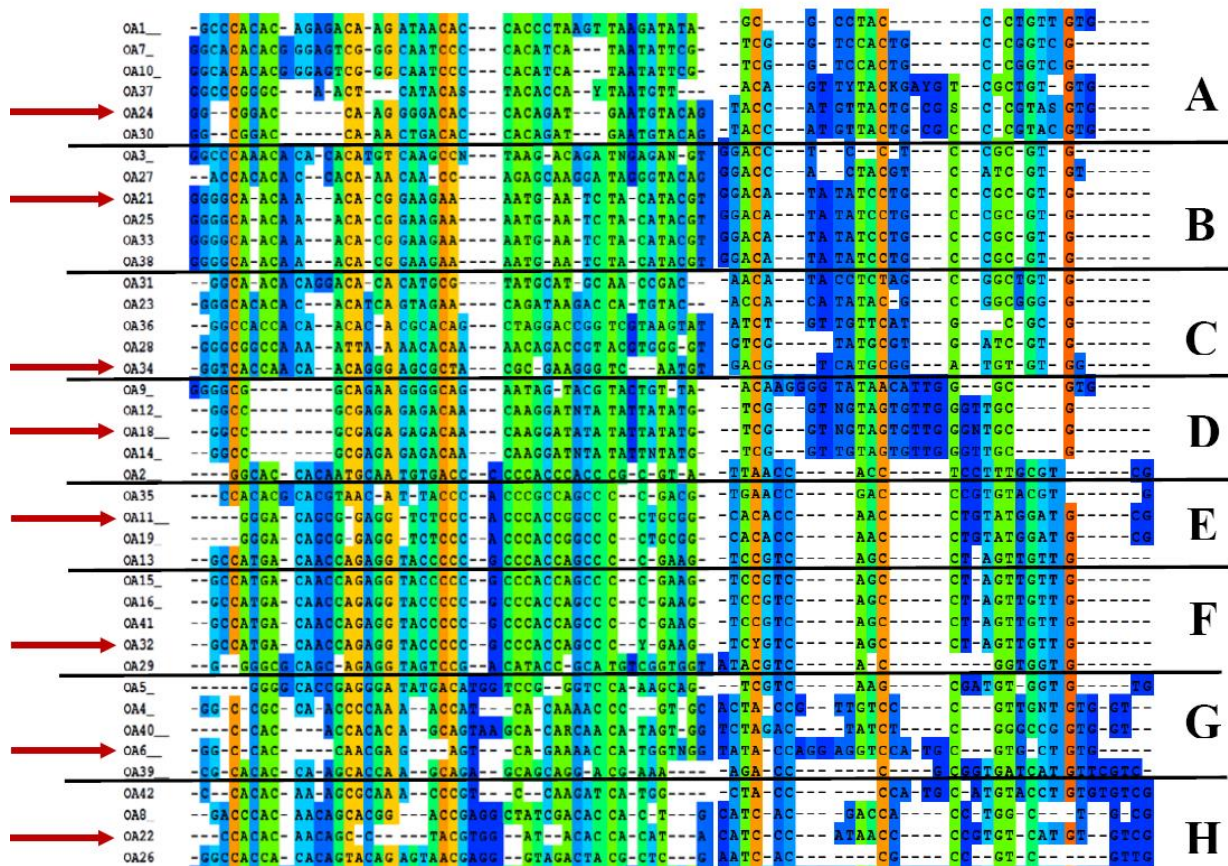


Figure 5.2 Analysis of the selected sequences by multiple sequence alignment using PRALINE software. The sequences were grouped into eight families (A-H) and a representative sequence was chosen from each group (OA 24, 21, 34, 18, 11, 32, 6, 26).

Therefore, one sequence from each group was randomly chosen for further binding affinity studies with OA as shown in Table 5.1. Binding assays using constant amount of OA beads and different concentrations of fluorescein-labelled aptamers (0-300nM) was performed using the same SELEX conditions. The beads were washed several times and the bound aptamers were eluted. The fluorescence of the eluted aptamers were then measured and plotted versus the aptamer concentration used for binding.

Table 5.1 Sequences and dissociation constants (K_d) between OA and selected aptamers.

Group	Clone number	Aptamer sequence	K_d (nM)
A	OA 24	GGCGGACCAAGGGGACACCACAGATGAATG TACAGTACCATGTTACTGCGCCCGTAGGTG	126 nM
B	OA 21	GGGGCAACAAACACGGAAGAAAATGAATCT ACATACGTGGACATATATCCTGCCGCGTG	983 nM
C	OA 34	GGTCACCAACAACAGGGAGCGCTACGCGAA GGGTCAATGTGACGTCATGCGGATGTGTGG	77 nM
D	OA 18	GGCCGCGAGAGAGACAACAAGGATATATAT TATATGTCGGTTGTAGTGTGGGTTGCG	--
E	OA 11	GGGACAGCGGAGGTCTCCCACCCACCGGCC CCTGCGGCACACCAACCTGTATGGATGCG	131 nM
F	OA 32	GCCATGACAACCAGAGGTACCCCCGCCAC CAGCCCCGAAGTCTGTGAGCCTAGTTGTTG	380 nM
G	OA 6	GGCCACCAACGAGAGTCAGAAAACCATGGT GGGTATAACCAGGAGGTCCAT GCGTGCTGTG	--
H	OA 22	CCACACAACAGCCTACGTGGATACACCACA TACATCCCATAACCCCGTGTCATGTGTCG	183 nM

The dissociation constants (K_d) of the selected aptamers were calculated by non-linear regression analysis (Figure 5.3). Six aptamers have shown good affinity to OA ranging from 77 nM to 980 nM and two aptamers did not exhibit binding. The highest affinity to OA was obtained for

aptamer (OA34) with a K_d of 77 nM, therefore, it was used for our further experiments. The binding of OA34 was then tested with the negative agarose beads and the cross reactivity with DTX-1 and DTX2 beads was also performed. As shown in Figure 5.3(A), OA34 did not exhibit binding to both negative, DTX-1 and DTX-2 beads. These results indicate the high selectivity of OA34 against DTX-1 and DTX-2, toxins closely related to OA differing only by 2 methyl groups. We then used circular dichroism in order to gain insight on the conformation of the free and target-bound form of OA34. As shown in Figure 5.3(B) before the addition of OA into the solution containing aptamer, the circular dichroism spectrum of the aptamer showed a positive band at 277 nm and a negative band at about 245 nm. Upon OA binding, an increase of the ellipticity at 277 nm and 245 nm were observed. This change in the CD spectra indicates the folding of the aptamer into a different conformation upon binding with OA.

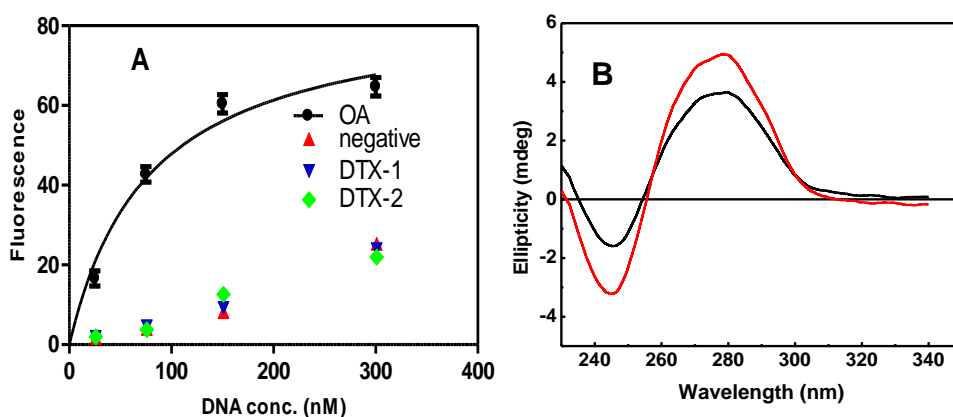


Figure 5.3(A) Fluorescence binding assay of OA and aptamer OA34. The K_d was determined to be 77 nM. Each point is the mean of three experiments and error bars represent the standard deviations of the measurements, (B) Circular dichroism spectra of 0.67 μ M aptamer OA34 in binding buffer before (black) and after (red) binding with 0.66 μ g/ml of OA at room temperature.

5.1.2 Impedimetric aptasensor for OA detection

The aptamer with the highest affinity to OA (OA34) was then used to fabricate a label-free aptasensor based on EIS detection. As shown in schematic diagram (Figure 5.4), the aptasensor was constructed using self-assembled monolayer (SAM) of disulfide-modified aptamer on a polycrystalline gold electrode. Then the aptamer-modified electrodes were blocked by 6-

mercapto-1-hexanol in order to minimize the nonspecific adsorption of the aptamers on the gold surface which could affect the efficiency of the sensor²¹⁶⁻²¹⁹. The detection mechanism of the aptasensor is based on probing the change in the impedimetric signal upon aptamer-toxin binding induced by the change of the aptamer conformation.

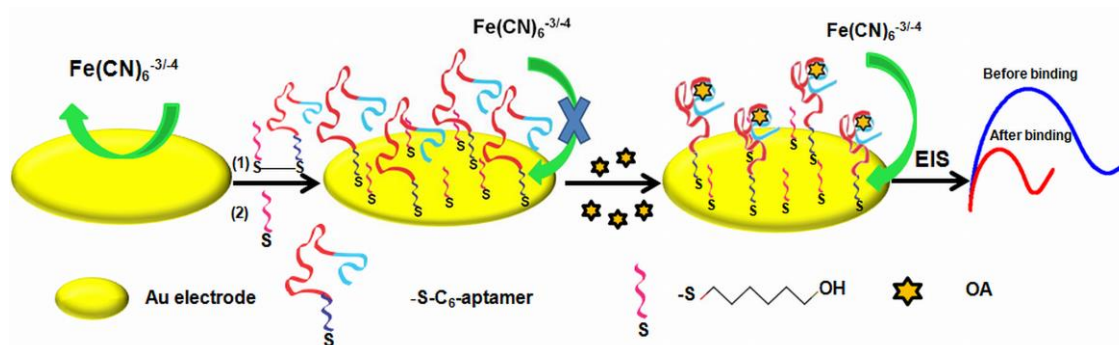


Figure 5.4 Scheme of the fabrication of the impedimetric aptasensor based on label-free target-induced folding of the aptamer.

The characterization of the aptasensor fabrication steps was performed using CV and EIS. Fig. 5.5(A) shows the CVs of the bare Au, Au/aptamer, Au/aptamer/MCH and after binding with 60 ng/ml OA in 5 mM solution of $[\text{Fe}(\text{CN})_6]^{4-/3-}$ couple in PBS buffer. The $[\text{Fe}(\text{CN})_6]^{4-/3-}$ redox probe exhibited a characteristic reversible behaviour on the bare gold electrode (Figure 5.5(A), black curve) with a peak to peak separation of almost 80 mV, indicating a clean gold surface. After the immobilization of the aptamer (Figure 5.5(A), red curve) the peak-to-peak separation increased, and a substantial decrease in the peak current was also observed. This change is due to the negative charge on the DNA aptamer which repels the negatively charged $[\text{Fe}(\text{CN})_6]^{4-/3-}$ anions, retarding the electron-transfer between the redox probe and the electrode surface. Then, a further increase in the peak-to-peak separation was observed after blocking the electrodes with MCH (Figure 5.5(A), green curve) indicating an additional decrease of the electron transfer rate due to filling the empty spaces on the gold surface. However, after the incubation of the aptasensor in 60 ng/ml OA, the redox peaks current increased and the peak-to-peak separation was decreased (Figure 5.5(A), blue curve).

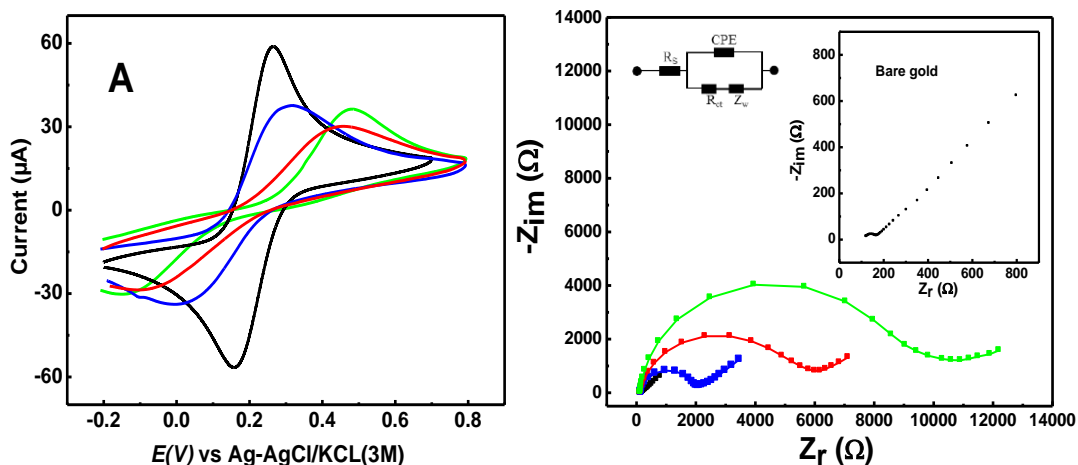


Figure 5.5 Cyclic voltammetry (A) and Nyquist plots (B) of 5 mM $[\text{Fe}(\text{CN})_6]^{4-/3-}$ redox couple in PBS, pH 7.4, for bare Au electrode (black), Au/ aptamer (red), Au/aptamer/MCH (green), and after binding with 60 ng/ml OA (blue). The cyclic voltammetry was performed at scan rate of 100 mV/s and the EIS was performed using a frequency range of 10^4 to 0.1 Hz, a DC potential of +0.23 V and AC amplitude of 5 mV. The inset is the equivalent circuit applied for fitting.

This result suggests a change of the conformation of the aptamer upon binding with OA favouring the access of the $[\text{Fe}(\text{CN})_6]^{3-/4-}$ redox couple to the sensor surface. Figure 5.5(B) shows the Nyquist plots for the bare Au, Au/ aptamer, and Au/ aptamer/MCH and after binding with OA. The bare gold electrode shows a characteristic very small semicircle domain which indicates very fast electron-transfer process with a diffusional limiting step (Figure 5.5(B), black curve). The self-assembly of the negatively charged aptamer on the electrode surface significantly increase the diameter (Figure 5.5(B), red curve) of the semicircle which indicates the increase in the charge-transfer resistance (R_{ct}) due to the repulsion of the aptamer on the electrode surface with the $[\text{Fe}(\text{CN})_6]^{4-/3-}$ anions. After the incubation with MCH the R_{ct} was further increased due to filling some of the exposed gold areas which introduces a barrier to the interfacial electron transfer (Figure 5.5(B), green curve). After OA binding, a large drop in R_{ct} was observed (Figure 5.5(B), blue curve). This decrease in the R_{ct} is consistent with the CV behaviour explained above and is likely due to the conformational change of the aptamer upon binding with the toxin to a more compact structure. The decrease of the R_{ct} induced by aptamer-target binding has been previously observed elsewhere ²²⁰⁻²²².

It is well established that addition of MCH to form mixed monolayer with the thiol modified DNA is essential step to control the film formation process and preserve the conformation of the surface-anchored DNA oligonucleotides²²³. Here, we utilised an 5'HO-(CH₂)₆-S-S-(CH₂)₆ modified aptamer to co-immobilise self-assembled monolayer of the OA aptamer and MCH, where the disulfide bond would break upon chemisorption and a mixed SAM would form. With the aim of studying the effect of adding extra MCH on the sensor response, a treatment of the aptamer-MCH modified electrodes was carried out with different concentrations of extra MCH. Figure 5.6(A) shows the different responses of the aptasensors blocked with different concentrations with MCH after incubation with 30 ng/ml OA solution. The aptasensor response was increased by the addition of extra MCH from 0 to 1 μM. These results indicate that the co-immobilisation process was not enough to remove the physisorbed DNA on the gold surface or to retain the conformation of the surface-attached DNA which affects the binding with OA. We found that when the electrodes were incubated with extra 1 μM concentration of MCH, the binding and consequently the sensor response was significantly improved. However, by adding higher concentration of MCH, the aptasensor response started to decrease again which could be due to the blocking of most of the pinholes on the gold surface. This higher coverage of the gold surface decreased the electron transfer rate and subsequently the change in the resistance upon target binding was decreased. Therefore, 1 μM of extra MCH was chosen for blocking the electrodes in the subsequent experiments.

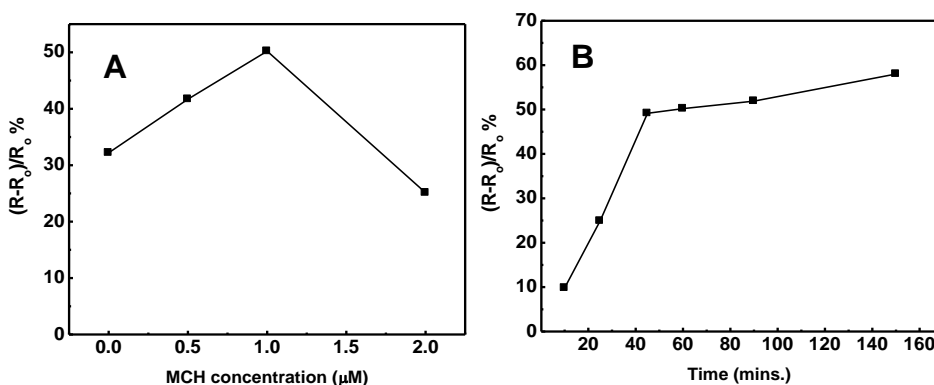


Figure 5.6(A) The effect of adding extra concentration of MCH, (B) the effect of the OA incubation time on aptasensor response towards 30 ng/ml OA in 10 mM PBS (pH 7.4) containing 5 mM [Fe(CN)₆]^{4-/3-} redox couple.

Since the assay time is a very important factor for biosensors performance and their practical application, it was crucial to optimize the incubation time of OA on the aptasensor. The aptasensor's response was monitored after incubating 30 ng/ml OA on the aptasensor at different time points. Figure 5.6(B) shows a significant difference in R_{ct} as sensor response with increasing incubation time. The maximum response ($(R_o-R)/R_o$ %) was observed after 45 min incubation, after which very small increase in response signal was observed. Therefore, 45 min was chosen as the optimum binding time in the following experiments.

We then studied the aptasensor impedimetric response towards OA concentrations in the range of (100 pg/ml to 100 ng/ml). As shown in Figure 5.7(A), marked drops in the diameter of the semicircle were observed with increasing concentrations of OA due to conformation change of the aptamer molecules upon binding with OA as explained above. A calibration plot based on the percentage change in the R_{ct} after the OA binding is shown in Figure 5.7(B). The data points in the calibration curve represent three independent measurements and the error bars show the standard deviations ranging from 1.0 % to 7.0 %, indicating good reproducibility of the aptasensor response. A good linear relationship was obtained in the concentration range from 100 pg/ml to 60 ng/ml which can be represented by the linear regression equation: $(R_o-R)/R_o$ % = $12.75 + 1.19 \times \log C$ [ng ml⁻¹], $R = 0.994$, with a detection limit (LOD) of 70 pg/ml. This detection limit is lower than the detection limit of the available commercial ELISA kit as well as other reported immunosensors^{64,84}.

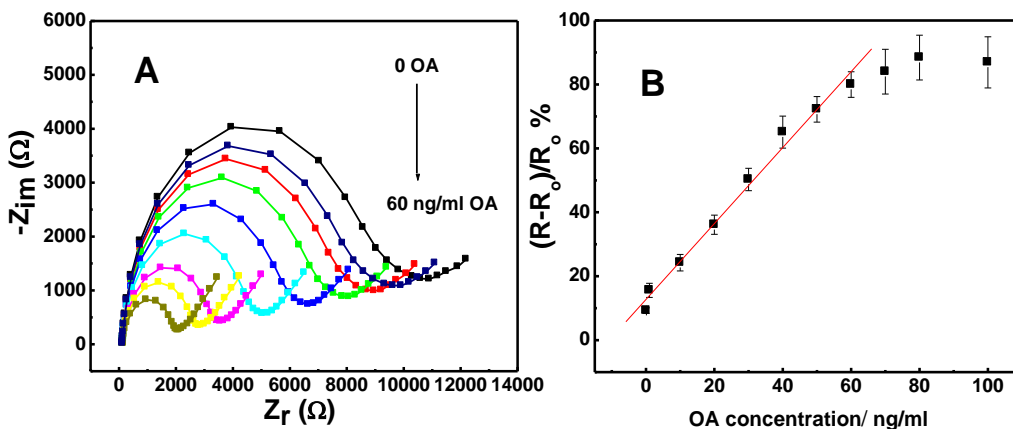


Figure 5.7(A) Nyquist plots of the aptasensor after incubation with different concentrations of OA 0.00, 0.1, 1.0, 10, 20, 30, 40, 50 and 60 ng/ml. (B). The calibration curve for OA, plot of $\Delta R_{ct}/R_o$ % vs. C_{OA} . The error bars show the standard deviation of three repetitive measurements.

In order to understand the effect of the gold surface immobilization of the aptamer on its binding affinity with OA, we calculated the dissociation constant of OA-aptamer using EIS. The calculations are based on the classical Langmuir isotherm ⁵⁶, which assumes equal binding energy for all binding sites on the surface and that the ability of the molecule to bind is independent of whether adjacent sites are filled. The equilibrium of OA and its aptamer (AP) binding can be represented as follow: $[AP-OA] \rightleftharpoons [AP]+[OA]$, so the $K_d = \frac{[AP][OA]}{[AP-OA]}$

Assuming that the surface coverage of the aptamer-OA complex $[AP-OA]$ is θ , the surface coverage of unbound aptamer $[AP]$ will be $(1 - \theta)$, so the $K_d = \frac{(1 - \theta) [OA]}{\theta}$

Based on Langmuir model, we assume that the change of R_{ct} is directly related to the OA-aptamer binding according to equation 3:

$$\Delta R = \theta \Delta R_{sat} \quad \text{Eq. 3}$$

Where $\Delta R = (R_o - R)/R_o$ and ΔR_{sat} is the maximum aptasensor response $(R_o - R_{sat})/R_o$. A linearized form of the Langmuir isotherm can be represented by equation 4:

$$\frac{C_{OA}}{\Delta R} = \frac{C_{OA}}{(\Delta R)_{sat}} + \frac{K_d}{(\Delta R)_{sat}} \quad \text{Eq. 4}$$

By plotting $C_{OA}/\Delta R$ as a function of the molar concentration of OA (C_{OA}) (Figure 5.8(A)) while avoiding the responses from low OA concentrations, K_d can be obtained by dividing the y-intercept by the slope. Using this method we obtained a K_d of 74 ± 6.2 nM which is in very good agreement with the value obtained by the fluorescence assay in solution. This result indicates that the binding affinity of the aptamer with OA was not affected by the disulfide modification and the subsequent immobilization on the gold surface.

A preliminary application of the proposed OA aptasensor in real samples was examined by performing measurements for spiked uncontaminated shellfish extracts. The extraction was done following the protocol reported previously, and then the samples were spiked with 10 ng/ml OA. The recovery % calculated using the calibration curve performed in binding buffer was about 92 % demonstrating possible applicability of the aptasensor in real samples.

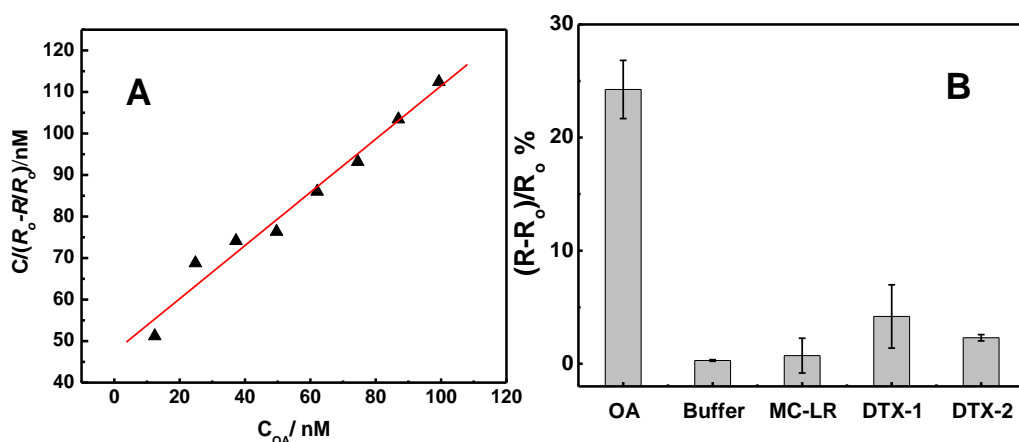


Figure 5.8(A) Linearized adsorption isotherm of OA binding to its aptamer immobilized on gold electrode based on the Langmuir model. The line is the best linear fit to the experimental data from which the dissociation constant K_d was determined. (B) Comparison of response of the aptasensor after incubation with 10 ng ml^{-1} OA, binding buffer, MC-LR, DTX-1, and DTX-2.

Negative control experiments using MC-LR and assessment of cross-reactivity to DTX-1 and DTX-2 were also performed using 10 ng/ml of each toxin. As shown in Figure 5.8(B), no significant response (change in the R_{ct}) was obtained with all the non-targeted toxins. In particular, the aptasensor did not exhibit cross-reactivity to DTX-1 and DTX-2, toxins closely related to OA differing only by 2 methyl groups. These results confirm that the developed aptasensor is very selective and highly specific to OA. We believe that the continual selection of high selectivity aptamers against the other analogues and their integration in single biosensor device will facilitate the routine monitoring of OA group of toxins with more accurate estimate of toxicity.

5.2 Brevetoxin aptasensor

The successful selection of an aptamer targeting OA and its incorporation in a label-free electrochemical biosensing platform which was presented in section 5.1²²⁶ have motivated us to extend our study to develop an aptamer against BTX-2. In the next sections, I show the first selection, identification and characterization of DNA aptamers against BTX-2. The binding of BTX-2 to aptamer pools/clones, the effects of the incubation time, pH and metal ions

concentrations on the aptamer-toxin binding are demonstrated. The integration of one of the new selected aptamers in a label-free competitive electrochemical biosensor is also presented.

5.2.1 Immobilization of brevetoxin-2 on the divinyl sulfone activated beads

The attachment of target to solid matrix is usually necessary to enable the separation of bound from unbound DNA through the selection process particularly for small molecule targets. The immobilization of BTX-2 on divinyl sulfone beads was achieved by coupling the terminal DVS groups on the beads with the hydroxyl groups on the BTX-2 molecules (Figure 5.9). The choice of the hydroxyl group as anchoring point of the BTX-2 molecule is used to retain the rest of the molecule accessible for DNA binding during the SELEX. This hydroxyl function is common in all BTX congeners, which may enable similar aptamer selection against the other congeners in the future. The success of the coupling reaction was then confirmed using direct competitive ELISA.

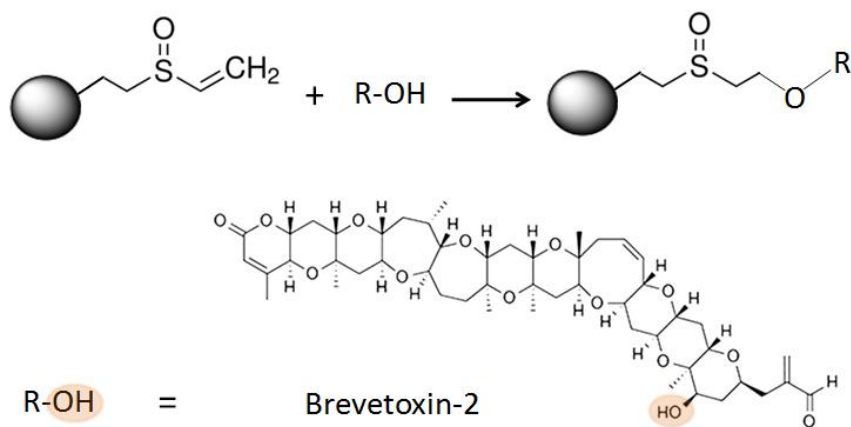


Figure 5.9 Attachment of BTX-2 to the divinyl sulfone beads.

5.2.2 Immobilization of Brevetoxin-2 on the gold electrodes

BTX-2 was also immobilized on the gold electrode surface via its hydroxyl group in order to keep the same exposition site of the molecules for the DNA binding as that used on the beads. First, the gold surface was functionalized through the formation of self-assembled monolayer of cysteamine. Then, the bifunctional linker, 1,4-phenylene diisocyanate, was used to covalently attach the terminal amine groups of Cys/Au to the hydroxyl groups of the BTX-2

molecules as shown in the scheme (Figure 5.10(A)). This linker offers high stability, low toxicity and capability to react efficiently with the amine groups yielding carbamide moiety as well as the hydroxyl groups yielding carbamate (urethane) moiety ²¹⁵. To confirm the successful modification of the gold electrodes and the subsequent immobilization of the BTX-2 molecules, CV and EIS were used.

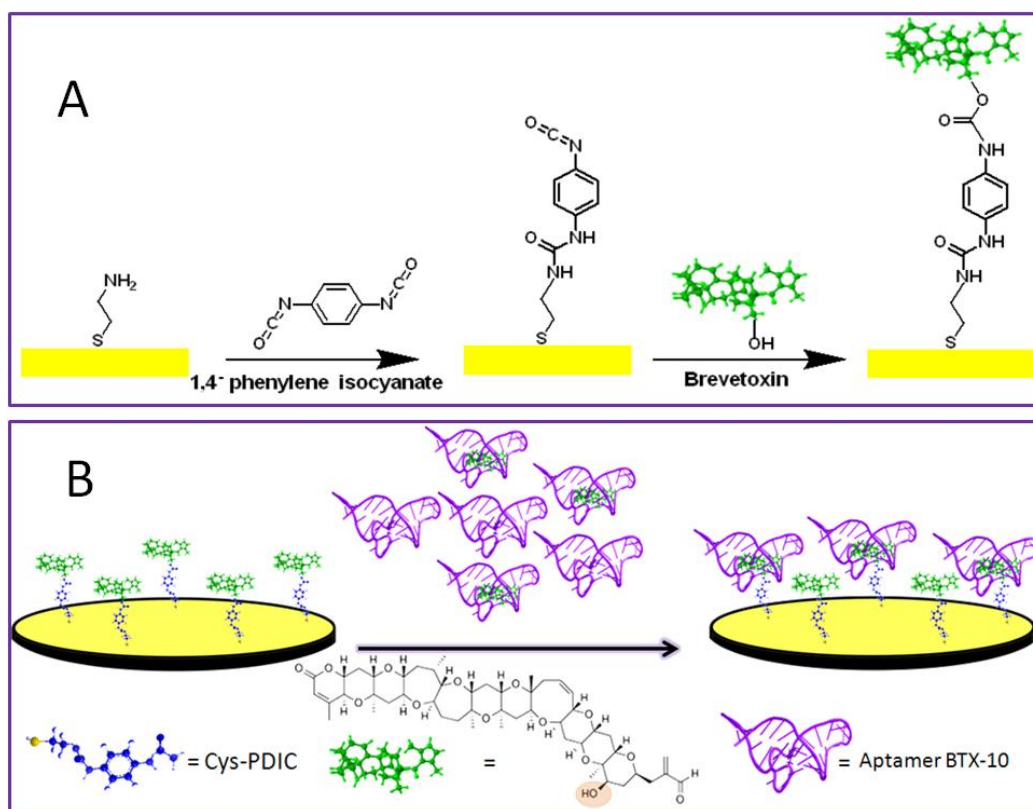


Figure 5.10(A) Modification of the gold electrode surface and covalent immobilization of BTX-2, (B) the working principal of the aptasensor with competitive assay.

Figure 5.11(A) shows cyclic voltammograms in $[\text{Fe}(\text{CN})_6]^{3-/4-}$ redox couple at bare Au electrode, Cys/Au and after activation with PDIC and immobilization of BTX-2. As expected, the CV of $[\text{Fe}(\text{CN})_6]^{3-/4-}$ redox solution showed a reversible behaviour on the bare Au electrode with a peak-to-peak separation (ΔE) of 80 mV. After the self assembly of cysteamine, the peak current was slightly increased and the ΔE was decreased likely due to the electrostatic attraction between the $[\text{Fe}(\text{CN})_6]^{3-/4-}$ anions and the positively charged terminal amine groups of the

Cys/Au²¹⁵. However, after the activation of the amine groups with the PDIC linker and immobilization of BTX-2, a drop in the peak current and an increase in the ΔE were observed, presumably due to the blocking of the surface with the BTX molecules leading to retardation of the electron transfer. Likewise, EIS was used to characterize the stepwise modification of the Au electrodes. Figure 5.11(B) shows the Faradiac impedance spectra in $[\text{Fe}(\text{CN})_6]^{3-/4-}$ solution represented as Nyquist plots. The self assembly of cysteamine on the electrode resulted in a decrease in the R_{CT} to a value of $45 \pm 6.2 \Omega$ than the bare gold electrode ($117 \pm 5.7 \Omega$) and only a straight line was observed confirming the enhancement of the electron transfer due to the introduction of the positive amine groups to the surface. On the other hand, the immobilization of BTX led to remarkable increase in R_{CT} to $398 \pm 4 \Omega$ as a result of the blocking effect of the toxin molecules that causes hindrance to the flow of the redox probe to the gold surface. Hence, the results obtained from both EIS and CV confirms the successful immobilization of BTX molecules on the gold electrode.

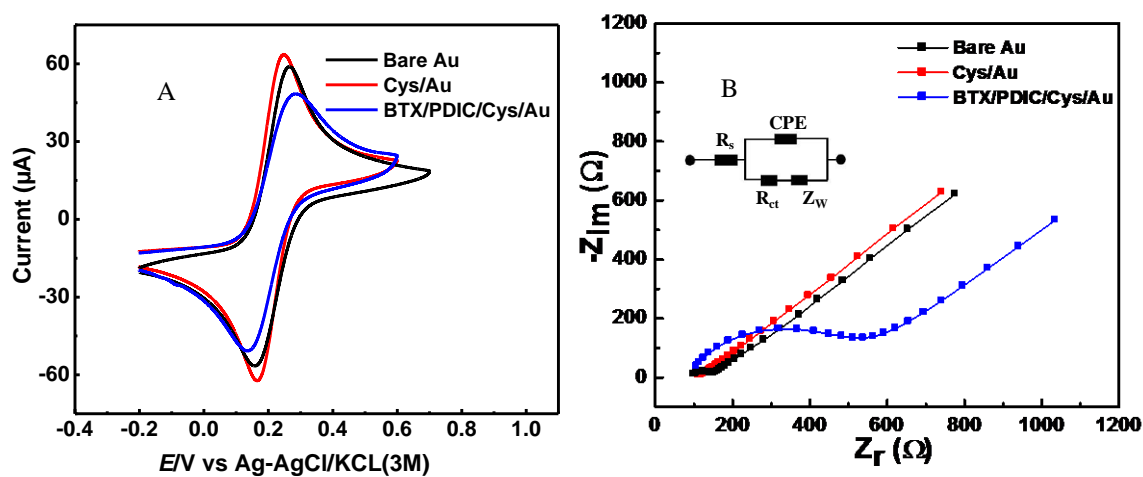


Figure 5.11 Cyclic voltammetry (A) and Nyquist plots (B) of 5 mM $[\text{Fe}(\text{CN})_6]^{4-/3-}$ redox couple in PBS, pH 7.4, for bare Au electrode (black), Cys/Au (red) and BTX/PDIC/Cys/Au (blue). The CV was performed at scan rate of 100 mV/s and the EIS was performed using a frequency range of 10^4 to 0.1 Hz, a DC potential of +0.20 V and AC amplitude of 10 mV. The inset in Figure 5.11(B) is the equivalent circuit applied to fit the impedance spectra.

5.2.3 In Vitro Selection of the DNA aptamers

The aptamers selection was performed using a DNA library consists of 1.8×10^{15} random 60-nucleotide sequences. As explained in details in the experimental section, five consecutive steps were carried out in each round: (1) incubation of the random library with the BTX-beads, (2) separation of the unbound and weakly bound DNA to the BTX- beads by washing, (3) Elution of the bound DNA sequences to BTX, (4) Desalting and PCR amplification of the eluted DNA pool and (5) purification of the fluorescent ssDNA (aptamer) from the PCR product using denaturing PAGE. Two successive counter selection steps after the seventh and eighth rounds were introduced against negative DVS beads, which were used as a matrix for immobilizing the BTX-2. The purpose of these counter selection rounds was to eliminate the ssDNA sequences that were nonspecifically bound to the beads matrix.

In order to monitor the enrichment of the specific DNA to BTX-2 during the SELEX rounds, both fluorescence and EIS methods were utilized. The amount of bound DNA was assessed by measuring the fluorescence of the eluted DNA in each round. Moreover, the binding was evaluated by measuring the % R_{CT} change after incubating the PCR amplified pools with BTX electrodes. The binding of the DNA to BTX electrodes leads to an increase in the total negative charge due to the phosphate backbone of the DNA which retards the access of the $[\text{Fe}(\text{CN})_6]^{3-/4-}$ anions to the electrode surface and thus increases the R_{CT} . As shown in Figure 5.12, a progressive increase in the DNA binding was noticed throughout the selection rounds as demonstrated by the fluorescence and the EIS measurements, suggesting the gradual enrichment of the DNA pools with the specific sequences. We have not seen any decrease in the DNA binding after the counter selection steps which indicates that no significant enrichment in the nonspecifically bound DNA to the DVS beads has occurred. However, a remarkable increase in the bound DNA was observed in the last three rounds where the binding reached a plateau, suggesting enrichment in the specific aptamers for BTX-2. Therefore, the DNA pool from round 10 was cloned and 27 clones were randomly chosen for sequencing. The identified sequences were analysed by multiple sequence alignment using PRALINE software¹⁹⁵. A significant sequence convergence in the DNA pool from round 10 sequences was observed confirming the successful enrichment of that pool. Six different families (A-F) were identified according to their similarities showing high degree of homology among the members of each group (Figure 5.13).

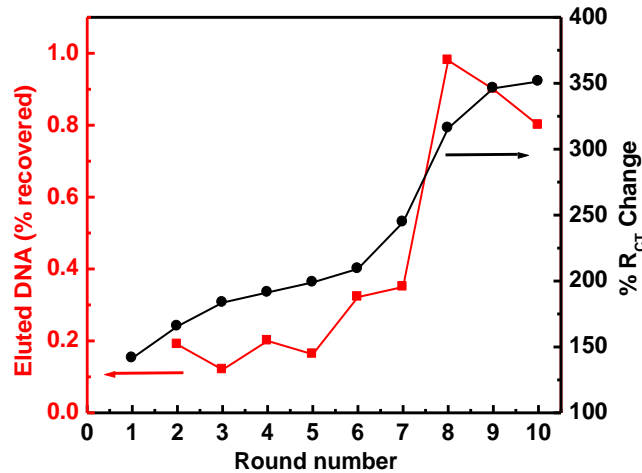


Figure 5.12 Binding of ssDNA pools to BTX-2 after each selection round monitored by calculating the recovery percentage from the fluorescence of eluted DNA (red) and % R_{CT} change ; $(R_{CT}-R_1)/R_1\%$; of the BTX electrodes after binding (black).

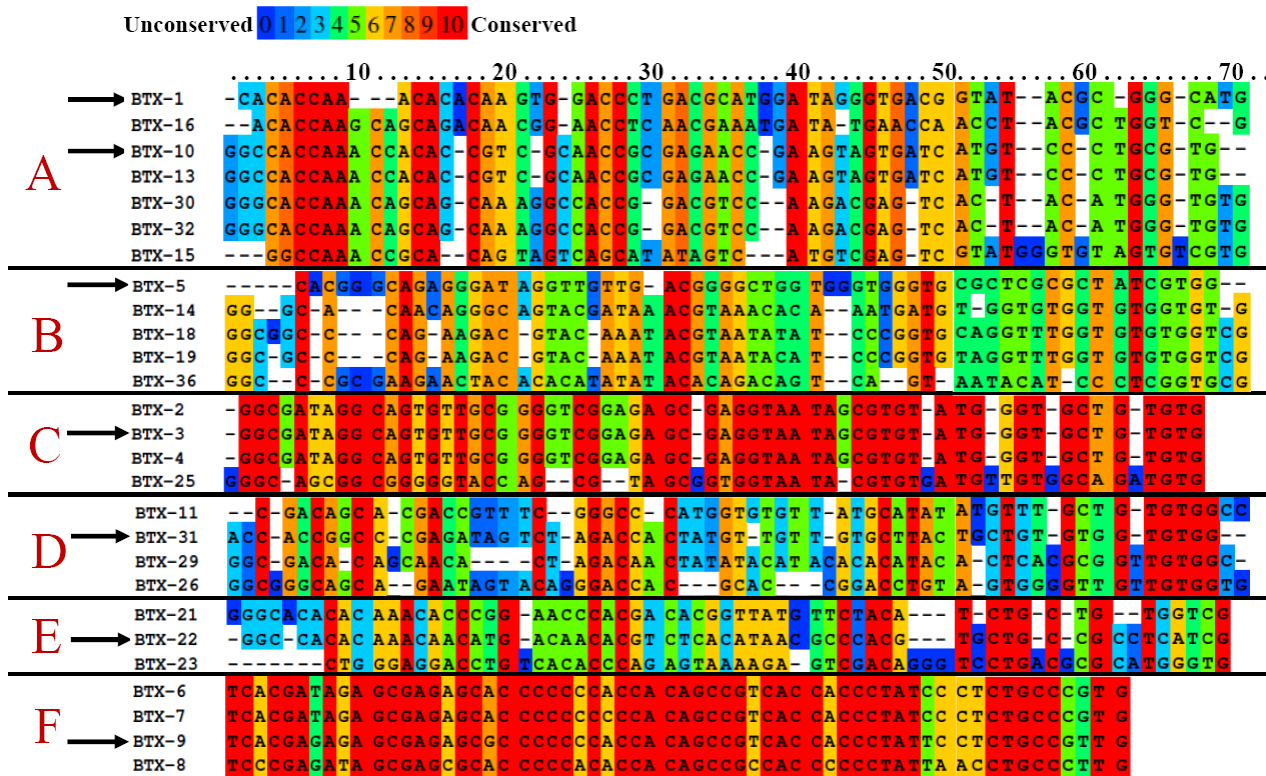


Figure 5.13 Multiple sequence alignment of the selected aptamers

5.2.4 Binding affinity analysis of the aptamers

Representative sequences from each group were chosen for further binding analysis. Initial screening of the selected aptamer clones (BT 1, 10, 5, 3, 31, 22, 9) to confirm their successful binding to BTX-2 using fluorescence as well as EIS was performed. Figure 5.14(A) shows a comparative estimation of the relative binding ability of each aptamer clone to BTX-2 based on the fluorescence measurement of the eluted DNA from the beads as well as the % change of the R_{CT} of BTX electrodes upon binding. Specific binding of all the tested aptamer clones to the BTX-2 was observed compared to binding of the initial library (Control pool). We then determined the binding affinity of the selected aptamers using a fluorescence binding assay. A constant amount of BTX-2 beads and different concentrations of fluorescein-labelled aptamers (0-300 nM) were used to evaluate the dissociation constant of the aptamers under the same conditions which were used for selection.

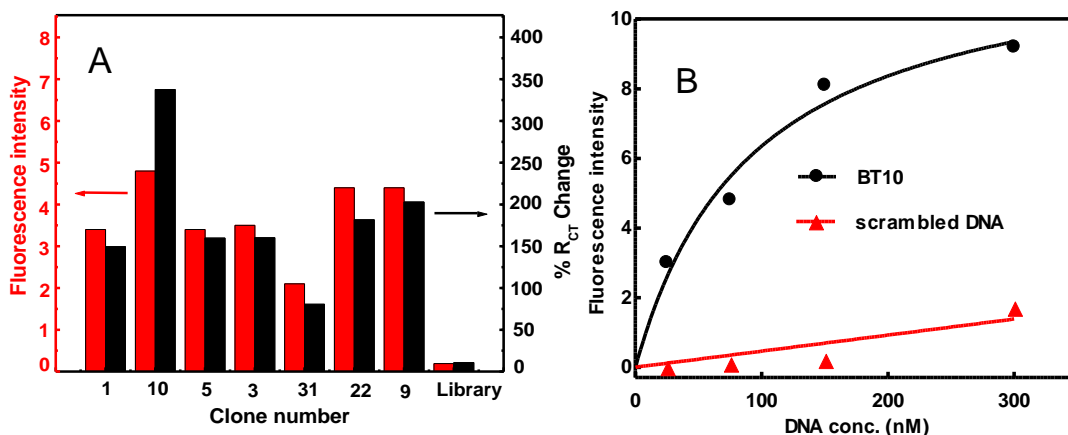


Figure 5.14(A) Binding assays with the individual aptamer clones BTX 1, 10, 5, 3, 31, 22 and 9, to test their ability to bind to BTX-beads (red) and BTX electrodes (black). The unenriched initial library was used as the negative control. (B) Fluorescence binding curve of BTX-2 to aptamer BT10 (black) and a scrambled DNA sequence (red).

As shown in Figure 5.14(B), by plotting the fluorescence intensity of the eluted DNA versus the aptamer concentration, the K_d was calculated using non linear regression analysis. A scrambled DNA sequence was used as a control for the binding experiments showing non-significant binding to the BTX-beads. Table 5.2 shows the calculated K_d values of the selected aptamers ranging from 92 to 1296 nM. It was observed that the aptamer BT10 have shown the highest

binding affinity to BTX-2 ($K_d= 92$ nM), therefore, it was chosen for our application. The secondary structure predictions for the BT10 aptamer sequence without the primer binding regions is shown in Figure 5.15. The image were generated with mfold software ²²⁷. The structure with the lowest minimum free energy is shown. The predicted structure exhibited stem-loop motifs commonly found with in vitro selected aptamers ²²⁸.

Table 5.2 Sequences and dissociation constants (K_d) between BTX-2 and selected aptamers.

Group	Clone number	Aptamer sequence	K_d (nM)
A	BT 1	CACACCAAACACACAAGTGGACCCTGACGCATGGA TAGGGTGACGGTATACGCGGGCATG	385
	BT 10	GGCCACCAAACCACACCGTTCGCAACCGCGAGAACC GAAGTAGTGATCATGTCCCTGCGTG	92
B	BT 5	CACGGGCAGAGGGATAGGTTGTTGACGGGGCTGGT GGGTGGGTGCGCTC GCGCTATCGTGG	311
C	BT 3	GGCGATAGGCAGTGTTCGCGGGTTCGGAGAGCGAGG TAATAGCGTGTATGGGTGCTGTGTG	278
D	BT 31	ACCACCGGCCCGAGATAGTCTAGACCACTATGTTGT TGTGCTTACTGCTGTGTGGTGTGG	1296
E	BT 22	GGCCACACAAACAACATGACAACACGTCTCACATA ACGCCACGTGCTGCCGCTCATCG	258
F	BT 9	TCACGAGAGAGCGAGAGCGCCCCCCCACACAGCC GTCACCACCCTATTCTCTGCCGTTG	166

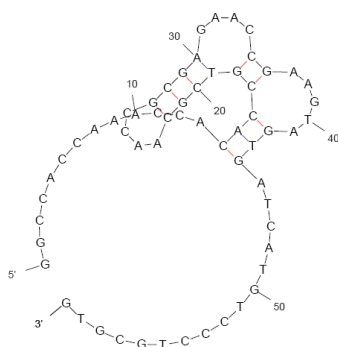


Figure 5.15 Secondary structure prediction for the BT10 aptamer.

5.2.5 Optimization of the aptamer-toxin binding conditions

With the aim to shed light on the factors that can influence the BT10 aptamer-toxin binding and to optimise the binding conditions for achieving the highest possible affinity, the incubation time, sodium and magnesium ions concentrations, and the pH of the binding buffer were studied. Figure 5.16(A) shows the % R_{CT} change of the BTX electrodes after incubation with 500 nM BTX-2 at different time points. An enhancement in the % R_{CT} change was observed until 30 min binding time when saturation was reached.

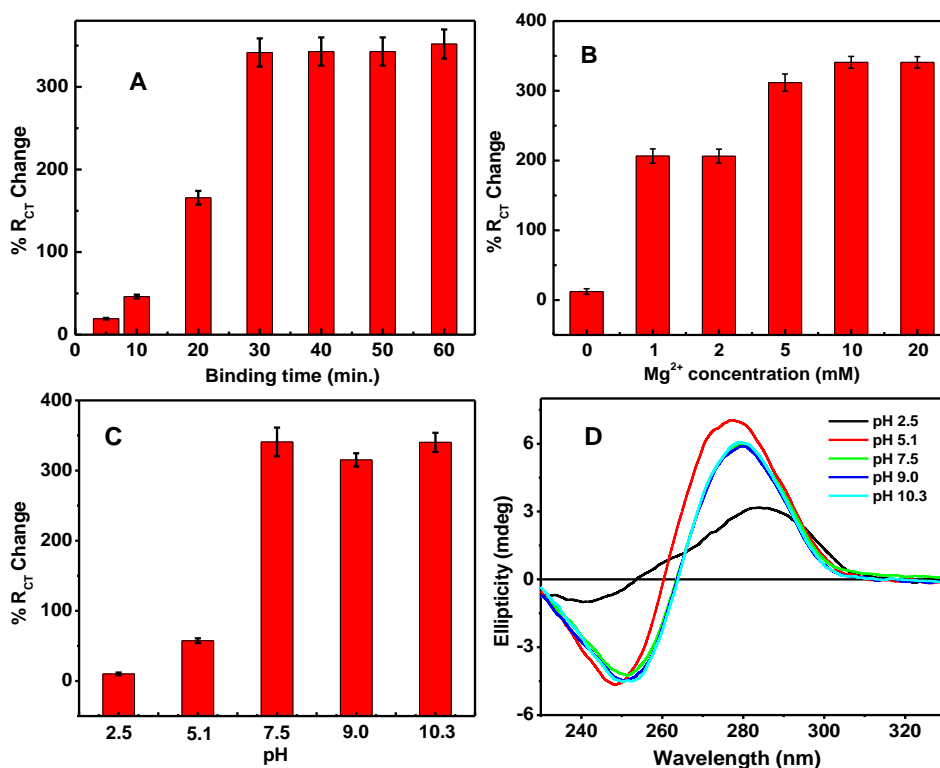


Figure 5.16 The effect of incubation time (A), Mg^{2+} ions concentration (B) and pH of the binding buffer (C) on BTX-aptamer binding, monitored by measuring the % R_{CT} change in 10 mM PBS (pH 7.4) containing 5 mM $[Fe(CN)_6]^{4-/3-}$ redox couple after incubating the BTX electrodes with 500 nM aptamer. The error bars represent the standard deviation of the measurements. (D) The CD spectra of the BTX aptamer in binding buffer with different pHs.

Figure 5.16(B) shows a clear dependence of the aptamer-toxin binding on the Mg^{2+} concentration which is in agreement with previous studies on other aptamers^{180,229}. An increase in the R_{CT} with increasing the concentration of Mg^{2+} cations was observed until 10 mM Mg^{2+}

after which no further change was seen. Such affinity change is likely due to the effect of Mg^{2+} on the DNA conformation. On the other hand, by changing the concentration of sodium ions in the binding buffer from 0-200 mM, no effect on the aptamer-toxin binding have been observed. Figure 5.16(C) shows the effect of pH of the binding buffer on the aptamer-toxin binding monitored by the % change in the R_{CT} . It was clearly observed that the binding of the aptamer to BTX-2 was significantly diminished at acidic pHs (2.5, 5.1). However, no significant effect on the binding at $pH > 7.5$ was seen. To better understand the origin of such effect, systematic circular dichroism spectra of the aptamer at different pHs were recorded (Figure 5.16(D)). A comparable spectra of the aptamer at $pHs > 7.5$, in comparison to significant difference in the spectra in acidic pHs confirms the important role of the pH on the DNA aptamer conformation, and consequently, the binding with BTX-2. Therefore, an incubation time of 30 min and binding buffer which consists of 50 mM Tris, pH 7.5, and 10 mM $MgCl_2$ were used in the subsequent experiments to improve the affinity and to enhance the signal associated with the aptamer-toxin binding. Under these optimum conditions, we have again estimated the binding affinity of the BT10 aptamer and a K_d value of 42 nM was obtained.

5.2.6 Electrochemical Competitive Aptasensor

The aptamer with the highest affinity, BT10, was assessed for the detection of BTX-2 in a label-free electrochemical competitive assay. The competition was established between the immobilized BTX-2 on the gold electrode and free BTX-2 in solution in the presence of a fixed amount of the aptamer. The electrochemical detection was realized based on the change of R_{CT} of the $[Fe(CN)_6]^{4-/3-}$ redox couple. With increasing the concentration of BTX-2 in solution, the amount of free aptamer available for binding to the immobilized BTX-2 on the gold surface decreases resulting in lower R_{CT} change. Since the aptamer concentration used for the competition step is a crucial factor in the aptasensor fabrication, it was important to perform initial optimization of the aptamer concentration without competition. Generally, higher aptamer concentration will lead to decreased sensitivity and lower aptamer concentration will lead to reduced signal value⁸⁵. Based on our optimization experiment, a concentration of 500 nM BT10 aptamer was chosen to strike a balance between the two effects. Figure 5.17(A) shows the decrease in the R_{CT} with increasing the concentration of BTX-2 from 0.01 to 2000 ng/ml.

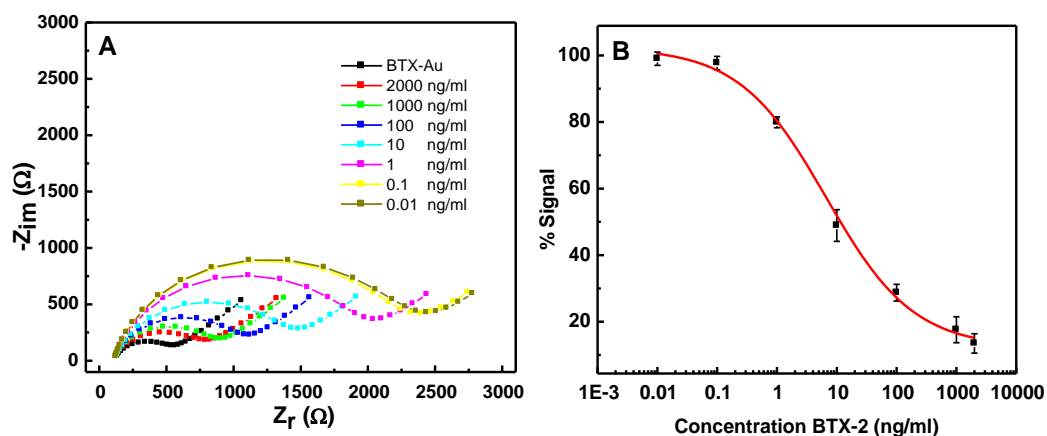


Figure 5.17(A) Nyquist plots of the BTX electrode before and after incubation with different concentrations of BTX-2 mixed with 500 nM aptamer, (B) the calibration curve for BTX-2, plot of analytical response (% Signal, $[(R_{CT} - R_i)/(R_{max} - R_i) \times 100]$) vs. BTX-2 concentration. The error bars show the standard deviation of two repetitive measurements.

A sigmoidal dose response curve was obtained (Figure 5.17(B)) by plotting the analytical response (% signal) expressed as a percentage of the maximum signal obtained when no BTX-2 was added $[(R_{CT} - R_i)/(R_{max} - R_i) \times 100]$ vs. toxin concentration. R_{CT} is the resistance after incubation with certain concentration of BTX-2, R_{max} is the resistance at zero BTX-2 and R_i is the background signal of the BTX electrode. The calibration curve was fitted to a sigmoidal logistic four-parameter equation 5:

$$Y = A + \frac{(B - A)}{1 + \left(\frac{x}{EC50}\right)^b} \quad \text{Eq. 5}$$

where A, B are the minimum and maximum analytical response, respectively. b is the slope at the inflection point and EC50 is the concentration leading to 50% of the maximum signal. The best-fit values of the experimental data are the following: $y = 12.2 + (102.35 - 12.2)/(1 + (x/6.66)^{0.59})$, with a correlation coefficient $R^2 = 0.997$. The limit of detection (LOD) was calculated as the concentration that leads to 95% of the maximum signal to be 106 pg/ml. This LOD is comparable with the LOD of reported aptasensors for other small molecules²²⁶ as well as the previously reported electrochemical immunosensor for BTX-2⁸⁶. However, compared to

the present work, the reported work uses much more complicated sensor designs and signal amplification reagents.

Cross reactivity experiment with BTX-3, a similar analogue to BTX-2 (Figure 1.2), and negative control experiments with OA and MC-LR were studied using 1 ng/ml of each toxin. As shown in Figure 5.18, the response shown as (100- % Signal) of the aptasensor was comparable for both BTX-2 and BTX-3 indicating high degree of cross reactivity which can be exploited to detect the total concentrations of both congeners in a sample similar to the case of immunoassays. However, less than 5 % negative response was obtained with MC-LR and OA due to little nonspecific adsorptions of these toxins on the aptasensor surface. These results indicate the non significant interference of these toxins with the competitive assay and the high selectivity of the aptasensor.

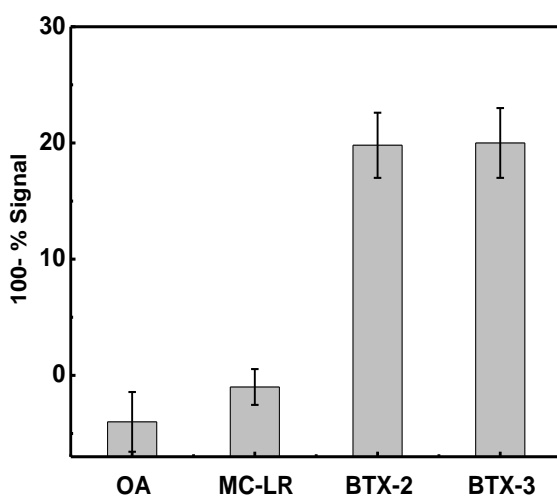


Figure 5.18 Comparison of response of the aptasensor to 1 ng/ml BTX-2, BTX-3, MC-LR, and OA.

5.2.7 Analysis of brevetoxin-2 in Spiked Shellfish Samples

In order to demonstrate the feasibility of detecting BTX-2 in food matrix, a spiked shellfish extracts were analyzed using the developed aptasensor. As shown in Table 5.3, a good recovery percentage was obtained for BTX-2 in the shellfish extracts indicating non significant interference from the shellfish matrix on the aptasensor response. Thus, these results confirm the possible applicability of the developed aptasensor in real sample analysis.

Table 5.3 Application of the BTX aptasensor in spiked shellfish extracts

Sample	Spiked shellfish BTX-2 (ng/ml)	Recovery %	RSD%
1	0.1	107	6.0
2	10	102	3.4
3	100	110	4.0

5.3 Conclusions

In this chapter, selection, identification and biosensing application of DNA aptamers against the marine toxins OA and BTX-2 have been shown for the first time. The highest affinity OA aptamer ($K_d = 77$ nM) showed remarkable sensitivity and selectivity for OA against DTX-1 and DTX-2. We showed that the affinity of the aptamer towards OA was preserved and not affected by surface immobilization. The circular dichroism spectra also demonstrated the conformation change of the aptamer upon OA binding which can be exploited in several biosensing applications. Through monitoring of the OA binding-induced conformational change within the aptamer, we achieved a limit of detection of 70 pg/ml with a label-free aptasensor based on EIS. For BTX, the highest affinity aptamer BT10, $K_d = 42$ nM under the optimum binding condition, was applied for the detection of BTX-2 in an electrochemical competitive aptasensor showing remarkable sensitivity. Moreover, the aptasensor showed good selectivity to BTX-2 against other toxins from different groups such as OA and MCs. However, high degree of cross reactivity between the two similar analogues BTX-2 and BTX-3 was observed. We believe that the continual emergence of novel library-selected, high-affinity aptamers will open the way to a variety of biosensing architectures, particularly for sensitive and high-specificity small molecule toxin detection in complex samples. Moreover, the combination of aptamers with graphene materials is expected to offer promising platform with further lower cost and improved stability. An example for this integration will be shown in the subsequent chapter.

CHAPTER 6. LABEL-FREE VOLTAMMETRIC APTASENSOR FOR THE SENSITIVE DETECTION OF MICROCYSTIN-LR USING GRAPHENE-MODIFIED ELECTRODES

The development of successful biosensing platforms is highly dependent upon the biorecognition properties of the recognition receptor and the sensitivity of the transducer to the binding signal. We have shown the successful use of graphene electrodes for immunosensing in chapter 3 and 4 and the selection of aptamers against small molecule toxins as new recognition receptors in chapter 5. In this chapter, the integration of the high affinity and specificity of DNA aptamers with the graphene is presented as an excellent avenue for low cost, sensitive and selective biosensing architectures. Here, MC-LR aptamer is used as a model which has been recently identified ¹⁸⁶. The aptamer immobilization on GSPE was monitored by SWV in $[\text{Fe}(\text{CN})_6]^{4-/3-}$ redox couple solution. The optimization of the aptamer-target binding conditions is presented and the mechanism of the sensing detection is also investigated.

6.1 Characterization and mechanism of the aptasensor

We investigated in this work the suitability of a 60-nucleotide DNA aptamer ¹⁸⁶, which has been shown to bind MC-LR with a dissociation constant of 50 nM, for applications in sensitive and label-free electrochemical detection. In addition to its high affinity to MC-LR, this aptamer exhibits very high degree of selectivity against other MC congeners such as MC-LA and MC-YR. As shown in schematic diagram (Figure 6.1), we employed GSPE as a sensing electrode on which the aptamer was physically adsorbed via the π - π stacking interactions between the graphene hexagonal cells and the nucleobases of the DNA as previously reported ¹⁹⁰. The binding of MC-LR to the aptamer leads to a change in the square wave voltammetric signal.

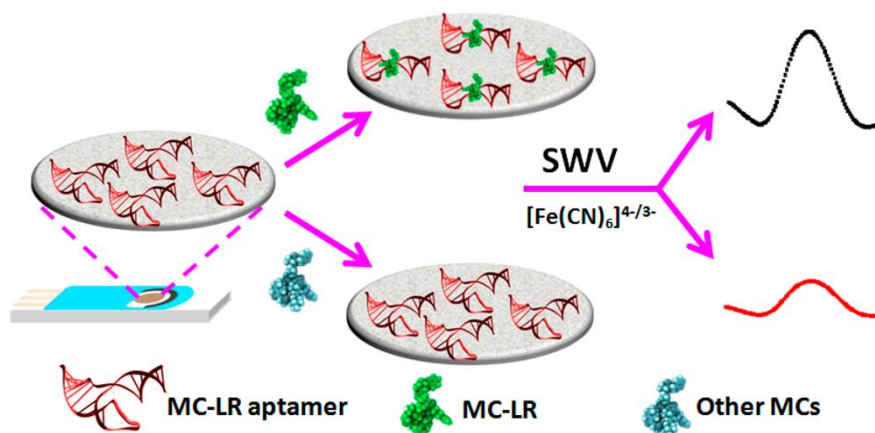


Figure 6.1 Schematic of MC-LR detection based on SWV on aptamer-functionalized GSPE

Figure 6.2(A) shows the SWV response of different experiment steps. We observed a marked change in the SWV reduction peak current of the $[\text{Fe}(\text{CN})_6]^{3-/4-}$ redox couple on the GSPE after the aptamer immobilization step as well as after the introduction of MC-LR. The SWV of $[\text{Fe}(\text{CN})_6]^{3-/4-}$ reduction on the bare GSPE is characterized by a well-defined cathodic peak as shown in Figure 6.2(A). However, the aptamer-modified electrodes exhibit a lower reduction peak current of $[\text{Fe}(\text{CN})_6]^{3-/4-}$ in the square wave voltammetry compared with the bare GSPE. This decrease in reduction peak current is due to the electrostatic repulsion between the negatively charged phosphate backbone of the DNA aptamer and the $[\text{Fe}(\text{CN})_6]^{3-/4-}$ anions. Furthermore, the shielding of the graphene surface by the immobilized aptamers attenuates the accessibility of the $[\text{Fe}(\text{CN})_6]^{3-/4-}$ redox probe to the electrode surface. On the other hand, upon the binding of MC-LR to the aptamer, the $[\text{Fe}(\text{CN})_6]^{3-/4-}$ reduction peak current increased, indicating an increase in electron transfer efficiency between the $[\text{Fe}(\text{CN})_6]^{3-/4-}$ redox probe and the electrode surface. This behaviour forms the basis of MC-LR detection.

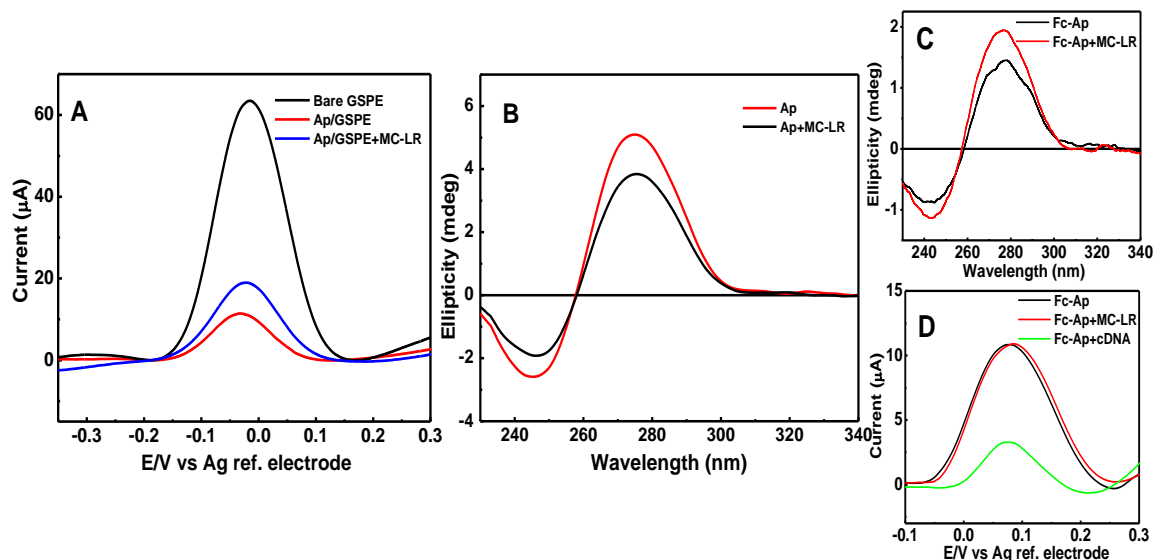


Figure 6.2(A) SWVs of 1 mM $[\text{Fe}(\text{CN})_6]^{4-/3-}$ probe in PBS, pH 7.4 for bare GSPE (black), MC-LR aptamer-functionalized GSPE (red), and after MC-LR toxin incubation (blue) (concentration of the aptamer, 10 μM ; concentration of MC-LR, 1 nM); (B) CD spectra of 0.67 μM MC-LR aptamer in binding buffer before (black) and after (red) binding with 0.67 μM of MC-LR at room temperature; (C) CD spectra of 0.4 μM Fc/Ap in binding buffer before (black) and after (red) binding with 0.4 μM of MC-LR at room temperature; (D) SWV in blank 10 mM PBS buffer solution pH 7.4 for Fc/Ap/GSPE (black), after incubation of Fc/Ap/GSPE with 1 nM MC-LR (red), and after incubation of Fc/Ap/GSPE with cDNA (green).

This phenomenon is in agreement with other reports which have shown faster electron transfer of $[\text{Fe}(\text{CN})_6]^{3-/4-}$ couple on GSPEs upon aptamer-protein binding monitored using EIS¹⁹⁰. They attributed this phenomenon to the analyte-induced conformational change of the aptamer, which leads to complete dissociation of some aptamer molecules from the surface, thereby decreasing the total negative charge on the graphene surface. However, such explanation cannot be generalized for any target analyte, particularly, small molecules which may not lead to a change in the conformation of the entire aptamer sequence to cause a release from the graphene surface. Therefore, in order to gain more insight about the detection mechanism, we first studied the conformation of the free and target-bound form of MC-LR aptamer using circular dichroism. As shown in Figure 6.2(B), the circular dichroism spectrum of the aptamer in binding buffer pH 7.5

showed a positive band at 276 nm and a negative band at about 245 nm. However, after MC-LR binding, an increase of the ellipticity at 276 and 245 nm was observed which indicates the folding of the aptamer into a different conformation upon binding with MC-LR as previously reported¹⁸⁶. We then investigated the effect of the MC-LR binding on a 3'-terminal-ferrocene-labelled MC-LR aptamer (Fc/Ap) attached to gold electrode by self-assembly via thiol chemistry. We found that upon binding with MC-LR, no change in the ferrocene signal was observed. Nonetheless, a change of the CD spectra of Fc/Ap in solution was observed upon binding with MC-LR (Figure 6.2(C)), which may indicate that the change in conformation induced by MC-LR binding was localized within the aptamer. We speculate that this partial conformational change did not affect significantly the distance of the ferrocene label from the surface, hence the lack of signal change. We then investigated the effect of MC-LR binding on ferrocene-labelled MC-LR aptamer physically assembled on GSPE (Fc/Ap/GSPE). As shown in Figure 6.2(D), a sharp SWV reduction peak of the ferrocene was observed after the physical adsorption of the aptamer on the electrode surface (black curve). Interestingly, no significant current change was observed upon MC-LR binding (red curve). This lack of response ruled out the possibility of the complete dissociation of the aptamer from the graphene surface upon MC-LR binding. In comparison, similar experiment carried out by incubating the Fc/Ap GSPE with fully length complementary DNA sequence of the aptamer showed significant decrease of the ferrocene signal (green curve) as expected due to the release of the Fc/Ap from graphene surface upon binding with cDNA. Such finding indicates that the proposed detection scheme can be extended to other small molecules which might not induce significant conformational change in the entire aptamer sequence.

6.2 Optimization of aptamer immobilization

The required time for aptamer immobilization on the GSPE was optimized in a time course experiment to achieve the maximum drop of SWV reduction peak current of $[\text{Fe}(\text{CN})_6]^{3-/4-}$ caused by aptamer adsorption on the graphene surface. As shown in Figure 6.3(A), the reduction peak current of $[\text{Fe}(\text{CN})_6]^{3-/4-}$ decreased by 55% after 2 min incubation with the aptamer (inset of Figure 6.3(A)), suggesting a high adsorption of the aptamer to graphene. The largest drop in the SWV signal was obtained after 10 min of incubation; while no further

decrease in the current was observed with incubation longer than 10 min. Therefore, a 10 min incubation time was established for the aptamer immobilization on the GSPEs in the further experiments. The stability of the prepared aptamer-graphene electrodes were then studied over a period of two weeks and no loss of signal was observed. The immobilization step was also optimized by monitoring the SWV reduction peak current of $[\text{Fe}(\text{CN})_6]^{3-/4-}$ after 10 min incubation of different concentrations of the aptamer (0.0 - 20 μM) on the electrode surface. Figure 6.3(B) shows the drop in SWV reduction peak current of $[\text{Fe}(\text{CN})_6]^{3-/4-}$ became larger with increasing aptamer concentration. At 10 μM , a maximum drop in reduction peak current was reached after 10 min incubation and additional increase in the MC-LR aptamer concentration did not result in further decrease in the reduction peak current (inset of Figure 6.3(B)). Therefore, an aptamer concentration of 10 μM was chosen for all subsequent experiments for maximum coverage of the graphene electrode surface, minimizing possible nonspecific adsorption of the toxin.

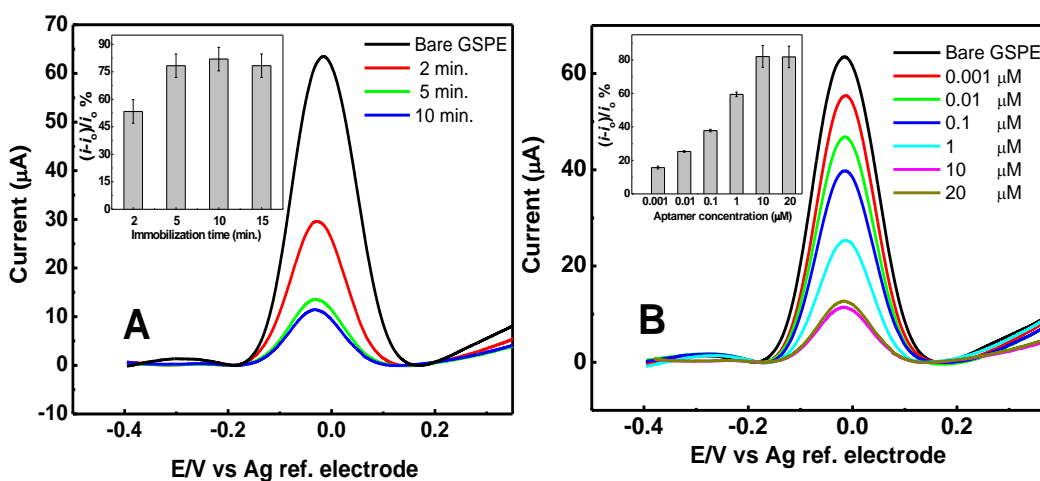


Figure 6.3(A) SWVs of 1 mM $[\text{Fe}(\text{CN})_6]^{4-/3-}$ probe in PBS, pH 7.4 for GSPE after 2, 5 and 10 min incubation with 10 μM MC-LR aptamer. The inset is the percentage of the $[\text{Fe}(\text{CN})_6]^{4-/3-}$ peak current change vs. the immobilization time of MC-LR aptamer on GSPE. (B) SWVs of 1 mM $[\text{Fe}(\text{CN})_6]^{4-/3-}$ probe in PBS, pH 7.4 for GSPE incubated with different concentrations of MC-LR aptamer for 10 min. The inset is the percentage of the $[\text{Fe}(\text{CN})_6]^{4-/3-}$ peak current change vs. the MC-LR aptamer concentration.

6.3 Optimisation of MC-LR aptasensor

Since, the binding of MC-LR to the aptamer may be influenced by several factors such as the incubation time, presence of ions such as sodium and magnesium, and the pH of the solution, it was important to study these factors. Figure 6.4(A) shows the aptasensor response (expressed as $(i_p - i)/i_p$ %) after incubation with 1 nM MC-LR at different time points. With increasing the binding time, the sensor response was increased until reached an optimum binding after 45 min. We found also that the binding of MC-LR to the DNA aptamer depended on the presence of magnesium cations (Figure 6.4(B)). With increasing concentration of Mg^{2+} ions, the binding was increased until 2mM Mg^{2+} after which no further change was observed. Similar dependence on Mg^{2+} ions for an aptamer/target binding was previously reported for ochratoxin A¹⁸⁰. In that case, it was suggested that the dependence on Mg^{2+} ions was due to the formation of a coordination complex between the toxin and the Mg^{2+} ions with the aid of the carboxyl and the hydroxyl groups in ochratoxin A, which enhances the binding to the aptamer. In the case of MC-LR, previous study²³⁰ has shown that there is no complexation of MC-LR with earth metal ions such as Mg^{2+} which rules out the effect of any possible complexation with Mg^{2+} on the binding. Therefore, we believe that such effect originated from the effect of Mg^{2+} on the DNA conformation²¹⁶, which in turn plays an important role in the binding with MC-LR. However, the binding between MC-LR and the aptamer was not significantly influenced by the concentration of sodium, which indicates that the ionic strength of the solution doesn't have significant effect on the binding. In order to check whether the pH affects the binding of the aptamer to MC-LR, we measured the sensor response at 1nM concentration of MC-LR in binding buffer with three different pHs. Only little difference (about 8%) in the sensor response to MC-LR at pH 7.5 and pH 8.8 was observed (Figure 6.4(C)). However, a significant decrease in the response was observed in acidic pH 3.4 (about 30 %). This effect is not expected to be due to change in the charge of the MC-LR molecule as MC-LR is negatively charged at most pH values ($3 < \text{pH} < 12$)²³¹. Therefore, we also attribute this pH effect to the change of the conformation of the DNA at the different pHs. This has been also confirmed by measuring the CD spectra of the aptamer at the different pHs. As shown in Figure 6.4(D), the CD spectra of the aptamer at both pH 7.5 and 8.8 were very similar, however, significant change in the spectra was

obtained at pH 3.4 which corroborate the crucial role of the pH on the aptamer conformation, and thus, the binding with MC-LR. Therefore, a pH of 7.5 was used in the subsequent experiments.

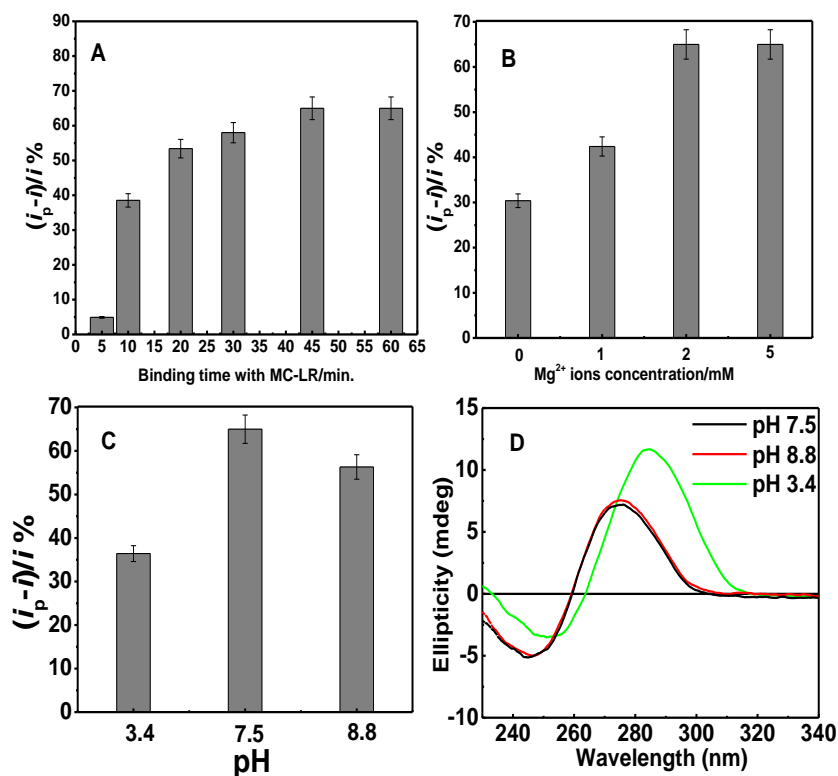


Figure 6.4(A) The effect of incubation time on aptasensor response towards 1 nM MC-LR. (B) The aptasensor response towards 1 nM MC-LR in binding buffer contains different concentration of $MgCl_2$. (C) The aptasensor response towards 1 nM MC-LR in binding buffer with different pHs. All the measurements were done in 10 mM PBS (pH 7.4) containing 1 mM $[Fe(CN)_6]^{4-/3-}$ redox couple. (D) The CD spectrum of the MC-LR aptamer in binding buffer with pH 7.5 (black), 8.8 (red), and 3.4 (green curve).

6.4 Dose response of the aptasensor

We then studied the SWV response of the aptasensor by monitoring the reduction of $[Fe(CN)_6]^{3-/4-}$ in presence of different concentrations of MC-LR. To determine the detection range, SWV was recorded after incubation with 0.1 pM to 5 nM MC-LR. Figure 4A shows a

clear dose-dependent response of the SWV peak current (i_p) up to 1.0 nM MC-LR, after which any increase in the MC-LR concentration ceased to cause further change in the peak current. As shown in the inset of Figure 6.5(A), a good linear relationship in the range of 0.1 pM to 1.0 nM was obtained between the logarithm of the MC-LR concentration and the analytical response ($(i_p - i)/i\%$) in binding buffer, which can be represented by the equation, $(i_p - i)/i\% = 28.35 + 12.20 \times \log C$ [pM], with a correlation coefficient of 0.988 (N=5), respectively. The detection limits (defined as $3\sigma/\text{slope}$, with σ being the standard deviation of the blank samples) of the proposed aptasensor were calculated to be 1.9 pM in binding buffer.

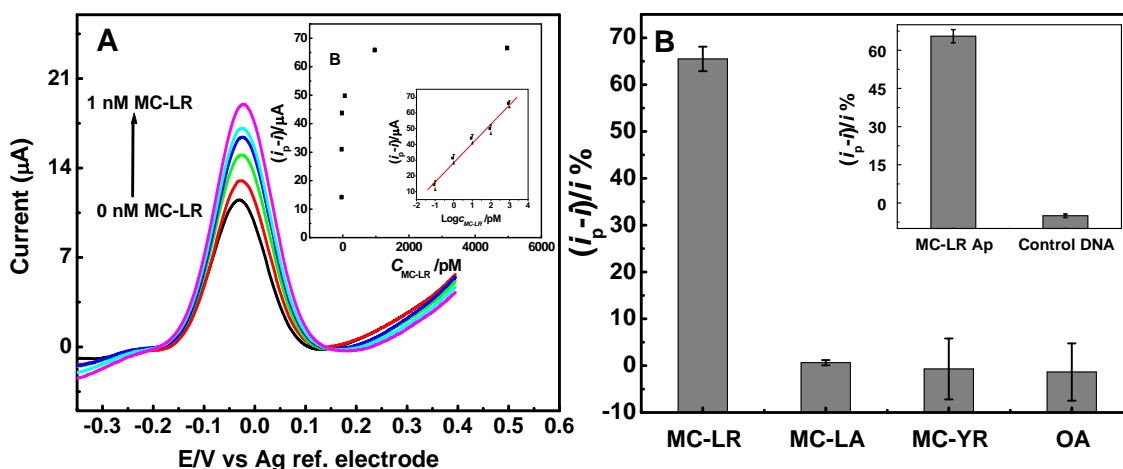


Figure 6.5(A) SWVs of the aptasensor after 45 min incubation with 0.00, 0.1, 1.0, 10, 100 and 1000 pM MC-LR. The inset is the dependence of the aptasensor response on MC-LR concentration (plot of the percentage of the peak current change vs. C_{MC-LR}), the small Inset: calibration curve for MC-LR detection in binding buffer; is a plot of the percentage change in the peak current versus the logarithm of the MC-LR concentrations. (B) Response of the aptasensor to 1.0 nM of MC-LR, OA, MC-LA, and MC-YR. The inset is the comparison between the response of modified GSPE with MC-LR aptamer and non specific DNA sequence to 1 nM MC-LR. Error bars correspond to duplicate measurements.

6.5 Selectivity of the aptasensor

Negative control experiments were performed to study the specificity of the aptasensor. The aptamer-modified GSPEs were first incubated with OA, a toxin with similar molecular weight to MC-LR and protein phosphatase inhibitory effect. The cross-reactivity of the aptasensor to other microcystin congeners was also assessed with MC-LA and MC-YR, which differ from MC-LR by only 1 amino acid within the heptapeptide framework. As shown in Figure 6.5(B), the change in the peak current in the case of MC-LR is much greater than the negative controls. In fact, no significant response (increase or decrease in reduction peak current) was obtained with OA acid, MC-LA and MC-YR. More importantly, the aptasensor was only responsive to MC-LR and did not exhibit cross-reactivity with structurally-similar MC-LA and MC-YR. Despite that the aromatic rings in the structures of OA and microcystins could be normally adsorbed on the graphene surface by π - π stacking, the lack of response indicates that the non-specific adsorption on the developed graphene platform is not significant. We attribute this to the effective coverage of the graphene surface by the aptamer molecules. To eliminate the possibility of the nonspecific adsorption of MC on the graphene, we have also done a control experiment using non specific DNA sequence immobilized on the GSPE using the same protocol and incubated with 1 nM MC-LR. However, we have not seen any significant change in the response (inset of Fig. 6.5(B)). When the prepared aptasensor was not in use, it was stored at 4°C. A small change (2.9 % decrease in response) was observed after storage for 1 month that indicates good stability of the prepared aptasensors.

6.6 Application of the aptasensor for spiked fish extracts and tap water samples

In order to demonstrate the feasibility of applying the proposed aptasensor in food matrixes, uncontaminated and spiked fish samples with MC-LR were tested. As shown in Table 6.1. The negative fish sample extract in binding buffer did not give any significant analytical signal. A good recovery percentage was obtained for the spiked fish extract with 1 nM MC-LR (16.5 nmol/kg), which indicates a non-significant effect of the fish matrix on the aptasensor. The spiked tap water samples have shown less recovery percentages. We attribute that to the presence

of uncontrolled amount of cations which can affect the binding of the aptamer with MC-LR. Moreover, the decrease of the microcystin recovery could be due to the decomposition of some of the MC-LR molecules by chlorine which usually added as a disinfectant in the drinking water. However, seeing the low detection limit of the proposed aptasensor compared with other reported sensors^{36,73,232} which use sophisticated detection schemes, we believe in the usefulness of the proposed aptasensor for the detection of low amount of MC-LR in real samples. Particularly, the detection limit is much lower than the standard of the WHO requirements for MC-LR content in drinking water (1 nM).

Table 6.1 Results of the detection of MC-LR in fish extracts and water samples (n = 2)

Sample	Standard concentration (nM)	Found (nM)	Recovery %	RDS %
Fish extract	Negative	-	-	-
Spiked fish extract	1.0	0.9810	98.10	1.67
Spiked tap water	0.1	0.0917	91.70	10.93

6.7 Conclusions

We demonstrated in this chapter a novel electrochemical aptasensor for the detection of MC-LR by exploiting graphene as electrode material as well as the excellent affinity and selectivity of a MC-LR-targeting aptamer. This new approach has led to a rapid, low-cost, sensitive and specific detection method for MC-LR in buffer, spiked fish extracts and tap water samples, offering advantages over previously reported approaches. First, the aptasensor was fabricated without labelling, minimizing cost and complexity, as well as preserving the affinity of the aptamer to MC-LR. Second, the use of graphene have lead to simpler detection scheme and also reduce the cost. Moreover, by comparing the response of Fc/Ap upon binding with MC-LR and cDNA, we demonstrated in this work that the mechanism of the detection was based on the conformation change in part of the aptamer without complete release of the aptamer from the graphene surface. We believe that this finding is of relevance for the future fabrication of graphene-based aptasensing platforms for other small molecules.

CHAPTER 7. INFLUENCE OF GRAPHENE OXIDE SHEETS SIZE ON ELECTROCHEMICAL BIOSENSORS PERFORMANCE

In the previous chapters immunosensors and aptasensors have been developed by covalent and physical immobilization of antibodies and aptamers on graphene electrodes for the detection some allergens and toxins. In this chapter, we investigate the effect of varying the lateral size of graphene oxide sheet produced from graphite route on the sensitivity of two representative label-free electrochemical aptasensing and immunosensing systems employing either physical or covalent immobilization. First, we performed a separation step for different graphene oxide fractions with varying size ranges from GO bulk solution prepared using modified Hummers method ¹⁹². The structural properties of the separated sheets were characterized using Raman spectroscopy and X-ray photoelectron spectroscopy. Then, the separated GO fractions were deposited on the surface of screen printed electrodes and used for the biosensors fabrication.

7.1 Separation and characterization of graphene oxide sheets according to their size

Since the production of monodisperse GO remains major challenge, a post processing approach has been performed herein after GO synthesis for the flakes separation. To avoid the introduction of additional impurities to the highly adsorbing GO sheets, we did not use a density gradient ultracentrifugation for the separation step ²³³. Moreover, the gradient making medium that is often used for this method such as sucrose ²³³ can result in the reduction of GO.

To prepare size-selected GO suspensions from 200 nm to >100 μm , we used two-step separation methodology. First, an ultracentrifugation step was carried out, which takes advantage of the difference in sedimentation rate between various sized flakes. When a GO suspension in water is placed on a centrifuge tube, the action of centrifugal force results in faster sedimentation rate of the larger and heavier sheets while slowing down the smaller sheets. Thus, the separation of GO sheets with different lateral sizes can be obtained by collecting two fractions along the

centrifuge tube. This process is repeated for each collected fraction and again separated. Images for the tubes after centrifugation are shown in Figure 7.1A. However, based on SEM characterisation of some separated fractions (Figure 7.1B), the centrifugation step alone was not enough to achieve efficient GO's separation over specific range of sizes. A second step was therefore needed to ensure effective separation, thus, the GO fractions were filtered by using membranes with different pore sizes.

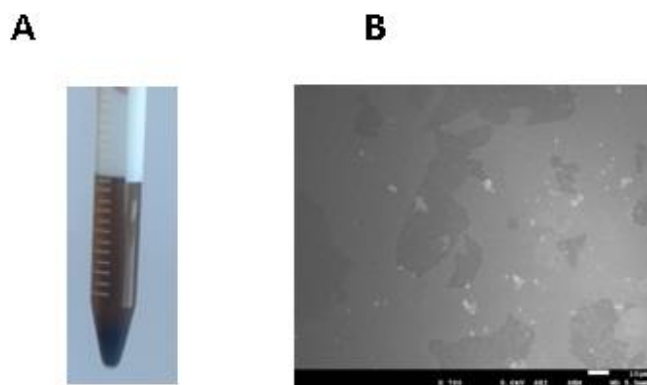


Figure 7.1(A) Digital camera images of the ultracentrifuge tubes after centrifugation, (B) SEM image of graphene oxide sheets separated only by centrifugation.

The separated GO sheets were then characterised using atomic force microscopy (AFM) and scanning electron microscopy (SEM) to determine the sheets size and thickness and to evaluate the surface morphology. AFM and SEM images of the GO sheets on cleaved mica surfaces showed that the separated GO flakes were diverse and irregular in shape (Figure 7.2). The lateral dimensions of the GO flakes determined using AFM and SEM images confirmed the successful separation of different GO samples with specific size ranges from 200 nm to >100 μm . The size distribution of the GO sheets obtained from statistical analysis of the AFM and SEM images (examples are shown in Figure 7.2) indicates that the sheet sizes maximum are mostly 0.22, 0.45, 0.7, 2.5, 5, 10, 30, 60, and >100 μm . Cross-sectional profiles from the AFM images (Figure 7.2I) reveal that all the GO sheets have height ranging from 0.7 to 1.1 nm, which is characteristic of a fully exfoliated GO sheet^{165-166,233}. This indicates that most of the separated GO sheets were single layers. SEM images for three different GO-modified electrodes prepared using different sized sheets (0.22, 0.7, >100) indicates different surface morphology (Figure 7.3).

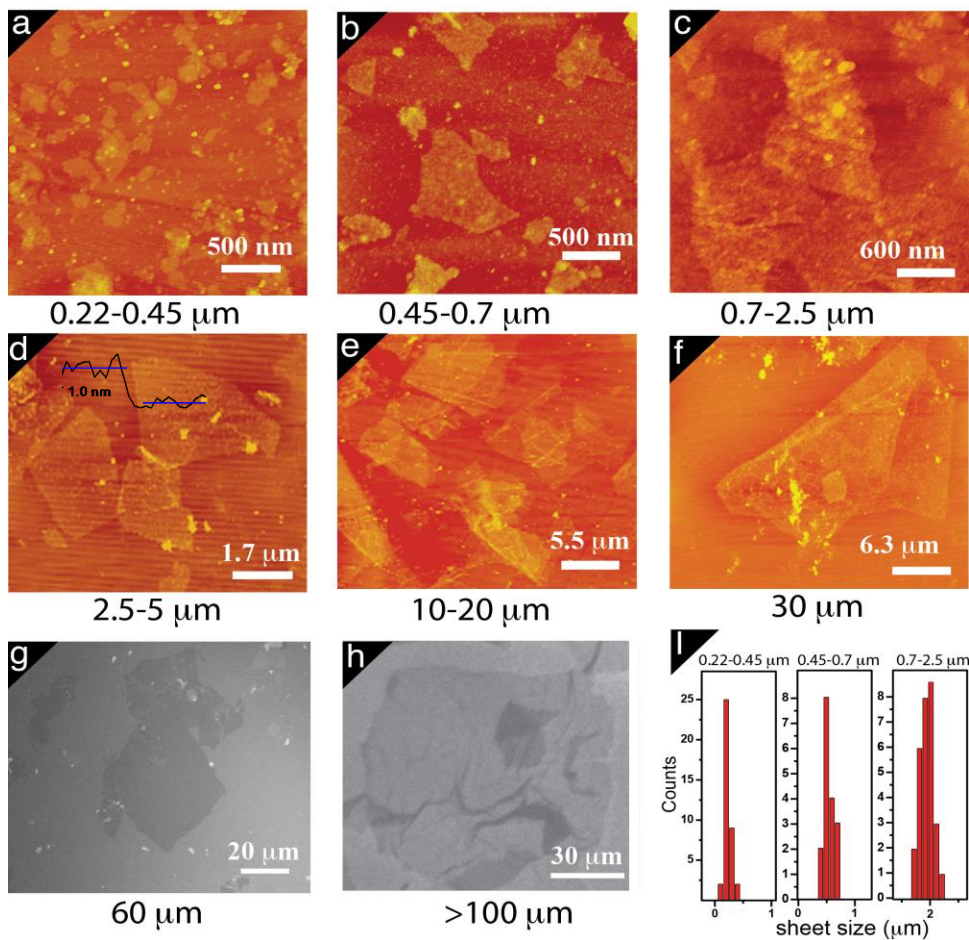


Figure 7.2 AFM and SEM images of the graphene oxide sheets.

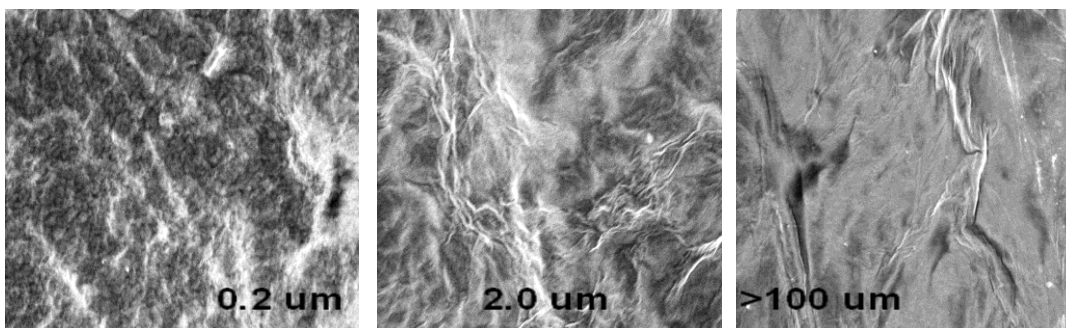


Figure 7.3 Scanning electron micrographs of the GO-modified electrodes (sheet sizes: 0.2, 2.0, 300 μm)

Other structural properties of the GO sheets such as defect density and oxygen functionalities which may affect their electrochemical properties were examined using Raman spectroscopic measurements, XPS and solid state ^{13}C NMR, respectively. As shown in Figure 7.4, the Raman spectra of all GO materials exhibited a G-band at 1580 cm^{-1} and a D band at 1350 cm^{-1} associated with the sp^2 -hybridised carbon vibrations and sp^3 -like defects in the backbone, respectively. The degree of disorder in the carbon structure is usually estimated by the ratio between the D and G band intensities (D/G ratio). The results showed that the D/G ratio of most of the GO samples were close in value. The samples with the smallest lateral sizes (0.22 and $0.45\text{ }\mu\text{m}$) exhibited the highest D/G ratios (0.81) which indicates the presence of more defects presumably due to presence of smaller sp^2 domains on the smaller GO sheets. With increasing the GO sheet size the D/G ratio was slightly decreased to 0.79 and 0.77 for the 0.7 and $2.5\text{ }\mu\text{m}$ GO samples, respectively. Then a ratio of 0.75 was obtained for all the larger sheets ($>5\text{ }\mu\text{m}$) suggesting similarity in the average amount of defects for all the large GO samples.

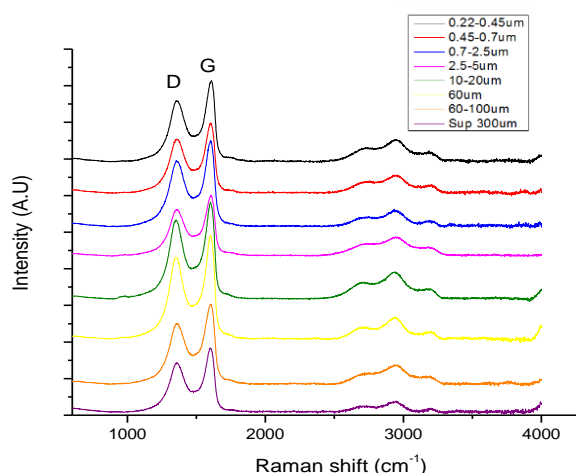


Figure 7.4 Raman spectra of the different GO samples.

XPS was then used to characterise the oxygen functionalities of the GO samples. We did not rely on the C/O ratio for the estimation of the relative degree of oxidation of the different samples because it is hard to fully dehydrate GO ²³⁴. Therefore, the ratios of the total peak area of all oxidised carbon divided by total C1s spectral area ($P_{\text{GO}}/P_{\text{G}}$) were compared for all samples ²³⁵. As shown in Figure 7.5A, each C1s spectrum was deconvoluted into four peaks at binding energies of 284.5 , 286.5 , 288.0 and 289.0 eV corresponds to $\text{sp}^2\text{ C}=\text{C}$, hydroxyl/epoxide C–O,

carbonyl C=O, carboxylic O-C=O, respectively. It can be seen that the peaks for the various carbon–oxygen functional groups diminish from smaller sized GO samples (0.22 μm) to the larger sized sheets (>100 μm). A plot of the $P_{\text{GO}}/P_{\text{G}}$ ratio versus GO sheet size (Figure 7.5B) shows a gradual decrease in the degree of oxidation with increasing sheet size.

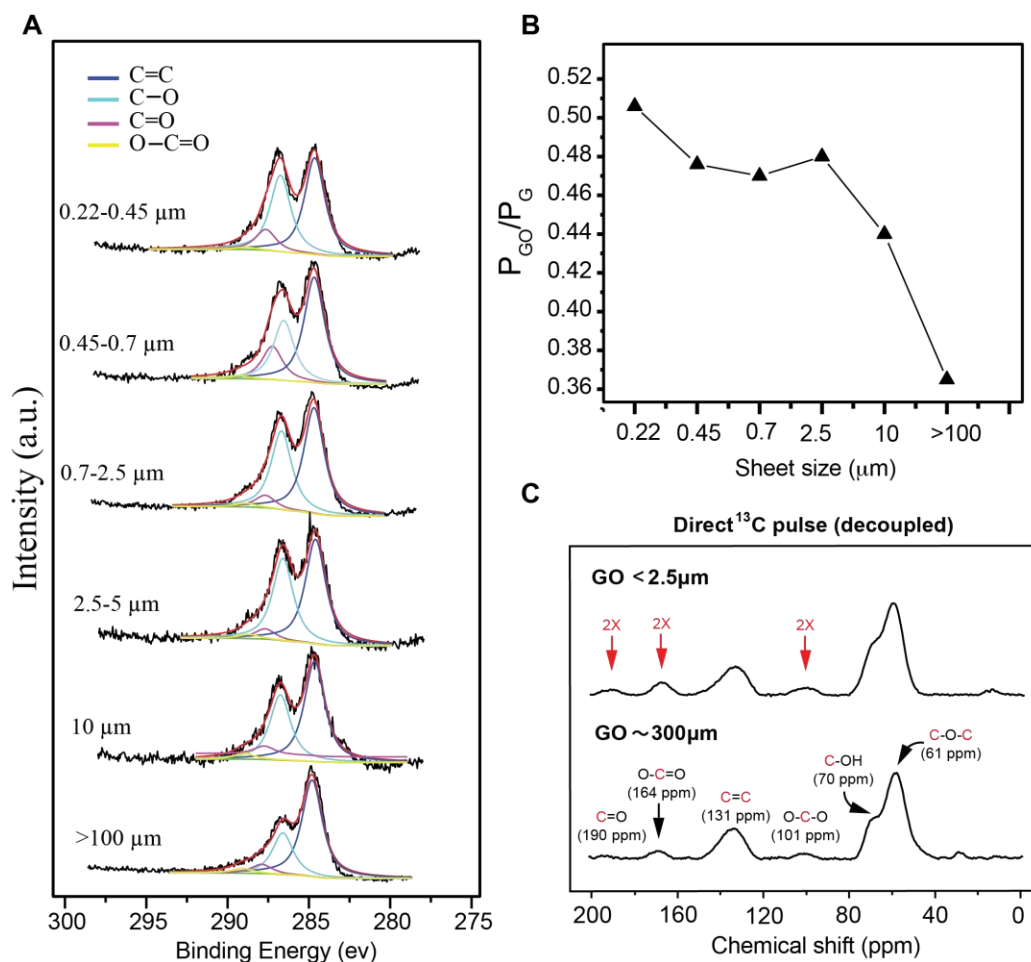


Figure 7.5(A) XPS C 1s spectra of different sized graphene oxide sheets, (B) a plot of $P_{\text{GO}}/P_{\text{G}}$ versus the size of GO sheet and (C) ^{13}C NMR spectra for the smallest (0.22 μm) and largest (>100 μm) GO sheets.

In order to confirm these results, we performed high-resolution SSNMR ^{13}C analysis for the smallest (0.22 μm) and the largest (>100 μm) sized GO sheets. Figure 2C shows SSNMR ^{13}C spectra of two samples. Three major peaks located at 61, 70, 131 ppm were observed in the SS NMR spectra and assigned to epoxide ^{13}C , $^{13}\text{C-OH}$ and sp^2 ^{13}C , respectively as previously reported by Ruoff et al.²³⁶ Well-resolved minor peaks were also observed at 101, 164, and 190 ppm, which are attributed to the O-C-O, O-C=O and C=O, respectively²³⁷. A thorough analysis for Figure 7.5C shows clearly that the degree of oxidation for the smallest sized sheets sample is higher than the largest GO sheets. Particularly, for the smallest sized sheets, the integration of the peaks at 101, 164, and 190 ppm is almost double than those observed in the largest sized sheets. This data confirms that samples with the smaller sheets have more carboxylic groups than that of the larger sheets.

7.2 Electrochemical biosensing performance of the various sheet sizes

After characterization of GO samples, we proceeded to systematically investigate their electrochemical biosensing performance. For that, we studied two representative label-free biosensors –an immunosensor directed against the milk protein β -LG and a DNA aptasensor directed against the small molecule MC-LR toxin. The immunosensor is comprised of a polyclonal antibody against β -LG and the aptasensor involves a 60 nucleotides DNA aptamer sequence that binds specifically to MC-LR showing a K_d of 50 nM¹⁸⁶. The two platforms were fabricated as shown in the scheme (Figure 7.6) by attaching the aptamer or the antibody onto the GO-DEP electrodes employing either physical adsorption (Apt/Phys, Imm/Phys) or covalent attachment immobilization protocol (Apt/Cov, Imm/Phys).

We employed here square wave voltammetry for the electrochemical measurements in the presence of the $[\text{Fe}(\text{CN})_6]^{3-/4-}$ redox couple. The SWV characterisation of the different experimental steps for the biosensors are shown in Figure 7.7. Figure 7.7A shows the SWV of the aptasensor fabricated using physical adsorption (Apt/Phys) via the π - π stacking interactions between the graphene hexagonal cells and the nucleobases of the DNA. Figure 7.7B shows the SWV of the aptasensor fabricated using covalent attachment of the NH_2 -MCAP to the carboxylic groups on the graphene surface via EDC/NHS chemistry (Apt/Cov). The SWV of $[\text{Fe}(\text{CN})_6]^{3-/4-}$

reduction on the bare GO-DEP electrodes is characterized by a well-defined cathodic peak (black lines).

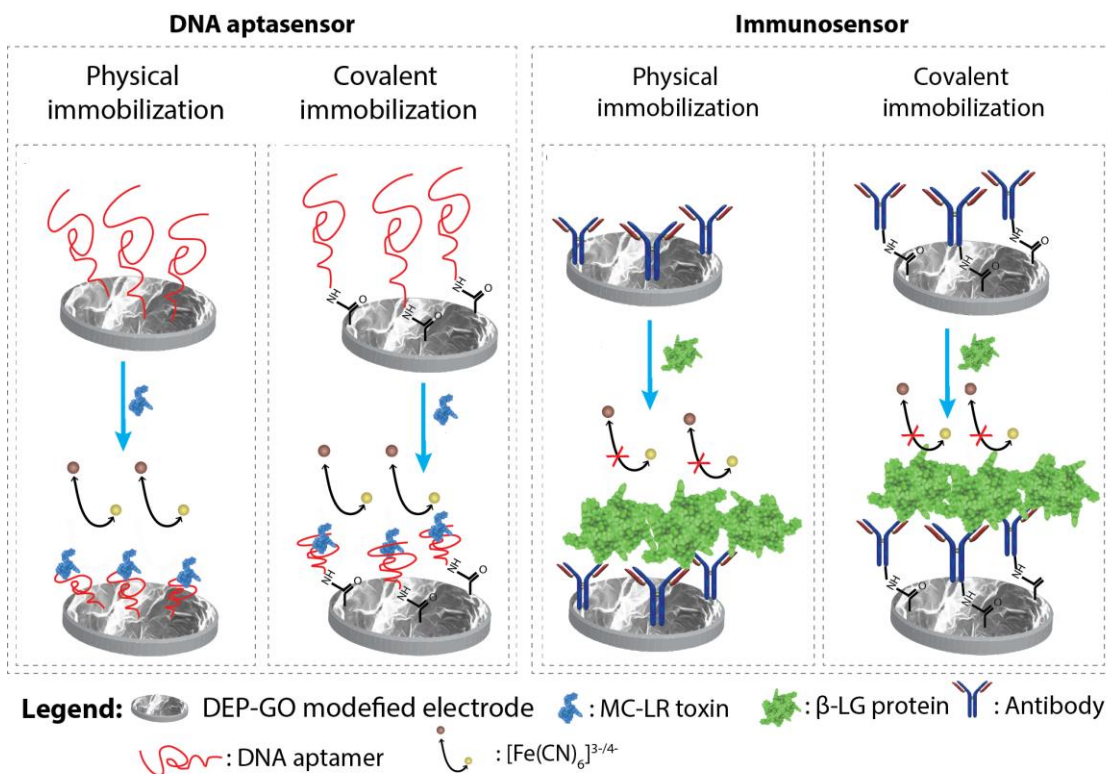


Figure 7.6 Schematic diagrams of the four different biosensing platforms

This intensity of the reduction peak was decreased upon the immobilization of the aptamer on the GO electrodes due to the shielding of the GO surface by the immobilized aptamers as well as by the electrostatic repulsion between the negatively charged phosphate backbone of the DNA aptamer and the $[\text{Fe}(\text{CN})_6]^{3-/4-}$ anions (Figures 7.7A and 7.7B, red lines). However, upon MC-LR binding, the $[\text{Fe}(\text{CN})_6]^{3-/4-}$ reduction peak current increased (Figures 7.7A and 7.7B, blue lines). This indicates an enhancement in electron transfer efficiency between the $[\text{Fe}(\text{CN})_6]^{3-/4-}$ redox probe and the GO electrode which is presumably attributed to the target induced conformation change within the aptamer as previously reported²²⁹. On the other hand, for the immunosensors (Imm/Phys, Imm/Cov) as shown in Figure 7.7C and 7.7D, a decrease in the $[\text{Fe}(\text{CN})_6]^{3-/4-}$ reduction peak was observed after the β-LG antibody immobilization on the GO electrode due to the blocking effect of this bulky protein (red lines). Upon β-LG binding, a further decrease in the

peak current was observed (blue lines) as a result of the additional steric hindrance induced by the bound β -LG molecules. Moreover, the negative charge of the β -LG molecules at pH 7.4¹⁵⁶ acts as electrostatic barrier for the electron transfer which also contributes to the decrease in the current. Thus, the change in the electron transfer efficiency of the $[\text{Fe}(\text{CN})_6]^{3-/4-}$ redox probe upon target binding which results in either increase (aptasensors) or decrease (immunosensors) in the reduction peak current represent the basis of the electrochemical sensing.

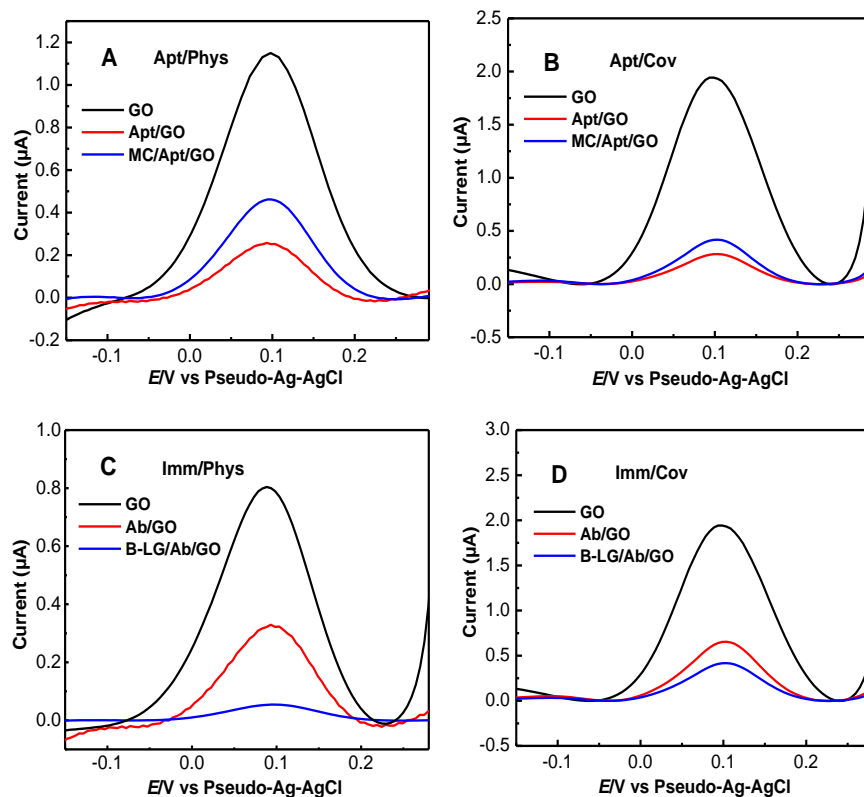


Figure 7.7 SWVs of the aptasensor fabricated using physical adsorption (A) and covalent immobilization (B) for bare GO-DEP electrodes (black), MC-LR aptamer-functionalized electrodes (red), and after MC-LR toxin incubation (blue) (concentration of the aptamer, 10 μM ; concentration of MC-LR, 1 nM); SWVs of the immunosensors fabricated using physical adsorption (C) and covalent immobilization (D) for bare GO-DEP electrodes (black), β -LG antibody-functionalized electrodes (red), and after β -LG incubation (blue) (concentration of the antibody, 10 $\mu\text{g/ml}$; concentration of β -LG, 1 $\mu\text{g/ml}$). All measurements were done in 1 mM $[\text{Fe}(\text{CN})_6]^{4-/3-}$ probe in PBS, pH 7.4.

First, MC aptamer and β -LG antibody concentrations were optimized in each case to establish the optimum amount to be used for the aptasensors and immunosensors fabrication. As shown in Figure 7.8A-D, SWV peak current variations ($(i_0 - i) / i_0\%$, where i_0 is the peak current of the bare GO electrodes and i is the peak current after bioreceptor immobilization) obtained from the experiments at different aptamer and antibody concentrations were analyzed and depicted in the form of histograms for the four cases. The experiments were performed using both small and large GO sheets (0.22 and $>100 \mu\text{m}$) for comparison. In all cases, we observed an increase in the current variation with increasing the amount of aptamer or antibody used for immobilization due to the increased shielding of the GO surface by the probes. It can be concluded that the optimum amount of aptamer and antibody to be immobilized onto the GO electrodes to ensure maximum surface coverage are $10 \mu\text{g/ml}$ and $10 \mu\text{M}$, respectively.

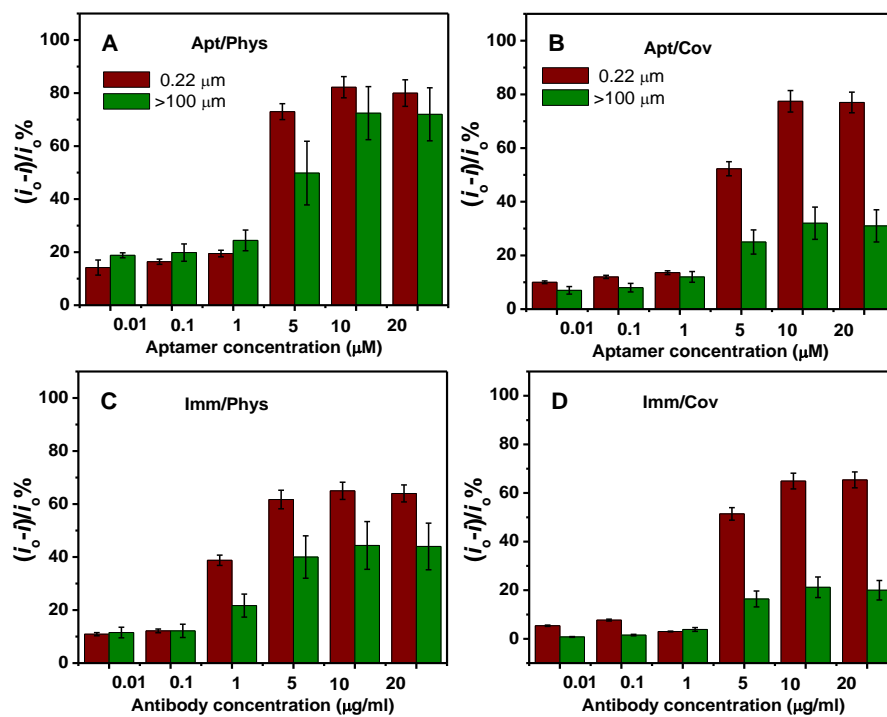


Figure 7.8 Comparison of the change in the SWV peak current towards the various amounts of A) MCAP, B) NH₂-MCAP, C) β -LG antibody and D) covalently immobilized β -LG antibody deposited onto graphene oxide modified DEP electrode surface. Signal is represented as $(i_0 - i) / i_0\%$. Red columns represent the smallest GO sized sheets and green columns represent the largest GO sized sheets. Error bars correspond to duplicate measurements. All measurements were performed with $10 \text{ mM } [\text{Fe}(\text{CN})_6]^{4-/3-}$ in PBS buffer, pH 7.4 at room temperature.

Despite that a similar trend was seen for all cases, a higher current variation was obtained for the aptasensors. This is likely due to the difference in the electric charge between the aptamer and antibody. While the negative charge of the aptamer causes an electrostatic repulsion with the redox probe enhancing the decrease in the current, the positive charge of the antibody may attract the redox probe causing less signal change. Moreover, the influence of the change in the GO sheet size on the signal was more pronounced on the biosensors prepared by covalent immobilization than on the physical adsorption biosensors. We believe that such difference is induced by the difference in the amount of carboxylic groups that are used for the covalent immobilization of the probe. Therefore, the smaller sized GO electrodes has shown more signal variation because of the presence of more edges on their surfaces that contains higher number of carboxylic groups, as confirmed by both the XPS and SS NMR data above (Figure 7.5), which in turn leads to an increase in the number of immobilized probes.

The figure of merit of the developed biosensors is the signal gain or suppression observed at a given target concentration. For better comparison of the experiments, the signal is expressed as the relative increase (aptasensor, $(i_{\text{target}} - i_{\text{aptamer}}) / i_{\text{aptamer}}\%$ $((i_p - i) / i\%)$) or decrease (immunosensor, $(i_{\text{Ab}} - i_{\text{target}}) / i_{\text{Ab}}\%$ $((i - i_p) / i\%)$) in peak current upon addition of target from the original signal observed in the absence of target. We thus now focus on the effect of varying GO sheet size on this measure for the four studied biosensing cases at the optimized probes concentrations. In general, improved biosensor response signal can be obtained through changes in the immobilized bioreceptor binding efficiency or through changes in the electron transfer efficiency of the redox probe to the GO surface. For example, the signal gain of the MC-LR aptasensors will increase if electron transfer from the redox probe to the GO surface after target binding is enhanced or if the fraction of the aptamers/target complex increased. However, an increase of the signal suppression of the β -LG immunosensor will occur if the electron transfer was more retarded after analyte binding or if the fraction of bound antibody on the GO surface increased.

It can be clearly seen from the histograms, Figure 7.9, that the biosensors response signal is a strong function of the GO sheet size. As shown in Figure 7.9A (Apt/Phys), the smallest size GO gives the lowest signal. With increasing the size of the GO sheet, we observed gradual increase in the aptasensor response. However, the opposite trend is observed for the Apt/Cov (Figure 7.9B) where the smallest sized-GO sheets show the highest signals and the signal

decreases with increasing the sheet size with almost comparable signals obtained for the larger sizes (>2.5 μm). This signal enhancement in the Apt/Phys case at larger GO sheet size seems to be associated with the increased efficiency of the electron transfer on the larger sheets that showed less degree of oxidation as confirmed by the XPS and NMR results. The enhancement in electron transfer efficiency of the $[\text{Fe}(\text{CN})_6]^{4-/3-}$ redox couple with decreasing the oxygen content on the graphene electrodes has been reported previously¹⁶⁰. This is attributed to the less electrostatic repulsion between less oxidized graphene and the negatively charged $[\text{Fe}(\text{CN})_6]^{4-/3-}$. In contrast, for the Apt/Cov case, the covalent immobilization of the aptamers on the graphene via the carboxylic groups located on the graphene edges leads to higher amount of immobilized probes on the small-sized GO platforms (Figure 7.8B) and therefore, more binding signal (Figure 7.9B). The crowding of the aptamer on the small-sized GO surface may lead to hindrance of target accessibility²¹⁹, an effect that might be expected to reduce the sensor gain. However, this steric hindrance effect was not pronounced in this case presumably due to the small size of MC-LR molecule, in addition to the folding of the aptamer occurring upon binding.

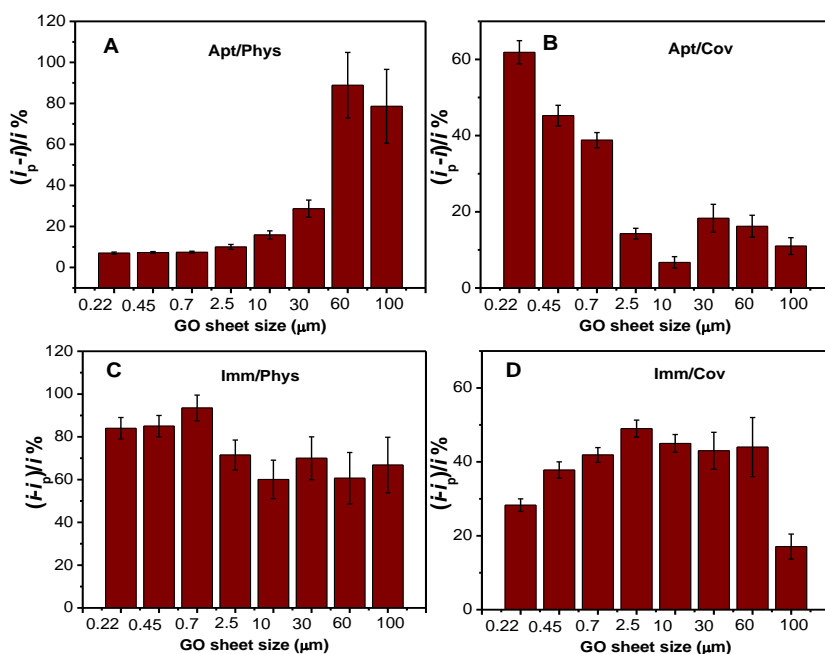


Figure 7.9 Comparison of change in SWV peak current of the different GO sized-sheets electrodes after the incubation with MC-LR (1 nM) or β -LG (1 $\mu\text{g}/\text{ml}$) for the four different cases. Binding signal response represented as $(i_p - i)/i\%$ for the aptasensors fabricated by physical adsorption (A), and covalent immobilization (B) and as $(i - i_p)/i\%$ for the immunosensors fabricated by physical adsorption (C), and covalent immobilization (D).

However, for the Imm/Phys, as shown in Figure 7.9C, the optimal signaling (93%) is obtained at intermediate GO sheet size (0.7 μm), with signaling decreasing at both smaller and larger sheet sizes. For the Imm/Cov, as shown in Figure 5D, optimal signaling (50%) is obtained also at intermediate GO sheet size (2.5 μm). This may arise from two competing factors: while smaller sized GO sheets allow the immobilization of more antibodies (Figure 7.8C and D), which in turn may lead to reduction in the affinity of some antibodies due to crowding, larger-sized GO may reduce the signal suppression due to the higher electron transfer efficiency of $[\text{Fe}(\text{CN})_6]^{4-/3-}$ on the large sheets. These results indicate that proper match between the GO sheet size, the immobilization protocol of the probe, and target size has to be taken into consideration when designing a biosensor in order to obtain the best performance.

7.3 Selectivity of the biosensors

The extent to which GO sheet size changes the response signal of the studied biosensors raises the parallel question whether the selectivity of biosensors is also sensitive to this parameter. To answer this question, the selectivity of the four biosensors were studied at the smallest (0.22 μm) and the largest (>100 μm) GO sheet sizes. The MC aptasensors (Apt/Phys and Apt/Cov) were incubated with OA and MC-LA as non-specific toxins which have similar molecular weight. The β -LG immunosensors (Imm/Phys and Imm/Cov) were incubated with OVA and BSA as non-specific proteins. Figure 7.10 shows a comparison of the relative change in the peak current for the specific and non-specific targets at the two GO sheet sizes for the four studied cases. For all cases, we observed higher response for the specific analytes against the non-specific analytes. Higher difference between the signal of the specific analytes and the non-specific analytes was obtained with the small-sized GO sheets than the large sheets, particularly for the immunosensors cases. The results indicate good selectivity for the aptasensors prepared by either physical adsorption or covalent immobilization. However, the immunosensors fabricated on the larger sized GO sheets does not display satisfactory selectivity towards β -LG compared to the smaller sheets.

The standard deviations of the signals for the four platforms using the small sized GO sheets were ranging from 5 to 7 % indicating good reproducibility of the sensors. However, the

standard deviations of the signals using the large-sized GO sheets were ranging from 15 to 25 %, suggesting poor reproducibility of these sensors. We attribute this low reproducibility to the inhomogeneity of the large-sized GO sheet samples. Despite producing the highest signal in the Apt/Phys case, the larger GO sheets tends to aggregate due to the low hydrophilicity of these sheets, which in turn leads to inhomogeneous dispersions. It thus appears that the choice of specific GO sheet size for particular biosensing application should represent a compromise between signal gain/suppression and reproducibility.

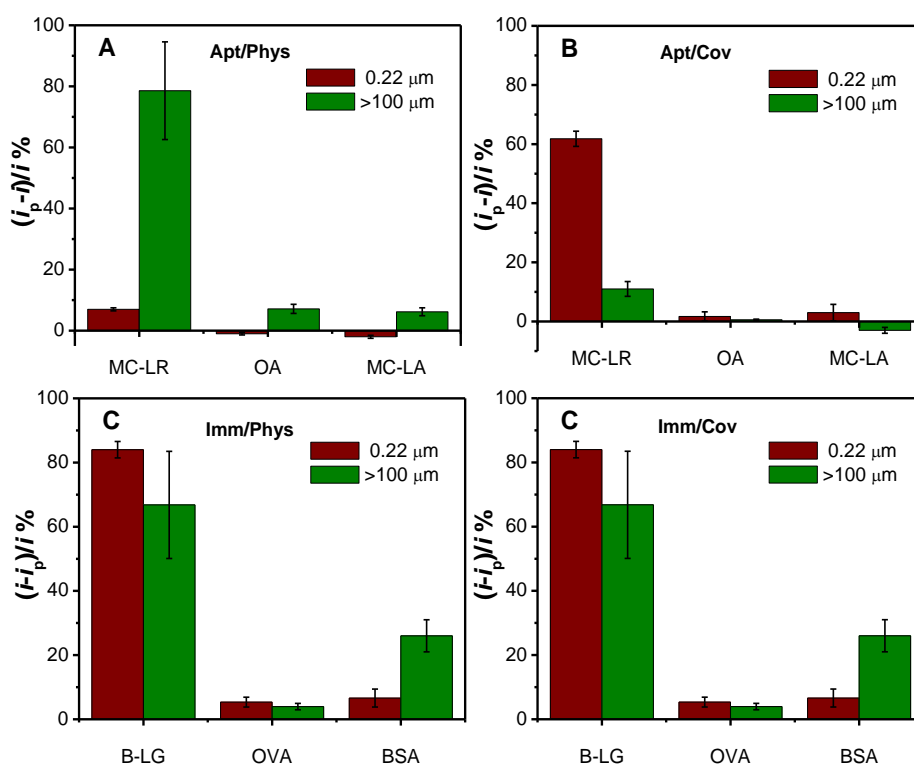


Figure 7.10 Selectivity experiments of the biosensors prepared using smallest GO sized sheets (red columns) and largest GO sized sheets (green columns); response of the aptasensors fabricated using physical adsorption (A) and covalent immobilization (B) to 1.0 nM of MC-LR, OA, and MC-LA; response of the immunosensors fabricated using physical adsorption (C) and covalent immobilization (D) to 1.0 $\mu\text{g}/\text{ml}$ of β -LG, OVA, and BSA.

7.4 Conclusions

In this chapter, graphene oxide suspensions with different sheet sizes have been successfully separated. The morphology and structural properties of these samples were characterized and compared using AFM, SEM, XPS, Raman spectroscopy and NMR. The smallest graphene oxide sheets showed higher defect density and degree of oxidation based on the Raman spectroscopy and XPS results. The biosensing performance of the different GO samples was compared using DNA aptamer against microcystin-LR toxin as well as an antibody against β -lactoglobulin in label-free detection format. We observed different trends between the size of GO sheets and the performance of MC-LR aptasensors and β -LG immunosensors fabricated either using covalent attachment or physical adsorption. Our results have shown strong dependency of the biosensors response signals, selectivity and reproducibility on the GO sheet size.

CHAPTER 8. CONCLUSIONS AND FUTURE PROSPECTIVE

8.1 Conclusions

The potential harmful effect of food contaminants on human health and the subsequent need to detect them have led to significant interest for the development of biosensors for this purpose. Recent advances in nanobiotechnology and its integration in a variety of areas including biosensors results in the development of novel sensing platforms with highly improved performance. New biorecognition elements and nanomaterial-based transduction systems are among those nanobiotechnological concepts that are revolutionising the development of electrochemical biosensors. Therefore, the overall objective of this thesis was to explore the use of graphene platforms as transducers as well as DNA aptamers as recognition receptors in developing novel electrochemical biosensors for some foodborne contaminants, particularly allergens and toxins. In summary, the objectives of this work were realised and the developed biosensors have shown advantages in terms of simplicity, specificity, selectivity, stability, low cost and in some cases shorter analysis times.

In chapter 3, a controlled electrografting method of organic film based on the reduction of diazonium salt on graphene-modified screen printed electrodes was successfully achieved. We showed that by controlling the number of cyclic voltammetry scan used for the electrografting step, we can control the surface coverage of the grafted molecules on the graphene surface. This enabled a simple, fast and versatile platform for the immobilization of antibodies and immunosensors fabrication. The functionalized graphene electrodes by nitrophenyl and carboxyphenyl diazonium salts was used to develop sensitive label-free voltammetric immunosensors for the detection of β -lactoglobulin and ovalbumin, respectively. The differential pulse voltammetric immunosensors developed using this approach offered linear ranges of 0.001–100 ng/mL for β -lactoglobulin and 1.0 pg/ml to 0.5 μ g/ml for OVA without any amplification step. The immunosensors were successfully applied for the detection of β -LG and OVA in food samples and the results were comparable to those of commercial ELISA method. The electrografting method was also applied on CVD graphene. We have investigated for the first time the behaviour of the functionalized monolayer graphene for impedimetric immunosensing of protein. Our results show that carboxyphenyl functionalized CVD monolayer

graphene can be used as a platform for protein biosensing. Thus, the present sensing platform appears to be promising and is expected to pave the way for extended biosensing applications of graphene.

In Chapter 4, we have shown an application of the developed functionalized graphene electrodes in the biosensing of the small molecule toxin OA. The carboxyphenyl modified graphene electrodes were exploited to develop a simple voltammetric immunosensor for the detection of OA. After the immobilisation of OA antibodies using EDC/NHS chemistry, a direct competitive assay was performed based on the competition between free OA and OA-OVA conjugate in the sample for the immobilized antibody. The more OA in the sample, the less OA-OVA binds to the immunosensor. The OA-OVA binding to the immunosensor was then monitored using $[\text{Fe}(\text{CN})_6]^{-3/4}$ redox couple. This approach enabled simpler detection scheme compared to the reported approaches that were based on indirect competitive assays. This method proved to be very simple with good sensitivity and selectivity against other groups of toxins such as MCs. However, cross reactivity of this immunosensor with OA analogues such as DTX1 and DTX2 is expected due to cross reactivity of the used antibody. Finally, the immunosensor was successfully applied for the detection of OA in spiked mussel extracts showing good recovery percentage and has been also validated using certified reference mussel samples.

In Chapter 5, the selection, identification, characterization and biosensing application of DNA aptamers for the marine toxins OA and brevetoxin-2 was shown for the first time. The highest affinity aptamer for OA ($K_d = 77$ nM) showed remarkable sensitivity and selectivity for OA against DTX-1 and DTX-2. We showed that the affinity of the aptamer towards OA was preserved and not affected by surface immobilization. The circular dichroism spectra also demonstrated the conformation change of the aptamer upon OA binding can be exploited in several biosensing applications. Through monitoring of the OA binding-induced conformational change within the aptamer, we achieved a limit of detection of 70 pg/ml with a label-free aptasensor based on EIS. For BTX-2, all the tested aptamers have shown good binding to BTX-2 with dissociation constants in the nanomolar range under the SELEX conditions. The highest affinity aptamer BT10, $K_d = 42$ nM under the optimum binding condition, was applied for the detection of BTX-2 in an electrochemical competitive aptasensor showing remarkable sensitivity compared with other reported approaches. Moreover, the aptasensor showed good selectivity to

BTX-2 against other toxins from different groups such as OA and microcystins. However, high degree of cross reactivity between the two similar analogues BTX-2 and BTX-3 was observed. The simplicity along with the improved stability and lower cost of the proposed aptasensor could facilitate the routine quantification of the two most predominant forms of BTXs: BTX-2 and BTX-3, in shellfish. We believe that the continual emergence of novel library-selected, high-affinity aptamers will open the way to a variety of biosensing architectures, particularly for sensitive and high-specificity small molecule toxin detection in complex samples.

In chapter 6, we have demonstrated an electrochemical aptasensor for the detection of MC-LR by exploiting graphene and the excellent affinity and selectivity of a MC-LR-targeting aptamer. This new approach has led to a rapid, low-cost, sensitive and specific detection method for MC-LR in buffer, spiked tap water and fish extract samples offering several advantages over previously reported methods. First, the aptasensor was fabricated without labelling, minimizing cost and complexity, as well as preserving the affinity of the aptamer to MC-LR. Second, the use of graphene have simplified the detection, particularly when compared with other MC-LR sensors with sophisticated fabrication protocols and detection schemes. Lastly, this SWV graphene-based aptasensor is highly specific to MC-LR, with selectivity against other microcystin congeners hardly achievable by previous attempts. Moreover, we demonstrated in this work that the mechanism of the detection was based on the conformation change in part of the aptamer without its complete release from the graphene surface. We believe that this finding is important for exploiting aptamers in the detection of other small molecules using graphene platforms in the future. In particular, with the continuous development of aptamers targeting other microcystin congeners and related toxins, we envisage a high-throughput, multiplexed and sensitive detection platform suitable for routine analysis of water samples.

For using graphene as electrode material, bulk quantities are needed which are usually synthesized by oxidation of graphite to graphite oxide and subsequent exfoliation to graphene oxide. However, during reaction and processing at various conditions, the size of the resultant GO sheets changes from the parent graphitic material yielding a polydispersed solution of sizes ranging from a few nanometers to tens of micrometers. In chapter 7, we investigated to which extent the size of GO sheets influence their structural properties and therefore, their biosensing performance. First, we have successfully separated GO sheets with different sizes in the range of 0.22, 0.45, 0.7, 2.5, 10, 30, 60, and 100 μm . The GO sheets were characterized via atomic force

microscopy, scanning electron microscopy, Raman spectroscopy, X-ray photoelectron spectroscopy and solid state NMR. The smallest graphene oxide sheets showed higher defect density and degree of oxidation based on the Raman spectroscopy and XPS results. The biosensing performance of these samples was compared using DNA aptamer against microcystin-LR toxin as well as an antibody against β -lactoglobulin in label-free detection format. We observed different trends between the size of GO sheets and the performance of MC-LR aptasensors and β -LG immunosensors fabricated either using covalent attachment or physical adsorption. We found that the smallest GO sheet size electrodes showed more immobilized receptors than the larger sheets. The influence of the GO sheet size on the amount of immobilized bioreceptor was more pronounced in the biosensors prepared by covalent immobilization than the physical adsorption biosensors. For the aptasensor fabricated using physical adsorption, with increasing the GO sheet size, the binding signal variation was dramatically increased from 7.0 to 78 %, with maximum signal observed near the largest sheet size. In contrast, for the aptasensor fabricated using covalent immobilization, the binding signal variation decreased with increasing GO sheet size from 61 to 11 %. However, the signal change of β -LG immunosensors varies from 84% to 76% and 30 to 17% for the physically adsorbed and covalently immobilized sensors, respectively and optimum signals were observed at intermediate GO sheet size. Our results demonstrate that controlling the size of GO sheets may have a profound impact on their use in specific biosensing applications.

8.2 Final remarks and Future perspectives

Overall, this thesis contributed to the improvement of electrochemical biosensors for some foodborne contaminants by introducing novel recognition receptors (aptamers) and nanomaterial (graphene). The incorporation of such nanobiotechnological improvements has enabled the development of novel high performance biosensing platforms for the detection of some allergenic proteins and small molecule toxins. First, the functionalization of graphene electrodes have been successfully demonstrated using a simple electrografting methodology which enabled the fabrication of different immunosensors. This methodology can be expanded to detect other analytes in the future. It will be necessary to study other functionalization methods and compare their efficiency and long-term stability in order to improve their application in biosensors. The

effect of graphene oxide sheet size on the biosensor performance has been also studied. It will be also important for the next step to investigate in detail the effect of the graphene preparation method on their structural properties as well as their biosensing behaviour. Several research studies have shown that the graphene materials prepared using different approaches exhibit significantly different thickness, oxygen content and defect density. This in turn dramatically influences the electrochemical properties of these materials. Thus, the comparison of the biosensing performance of different graphene materials in several biosensing systems may help in better identifying the best material for specific biosensing application.

Second, my efforts for selecting and identifying new aptamers against OA and BTX-2 have met great success. However, it will be necessary to study these aptamers in depth, for example, by studying their secondary structures in order to gain control over their properties.

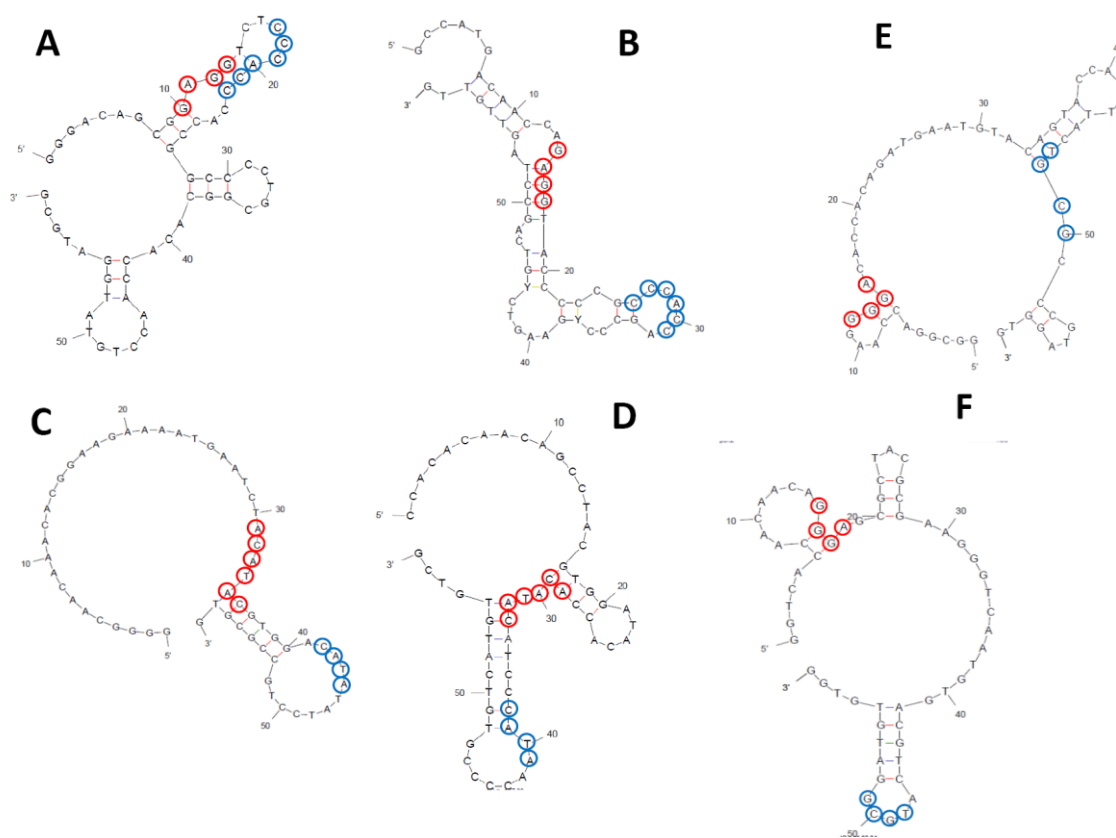


Figure 8.1 Schematic representation of the secondary structures of the aptamers which exhibited good binding to okadaic acid as predicted by the mfold program. (A) OA 11, (B) OA 32, (C) OA 21, (D) OA 22, (E) OA 24, and (F) OA 34.

Previous studies on other aptamers have shown that a small fraction of the aptamer sequence is usually involved in binding with the target. Identifying the part of the sequence that is critical for target binding and minimizing the size of the aptamer have shown great improvement in affinity of the aptamers. For instance, Le *et al.*²³⁸ have reported and enhanced affinity by an order of magnitude for the 39-nucleotides truncated aptamer than an originally selected 77-nucleotides aptamer. They attribute this higher affinity to the loss of intramolecular hydrogen bonds. Therefore, it would be very useful to study several different truncation series of our originally selected 60- nucleotides aptamers to ascertain which part among the full aptamer sequence was essential for the target binding and probe the relationship between sequence and affinity.

Finally, the successful identification of new specific aptamers against various food target such as allergenic proteins, pesticides or toxins and their integration into electrode arrays will facilitate the expansion of the developed detection platforms to include multiple targets. These detection electrode arrays can be also integrated with lab-on-a-chip chambers for sample processing and analyte fishing prior to analysis. An integrated system will have an enormous potential to concentrate and enhance analytes from complex food samples. This integration will improve the detection limit and shorten the analysis time, while minimizing non-specific adsorption.

We have recently reported²³⁹ the design and fabrication of magnetically assisted multianalyte sensing platform comprising magnetic micro-coils to trap magnetic beads on the surface of sensing electrodes; integrated sensing electrode array for multianalyte sensing; and the additional micro-coils for removing the unbounded magnetic beads from the sensing electrodes' surfaces. Prototype device was designed and successfully fabricated by Dr. Irina Stateikina using customized fabrication flow. I have done the testing of the sensing electrodes in order to prove the successful implementation of magnetically assisted manipulation of micro-beads. The results of these tests clearly indicated electro-addressing process on individual electrodes without cross talk thus enabling this device application for multianalyte biosensing in the future. The multiplex detection technology will be an economically attractive choice for food contaminants monitoring. Once implemented, these miniaturized biosensing devices will have a high potential to become the next generation industry standards.

CHAPTER 9. REFERENCES

- 1 Diaz-Amigo, C. Towards a Comprehensive Validation of ELISA Kits for Food Allergens: Case 1—Egg. *Food Anal. Methods* **3**, 344–350 (2010).
- 2 Bánáti, D. The EU and candidate countries: How to cope with food safety policies? *Food Control* **14**, 89-93 (2003).
- 3 Hohensinner, V., Maier, I. & Pittner, F. A ‘gold cluster-linked immunosorbent assay’: Optical near-field biosensor chip for the detection of allergenic β -lactoglobulin in processed milk matrices. *Journal of Biotechnology* **130**, 385–388 (2007).
- 4 Maier, I., Morgan, M. R. A., Lindner, W. & Pittner, F. Optical Resonance-Enhanced Absorption-Based Near-Field ImmunoChip Biosensor for Allergen Detection. *Analytical Chemistry* **80**, 2694-2703 (2008).
- 5 Cianferoni, A. & Spergel, J. M. Food Allergy: Review, Classification and Diagnosis. *Allergology International* **58**, 457-466 (2009).
- 6 Sicherer, S. H. & Sampson, H. A. Food Allergy: Recent Advances in Pathophysiology and Treatment. *Annual Review of Medicine* **60**, 261-277 (2009).
- 7 Roehr, C. C. *et al.* Food allergy and non-allergic food hypersensitivity in children and adolescents. *Clinical & Experimental Allergy* **34**, 1534-1541 (2004).
- 8 Sampson, H. A. *et al.* Symposium on the Definition and Management of Anaphylaxis: Summary report. *Journal of Allergy and Clinical Immunology* **115**, 584-591 (2005).
- 9 Ross, M. P. *et al.* Analysis of food-allergic and anaphylactic events in the National Electronic Injury Surveillance System. *Journal of Allergy and Clinical Immunology* **121**, 166-171 (2008).
- 10 Liew, W. K., Williamson, E. & Tang, M. L. K. Anaphylaxis fatalities and admissions in Australia. *Journal of Allergy and Clinical Immunology* **123**, 434-442 (2009).

- 11 Taylor, S., Nordlee, J., Niemann, L. & Lambrecht, D. Allergen immunoassays—considerations for use of naturally incurred standards. *Anal Bioanal Chem* **395**, 83-92, (2009).
- 12 Ng, T. W., Holt, P. G. & Prescott, S. L. Cellular immune responses to ovalbumin and house dust mite in egg-allergic children. *Allergy: European Journal of Allergy and Clinical Immunology* **57**, 207-214 (2002).
- 13 Caubet, J. C. & Wang, J. Current Understanding of Egg Allergy. *Pediatric Clinics of North America* **58**, 427-443 (2011).
- 14 Heine, R. G., Laske, N. & Hill, D. J. The diagnosis and management of egg allergy. *Current Allergy and Asthma Reports* **6**, 145-152 (2006).
- 15 Mine, Y. & Yang, M. Recent advances in the understanding of egg allergens: Basic, industrial, and clinical perspectives. *Journal of Agricultural and Food Chemistry* **56**, 4874-4900 (2008).
- 16 Anet, J. *et al.* Allergens in the white and yolk of hen's egg. A study of IgE binding by egg proteins. *Int. Arch. Allergy Appl. Immunol.* **77**, 364 (1985).
- 17 Bernhisel-Broadbent, J., Dintzis, H. M., Dintzis, R. Z. & Sampson, H. A. Allergenicity and antigenicity of chicken egg ovomucoid (Gal d III) compared with ovalbumin (Gal d I) in children with egg allergy and in mice. *J. Allergy Clin. Immunol.* **93**, 1047 –1059 (1994).
- 18 Host, A. & Halken, S. A prospective study of cow milk allergy in Danish infants during the first 3 years of life. *Allergy* **45** 587–596 (1990).
- 19 Host, A. Frequency of cow's milk allergy in childhood. *Ann Allergy Asthma Immunol* **89** 33–37 (2002).
- 20 LA, L. & AW, B. Food allergies: prevalence, molecular characterization, and treatment/prevention strategies. *Annu Rev Nutr* **26**, 539–565 (2006).
- 21 Steidinger, K. A. *Algal Toxins in Seafood and Drinking Water.* 1–28 (Academic Press, 1993).

- 22 Morton, S. L. & Tindall, D. R. Determination of OA content of dinoflagellate cells: a comparison of the HPLC-fluorescent method and two monoclonal antibody elisa test kits. *Toxicon* **34**, 947–954 (1996).
- 23 Dounay, A. B. & Forsyth, C. J. Okadaic acid: the archetypal serine/threonine protein phosphatase inhibitor. *Curr. Med. Chem.* **9**, 1939–1980 (2002).
- 24 Mestrovic, V. & Pavela Vrancic, A. Inhibition of alkaline phosphatase activity by okadaic acid, a protein phosphatase inhibitor. *Biochimie* **85**, 647–650 (2003).
- 25 Suganuma, M. *et al.* Okadaic acid: an additional non-phorbol-12-tetradecanoate-13-acetate-type tumor promoter. *Proc. Natl. Acad. Sci. U.S.A.* **85**, 1768–1773 (1988).
- 26 Flewelling, L. J. *et al.* Brevetoxicosis: Red tides and marine mammal mortalities. *Nature* **435**, 755–756 (2005).
- 27 Landsberg, J. H. The Effects of Harmful Algal Blooms on Aquatic Organisms. *Reviews in Fisheries Science* **10**, 113–390 (2002).
- 28 Baden, D. G., Bourdelais, A. J., Jacocks, H., Michelliza, S. & Naar, J. Natural and Derivative Brevetoxins: Historical Background, Multiplicity, and Effects. *Environ Health Perspect.* **113**, 621–625 (2005).
- 29 Kull, T. P. J., Backlund, P. H., Karlsson, K. M. & Meriluoto, J. A. O. Oxidation of the cyanobacterial hepatotoxin microcystin-LR by chlorine dioxide: Reaction kinetics, characterization, and toxicity of reaction products. *Environ. Sci. Technol.* **38** 6025–6031 (2004).
- 30 Carmichael, W. W. Cyanobacteria secondary metabolites--the cyanotoxins. *J. Appl. Bacteriol.* **72**, 445–459 (1992).
- 31 Poste, A. E., Hecky, R. E. & Guildford, S. J. Evaluating Microcystin Exposure Risk through Fish Consumption. *Environmental Science & Technology* **45**, 5806–5811 (2011).
- 32 Nishiwaki-Matsushima, R. *et al.* Liver tumor promotion by the cyanobacterial cyclic peptide toxin microcystin-LR. *J. Cancer Res. Clin.* **118**, 420–424 (1992).
- 33 Magalhães, V. F. *et al.* Microcystins (cyanobacteria hepatotoxins) bioaccumulation in fish and crustaceans from Sepetiba Bay (Brasil, RJ). *Toxicon* **42**, 289–295 (2003).

- 34 MacKintosh, C., Beattie, K. A., Klumpp, S., Cohen, P. & Codd, G. A. Cyanobacterial microcystin-LR is a potent and specific inhibitor of protein phosphatases 1 and 2A from both mammals and higher plants. *FEBS Lett.* **264**, 187–192 (1990).
- 35 Dawson, R. M. The toxicology of microcystins. **36**, 953–962 (1998).
- 36 Liu, M., Zhao, H., Chen, S., Yu, H. & Quan, X. Colloidal Graphene as a Transducer in Homogeneous Fluorescence-Based Immunosensor for Rapid and Sensitive Analysis of Microcystin-LR. *Environmental Science & Technology* **46**, 12567-12574 (2012).
- 37 Gupta, N., Pant, S. C., Vijayaraghavan, R. & Rao, P. V. L. Comparative toxicity evaluation of cyanobacterial cyclic peptide toxin microcystin variants (LR, RR, YR) in mice. *Toxicology* **188** 285–296 (2003).
- 38 WHO. Guidelines for Drinking-Water Quality, 2nd ed.; addendum to Vol. 2, Health Criteria and Other Supporting Information; World Health Organization: Geneva, Switzerland, 1998.
- 39 Luis, R. d., Lavilla, M., Sánchez, L., Calvo, M. & Pérez, M. D. Development and evaluation of two ELISA formats for the detection of b-lactoglobulin in model processed and commercial foods. *Food Control* **20** 643–647 (2009).
- 40 Rena, Y. *et al.* Simultaneous determination of bovine alpha-lactalbumin and beta lactoglobulin in infant formulae by ultra-high-performance liquid chromatography-mass spectrometry. *Analytica Chimica Acta* **667** 96–102 (2010).
- 41 Janssen, F. W., Voortman, G. & Baaij, J. Detection of wheat gluten, whey protein, casein, ovalbumin, and soy protein in heated meat products by electrophoresis, blotting, and immunoperoxidase staining. *Journal of Agricultural and Food Chemistry* **35**, 563-567 (1987).
- 42 Besler, M., Steinhart, H. & Paschke, A. Immunological characterization of egg white allergens collected by capillary electrophoresis. *Food and Agricultural Immunology* **10**, 157-160 (1998).
- 43 Pelaez-Lorenzo, C., Diez-Masaa, J. C., Vasallo, I. & Frutosa, M. d. A new sample preparation method compatible with capillary electrophoresis and laser-induced

- fluorescence for improving detection of low levels of β -lactoglobulin in infant foods. *Analytica Chimica Acta* **649**, 202–210 (2009).
- 44 Puerta, A., Diez-Masa, J. C. & Frutos, M. d. Development of an immunochromatographic method to determine β -lactoglobulin at trace levels. *Analytica Chimica Acta* **537**, 69–80 (2005).
- 45 Romero-Rodríguez, M. A., Barcia-Vieitez, R. & Vázquez-Odériz, M. L. An immunochemical technique for the detection of ovalbumin in surimi-derived products. *Journal of the Science of Food and Agriculture* **82**, 1614-1616 (2002).
- 46 Kobori, T., Matsumoto, A., Takahashi, H. & Sugiyama, S. Rolling circle amplification for signal enhancement in ovalbumin detection. *Analytical Sciences* **25**, 1381-1383 (2009).
- 47 Kreuzer, M. P., Pravda, M., O'Sullivan, C. K. & Guilbault, G. G. Novel electrochemical immunosensors for seafood toxin analysis. *Toxicon* **40**, 1267-1274 (2002).
- 48 (APHA (American Public Health Association). Recommended procedures for the examination of sea water and shellfish, Fourth Edition, 61-66 (1970).
- 49 Shon, D. H., Kim, H. J., Kim, S. H. & Kwak, B. Y. Enzyme-linked immunosorbent assay for the detection of hen's egg proteins in processed foods. *Korean Journal for Food Science of Animal Resources* **30**, 36-41 (2010).
- 50 Fæste, C. K., Løvberg, K. E., Lindvik, H. & Egaas, E. Extractability, stability, and allergenicity of egg white proteins in differently heat-processed foods. *Journal of AOAC International* **90**, 427-436 (2007).
- 51 Akiyama, H. *et al.* Inter-laboratory Evaluation Studies of Notified ELISA Methods for Allergic Substances (Egg). *Journal of the Food Hygienic Society of Japan* **44**, 213-219 (2003).
- 52 Watanabe, Y. *et al.* Novel ELISA for the detection of raw and processed egg using extraction buffer containing a surfactant and a reducing agent. *Journal of Immunological Methods* **300**, 115-123 (2005).

- 53 Rolland, J. M., Apostolou, E., De Leon, M. P., Stockley, C. S. & O'Hehir, R. E. Specific and sensitive enzyme-linked immunosorbent assays for analysis of residual allergenic food proteins in commercial bottled wine fined with egg white, milk, and nongrape-derived tannins. *Journal of Agricultural and Food Chemistry* **56**, 349-354 (2008).
- 54 Watanabe, H., Kai, S., Mitani, T., Yokoyama, H. & Kishi, M. Study on detection of allergenic substances (egg and milk) in processed meat products and frozen foods. *Journal of the Food Hygienic Society of Japan* **46**, 139-147 (2005).
- 55 Naar, J. *et al.* A competitive ELISA to detect brevetoxins from *Karenia brevis* (formerly *Gymnodinium breve*) in seawater, shellfish, and mammalian body fluid. *Environmental Health Perspectives*, **110**, 179-185 (2002).
- 56 Zhou, Y. Development of a new monoclonal antibody based direct competitive enzyme-linked immunosorbent assay for detection of brevetoxins in food samples. *Food Chemistry*, **118**, 467-471 (2010).
- 57 Hohensinner, V., Maier, I. & Pittner, F. A 'gold cluster-linked immunosorbent assay': Optical near-field biosensor chip for the detection of allergenic β -lactoglobulin in processed milk matrices. *Journal of Biotechnology* **130**, 385-388 (2007).
- 58 Billakanti, J. M., Fee, C. J., Lane, F. R., Kash, A. S. & Fredericks, R. Simultaneous, quantitative detection of five whey proteins in multiple samples by surface plasmon resonance. *International Dairy Journal* **20**, 96-105 (2010).
- 59 Anraku, Y., Takahashi, Y., Kitano, H. & Hakari, M. Recognition of sugars on surface-bound cap-shaped gold particles modified with a polymer brush. *Colloids and Surfaces B: Biointerfaces* **57**, 61-68 (2007).
- 60 Shriver-Lake, L. C., Taitt, C. R. & Ligler, F. S. Applications of array biosensor for detection of food allergens. *Journal of AOAC International* **87**, 1498-1502 (2004).
- 61 Marquette, C. A., Coulet, P. R. & Blum, L. J. Semi-automated membrane based chemiluminescent immunosensor for flow injection analysis of okadaic acid in mussels. *Analytica Chimica Acta* **398**, 173-182 (1999).

- 62 Prieto-Simón, B., Miyachi, H., Karube, I. & Saiki, H. High-sensitive flow-based kinetic exclusion assay for okadaic acid assessment in shellfish samples. *Biosensors and Bioelectronics* **25**, 1395-1401 (2010).
- 63 Vaughan, R. D., Geary, E., Pravda, M. & Guilbault, G. G. Piezoelectric immunosensors for environmental monitoring. *International Journal of Environmental Analytical Chemistry* **83**, 555-571 (2003).
- 64 Tang, A. X. J., Pravda, M., Guilbault, G. G., Piletsky, S. & Turner, A. P. F. Immunosensor for okadaic acid using quartz crystal microbalance. *Analytica Chimica Acta* **471**, 33-40 (2002).
- 65 Tang, D., Zhang, B., Tang, J., Hou, L. & Chen, G. Displacement-type Quartz Crystal Microbalance Immunosensing Platform for Ultrasensitive Monitoring of Small Molecular Toxins. *Analytical Chemistry* **85**, 6958-6966 (2013).
- 66 Long, F., He, M., Zhu, A. N. & Shi, H. C. Portable optical immunosensor for highly sensitive detection of microcystin-LR in water samples. *Biosens. Bioelectron.* **24**, 2346 (2009).
- 67 Long, F., Shi, H. C., He, M., Sheng, J. W. & Wang, J. F. Sensitive and rapid chemiluminescence enzyme immunoassay for microcystin- LR in water samples. *Anal. Chim. Acta* **649**, 123-127 (2009).
- 68 Lindner, P., Molz, R., Yacoub-George, E. & Wolf, H. Rapid chemiluminescence biosensing of microcystin-LR. *Analytica Chimica Acta* **636**, 218-223 (2009).
- 69 Lindner, P., Molz, R., Yacoub-George, E., Dürkop, A. & Wolf, H. Development of a highly sensitive inhibition immunoassay for microcystin-LR. *Anal. Chim. Acta* **521**, 37-44 (2004).
- 70 Herranz, S., Bocková, M., Marazuela, M. D., Homola, J. & Moreno-Bondi, M. C. An SPR biosensor for the detection of microcystins in drinking water. *Analytical and Bioanalytical Chemistry* **398**, 2625-2634 (2010).
- 71 Ding, Y. & Mutharasan, R. Highly Sensitive and Rapid Detection of Microcystin-LR in Source and Finished Water Samples Using Cantilever Sensors. *Environmental Science & Technology* **45**, 1490-1496 (2010).

- 72 Zhang, F. *et al.* A rapid competitive binding nonseparation electrochemical enzyme immunoassay (NEEIA) test strip for microcystin-LR (MCLR) determination. *Biosensors and Bioelectronics* **22**, 1419-1425 (2007).
- 73 Lotierzo, M., Abuknesha, R., Davis, F. & Tothill, I. E. A Membrane-Based ELISA Assay and Electrochemical Immunosensor for Microcystin-LR in Water Samples. *Environmental Science & Technology* **46**, 5504-5510 (2012).
- 74 Campàs, M. & Marty, J.-L. Highly sensitive amperometric immunosensors for microcystin detection in algae. *Biosensors and Bioelectronics* **22**, 1034-1040 (2007).
- 75 Wang, L. *et al.* Simple, rapid, sensitive, and versatile SWNT-paper sensor for environmental toxin detection competitive with ELISA. *Nano Lett.* **9**, 4147–4152 (2009).
- 76 Zhu, Y. Y. *et al.* G-quadruplex DNAzyme-based microcystin-LR (toxin) determination by a novel immunosensor. *Biosens. Bioelectron.* **26**, 4393–4398 (2011).
- 77 Loyprasert, S. *et al.* P. Label-free capacitive immunosensor for microcystin-LR using self-assembled thiourea monolayer incorporated with Ag nanoparticles on gold electrode. *Biosens. Bioelectron.* **24**, 78–86 (2008).
- 78 Yu, H. W., Jang, A., Kim, L. H., Kim, S. J. & Kim, I. S. Bead-based competitive fluorescence immunoassay for sensitive and rapid diagnosis of cyanotoxin risk in drinking water. *Environ. Sci. Technol.* **45**, 7804–7811 (2011).
- 79 Campàs, M. & Marty, J.-L. Enzyme sensor for the electrochemical detection of the marine toxin okadaic acid. *Analytica Chimica Acta* **605**, 87-93 (2007).
- 80 Volpe, G. *et al.* A bienzyme electrochemical probe for flow injection analysis of okadaic acid based on protein phosphatase-2A inhibition: An optimization study. *Analytical Biochemistry* **385**, 50-56 (2009).
- 81 Campàs, M., Szydłowska, D., Trojanowicz, M. & Marty, J.-L. Enzyme inhibition-based biosensor for the electrochemical detection of microcystins in natural blooms of cyanobacteria. *Talanta* **72**, 179-186 (2007).

- 82 Ricci, F., Volpe, G., Micheli, L. & Palleschi, G. A review on novel developments and applications of immunosensors in food analysis. *Analytica Chimica Acta* **605**, 111-129, (2007).
- 83 Campàs, M. *et al.* Enzymatic recycling-based amperometric immunosensor for the ultrasensitive detection of okadaic acid in shellfish. *Biosensors and Bioelectronics* **24**, 716-722 (2008).
- 84 Hayat, A., Barthelmebs, L. & Marty, J.-L. Enzyme-linked immunosensor based on super paramagnetic nanobeads for easy and rapid detection of okadaic acid. *Analytica Chimica Acta* **690**, 248-252 (2011).
- 85 Hayat, A., Barthelmebs, L., Sassolas, A. & Marty, J.-L. An electrochemical immunosensor based on covalent immobilization of okadaic acid onto screen printed carbon electrode via diazotization-coupling reaction. *Talanta* **85**, 513-518 (2011).
- 86 Tang, D., Tang, J., Su, B. & Chen, G. Gold nanoparticles-decorated amine-terminated poly(amidoamine) dendrimer for sensitive electrochemical immunoassay of brevetoxins in food samples. *Biosensors and Bioelectronics* **26**, 2090-2096 (2011).
- 87 Tang, J. *et al.* Magneto-controlled electrochemical immunoassay of brevetoxin B in seafood based on guanine-functionalized graphene nanoribbons. *Biosensors and Bioelectronics* **38**, 86-93 (2012).
- 88 Daniels, J. S. & Pourmand, N. Label-Free Impedance Biosensors: Opportunities and Challenges. *Electroanalysis* **19**, 1239-1257 (2007).
- 89 Barsoukov, E.; Macdonald, J. R. Impedance Spectroscopy: Theory, Experiment, and Applications. John Wiley & Sons: New York, 2005.).
- 90 Novoselov, K. S. *et al.* Electric field effect in atomically thin carbon films. *Science* **306**, 666-669 (2004).
- 91 Geim, A. K. Graphene: Status and Prospects. *Science* **324**, 1530-1534 (2009).
- 92 Wei, Z. *et al.* Nanoscale Tunable Reduction of Graphene Oxide for Graphene Electronics. *Science* **328**, 1373-1376 (2010).

- 93 Moon, I. K. *et al.* 2D Graphene Oxide Nanosheets as an Adhesive Over-Coating Layer for Flexible Transparent Conductive Electrodes. *Sci. Rep.* **3**, 1112 (2013).
- 94 Potts, J. R., Dreyer, D. R., Bielawski, C. W. & Ruoff, R. S. Graphene-based polymer nanocomposites. *Polymer* **52**, 5-25 (2011).
- 95 Dreyer, D. R. & Bielawski, C. W. Carbocatalysis: Heterogeneous carbons finding utility in synthetic chemistry. *Chemical Science* **2**, 1233-1240 (2011).
- 96 Gao, W. *et al.* Direct laser writing of micro-supercapacitors on hydrated graphite oxide films. *Nat Nano* **6**, 496-500 (2011).
- 97 Loh, K. P., Bao, Q., Eda, G. & Chhowalla, M. Graphene oxide as a chemically tunable platform for optical applications. *Nat Chem* **2**, 1015-1024 (2010).
- 98 Pumera, M. Graphene in biosensing. *Materials Today* **14**, 308-315 (2011).
- 99 Lu, C.-H., Yang, H.-H., Zhu, C.-L., Chen, X. & Chen, G.-N. A Graphene Platform for Sensing Biomolecules. *Angewandte Chemie International Edition* **48**, 4785-4787 (2009).
- 100 Chang, H., Tang, L., Wang, Y., Jiang, J. & Li, J. Graphene Fluorescence Resonance Energy Transfer Aptasensor for the Thrombin Detection. *Analytical Chemistry* **82**, 2341-2346 (2010).
- 101 Jung, J. H., Cheon, D. S., Liu, F., Lee, K. B. & Seo, T. S. A graphene oxide based immuno-biosensor for pathogen detection. *Angew. Chem. Int. Ed.* **49**, 5708-5711 (2010).
- 102 Islam, M. S., Kouzani, A. Z., Dai, X. J., Michalski, W. P. & GholamHosseini, H. in *Engineering in Medicine and Biology Society, EMBC, 2011 Annual International Conference of the IEEE*. 1851-1854.
- 103 Choi, S. H., Kim, Y. L. & Byun, K. M. Graphene-on-silver substrates for sensitive surface plasmon resonance imaging biosensors. *Opt. Express* **19**, 458-466 (2011).
- 104 Song, Y., Qu, K., Zhao, C., Ren, J. & Qu., X. Graphene oxide: intrinsic peroxidase catalytic activity and its application to glucose detection. *Adv. Mater.* **22**, 2206-2210 (2010).

- 105 Song, Y., Chen, Y., Feng, L., Ren, J. & Qu., X. Selective and quantitative cancer cell detection using target-directed functionalized graphene and its synergetic peroxidase-like activity. *Chem. Commun.* **47**, 4436–4438 (2011).
- 106 Guo, Y. *et al.* Hemin-graphene hybrid nanosheets with intrinsic peroxidase-like activity for label-free colorimetric detection of single-nucleotide polymorphism. *ACS Nano* **5**, 1282–1290 (2011).
- 107 Mao, S. *et al.* Direct Growth of Vertically-oriented Graphene for Field-Effect Transistor Biosensor. *Sci. Rep.* **3**, 1696 (2013).
- 108 Ohno, Y., Maehashi, K. & Matsumoto, K. Label-Free Biosensors Based on Aptamer-Modified Graphene Field-Effect Transistors. *Journal of the American Chemical Society* **132**, 18012-18013 (2010).
- 109 Wan, Y., Lin, Z., Zhang, D., Wang, Y. & Hou, B. Impedimetric immunosensor doped with reduced graphene sheets fabricated by controllable electrodeposition for the non-labelled detection of bacteria. *Biosensors and Bioelectronics* **26**, 1959-1964 (2011).
- 110 Feng, L., Chen, Y., Ren, J. & Qu, X. A graphene functionalized electrochemical aptasensor for selective label-free detection of cancer cells. *Biomaterials* **32**, 2930-2937 (2011).
- 111 Du, D. *et al.* Sensitive Immunosensor for Cancer Biomarker Based on Dual Signal Amplification Strategy of Graphene Sheets and Multienzyme Functionalized Carbon Nanospheres. *Anal. Chem.* **82**, 2989–2995 (2010).
- 112 Du, D. *et al.* Functionalized Graphene Oxide as a Nanocarrier in a Multienzyme Labeling Amplification Strategy for Ultrasensitive Electrochemical Immunoassay of Phosphorylated p53 (S392). *Analytical Chemistry* **83**, 746-752 (2011).
- 113 Alwarappan, S., Erdem, A., Liu, C. & Li, C.-Z. Probing the Electrochemical Properties of Graphene Nanosheets for Biosensing Applications. *The Journal of Physical Chemistry C* **113**, 8853-8857 (2009).
- 114 Wang, Y., Li, Y., Tang, L., Lu, J. & Li, J. Application of graphene-modified electrode for selective detection of dopamine. *Electrochemistry Communications* **11**, 889-892 (2009).

- 115 Pumera, M., Ambrosi, A., Bonanni, A., Chng, E. L. K. & Poh, H. L. Graphene for electrochemical sensing and biosensing. *TrAC Trends in Analytical Chemistry* **29**, 954-965 (2010).
- 116 Tang, L. *et al.* Preparation, Structure, and Electrochemical Properties of Reduced Graphene Sheet Films. *Advanced Functional Materials* **19**, 2782-2789 (2009).
- 117 Zhang, Y., Zhang, L. & Zhou, C. Review of Chemical Vapor Deposition of Graphene and Related Applications. *Accounts of Chemical Research* **46**, 2329-2339 (2013).
- 118 Oliveira, M. H., Schumann, T., Ramsteiner, M., Lopes, J. M. J. & Riechert, H. Influence of the silicon carbide surface morphology on the epitaxial graphene formation. *Applied Physics Letters* **99**, 111901 (2011).
- 119 Kosynkin, D. V. *et al.* Longitudinal unzipping of carbon nanotubes to form graphene nanoribbons. *Nature* **458**, 872-876 (2009).
- 120 Pumera, M. Graphene-based nanomaterials and their electrochemistry. *Chemical Society Reviews* **39**, 4146-4157 (2010).
- 121 Sutter, P. W., Flege, J. I. & Sutter, E. A. Epitaxial graphene on ruthenium. *Nat. Mater.* **7**, 406-411 (2008).
- 122 Kim, K. S. *et al.* Large-scale pattern growth of graphene films for stretchable transparent electrodes. *Nature* **457**, 706-710 (2009).
- 123 Reina, A. *et al.* Large area, few-layer graphene films on arbitrary substrates by chemical vapor deposition, *Nano Lett.* **9**, 30-35 (2009).
- 124 Li, X. S. *et al.* Large-area synthesis of high-quality and uniform graphene films on copper foils. *Science* **324**, 1312-1314 (2009).
- 125 Dato, A., Radmilovic, V., Lee, Z. H., Phillips, J. & Frenklach, M. Substrate-Free Gas-Phase Synthesis of Graphene Sheets. *Nano Lett.* **8**, 2012-2016 (2008).
- 126 Li, W., Tan, C., Lowe, M. A., Abruña, H. D. & Ralph, D. C. Electrochemistry of Individual Monolayer Graphene Sheets. *ACS Nano* **5**, 2264-2270 (2011).
- 127 Qu, L., Liu, Y., Baek, J.-B. & Dai, L. Nitrogen-Doped Graphene as Efficient Metal-Free Electrocatalyst for Oxygen Reduction in Fuel Cells. *ACS Nano* **4**, 1321-1326 (2010).

- 128 L. Staudenmaier, B. D. C. G. Verfahren zur Darstellung der Graphitsäure. *European Journal of Inorganic Chemistry* **31**, 1481-1487 (1898).
- 129 U. Hofmann and E. König., Z. A. A. C., Untersuchungen über Graphitoxyd. *Journal of Inorganic and General Chemistry* **234**, 311-336 (1937).
- 130 W. S. Hummers and R. E. Offeman, J. A. C. S., Preparation of Graphitic Oxide. *Journal of American Chemical Society* **80**, 1339-1339 (1958).
- 131 Shao, Y. *et al.* Graphene Based Electrochemical Sensors and Biosensors: A Review. *Electroanalysis* **22**, 1027-1036 (2010).
- 132 Gomez-Navarro, C. *et al.* Electronic transport properties of individual chemically reduced graphene oxide sheets. *Nano Lett.* **7**, 3499-3503 (2007).
- 133 Wei, Z. Q., Barlow, D. E. & Sheehan, P. E. The Assembly of Single-Layer Graphene Oxide and Graphene Using Molecular Templates. *Nano Lett.* **8**, 3141-3145 (2008).
- 134 Yang, D. *et al.* Chemical analysis of graphene oxide films after heat and chemical treatments by X-ray photoelectron and Micro-Raman spectroscopy. *Carbon* **47**, 145-152 (2009).
- 135 McCreery, R. L. Advanced carbon electrode materials for molecular electrochemistry. *Chem. Rev.* **108**, 2646-2687 (2008).
- 136 Banks, C. E., Davies, T. J., Wildgoose, G. G. & R. G. Compton. Electrocatalysis at graphite and carbon nanotube modified electrodes: edge-plane sites and tube ends are the reactive sites. *Chem. Commun.* 829-841 (2005).
- 137 Dumitrescu, I., Unwin, P. R. & Macpherson, J. V. Electrochemistry at carbon nanotubes: Perspective and issues. *Chem. Commun.* 6886-6901 (2009).
- 138 Wang, J. Carbon-Nanotube Based Electrochemical Biosensors: A Review. *Electroanalysis* **17**, 7-14 (2005).
- 139 Lahiri, J., Ostuni, E. & Whitesides, G. M. Patterning Ligands on Reactive SAMs by Microcontact Printing. *Langmuir* **15**, 2055–2060 (1999).
- 140 Patolsky, F., Katz, E., Bardea, A. & Willner, I. Enzyme-Linked Amplified Electrochemical Sensing of Oligonucleotide–DNA Interactions by Means of the

- Precipitation of an Insoluble Product and Using Impedance Spectroscopy. *Langmuir* **15**, 3703–3706 (1999).
- 141 Ruckenstein, E. & Li, Z. F. Surface modification and functionalization through the self-assembled monolayer and graft polymerization. *Adv. Colloid Interf. Sci.* **113**, 43–63 (2005).
- 142 Popovich, N. D., Yen, B. K. & Wong, S. S. Effect of Tin-Doped Indium Oxide Electrode Preparation Methods on the Mediated Electrochemical Detection of Nucleic Acids. *Langmuir* **19**, 1324–1329 (2003).
- 143 Bełanger, D. & Pinson, J. Electrografting: a powerful method for surface modification. *Chem. Soc. Rev.* **40**, 3995–4048 (2011).
- 144 Andrieux, C. P. & Pinson, J. The Standard Redox Potential of the Phenyl Radical/Anion Couple. *Journal of the American Chemical Society* **125**, 14801-14806 (2003).
- 145 Allongue, P. *et al.* Covalent Modification of Carbon Surfaces by Aryl Radicals Generated from the Electrochemical Reduction of Diazonium Salts. *Journal of the American Chemical Society* **119**, 201-207 (1997).
- 146 Georgakilas, V. *et al.* Functionalization of Graphene: Covalent and Non-Covalent Approaches, Derivatives and Applications. *Chemical Reviews* **112**, 6156-6214 (2012).
- 147 Paulus, G. L. C., Wang, Q. H. & Strano, M. S. Covalent Electron Transfer Chemistry of Graphene with Diazonium Salts. *Accounts of Chemical Research* **46**, 160-170 (2012).
- 148 Bekyarova, E. *et al.* Chemical Modification of Epitaxial Graphene: Spontaneous Grafting of Aryl Groups. *Journal of the American Chemical Society* **131**, 1336-1337 (2009).
- 149 Jin, Z. *et al.* Mechanically Assisted Exfoliation and Functionalization of Thermally Converted Graphene Sheets. *Chemistry of Materials* **21**, 3045-3047 (2009).
- 150 Lomeda, J. R., Doyle, C. D., Kosynkin, D. V., Hwang, W.-F. & Tour, J. M. Diazonium Functionalization of Surfactant-Wrapped Chemically Converted Graphene Sheets. *Journal of the American Chemical Society* **130**, 16201-16206 (2008).

- 151 Lim, H., Lee, J. S., Shin, H.-J., Shin, H. S. & Choi, H. C. Spatially Resolved Spontaneous Reactivity of Diazonium Salt on Edge and Basal Plane of Graphene without Surfactant and Its Doping Effect. *Langmuir* **26**, 12278-12284 (2010).
- 152 Wang, Q. H. *et al.* Understanding and controlling the substrate effect on graphene electron-transfer chemistry via reactivity imprint lithography. *Nat Chem* **4**, 724-732 (2012).
- 153 Jin, Z. *et al.* Click Chemistry on Solution-Dispersed Graphene and Monolayer CVD Graphene. *Chemistry of Materials* **23**, 3362-3370 (2011).
- 154 Sharma, R., Baik, J. H., Perera, C. J. & Strano, M. S. Anomalous Large Reactivity of Single Graphene Layers and Edges toward Electron Transfer Chemistries. *Nano Letters* **10**, 398-405 (2010).
- 155 Eissa, S., L'Hocine, L., Siaj, M. & Zourob, M. A graphene-based label-free voltammetric immunosensor for sensitive detection of the egg allergen ovalbumin. *Analyst* **138**, 4378-4384 (2013).
- 156 Eissa, S., Tlili, C., L'Hocine, L. & Zourob, M. Electrochemical immunosensor for the milk allergen β -lactoglobulin based on electrografting of organic film on graphene modified screen-printed carbon electrodes. *Biosensors and Bioelectronics* **38**, 308-313 (2012).
- 157 Eissa, S. & Zourob, M. A graphene-based electrochemical competitive immunosensor for the sensitive detection of okadaic acid in shellfish. *Nanoscale* **4**, 7593-7599 (2012).
- 158 Gan, L., Zhang, D. & Guo, X. Electrochemistry: An Efficient Way to Chemically Modify Individual Monolayers of Graphene. *small* **8**, 1326-1330 (2012).
- 159 Lillethorup, M. *et al.* High- versus Low-Quality Graphene: A Mechanistic Investigation of Electrografted Diazonium-Based Films for Growth of Polymer Brushes. *Small* **10**, 922-934 (2014).
- 160 Tan, S. M., Ambrosi, A., Chua, C. K. & Pumera, M. Electron transfer properties of chemically reduced graphene materials with different oxygen contents. *Journal of Materials Chemistry A* **2**, 10668-10675 (2014).

- 161 Allen, M. J., Tung, V. C. & Kaner, R. B. Honeycomb Carbon: A Review of Graphene. *Chemical Reviews* **110**, 132-145 (2010).
- 162 Luo, J. *et al.* Graphene Oxide Nanocolloids. *Journal of the American Chemical Society* **132**, 17667-17669 (2010).
- 163 Compton, O. C. & Nguyen, S. T. Graphene Oxide, Highly Reduced Graphene Oxide, and Graphene: Versatile Building Blocks for Carbon-Based Materials. *Small* **6**, 711-723 (2010).
- 164 Pan, S. & Aksay, I. A. Factors Controlling the Size of Graphene Oxide Sheets Produced via the Graphite Oxide Route. *ACS Nano* **5**, 4073-4083 (2011).
- 165 McAllister, M. J. *et al.* Single Sheet Functionalized Graphene by Oxidation and Thermal Expansion of Graphite. *Chemistry of Materials* **19**, 4396-4404 (2007).
- 166 Zhang, L. *et al.* Size-controlled synthesis of graphene oxide sheets on a large scale using chemical exfoliation. *Carbon* **47**, 3365-3368 (2009).
- 167 Zhao, J., Pei, S., Ren, W., Gao, L. & Cheng, H.-M. Efficient Preparation of Large-Area Graphene Oxide Sheets for Transparent Conductive Films. *ACS Nano* **4**, 5245-5252 (2010).
- 168 Botas, C. *et al.* Optimization of the size and yield of graphene oxide sheets in the exfoliation step. *Carbon* **63**, 576-578 (2013).
- 169 Su, C.-Y. *et al.* Electrical and Spectroscopic Characterizations of Ultra-Large Reduced Graphene Oxide Monolayers. *Chemistry of Materials* **21**, 5674-5680 (2009).
- 170 Kim, J. *et al.* Graphene Oxide Sheets at Interfaces. *Journal of the American Chemical Society* **132**, 8180-8186 (2010).
- 171 Hicks, J., Behnam, A. & Ural, A. A computational study of tunneling-percolation electrical transport in graphene-based nanocomposites. *Applied Physics Letters* **95**, 213103 (2009).
- 172 Li, C., Thostenson, E. T. & Chou, T.-W. Dominant role of tunneling resistance in the electrical conductivity of carbon nanotube-based composites. *Applied Physics Letters* **91**, 223114 (2007).

- 173 Kelly, A. & Tyson, W. R. Tensile properties of fibre-reinforced metals: Copper/tungsten and copper/molybdenum. *Journal of the Mechanics and Physics of Solids* **13**, 329-350, (1965).
- 174 Nielsen, L. E. Models for the Permeability of Filled Polymer Systems. *Journal of Macromolecular Science: Part A - Chemistry* **1**, 929-942 (1967).
- 175 Chee, S. Y. *et al.* Influence of parent graphite particle size on the electrochemistry of thermally reduced graphene oxide. *Physical Chemistry Chemical Physics* **14**, 12794-12799 (2012).
- 176 Tuerk, C. & Gold, L. Systematic evolution of ligands by exponential enrichment: RNA ligands to bacteriophage T4 DNA polymerase. *Science* **249**, 505-510 (1990).
- 177 Ellington, A. D. & Szostak, J. W. In vitro selection of RNA molecules that bind specific ligands. *Nature* **346**, 818-822 (1990).
- 178 Stoltenburg, R., Reinemann, C. & Strehlitz, B. SELEX—A (r)evolutionary method to generate high-affinity nucleic acid ligands. *Biomolecular Engineering* **24**, 381-403 (2007).
- 179 McKeague, M. & DeRosa, M. C. Challenges and Opportunities for Small Molecule Aptamer Development. *Journal of Nucleic Acids* **2012**, 20 (2012).
- 180 Cruz-Aguado, J. A. & Penner, G. Determination of Ochratoxin A with a DNA Aptamer. *Journal of Agricultural and Food Chemistry* **56**, 10456-10461 (2008).
- 181 Handy, S. M. *et al.* First report of the use of a saxitoxin–protein conjugate to develop a DNA aptamer to a small molecule toxin. *Toxicon* **61**, 30-37 (2013).
- 182 Elshafey, R., Siaj, M. & Zourob, M. DNA aptamers selection and characterization for development of label-free impedimetric aptasensor for neurotoxin anatoxin-a. *Biosensors and Bioelectronics* **68**, 295-302 (2015).
- 183 Elshafey, R., Siaj, M. & Zourob, M. In Vitro Selection, Characterization, and Biosensing Application of High-Affinity Cyindrospermopsin-Targeting Aptamers. *Analytical Chemistry* **86**, 9196-9203 (2014).

- 184 Sassolas, A., Hayat, A., Catanante, G. & Marty, J.-L. Detection of the marine toxin okadaic acid: Assessing seafood safety. *Talanta* **105**, 306-316 (2013).
- 185 Nakamura, C., Kobayashi, T., Miyake, M., Shirai, M. & Miyake, J. Usage of a DNA Aptamer as a Ligand Targeting Microcystin. *Molecular Crystals and Liquid Crystals Science and Technology. Section A. Molecular Crystals and Liquid Crystals* **371**, 369-374 (2001).
- 186 Ng, A. *et al.* Selection, Characterization, and Biosensing Application of High Affinity Congener-Specific Microcystin-Targeting Aptamers. *Environmental Science & Technology* **46**, 10697-10703 (2012).
- 187 Sheng, L., Ren, J., Miao, Y., Wang, J. & Wang, E. PVP-coated graphene oxide for selective determination of ochratoxin A via quenching fluorescence of free aptamer. *Biosensors and Bioelectronics* **26**, 3494-3499 (2011).
- 188 He, S. *et al.* A Graphene Nanoprobe for Rapid, Sensitive, and Multicolor Fluorescent DNA Analysis. *Advanced Functional Materials* **20**, 453-459 (2010).
- 189 Jang, H. *et al.* A Graphene-Based Platform for the Assay of Duplex-DNA Unwinding by Helicase. *Angewandte Chemie International Edition* **49**, 5703-5707 (2010).
- 190 Loo, A. H., Bonanni, A. & Pumera, M. Impedimetric thrombin aptasensor based on chemically modified graphenes. *Nanoscale* **4**, 143-147 (2012).
- 191 Eissa, S. *et al.* Functionalized CVD Monolayer Graphene for Label-Free Impedimetric Biosensing. *Nano Res.* **8**, 1698-1709 (2015).
- 192 Marcano, D. C. *et al.* Improved Synthesis of Graphene Oxide. *ACS Nano* **4**, 4806-4814 (2010).
- 193 Levine, L. *et al.* Production of antibodies and development of a radioimmunoassay for okadaic acid. *Toxicon* **26**, 1123-1128 (1988).
- 194 Stoltenburg, R., Reinemann, C. & Strehlitz, B. FluMag-SELEX as an advantageous method for DNA aptamer selection. *Anal Bioanal Chem* **383**, 83-91 (2005).
- 195 Simossis, V. A., Kleinjung, J. & Heringa, J. Homology-extended sequence alignment. *Nucleic Acids Research* **33**, 816-824 (2005).

- 196 Loo, A. H., Bonanni, A. & Pumera, M. Biorecognition on Graphene: Physical, Covalent, and Affinity Immobilization Methods Exhibiting Dramatic Differences. *Chemistry – An Asian Journal* **8**, 198-203 (2013).
- 197 Actis, P. *et al.* Functionalization of Glassy Carbon with Diazonium Salts in Ionic Liquids. *Langmuir* **24**, 6327-6333 (2008).
- 198 Radi, A.-E., Muñoz-Berbel, X., Cortina-Puig, M. & Marty, J.-L. An electrochemical immunosensor for ochratoxin A based on immobilization of antibodies on diazonium-functionalized gold electrode. *Electrochimica Acta* **54**, 2180-2184 (2009).
- 199 Gui, A. L. *et al.* A Comparative Study of Electrochemical Reduction of 4-Nitrophenyl Covalently Grafted on Gold and Carbon. *Electroanalysis* **22**, 1824-1830 (2010).
- 200 Saby, C., Ortiz, B., Champagne, G. Y. & Bélanger, D. Electrochemical Modification of Glassy Carbon Electrode Using Aromatic Diazonium Salts. 1. Blocking Effect of 4-Nitrophenyl and 4-Carboxyphenyl Groups. *Langmuir* **13**, 6805-6813 (1997).
- 201 Zhong, Y. L., Loh, K. P., Midya, A. & Chen, Z.-K. Suzuki Coupling of Aryl Organics on Diamond. *Chemistry of Materials* **20**, 3137-3144 (2008).
- 202 Laforgue, A., addou, T. & Belanger, D. Characterization of the Deposition of Organic Molecules at the Surface of Gold by the Electrochemical Reduction of Aryldiazonium Cations. *Langmuir* **21**, 6855-6865 (2005).
- 203 Combellas, C., Jiang, D.-e., Kanoufi, F., Pinson, J. & Podvorica, F. I. Steric effect on the reaction of aryl radical on surfaces. *Langmuir* **25**, 286-293 (2009).
- 204 Liu, Y.-C. & McCreery, R.L. Reactions of Organic Monolayers on Carbon Surfaces Observed with Unenhanced Raman Spectroscopy. *Journal of the American Chemical Society* **117**, 11254-11259 (1995).
- 205 Baranaton, S. & Belanger, D. Electrochemical derivatization of carbon surface by reduction of in situ generated diazonium cations. *J. Phys. Chem. B* **109**, 24401-24410 (2005).

- 206 Covaci, O., Bucur, B., Bucur, M. & Radu, G. Optimization of acetylcholinesterase immobilization on microelectrodes based on nitrophenyl diazonium for sensitive organophosphate insecticides detection. *Microchimica Acta* **169**, 335-343 (2010).
- 207 McKenzie, H. A. Vol. 2 (Academic Press, New York, 1971).
- 208 Nezlin, R. (Academic Press, New York, 1998).
- 209 Maier, I., Lindner, W. & Pittner, F. Antigenicity of heat-treated and trypsin-digested milk samples studied by an optical immunochip biosensor. *Monatsh Chem* **140**, 921-929 (2009).
- 210 Smith, E. R. B. THE INFLUENCE OF METHOD OF PREPARATION AND OF CATIONS ON THE ISOELECTRIC POINT OF OVALBUMIN. *J. Biol. Chem.* **113**, 473-478 (1936).
- 211 Ferrari, A. C. *et al.* Raman Spectrum of Graphene and Graphene Layers. *Physical Review Letters* **97**, 187401 (2006).
- 212 Guermoune, A. *et al.* Chemical vapor deposition synthesis of graphene on copper with methanol, ethanol, and propanol precursors. *Carbon* **49**, 4204-4210 (2011).
- 213 Lucchese, M. M. *et al.* Quantifying ion-induced defects and Raman relaxation length in graphene. *Carbon* **48**, 1592-1597 (2010).
- 214 Hayat, A., Barthelmebs, L., Sassolas, A. & Marty, J.-L. Development of a novel label-free amperometric immunosensor for the detection of okadaic acid. *Analytica Chimica Acta* **724**, 92-97 (2012).
- 215 Eissa, S., Siaj, M. & Zourob, M. Aptamer-based competitive electrochemical biosensor for brevetoxin-2. *Biosensors and Bioelectronics* **69**, 148-154 (2015).
- 216 La, R. Y., Plaxco, K. W. & Heeger, A. J. Aptamer-Based Electrochemical Detection of Picomolar Platelet-Derived Growth Factor Directly in Blood Serum. *Anal. Chem.* **79**, 229-233 (2007).
- 217 Steel, A. B., Herne, T. M. & Tarlov, M. J. Electrochemical Quantitation of DNA Immobilized on Gold. *Analytical Chemistry* **70**, 4670-4677 (1998).

- 218 Liu, Y., Tuleouva, N., Ramanculov, E. & Revzin, A. Aptamer-Based Electrochemical Biosensor for Interferon Gamma Detection. *Analytical Chemistry* **82**, 8131-8136 (2010).
- 219 White, R. J., Phares, N., Lubin, A. A., Xiao, Y. & Plaxco, K. W. Optimization of Electrochemical Aptamer-Based Sensors via Optimization of Probe Packing Density and Surface Chemistry. *Langmuir* **24**, 10513-10518 (2008).
- 220 Kashefi-Kheyraadi, L. & Mehrgardi, M. A. Design and construction of a label free aptasensor for electrochemical detection of sodium diclofenac. *Biosensors and Bioelectronics* **33**, 184-189 (2012).
- 221 Lin, Z. *et al.* Determination of microcystin-LR in water by a label-free aptamer based electrochemical impedance biosensor. *Talanta* **103**, 371-374 (2013).
- 222 Labib, M. *et al.* Aptamer-Based Viability Impedimetric Sensor for Viruses. *Analytical Chemistry* **84**, 1813-1816 (2012).
- 223 Lao, R. *et al.* Electrochemical Interrogation of DNA Monolayers on Gold Surfaces. *Analytical Chemistry* **77**, 6475-6480 (2005).
- 224 Cheng, A. K. H., Ge, B. & Yu, H.-Z. Aptamer-Based Biosensors for Label-Free Voltammetric Detection of Lysozyme. *Analytical Chemistry* **79**, 5158-5164 (2007).
- 225 Huang, Y., Bell, M. C. & Suni, I. I. Impedance Biosensor for Peanut Protein Ara h 1. *Analytical Chemistry* **80**, 9157-9161 (2008).
- 226 Eissa, S., Ng, A., Siaj, M., Tavares, A. C. & Zourob, M. Selection and Identification of DNA Aptamers against Okadaic Acid for Biosensing Application. *Analytical Chemistry* **85**, 11794-11801 (2013).
- 227 Zuker, M. Mfold web server for nucleic acid folding and hybridization prediction. *Nucleic Acids Research* **31**, 3406-3415 (2003).
- 228 Luo, X. *et al.* Computational approaches toward the design of pools for the in vitro selection of complex aptamers. *RNA* **16**, 2252-2262 (2010).
- 229 Eissa, S., Ng, A., Siaj, M. & Zourob, M. Label-Free Voltammetric Aptasensor for the Sensitive Detection of Microcystin-LR Using Graphene-Modified Electrodes. *Analytical Chemistry* **86**, 7551-7557 (2014).

- 230 Yan, F., Ozsoz, M. & Sadik, O. A. Electrochemical and conformational studies of microcystin–LR. *Analytica Chimica Acta* **409**, 247-255 (2000).
- 231 Cyanotoxins: New Generation of Water Contaminants. *Journal of Environmental Engineering* **131**, 1239-1243 (2005).
- 232 Reverté, L. *et al.* Magnetic Particle-Based Enzyme Assays and Immunoassays for Microcystins: From Colorimetric to Electrochemical Detection. *Environmental Science & Technology* **47**, 471-478 (2013).
- 233 Sun, X., Luo, D., Liu, J. & Evans, D. G. Monodisperse Chemically Modified Graphene Obtained by Density Gradient Ultracentrifugal Rate Separation. *ACS Nano* **4**, 3381-3389 (2010).
- 234 Stankovich, S., Piner, R. D., Nguyen, S. T. & Ruoff, R. S. Synthesis and exfoliation of isocyanate-treated graphene oxide nanoplatelets. *Carbon* **44**, 3342-3347 (2006).
- 235 Kim, S. *et al.* Room-temperature metastability of multilayer graphene oxide films. *Nat Mater* **11**, 544-549 (2012).
- 236 Cai, W. *et al.* Synthesis and Solid-State NMR Structural Characterization of ¹³C-Labeled Graphite Oxide. *Science* **321**, 1815-1817 (2008).
- 237 Gao, W., Alemany, L. B., Ci, L. & Ajayan, P. M. New insights into the structure and reduction of graphite oxide. *Nat Chem* **1**, 403-408 (2009).
- 238 Le, T. T., Chumphukam, O. and Cass, A E. G. Determination of minimal sequence for binding of an aptamer. A comparison of truncation and hybridization inhibition methods. *RSC Adv.* **4**, 47227-47233 (2014).
- 239 Stateikina, I., Eissa, S. and Zourob, M. Design and Fabrication of Integrated Multianalyte Sensing Platform With Magnetic Micro-Coils. *J. Microelectromech. Syst.*, **22**, 1339–1346 (2013).

RÉSUMÉ

La salubrité des aliments est un objectif majeur de santé global, et le contrôle de qualité des aliments est important pour les autorités et les professionnels du domaine agroalimentaire. La présence de niveaux élevés des contaminants d'origine alimentaire tels que les allergènes et les toxines dans les aliments représentent un problème majeur de santé publique qui nécessite l'élaboration d'outils efficaces pour leur détection. Malgré la sensibilité relativement élevée de certaines méthodes de détection utilisées présentement, ces dernières sont très laborieuses, nécessitent beaucoup de temps, exigent un personnel hautement qualifié et elles sont aussi coûteuses. Ces limitations encouragent la recherche d'autres alternatives pour les appliquer dans un régime de surveillance réglementaire afin de garantir un niveau élevé de protection des consommateurs. Par conséquent, les biocapteurs sont apparus récemment comme une solution intéressante, plus particulièrement, les biocapteurs électrochimiques sont devenus un choix attractif en raison de leur très faible coût, haute sensibilité, facilité d'utilisation et leur possibilité de miniaturisation. Toutefois, il y a deux principaux défis auxquels sont confrontés les biocapteurs électrochimiques disponibles pour la détection des contaminants alimentaires. Tout d'abord, les stratégies de détection qui sont généralement utilisées pour obtenir la sensibilité requise sont sophistiquées, et le temps d'analyse est long. En second lieu, on peut nommer une faible spécificité, leur coût élevé ainsi qu'une stabilité limitée. Pour relever ces défis, ce travail décrit le développement de plateformes à base de graphène en tant que transducteur et des aptamères d'ADN comme récepteurs de reconnaissance et explore leurs applications pour la détection de certains contaminants d'origine alimentaire.

Chapitre 3 Immunocapteur électrochimique basées sur l'électro-greffage de sels de diazonium aryle sur des électrodes de graphène pour la détection d'allergènes de lait et d'oeufs sans marqueur dont la β -lactoglobuline et l'ovalbumine

Une méthode de fonctionnalisation des électrodes de graphène a été démontrée par la réduction électrochimique de sels de diazonium aryle généré in situ dans une

solution acide aqueuse est présenté dans le chapitre 3. Deux sels de diazonium ont été utilisés afin de montrer la polyvalence de cette approche: le nitrophényl et le carboxyphényl. Le protocole de modification électrochimique a été optimisé afin de produire des monocouches de groupes aryles sur la surface du graphène sans passivation complète de l'électrode. Contrairement aux méthodes rapportées sur la fonctionnalisation du graphène, nous avons démontré ici la possibilité d'electro-greffer de manière contrôlée le sel de diazonium en choisissant le protocole de greffage approprié, dans l'optique de former un film organique à la surface du graphène. Ensuite, les électrodes de graphène fonctionnalisées ont servi à élaborer des immunocapteurs électrochimiques sans marquage qui ont montré une sensibilité élevée pour l'allergène β -lactoglobuline dans le lait et aussi pour l'ovalbumine des œufs.

Les voltampérogrammes cycliques consécutifs pour le cation généré 4-nitrobenzène diazonium sont montrés dans la Figure 1. Les CV sont caractérisés par une vague de réduction irréversible dans le premier cycle. Ce comportement correspond à l'électroréduction des sels de diazonium par un processus de transfert d'un électron aboutissant à l'élimination d'une molécule d'azote et à la production d'un radical aryle qui forme une liaison covalente avec la surface de graphène ¹⁴⁴.

La figure 1B montre les CVs successifs pour la réduction de 4-nitrophényle modifié GSPE dans une solution aqueuse de KCl 0,1 M de 0,4 à -1.4 V vs. l'électrode de référence Ag. Deux pics de réduction ont été observés dans les voltampérogrammes qui correspondent à la réduction irréversible des groupes 4-NP électrogreffés sur la surface de l'électrode de graphène. Les deux sommets cathodiques sont attribuables à la réduction des groupes nitro aux dérivés de l'hydroxylamine en processus ($4e^-/4 H^+$) à la suite des amines correspondantes ($2e^-/2H^+$). Ensuite, les pics de réduction significativement réduits dans les analyses ultérieures indiquent une réduction presque complète des groupes nitro en amines. Un comportement similaire a été signalé auparavant pour la réduction des groupes nitrophényl sur d'autres surfaces ¹⁹⁷⁻¹⁹⁹.

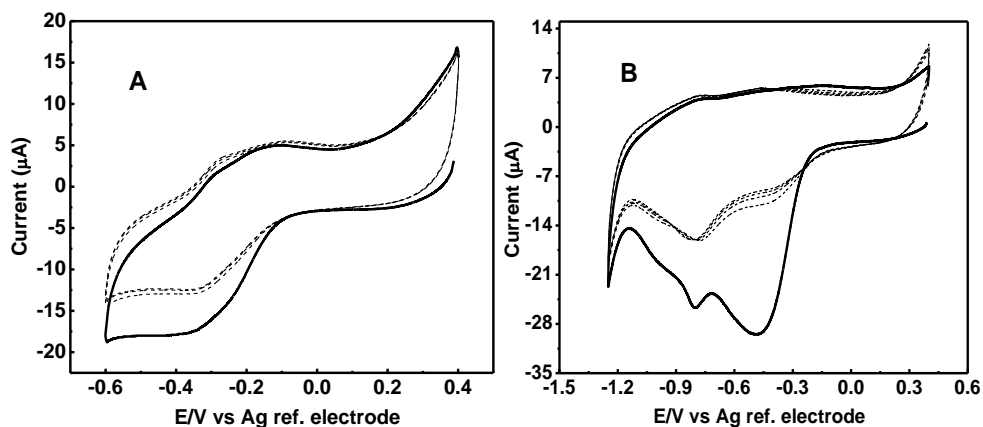


Figure 1(A) les voltammogramme cycliques pour la production du sel 4-nitrophényle de diazonium dans le mélange 2 mM NaNO₂ + 2 mM 4-nitroaniline (dans HCl 0,5 M) à la surface de GSPE, (B) Les voltampérogrammes cycliques successives pour la réduction de nitrophényl/GSPE en KCl 0,1 M à la vitesse de balayage de 100 mVs⁻¹. Les lignes pleines représentent le premier CV et les lignes pointillées représentent les cycles subséquents.

Comme indiqué dans le tableau 1, toutes les valeurs de la couverture de la surface avec des groupes nitrophényl greffés à l'aide de la méthode électrochimique sont nettement supérieures à ceux greffés en utilisant la réaction de transfert d'électron spontanée en immergeant l'électrode dans la solution de sel de diazonium pour 180 s sans appliquer un potentiel. En outre, les valeurs de couverture de la surface de graphène avec des groupes électrogreffés pendant 1 min ou moins étaient de $4,00 \times 10^{-10}$ allant jusqu'à $13,0 \times 10^{-10}$, ce qui se compare avec la valeur signalée précédemment pour les groupes de NP chimiquement greffés sur le graphène épitaxial¹⁴⁸ ainsi que a d'autres surfaces de carbone^{145,200-201}.

Tableau 1 Densité surfacique de groupes nitrophényl formés sur le GSPE à l'aide de différents protocoles.

Method	Surface coverage $\times 10^{-10}$ (mol. cm ⁻²)
Spontaneous reaction 180 s	0.80
One cyclic voltammetry	4.00
Five cyclic voltammetry	4.10
Linear weep voltammetry	4.80
Chronoamperometry 15 s	5.70
Chronoamperometry 45 s	7.35
Chronoamperometry 60 s	13.0
Chronoamperometry 180 s	19.9

La figure 2 compare les spectres N (1s) de l'AP-GSPE et du NP-GSPE. Un seul pic à 400.04 eV a été observé pour l'électrode modifiée aminophényl attribuable aux groupements aminés ce qui confirme la conversion des groupes nitro en amine, et démontre également la nature robuste du graphène modifié ¹⁴⁸.

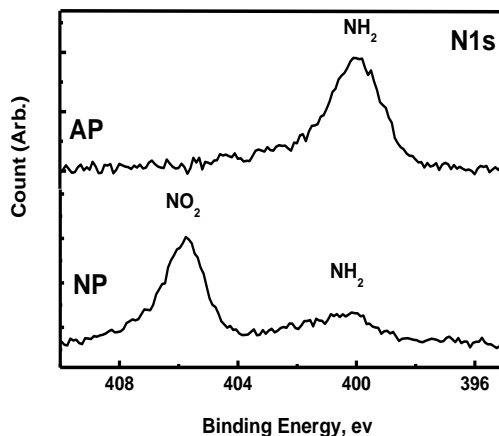


Figure 2 Spectres XPS N1s spectres du nitrophényl-GSPE et de l'aminophényl-GSPE.

La figure 3 montre une diminution dans le pic de réduction du voltamétrie impulsométrique différentielle de $[\text{Fe}(\text{CN})_6]^{4-/3-}$ avec l'incrément de la β -lactoglobuline. L'encart sur la Figure 3 montre une bonne relation linéaire entre la variation des courants pic cathodique obtenue par DPV et le logarithme de la concentration de β -lactoglobuline de $1,0 \text{ pg mL}^{-1}$ à 100 ng mL^{-1} . Chaque point de données dans le graphique d'étalonnage représente trois mesures indépendantes et les barres d'erreur affichent les écarts-types de mesures. Les écarts types relatifs ont été de 1,6 % à 6,0 %, ceci indique la bonne reproductibilité de l'immunocapteur. L'équation de régression linéaire a été $j_a i_o-i (\mu\text{A}) = 7.88 + 1,56 \times \log C [\text{ng mL}^{-1}]$, $R = 0.998$, avec une limite de détection (LOD) de $0,85 \text{ pg mL}^{-1}$ ($S/N = 3$). Les résultats indiquent que l'immunocapteur développé dans cette étude présente une limite de détection qui est inférieure aux autres méthodes déclarées^{3,58,209} sans aucune étape d'amplification. La figure 3B confirme que l'immunocapteur affiche une bonne sélectivité pour le dosage de la β -lactoglobuline.

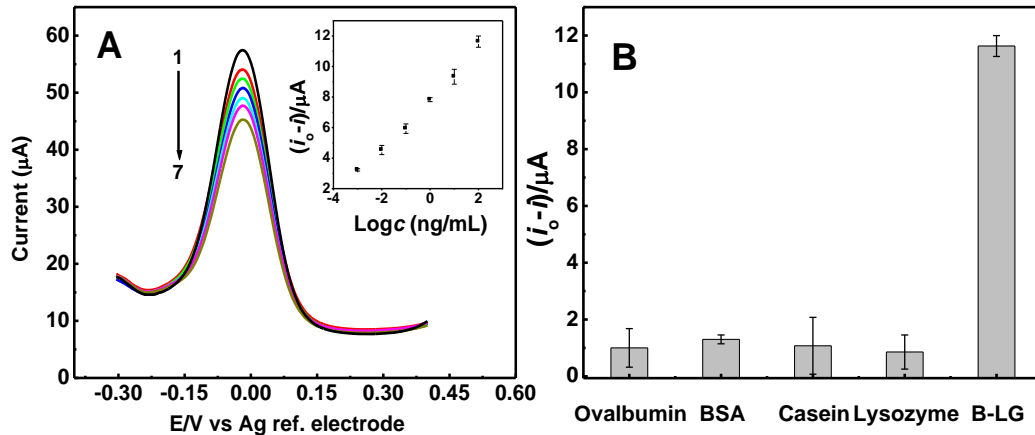


Figure 3(A) DPV l'immunocapteur incubé avec différentes concentrations de β -lactoglobuline (1 à 7): les concentrations de β -LG sont 0,000 0,001, 0,01, 0,1, 1,0, 10 et 100 ng mL^{-1} . L'encart est la courbe d'étalonnage basée sur la variation des courants de pointe DPV versus le logarithme de la concentration, (B) Comparaison de réponse du GSPE immunocapteur voltampérométrique à l'ovalbumine de 1000 ng mL^{-1} ou 100 ng mL^{-1} β -lactoglobuline.

Un seul pic cathodique irréversible à -0.12 V a été observé par rapport à l'électrode de référence d'Ag dans la CV pour le premier scan sur le GSPE tel qu'illustré à la Figure 4. Ce pic a ensuite graduellement diminué dans le deuxième et le troisième scanne du CV comme précédemment observées avec le sel de diazonium nitrophényl. Le comportement électrochimique des électrodes carboxyphényl modifié en utilisant les différents cycles de CV a été étudié plus loin à l'aide de voltampérométrie d'impulsions différentielles en présence de la sonde redox de $[\text{Fe}(\text{CN})_6]^{3-/4-}$. Comme montre la figure 4(B), le courant de crête DPV réduction des espèces $[\text{Fe}(\text{CN})_6]^{3-/4-}$ a diminué avec l'augmentation du nombre de cycles de réduction de voltampérométrie cyclique utilisé pour le greffage du carboxyphényl. Cette baisse dans le pic du courant réductif pour les espèces $[\text{Fe}(\text{CN})_6]^{3-/4-}$ redox indique l'effet de blocage de la couche de carboxyphényl pour la réduction de la $[\text{Fe}(\text{CN})_6]^{3-/4-}$ sur la surface de l'électrode modifiée. Cet effet est due à l'épaisseur de la couche organique ainsi qu'à la répulsion électrostatique entre la charge négative des groupements carboxyliques et la sonde redox $[\text{Fe}(\text{CN})_6]^{4-/3-}$. Les courants de DPV du couple redox $[\text{Fe}(\text{CN})_6]^{4-/3-}$ ont été tracés par rapport au nombre de CV des cycles de numérisation utilisés pour la réduction des cations diazonium.

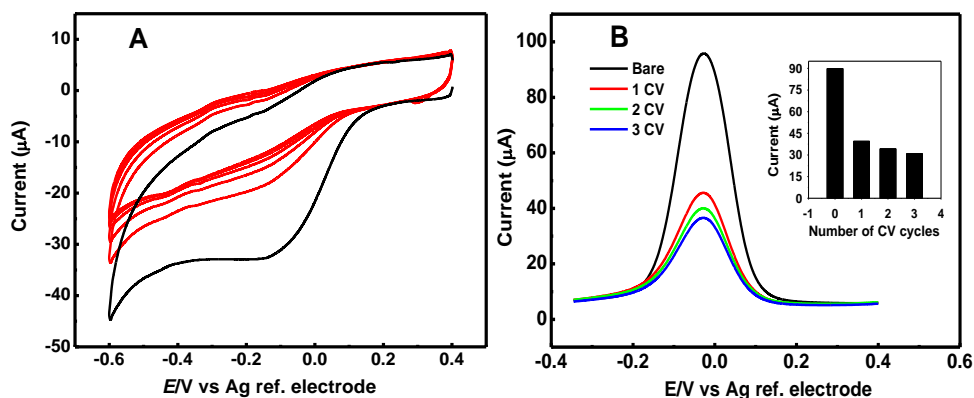


Figure 4 (A) CVs pour le sel de diazonium généré in situ 4-CP sur le GSPE, les lignes noires représentent le premier CV et les lignes rouges représentent les cycles subséquents, (B) DPV du GSPE à nu et 4-CP-GSPE fonctionnalisé par réduction de sel de diazonium en utilisant les différents cycles de CV à 5 mM $[\text{Fe}(\text{CN})_6]^{4-/3-}$. Le médaillon est l'intrigue de la crête de la réduction actuelle de 5 mM $[\text{Fe}(\text{CN})_6]^{4-/3-}$ mesuré à 4-CP-GSPE vs le nombre d'analyses de CV des cycles pour la réduction de diazonium sur GSPE.

Comme illustré dans l'encart de la Figure 5(A), une bonne relation linéaire a été obtenue entre le changement de la sonde de redox de pic cathodique actuel de $[\text{Fe}(\text{CN})_6]^{4-/3-}$ dans la DPV et le logarithme de la concentration de l'ovalbumine de $1,0 \text{ pg ml}^{-1}$ à $0,5 \text{ } \mu\text{g mL}^{-1}$. Les points de la courbe d'étalonnage représentent trois mesures indépendantes et les barres d'erreur affichent les écarts allant de 2,6 % à 5,0 % indiquant la bonne reproductibilité de l'immunocapteur. L'équation de régression linéaire a été $i_{o-i} (\mu\text{A}) = 9,98 + 2,81 \times \log C [\text{ng ml}^{-1}]$, $R = 0,997$, avec une limite de détection (LOD) de $0,83 \text{ pg mL}^{-1}$ ($S/N = 3$). Les résultats confirment que les expositions proposées de l'immunocapteur à une limite inférieure de détection comparée aux autres méthodes précédemment citée ^{4,60}. En outre, comme il est observé dans la Figure 5B, la diminution dans le courant de la β -lactoglobuline, BSA, lysozyme et caséine étaient beaucoup plus faible que celle de l'ovalbumine. Ces résultats indiquent que l'immunocapteur exposée à une bonne sélectivité pour la détermination de l'ovalbumine avec effet négligeable des protéines non spécifiques.

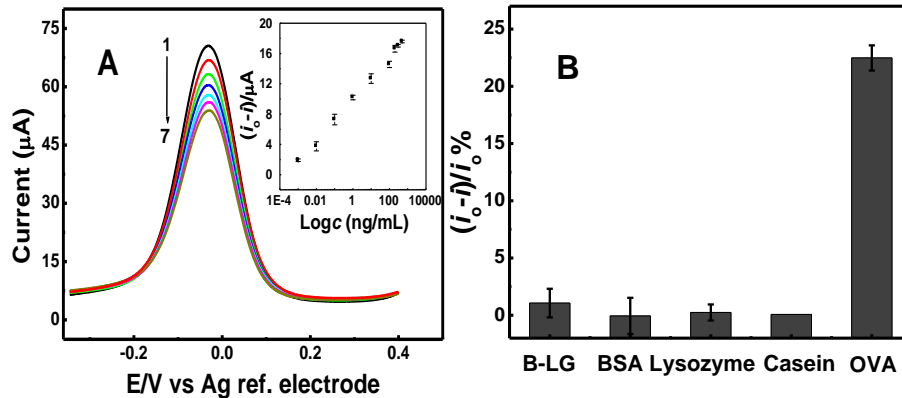


Figure 5 (A) DPV de l'immunocapteur incubée en présence de différentes concentrations de l'ovalbumine. Le médaillon est la courbe d'étalonnage. (B) Comparaison de la réponse de l'immunocapteur à 100 ng ml^{-1} d'ovalbumine, BSA, caséine, Lysozyme et la β -lactoglobuline.

En outre, l'approche d'électro-greffage appliquée sur une monocouche de graphène-CVD à permis une étude détaillée, la caractérisation des électrodes modifiées et par la suite l'application pour la biodétection impédimétrique d'ovalbumine. Cette première tentative d'utilisation de graphène fonctionnalisé de CVD en biodétection représente une preuve de concept qui peut être étendue à d'autres types d'applications de biodétection.

Les spectres Raman des électrodes de graphène avant et après la fonctionnalisation sont indiqués dans la figure 6(A). Le graphène nu (courbe noire), présente deux pics importants de Raman Stokes, un seul pic 2D symétrique à $\sim 2700 \text{ cm}^{-1}$ et un pic de G à $\sim 1580 \text{ cm}^{-1}$. L'intensité du pic 2D est presque deux fois plus grande que l'intensité du pic G sur la majeure partie de la zone de prélèvement. Ces résultats montrent que la monocouche de graphène transférée sur un substrat de verre est continue et uniforme²¹¹⁻²¹².

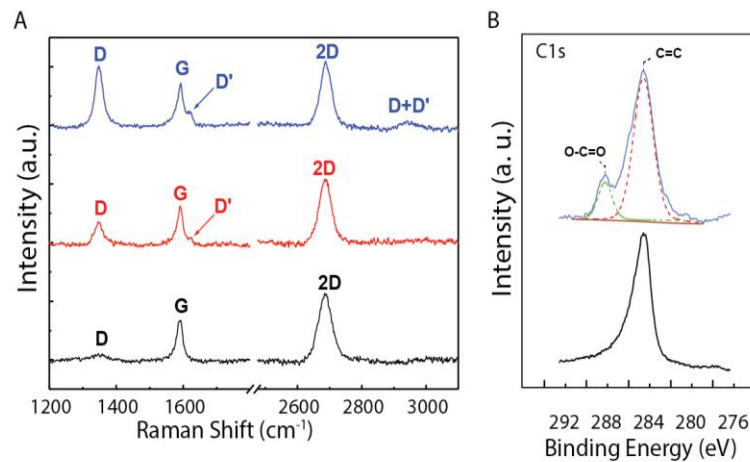


Figure 6(A) Spectres Raman de l'électrode de graphène avant (courbe noire) et après soumis au processus d'électro-greffage en utilisant un cycle (courbe rouge) et trois cycles de CV (courbe bleue) et (b) Spectre XPS C1s de l' électrode à base de graphène avant (en bas) et après la fonctionnalisation de la carboxyphényl (en haut).

Un petit pic de D à $\sim 1350 \text{ cm}^{-1}$ a également été observé dans le spectre Raman de graphène seul, correspondant à une faible densité de défaut. Après une modification

ultérieure du graphène en utilisant un (Figure 6 A, courbe rouge) à trois CV scans (Figure 3.15 (A), courbe bleue) dans la solution de diazonium, l'intensité du pic D s'est progressivement améliorée et les pics D', D+ et D* sont apparus respectivement à $\sim 1620 \text{ cm}^{-1}$ et $\sim 2950 \text{ cm}^{-1}$. Ces changements sont attribuables à la rupture de symétrie de translation du réseau en nid d'abeilles de C – C sp^2 obligatoires sur le plan de base de graphène dû à la formation localisée C – C sp^3 de liaisons par greffage carboxyphényl.

La figure 6 (B) montre les spectres XPS C1s des monocouches de graphène avant et après la fonctionnalisation de carboxyphényl. Pour le graphène nu, un pic à une énergie de liaison de 284,2 eV a été observé comme prévu pour les atomes de carbone hybridé sp^2 de graphène. Cependant, après la modification du carboxyphényl, il y a apparition d'un pic supplémentaire centré à 288,8 eV, ce pic est caractéristique des groupements carboxyliques greffés sur la surface de graphène. La figure 7 montre les images AFM obtenues en mode ScanAsyst révélant une différence significative entre le graphène avant et après modification par trois balayages de CV avec une valeur d'épaisseur moyenne estimée de 0,69 nm de la couche greffée. Cette valeur correspond à la longueur théorique de 0,69 nm pour la portion carboxyphényl estimée par le logiciel ChemDraw Ultra 13,0 (Figure 7D, ce qui indique que la couche mince greffée est principalement de type monocouches.

La figure 8(A) montre la détection de l'ovalbumine qui est représenté par une augmentation du taux de liaison de à l'anticorps, impliquant ainsi une augmentation de la R_{CT} . Une parcelle d'étalonnage basée sur la variation en pourcentage dans le R_{CT} suite à la liaison de l'ovalbumine est illustrée à la Figure 8(B). Une bonne relation linéaire a été obtenue entre la variation en pourcentage dans le R_{CT} de l'immunocapteur contre le logarithme de la concentration de l'ovalbumine dans la gamme de 1 pg mL^{-1} à 100 ng mL^{-1} . Les écarts-types des mesures ont été de 3,0 % à 7,0 % indiquant la bonne reproductibilité de l'immunocapteur. L'équation de régression linéaire est $(R-R^0) / r^0 \% = 39,0 + 4,29 \times \log C [\text{ng mL}^{-1}]$, $R = 0,98$, avec une limite de détection calculée (LOD) de $0,9 \text{ pg mL}^{-1}$ ($S/N = 3$). Le résultat confirme que la plate-forme de graphène CVD monocouche offre une bonne sensibilité et une limite de détection similaire à celle rapportée avec GSPE¹⁵⁵. La figure 8C montre la réponse de l'immunocapteur impédimétrique à la β -lactoglobuline et lysozyme. Celle-ci étant beaucoup plus faible que

celle de l'ovalbumine, elle illustre la bonne sélectivité et l'adsorption négligeable non spécifique sur la plate-forme de graphène

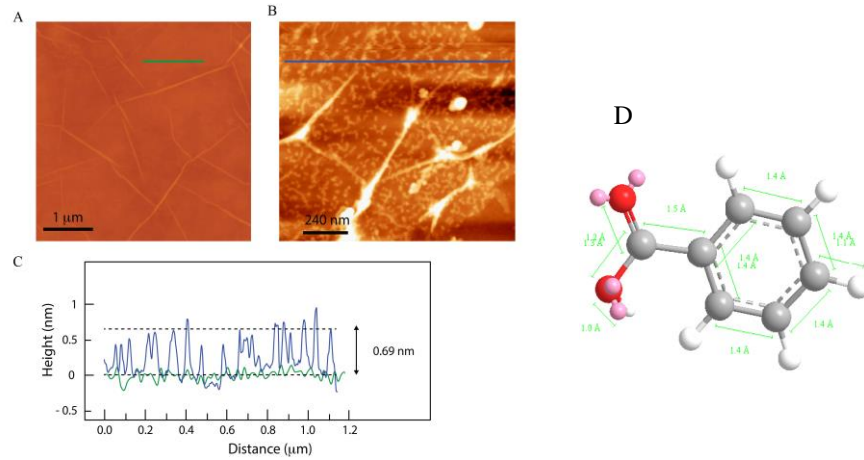


Figure 7(A) AFM images de graphène avant modification et (B) le graphène carboxyphényl modifié. (C) les profils de hauteur avec deux lignes scans sélectionnées. Ligne verte indique le graphène et ligne bleue indique le graphène modifié. La hauteur moyenne des groupes carboxyphényl est environ 0,69 nm et (D) estimation théorique de la longueur de la portion de carboxyphényl à l'aide du logiciel ChemDraw Ultra 13,0.

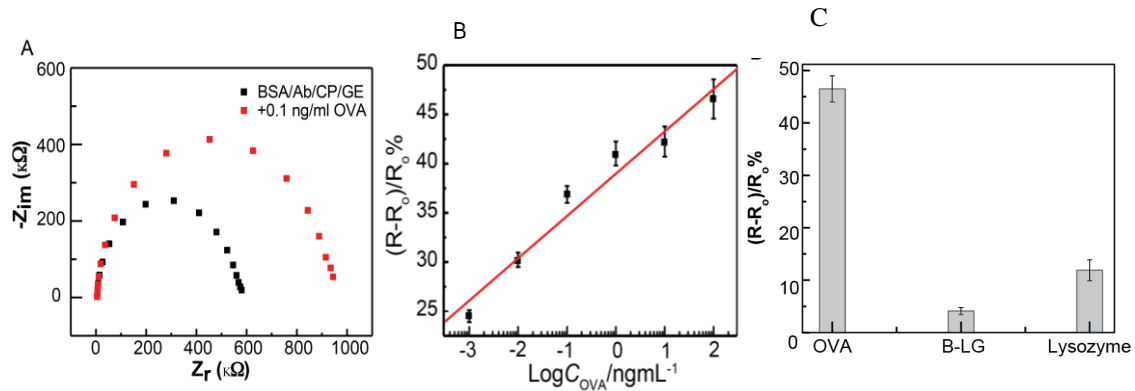


Figure 8(A) Le diagramme de Nyquist des OVA immunocapteur avant incubation (noir) et après (rouge) avec 0,1 ng/ml OVA. (B) dépendance à l'égard de la réponse de l'immunocapteur sur la concentration des OVA (parcelle de $(R-R_0) / R_0\%$ vs C_{OVA}) et (C) la comparaison de la réponse de l'immunocapteur à 100 ng ml⁻¹ d'ovalbumine, 1μg/ml Lysozyme et la β-lactoglobuline.

Les publications reliées au présent chapitre

- 9- Shima Eissa, Chaker Tlili, Lamia L'Hocine, Mohammed Zourob, Electrochemical immunosensor for the milk allergen β -lactoglobulin based on electrografting of organic film on graphene modified screen-printed carbon electrodes, *Biosens. Bioelectron.*, 2012, 38, 308–313.
- 10- Shima Eissa, Lamia L'Hocine, Mohamed Siaj, Mohammed Zourob, Graphene-based label free voltammetric immunosensor for sensitive detection of the egg allergen ovalbumin, *Analyst*, 2013, 138, 4378–4384.
- 11- Shima Eissa, Gaston Contreras Jimenez, Farzaneh Mahvash, Abdeladim Guermoune, Chaker Tlili, Thomas Szkopek, Mohammed Zourob, and Mohamed Siaj, Functionalized CVD monolayer graphene for label-free impedimetric biosensing, *Nano research*, 8, 1698-1709.

Chapitre 4. Un immunocapteur électrochimique compétitif axé sur le graphène pour la sensibilité de la détection de l'acide okadaïque des coquillages.

Les électrodes de graphène carboxyphényl modifiées (CP-GSPE) ont été également exploitées pour développer immunocapteurs voltampérométriques compétitif pour la détection de la conchyliculture toxine de l'acide okadaïque (OA). Cela a été présenté dans le chapitre 4. Une analyse concurrentielle entre OA et la concentration fixe de conjugué d'ovalbumine-acide okadaïque (OA-OVA) d'anticorps immobilisés sur le CP-GSPE a été employée pour détecter l'acide okadaïque. L'immunocapteur développé a permis la détection sensible d'OA dans le tampon PBS. L'effet de la matrice étudié avec des extraits de tissus de crustacés dopés a montré un bon pourcentage de récupération et la méthode était également validée avec des échantillons de moules de référence certifiée.

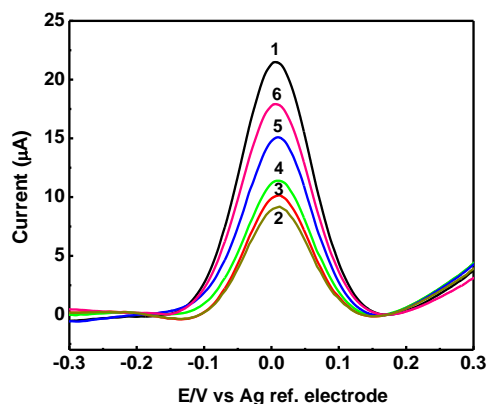


Figure 9 SWVs de l'immunocapteur avant l'étape de la compétition (1) et après incubation en présence de différentes concentrations de OA mélangée à 1 µg/ml de OA-OVA (2 – 6): les concentrations de l'arthrose sont 0,000, 1.00, 10.0, 100 et 1000 ng L⁻¹.

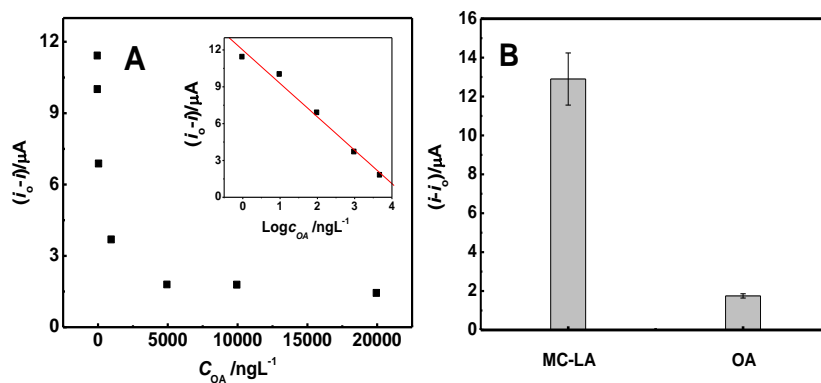


Figure 10 (A) La dépendance de la réponse de l'immunocapteur de la concentration de l'acide okadaïque (tracé de la différence de la crête du courant vs C_{OA}). En médaillon : courbe d'étalonnage pour OA, parcelle de crête du courant vs **log** C_{OA} , (B) Comparaison de la réponse du GSPE des immunocapteurs voltampérométriques 10 µgL⁻¹ OA et la MC.

Ce chapitre a été publié dans l'article suivant

4- Shima Eissa, Mohammed Zourob, A graphene-based electrochemical competitive immunosensor for the sensitive detection of okadaic acid in shellfish, *Nanoscale*, 2012, 4, 7593–7599.

Chapitre 5. La caractérisation et la sélection d'un aptacapteur électrochimique sans marqueur pour les toxines marines

Les aptamères qui se lient avec une grande affinité et spécificité à OA, brevetoxin-2 (BTX-2), les biotoxines marines qui s'accumulent dans les coquillages ont été sélectionné, identifié et caractérisé. Cela a été présenté au chapitre 5. Les aptamères ont été sélectionnés à l'aide d'une évolution systématique des ligands par enrichissement exponentiel (SELEX) et présentaient des constantes de dissociation dans une gamme nM. La liaison des toxines de la cible aux aptamères piscines/séquences a été suivie à l'aide de la fluorescence et les techniques de spectroscopie d'impédance électrochimique (SIE).

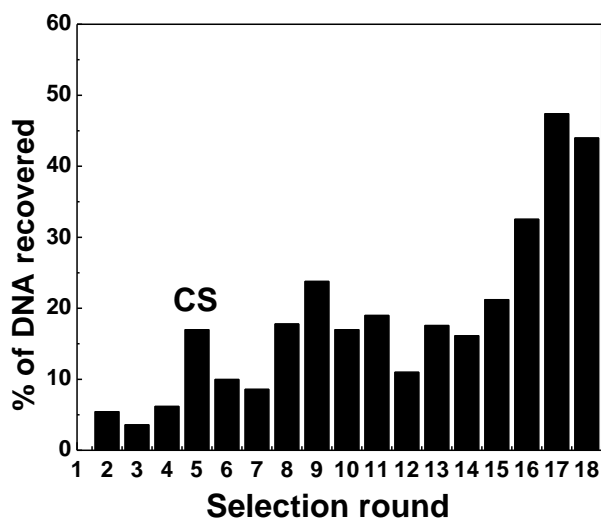


Figure 11 Enrichissement d'aptamères spécifiques d'acide okadaïque pendant SELEX. Le graphique à barres montre les quantités de ssDNA éluée des OA-enduit de billes dans chaque tour de sélection. Les cinq premières rondes, une étape de sélection du compteur (CS) a été introduite pour supprimer l'ADNs non spécifique lié à la matrice de billes.

Les constantes de dissociation (K_d) des aptamères sélectionnés ont été calculées par analyse de régression non linéaire (Figure 12, 13). Comme illustré dans la Figure 12 (B), le changement dans les spectres CD indique le pliage de l'aptamère en une conformation différente lors de la liaison avec OA.

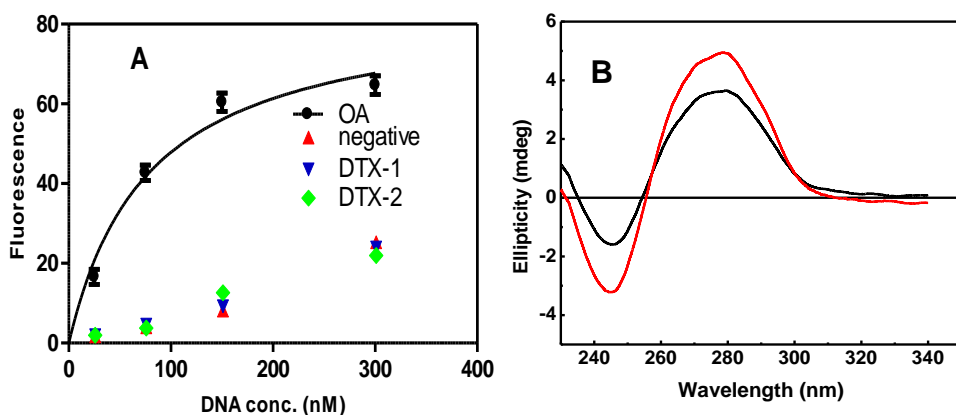


Figure 12 Teste de liaison du Fluorescence d'OA et aptamère OA34. Le K_d a été établi à 77 nM. Chaque point correspond à la moyenne de trois expériences et les barres d'erreur représentent les écarts types de la mesure (B) spectres de dichroïsme circulaire de 0,67 μ M de l'aptamère OA34 dans le tampon de liaison avant liaison (noir) et après liaison (rouge) avec 0,66 μ g/ml d'OA à température ambiante.

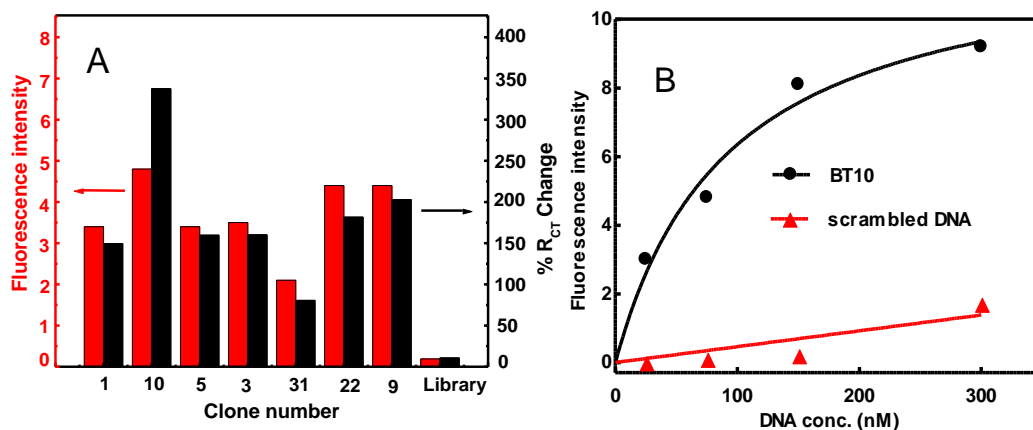


Figure 13 (a) Teste de liaison des séquences d'aptamère individuelles BTX 1, 10, 5, 3, 31, 22 et 9, pour tester leur capacité à se lier aux perles de BTX (rouge) et les électrodes BTX (noir). La bibliothèque initiale non enrichie a été utilisée comme contrôle négatif. (B) courbe de fluorescence de liaison de BTX-2 à l'aptamère BT10 (noir) et une séquence d'ADN brouillée (rouge).

Les aptamères avec les meilleures affinités ont ensuite été utilisés pour la fabrication de biocapteurs électrochimiques sans marqueur pour la détection des OA et BTX-2. Les aptamères

sélectionnés offrent des alternatives prometteuses aux anticorps actuellement employés et peuvent être exploités dans des test de détection de différentes toxines.

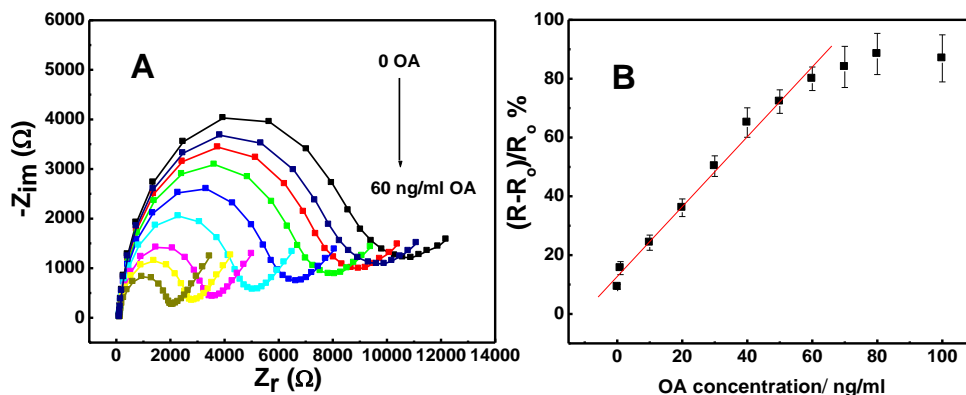


Figure 14 (A) Courbe de Nyquist de l'aptacapteur après incubation avec différentes concentrations d'OA 0,0, 0,1, 1,0, 10, 20, 30, 40, 50 et 60 ng / ml. (B) La courbe d'étalonnage pour l'arthrose, tracé de $\Delta R_{ct}/R_0\%$ vs C_{OA} . Les barres d'erreur affichent l'écart de trois mesures répétitives.

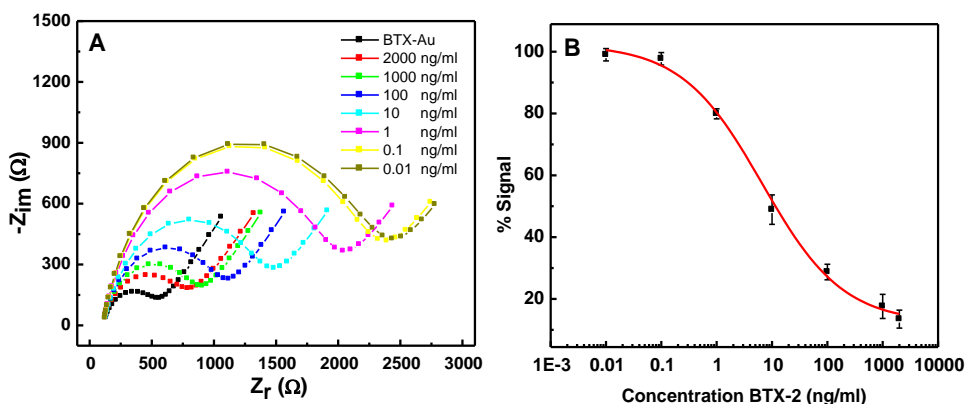


Figure 15 (A) Courbe de Nyquist de l'électrode BTX avant et après incubation avec différentes concentrations de BTX-2 mélangée à 500 nM d'aptamère, (B) courbe d'étalonnage pour BTX-2, tracé de la réponse analytique (% de Signale $[(R_{CT} - R_i) / (R_{max} - R_i) \times 100]$) vs. Concentration de BTX-2. Les barres d'erreur affichent l'écart pour deux mesures répétitives.

Les publications reliées au présent chapitre :

5- Shima Eissa, Andy Ng, Mohamed Sij, Ana C. Tavares, Mohammed Zourob, Selection and identification of DNA aptamers against okadaic acid for biosensing application, *Anal. Chem.*, 2013, 85, 11794–11801.

6- Shima Eissa, Mohamed Siaj, Mohammed Zourob, Aptamer-Based Competitive Electrochemical Biosensor for Brevetoxin-2, *Biosens. Bioelectron.*, 2015, 69, 148–154.

Chapitre 6. Aptacapteur voltampérométrique sans marqueur pour la détection sensible de la microcystine-LR à l'aide des électrodes de graphène modifiées.

Grâce à l'intégration de la grande affinité et spécificité des aptamères d'ADN et du graphène. Un aptacapteur fortement sensible et sélectif pour la microcystine-LR (MC-LR) a été développé avec succès. Ce dernier n'a pas démontré de réactivité croisée avec MC-LA et YR, il a été utilisé en tant que modèle. Une stratégie facile a été appliquée pour la fabrication d'aptacapteur issue de l'assemblage non covalent d'aptamère d'ADN sur le GSPE.

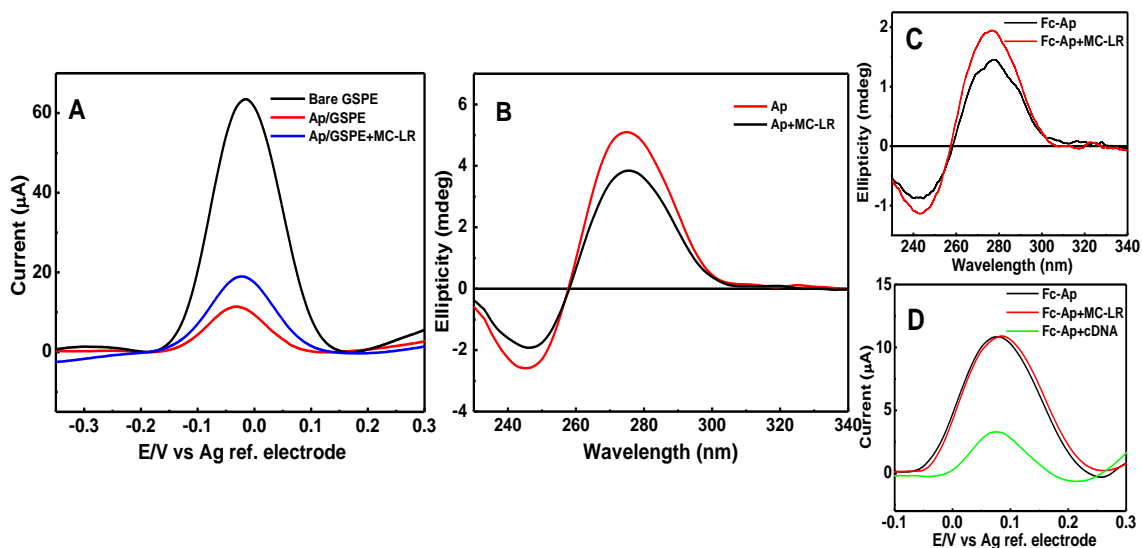


Figure 16(A) SWVs de 1 mM [Fe (CN)₆]^{4-/3-} dans du PBS, pH 7,4 pour GSPE (noir), GSPE fonctionnalisés avec l'aptamère MC-LR (rouge) et après une incubation de toxine de MC-LR (bleu) (la concentration de l'aptamère, 10 μM ; concentration du MC-LR, 1 nM) ; (B) Spectres CD de 0,67 μM d'aptamère MC-LR dans le tampon avant liaison (noir) et après (rouge) avec 0,67 μM de MC-LR à température ambiante ; (C) spectres CD de 0,4 μM Fc/Ap dans une solution tampon avant liaison (noir) et après (rouge) avec 0,4 μM de MC-LR à température ambiante ; (D) SWV en blanc 10 mM PBS solution tampon pH 7,4 pour Fc/Ap/GSPE (noir), après incubation de Fc/Ap/GSPE avec 1 nM MC-LR (rouge) et après incubation de Fc/Ap/GSPE avec l'ADNc (vert).

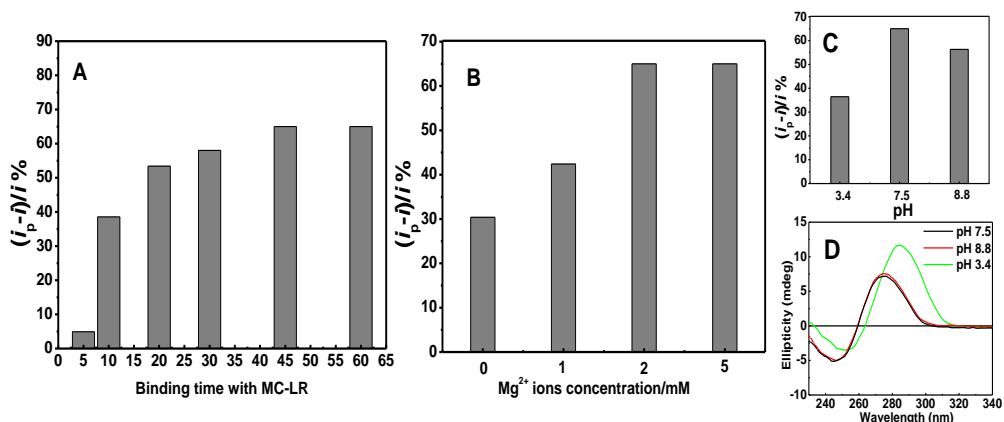


Figure 17(A) L'effet du temps d'incubation d'aptacpteur sur réponse vers 1 nM MC-LR. (B) Réponse d'aptacpteur envers 1 nM MC-LR dans une solution tampon contenant une concentration différente en $MgCl_2$. (C) Réponse de l'aptacpteur envers 1 nM MC-LR dans le tampon à différents pHs. Toutes les mesures ont été effectuées dans une solution de 10 mM PBS (pH 7,4) contenant 1 mM du couple redox $[Fe(CN)_6]$. (D) le spectre de CD de l'aptamère MC-LR dans le tampon de liaison avec pH 7.5 (noir), 8,8 (rouge) et 3.4 (courbe verte).

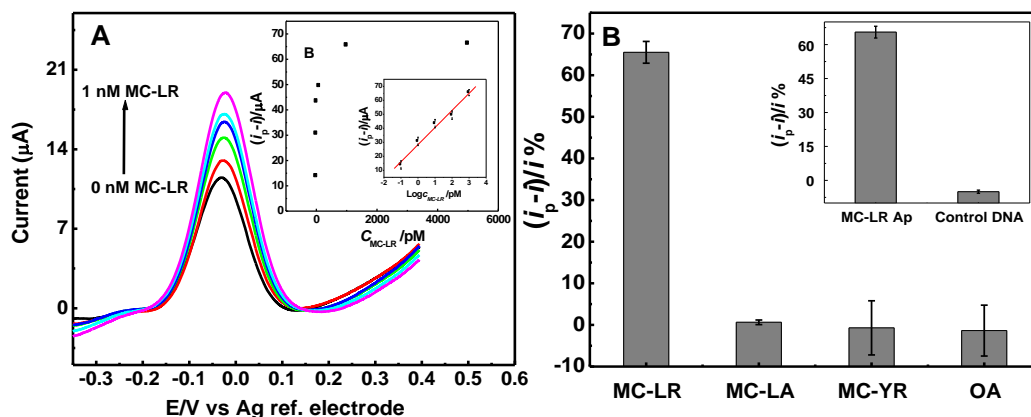


Figure 18 (A) SWVs de l'aptacpteur après 45 min d'incubation avec 0,00, 0,1, 1,0, 10, 100 et 1000 h MC-LR. L'encadré représente la dépendance à l'égard de la réponse de l'aptacpteur envers la concentration en MC-LR (tracé du pourcentage de la variation du courant vs C_{MC-LR}), le petit encadré représentant la courbe d'étalonnage pour la détection de MC-LR dans le tampon; est la courbe de la variation en pourcentage du pic du courant contre le logarithme de la concentration de MC-LR. (B) Réponse de l'aptacpteur à 1,0 nM de MC-LR, OA, MC-LA et MC-YR. L'encadré est la comparaison entre GSPE modifié et l'aptamère MC-LR et la séquence d'ADN non spécifique à 1 nM MC-LR.

Cette nouvelle approche a conduit à une méthode de détection rapide, peu coûteuse, sensible et spécifique pour la MC-LR dans un tampon et échantillons d'extrait de poissons enrichis, offrant ainsi plusieurs avantages par rapport aux méthodes rapportées antérieurement. Tout d'abord, l'aptacapteur a été fabriqué sans marqueur, réduisant au minimum les coûts, la complexité et préserver l'affinité de l'aptamère à MC-LR. Deuxièmement, l'utilisation d'électrodes de graphène a permis d'atteindre une bonne sensibilité, en comparaison avec d'autres capteurs pour le MC-LR, d'autres protocoles de fabrication sophistiqués et systèmes de détection. Enfin, cet aptasensor axé sur le graphène est hautement spécifique au MC-LR contrairement à d'autres microcystine congénères ce qui est difficilement réalisables par les tentatives précédentes. En outre, nous avons démontré dans ce travail que le mécanisme de la détection repose sur le changement de conformation dans une partie de la séquence d'aptamère sans libération complète de la surface de graphène. Nous pensons également que cette découverte est importante pour l'exploitation des aptamères dans la détection d'autres petites molécules à l'aide de plates-formes de graphène à l'avenir.

Chapitre 7. Influence de la taille des feuillets d'oxyde de graphène sur la performance de biocapteurs électrochimiques

Enfin, pour une meilleure compréhension du comportement de différents échantillons de graphène qui peuvent être utilisés pour la biodétection, une étude systématique a été réalisée afin d'examiner dans quelle mesure la taille des feuillets d'oxyde de graphène allait influencer leurs propriétés structurales ainsi que leurs performances de biodétection. Les feuillets d'oxyde de graphène avec des gammes de tailles différentes ont été séparés. Les feuillets étaient alors caractérisés par microscopie à force atomique (AFM), microscopie électronique à balayage (MEB), spectroscopie Raman et spectrométrie photoélectronique des rayons X (XPS).

La performance de biodétection de ces échantillons a été comparée en utilisant les ADN aptamère contre la toxine MC-LR, ainsi qu'un anticorps dirigé contre la β -LG en format de détection sans marqueur. Nous avons observé des tendances différentes entre la taille des feuillets de GO et la sensibilité de l'aptasensors MC-LR et de l'immunocapteurs β -LG fabriqués à l'aide de lien covalente ou d'adsorption physique. Nos résultats démontrent que le contrôle de la taille des feuillets de GO a un impact profond sur leur utilisation dans des applications spécifiques de biodétection.

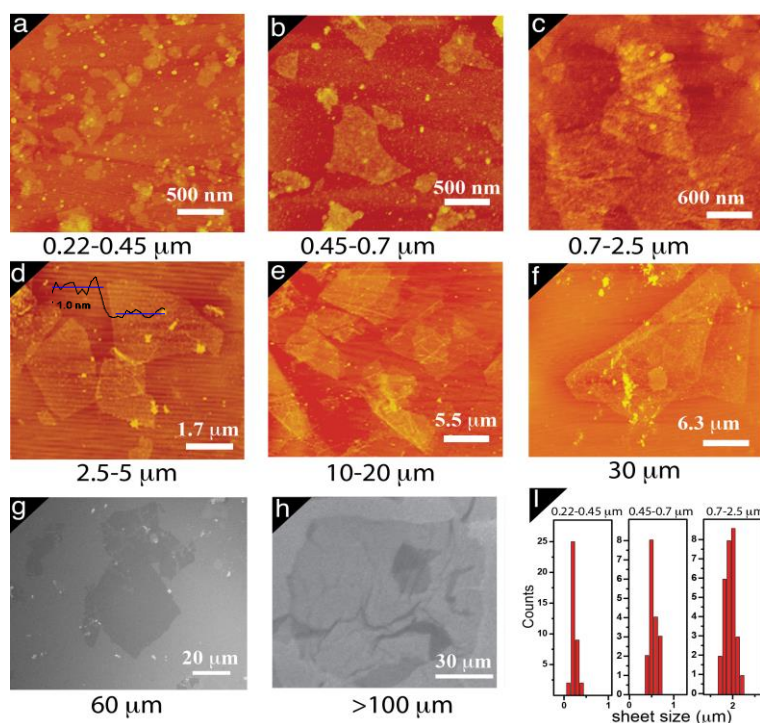


Figure 19 Images AFM et MEB des feuillets d'oxyde de graphène.

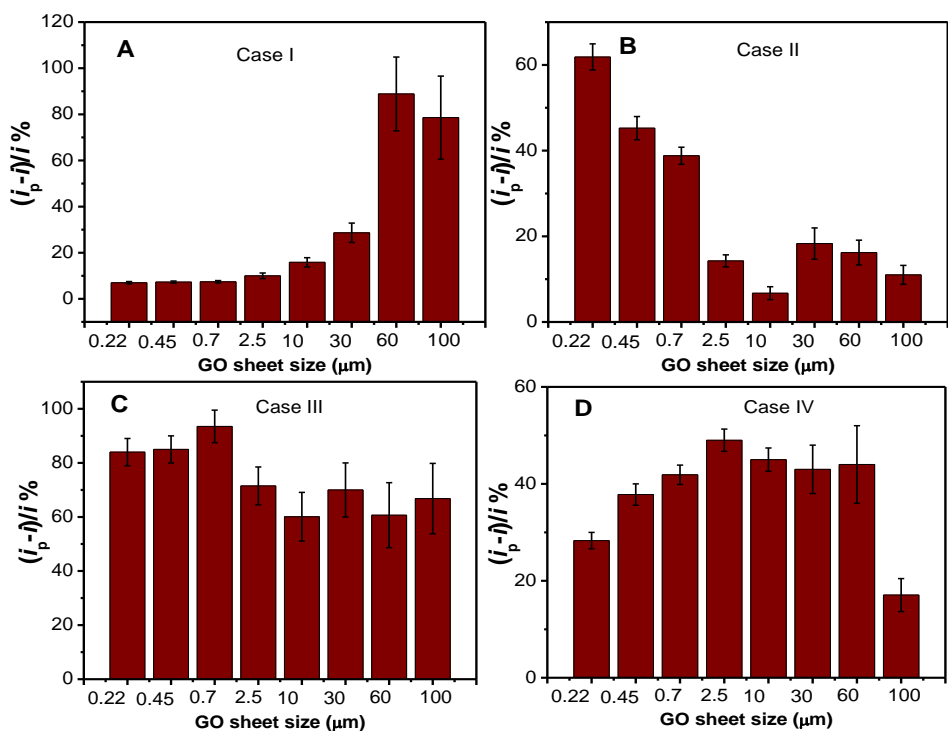


Figure 20 réponse des Aptasensor et immunocapteurs.